ISSN 0915-6348

NATIONAL INSTITUTE FOR FUSION SCIENCE

Workshop on

Extremely High Energy Density Plasmas and Their Diagnostics

Mar. 8-9, 2001

National Institute for Fusion Science

Edited by S. Ishii

(Received - Aug. 24, 2001)

NIFS-PROC-50 Sep. 2001

RESEARCH REPORT
NIFS-PROC Series

TOKI, JAPAN

Workshop on

Extremely High Energy Density Plasmas and Their Diagnostics

Edited by S. Ishii

March 8-9, 2001
National Institute for Fusion Science
Toki, Japan

Abstract

Compiled are the papers presented at the workshop on "Extremely High Energy Density Plasmas and Their Diagnostics" held at National Institute for Fusion Science. The papers cover physics and applications of extremely high-energy density plasmas such as dense z-pinch, plasma focus, and intense pulsed charged beams.

Keywords: high energy density plasma, z-pinch, plasma focus, high power pulsed ion beam, intense relativistic electron beam, intense soft x-ray source, material processing

PREFACE

The proceedings contain the paper presented at the workshop on "Extremely High Energy Density Plasmas and Their Diagnostics" held at National Institute for Fusion Science in Toki on March 8-9, 2001. The workshop was organized as a collaboration research programs of NIFS and attracted 51 participants from university ant institute. At the workshop, 32 papers were presented and cover physics and applications of extremely high-energy density plasmas such as dense z-pinch, plasma focus, and intense pulsed charged beams. We thank to NIFS for giving the opportunity to gather scientists in this particular field.

Shozo Ishii

CONTENTS

LIST OF PARTICIPANTS

H. Akiyama	Kumamoto University
R. Ando	Kanazawa University
Y. Doi	Toyama University
H. Fujii	Kanazawa University
S. Furuya	Nagaoka University of Technology
Y. Hashimoto	Kobe City College of Technology
K. Horioka	Tokyo Institute of Technology
S. Ibuka	Tokyo Institute of Technology
G. Imada	Nagaoka University of Technology
J. Irisawa	Nagaoka University of Technology
S. Ishii	Tokyo Institute of Technology
H. Itano	Gunma University
N. Iwami	Gunma University
K. Kamada	Kanazawa University
M. Kamada	Kanazawa University
Y. Kawahara	Toyama University
S. Kawata	Utsunomiya University
T. Kikuchi	Tokyo Institute of Technology
S. Kitayama	Nagaoka University of Technology
T. Kuraoka	Tokyo Institute of Technology
M. Masnavi	Tokyo Institute of Technology
K. Masugata	Toyama University
T. Miyamoto	Nihon University
H. Morishita	Kanazawa University
H. Mouri	Nagaoka University of Technology
K. Murayama	Yatsushiro National College of Technology
R. Muto	Nihon University
Y. Nakagawa	Osaka City University
M. Nakajima	Tokyo Institute of Technology
T. Nakamura	Utsunomiya University

T. Namihira	Kumamoto University
S. Narusawa	Nihon University
G. Niimi	Tokyo Institute of Technology
H. Nozawa	Tokyo Institute of Technology
K. Ogasawara	Tokyo Institute of Technology
A. Okino	Tokyo Institute of Technology
M. Sato	Gunma University
S. Seino	Nagaoka University of Technology
N. Shimomura	The University of Tokushima
T. Someya	Utsunomiya University
S. Sorasit	Nagaoka University of Technology
H. Suematsu	Nagaoka University of Technology
K. Takao	Toyama University
K. Takasugi	Nihon University
T. Tazima	National Institute of Fusion Science
Y. Teramoto	Kumamoto University
N. Toyosugi	Kanazawa University
S. Wada	Kanazawa University
T. Yamamoto	Fukushima National College of Technology
S. C. Yang	Nagaoka University of Technology
K. Yasuoka	Tokyo Institute of Technology
K. Yatsui	Nagaoka University of Technology

Generation of Intense Pulsed Ion Beam by a B_r Type Magnetically Insulated Ion Diode With Carbon Plasma Gun

Y. Doi, Y.Maetubo, I.Kitamura, T.Takahasi, K.Masugata,
Y.Tanaka*, H.Tanoue*, and K.Arai*

Faculty of Eng., Toyama Univ., Toyama, 930-8555 Japan
Electro technical Laboratory, 1-1-4, Tsukuba, Ibaraki, 305-8568 Japan*

ABSTRACT

To apply the pulsed heavy ion beam (PHIB) to an implantation process of semiconductor, purity of the ion beam is very important. To obtain a pure PHIB we have proposed a new type of accelerator using bipolar pulse. To develop the accelerator we are developing a new type of B_r ion diode using a carbon plasma gun. By using the plasma gun, ion source plasma of ion current density ≈ 30 A/cm^2 was obtained. The B_r ion diode was successfully operated with plasma gun at diode voltage ≈ 100 kV, diode current ≈ 1 kA, pulse duration ≈ 200 ns and 3 A/cm^2 of ion current density was obtained.

1. Introduction

Intense pulsed heavy ion beams (PHIB) such as carbon, nitrogen, or aluminum have a wide area of applications including nuclear fusion, materials science, etc. By the irradiation of PHIB on to the material, very attractive effects are expected as shown in the following, which seems to be very attractive for materials processes.

1) Pulsed surface heating,
2) Production of high dense ablation plasma
3) Production of strong pressure and shock wave,
4) Deposition of atoms.

Hence it is expected to apply for a surface treatment, thin films deposition, or an implantation process. Especially for the implantation of PHIB is expected as a new type of

ion implantation technology since the ion implantation and surface heat treatment or surface annealing is expected in the same time.

The PHIB can be easily generated in pulsed power ion diodes with surface flashover ion sources, however, since many kinds of atoms are attached on the surface, which are ionized and accelerated with expected ions [1]. Hence the purity of the conventional PHIB is very poor. To apply the PHIB to the implantation process of semiconductor, the purity is very important. For example, in a point pinch ion diode experiment we found that produced ion beam contains protons, multiply ionized carbons, organic ions, etc [1].

To improve the purity of the PHIB a new type of pulsed power accelerator using bi-directional pulse is proposed [2], [3]. As the first step of the development of the accelerator, we are developing an ion diode using a pulsed plasma gun. In the paper the preliminary result of the experiment is shown.

2. Ion diode experiment

As the first step of the development of pure PHIB source we are evaluating the B_r magnetically instated ion diode with pulsed plasma gun. Figure 1 shows the schematic of the experimental system. The system consists of a high voltage pulsed power generator, a carbon plasma gun as an ion beam source, and a B_r type magnetically insulated ion diode (acceleration gap).

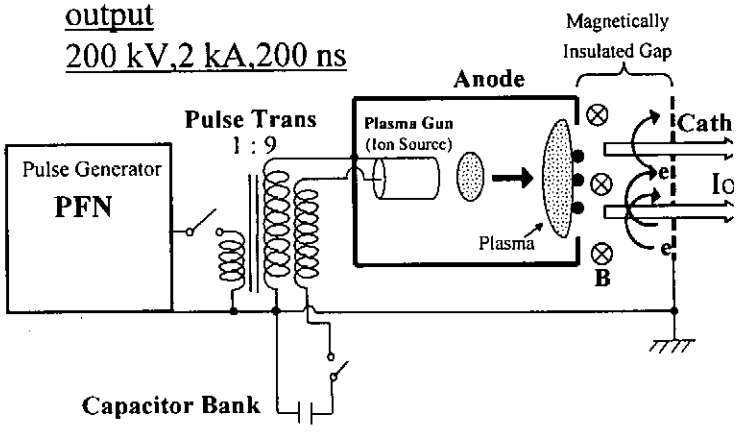

Fig.1. Schematic of the experimental system.

The pulsed power generator consists of a L-C pulse-forming network (PFN) and a step up transformer using a magnetic core of amorphous metallic material. In the PFN, high power square pulse of 25 kV, 25 kA, and 200 ns is generated when PFN is charged to the full charging voltage of 50 kV. The pulse is voltage magnified by the step up transformer and generates a pulse of 200 kV, 2 kA, 200 ns, which is applied to the anode of the ion diode. Since the plasma gun is placed inside the anode where high voltage pulse is applied, power feed cable of the gun is connected through the pulse transformer to the capacitor bank. The diode operation is as follows. 1) By applying pulsed voltage to the plasma gun, source plasma is generated and accelerated toward the acceleration gap. 2) When the plasma reaches the gap, high voltage pulse is applied to the gap and the ions in the anode plasma are accelerated toward the cathode. Since the insulating magnetic field is produced in the gap

prior to the main pulse, electron to the anode is insulated and ion is efficiently accelerated in the gap.

Figure 2 shows the cross-sectional view of the diode used in the experiment. As the acceleration gap B_r type magnetically insulated diode [4] is used. The anode of the diode is made of aluminum and the outer diameter, the inner diameter and the thickness are 50 mm, 30 mm, and 20 mm, respectively. The anode has two slits of width 6 mm (inner) and 6.5 mm (outer) to pass through the source plasma. The cathode is made of stainless steel and it consists of an inner cathode (outer diameter 30 mm) and an outer cathode (inner diameter 50 mm). Both cathodes have magnetic field coils inside them to produce pulsed insulating magnetic field of rise-time 100 μs. The coils are powered by a capacitor bank of 250 F, 3 kV. The magnetic coil is designed to produce magnetic field lines almost parallel to the anode surface.

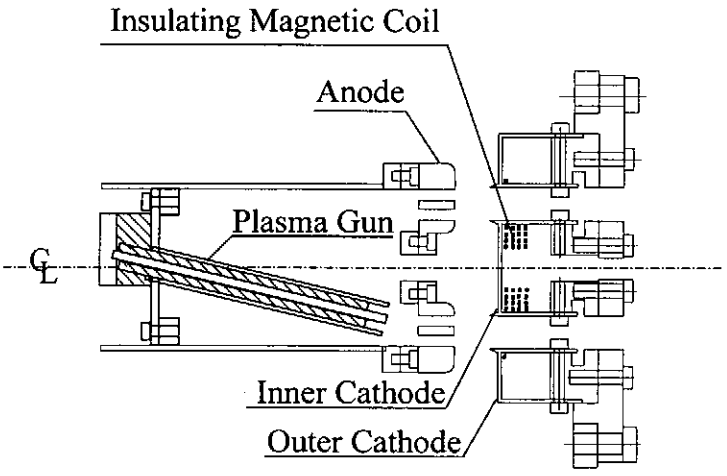

Fig.2. Cross-sectional view of the diode used in the experiment.

In the experiment, the anode cathode gap was adjusted to be 20 mm and insulating magnetic field on the anode surface at r = 30 mm of 0.5 T is obtained when charging voltage of the capacitor bank is 3 kV. The diode was evacuated to 10^{-4} Torr in the experiment.

The sequence of the diode operation is as follows.

1) The PFN, capacitor banks of the plasma gun and the magnetic field coils are charged.
2) At first (t_0) magnetic field coil is fired to produce insulating magnetic field.
3) 90 μs after t_0, plasma gun is fired to produce source plasma.
4) 100 μs after t_0, PFN is triggered to produce acceleration pulse.

3. Experimental results

Characteristics of the plasma gun were evaluated independently. The arrangement of the measurement is shown in Fig. 3. In the measurement, anode was removed

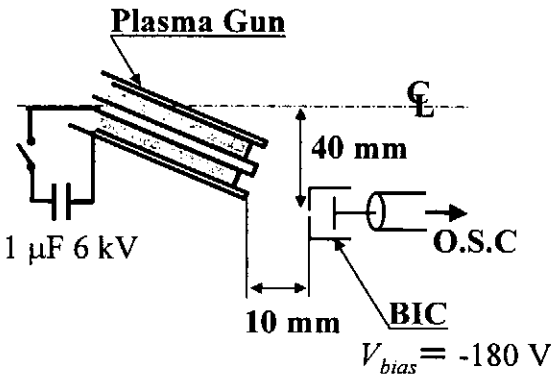

Fig. 3. Experimental setup of ion current density of plasma gun

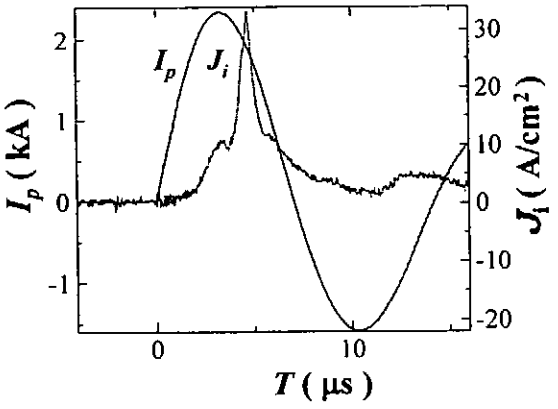

Fig.4. Typical waveforms of discharge current (I_p) and ion current density measured by BIC (J_{ip})

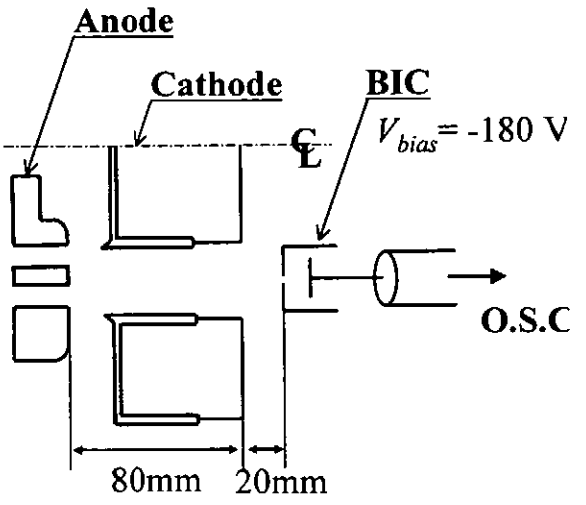

Fig.5. Setup of the ion diode experiment.

and a biased ion collector (BIC) was placed 1 cm downstream from the top of the plasma gun. The charging voltage of the capacitor bank was 6 kV.

Figure 4 shows the typical waveforms of discharge current (I_p) and ion current density measured by BIC (J_{ip}). As seen in the figure I_p has a sinusoidal waveform of peak current 2.3 kA and 4 μs after the rise of I_p, J_{ip} has a peak of 30 A/cm^2.

Figure 5 shows the setup of the ion diode experimental. The BIC was placed at r = 40 mm from the axis and 50 mm downstream from the surface of the anode. The charging voltage of the capacitor bank of the plasma gun and the magnetic coil was 6 kV and 3 kV, respectively. The PFN was 50 % of the full charge voltage.

Figure 6 shows the typical waveforms of diode voltage (V_d), diode current (I_d) and ion current density (J_i). As seen in the figure, V_d rises in 100 ns and has a plateau of 100 kV. On the other hand I_d rises with V_d and have a narrow peak of 1.1 kA and after that

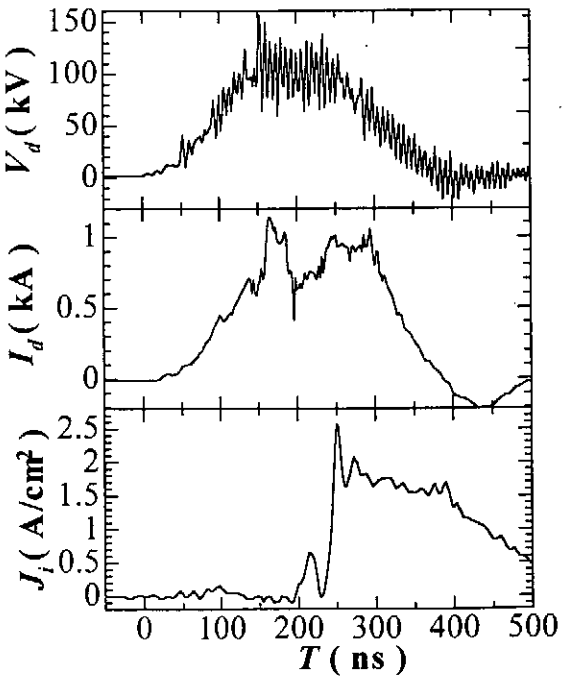

Fig.6. Typical waveforms of the diode voltage (V_d), the diode current (I_d) and ion current density (J_i)

decreases and have a second peak at t = 250 ns. The 1st peak and the 2nd peak seem to correspond to the ion current flow from the anode and the increase of leakage current, respectively. The ion current density of 2.5 kA/cm^2 was observed at t = 250 ns. Considering the time of flight delay, the ions corresponding the peak of J_i seems to be accelerated at the 1st peak of I_d.

Figure 7 shows the pinhole image of the ion beam obtained on an ion track detecting plastic of CR-39. The pinhole was placed 86 mm downstream from the anode. In the figure we see two large images each of which correspond to the ions accelerated from inner and outer slits of the anode. In addition, the image corresponding to the inner slit has two components, which suggest the existence of two components of ion species.

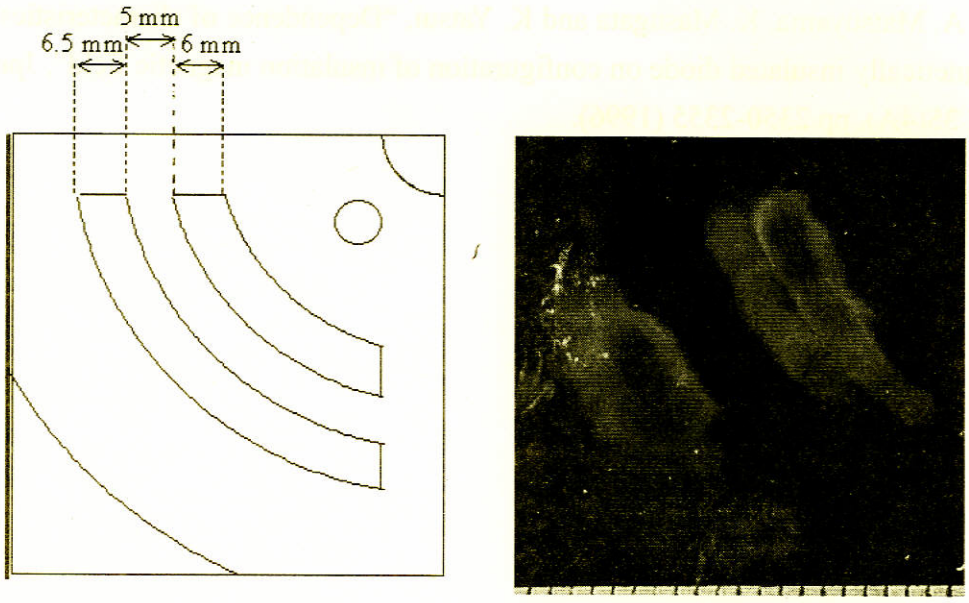

(a) (b)

Fig.7. An pinhole image of the ion beam obtained on an ion track detecting plastic of CR-39, a) 1/4 sector of the Anode, b) pinhole image.

4.Summary

A new type of B_r ion diode using a carbon plasma gun was successfully developed. I n the diode, ion source plasma of ion current density ≈ 30 A/cm^2 was obtained using a carbon plasma gun. The B_r ion diode was successfully operated with the plasma gun at diode voltage ≈ 100 kV, diode current ≈ 1 kA, pulse duration ≈ 200 ns and 3 A/cm^2 of ion current density was obtained.

References

[1] K. Masugata, H. Okuda, K. Yatsui and T. Tazima, "Diagnosis of high-brightness ion beams produced in point pinch diodes", J. Appl. Phys. **80**(9) pp. 4813-4818 (1996)

[2] K. Masugata, "High current pulsed ion beam accelerators using bi-directional pulses" Nuclear Instruments & Methods in Physics Research, Section **A 411** pp.205-209 (1998)

[3] K. Masugata, K. Kinbara, T. Atsumura, Y. Kawahara, T. Takao, I. Kitamura, and T. Takahashi, "Generation and Purification of High Current Pulsed Heavy Ion Beam using Bi-directional Pulses", Proceedings of 12th Symposium on High Current Electronics (1st Int'l Congress on Radiation Physics, High Current Electronics, and Modification of Materials, Tomsk, Russia, 24-29 September 2000), pp.111-114 (2000)

[4] E. Chishiro, A. Matsuyama, K. Masugata and K. Yatsui, "Dependence of characteristics of Br-type magnetically insulated diode on configuration of insulation magnetic field", Jpn. J. Appl. Phys., **35**(4A), pp.2350-2355 (1996).

HEAVY ION BEAM TRANSPORT AND FOCUSING WITH AN INSULATOR GUIDE IN INERTIAL CONFINEMENT FUSION

T.Someya, T.Nakamura, J.Sasaki, S.Kawata

Department of Energy and Environment Sciences, Utsunomiya University, Yohtoh 7-1-2, Utsunomiya 321-8585, Japan. mt013619@cc.utsunomiya-u.ac.jp

ABSTRACT

One of the key issues on the heavy ion beam inertial confinement fusion is an efficient transport and a beam focusing. To get a fine focusing on the fuel pellet, neutralization of the space change of an incident beam is required. The space charge of beam has to be neutralized for the fine focusing. In this paper, we propose to employ an insulator tube guide, through which a heavy ion beam is transported and focused. We confirm that the beam space charge is effectively neutralized by electrons emitted from the insulator beam guide and the ion beam fine focusing is realized. This result shows a possibility of a good beam focusing by the insulator beam guide.

I . Introduction

High-voltage and pulsed power charged-particle-beam technologies have been applied to various fields: particle acceleration, nuclear fusion, new material processing, microwave source, X-ray source, etc. Especially, a heavy ion beam may be one of promising energy-driver candidates for inertial confinement fusion[1,2]. In these fields, physics of particle beam behavior must be clarified. Consequently, we should establish a charged-particle-beam-transport control method for the above purposes.

In our previous papers[3,4], we proposed a transport system for electron and proton beams through an insulator beam guide. We reported that the particle beam charge is neutralized efficiently by electrons or protons extracted from a plasma generated on the surface insulator guide, and the charged-particle beam is efficiently transported through an insulator beam guide without a large expansion of beam radius caused by space charge. The particles extracted from the plasma on the surface of insulator guide are self-regulated by the

net space charge of the beam.

In this paper, in order to solve the beam space charge neutralization[5] and get a fine focusing for heavy ion beam inertial confinement fusion, we study on a heavy ion beam transport and focusing through an insulator beam guide by a particle-in-cell (PIC) simulation code.

II. Heavy Ion Beam Transportation and Focusing, and Simulation Model

The physical mechanism of insulator beam guide is as follows: the heavy ion beam creates a local electric field on the inner surface of the insulator beam guide. The local electric field induces the local discharge, and the plasma is produced on the insulator inner surface. Then, electrons are extracted from the plasma generated on the inner surface of the insulator beam guide, because of the heavy ion beam net space charge. The emitted electrons follow the ion beam, and the beam space charge is effectively neutralized by the emitted electrons. Therefore, the heavy ion beam can be transported efficiently and we can get a fine focusing through the insulator beam guide. In this paper, we employ a Pb^+ ion beam in order to demonstrate the viability of the proposed insulator beam guide system. Our simulation model is as follows (see Fig. 1): we assume that the phenomenon concerned is cylindrically symmetric. The PIC code used a 2.5-dimensional one[6].

The Pb^+ ion-beam-parameter values are as follows: the incident Pb^+ ion beam waveform is as follows: the maximum current is 5[kA], the particle energy is 8[GeV], the pulse width is 10[ns] and the rise and fall times is 2[ns] (see Fig. 2). The initial beam radius is 3[cm]. The initial mean velocity of Pb^+ is given to focus at Z=180[cm], and the average longitudinal speed of the beam ions injected is determined by the waveform. The beam temperature is 10[eV]. At the beam entrance, that is Z=0, the beam ions enter uniformly, and the transport area is in vacuum. The computation area is $0 \le z \le Z_l (= 2[m])$ and $0 \le r \le R_l (= 5[cm])$. In our simulation, a local plasma is generated on the insulator guide surface, when the magnitude of the electric field exceeds the threshold for the local discharge. The threshold is $1.0 \times 10^7 [V/m]$ in this study.

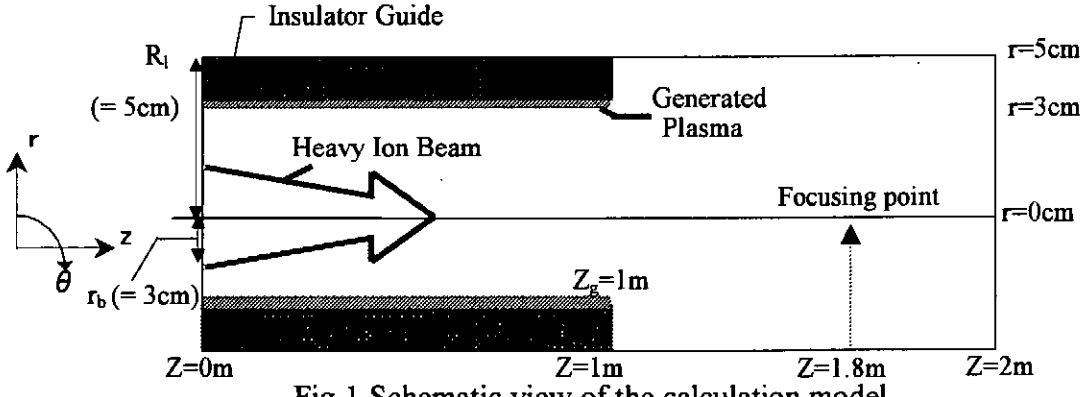

Fig.1 Schematic view of the calculation model

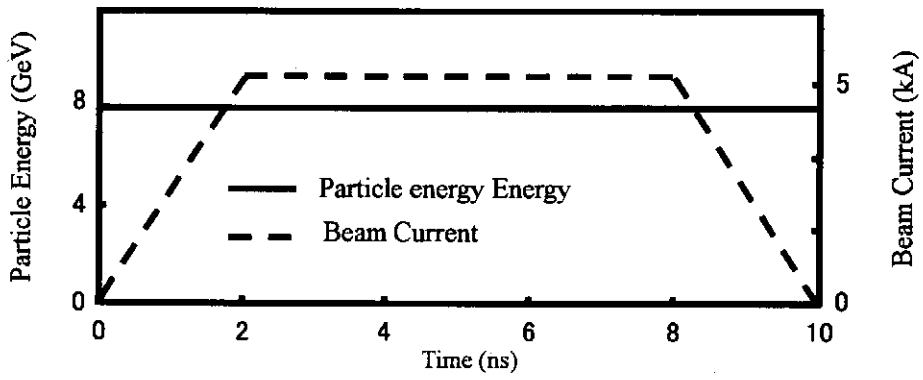

Fig.2 Incident ion beam waveform

Ⅲ. Simulation Results

First of all, we simulate the Pb^+ ion beam propagation in a vacuum without the insulator beam guide. The particle map of the Pb^+ beam ions is shown in Fig.3. In this case, due to the beam space charge, the beam radius at Z=180[cm](focusing point) expand to about 5[mm](see Fig.4-(a)). Fig.5 and Fig.6 present the particle map for using a proposed insulator guide system with the same initial conditions. The electrons extracted from the plasma generated on the insulator inner surface move along with the Pb^+ ion beam. The electrons effectively neutralized the space charge of the ion beam, and suppress the radial expansion of the beam. Figure 7 shows the history of the total space charges of the beam ions and the electrons in the whole transport region. The beam space charge is effectively neutralized by electrons emitted from the insulator beam guide. In this case, the beam radius at Z=180[cm] (focusing point) is about 2[mm](see Fig.4-(b)). Figure 8 present the Pb^+ distribution in the phase space and the normalized emittance ε.

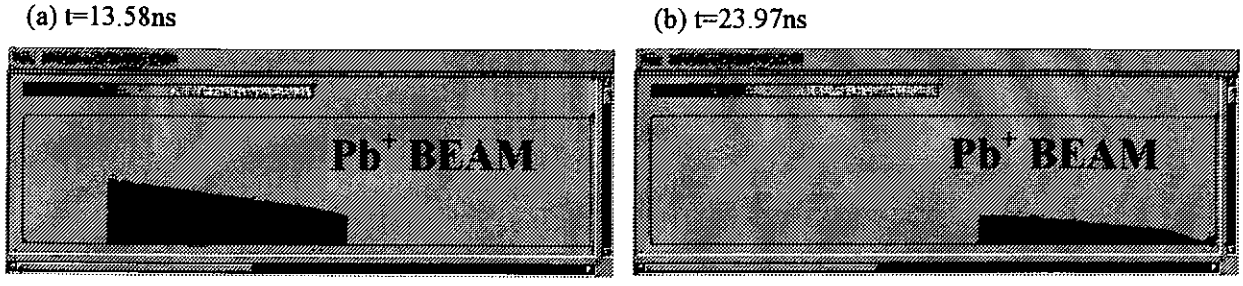

Fig.3 Ion beam particle maps without guide: these maps show particle maps without insulator guide at (a) 13.58[ns] and (b) 23.97[ns]. At the computation start, the mean velocity of the beam particle is given to focus at Z=180[cm]. By the space charge of ion, the focal radius of ion beam expands to 5[mm] at Z=180[cm].

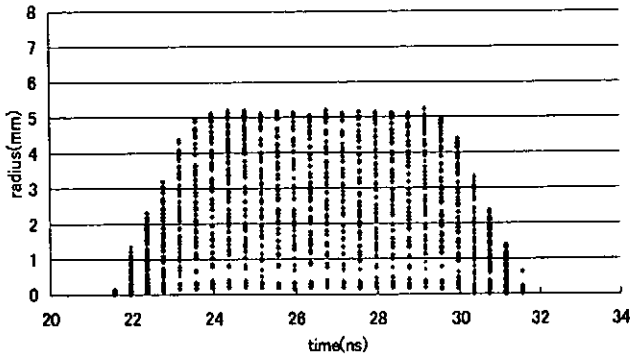

Fig.4 (a) Beam radius change in time at the focusing point without the guide.

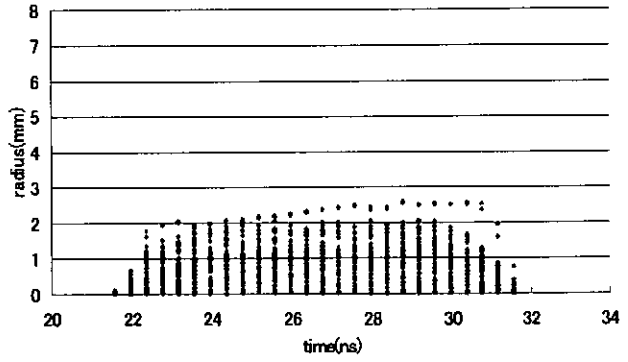

Fig.4 (b) Beam radius change in time at the focusing point with the guide.

(a) t=13.58ns

(b) t=23.97ns

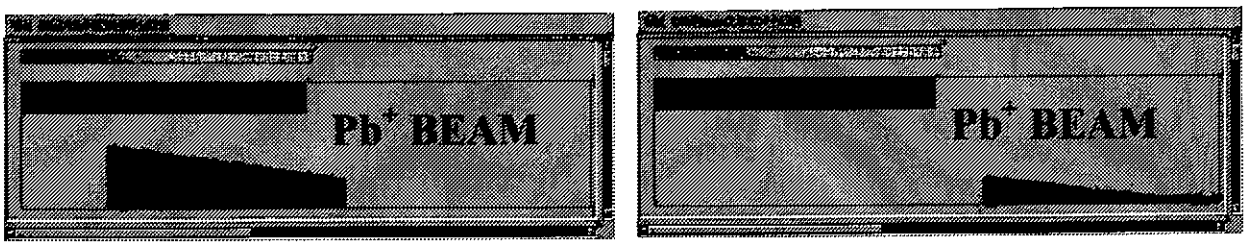

Fig.5 Ion beam particle maps with guide: these maps show particle maps with insulator guide at (a) 13.58[ns] and (b) 23.97[ns]. The beam particle is focused around Z=180cm. The focal radius of ion beam is 2mm at Z=180cm.

(a) t=13.58ns

(b) t=23.97ns

Fig.6 Emitted electron particle maps with guide: these maps show emitted electron particle maps with insulator guide at (a) 13.58[ns] and (b) 23.97[ns]. The electrons emitted from the insulator inner surface. The emitted electrons follow the ion beam and neutralize the ion beam charge.

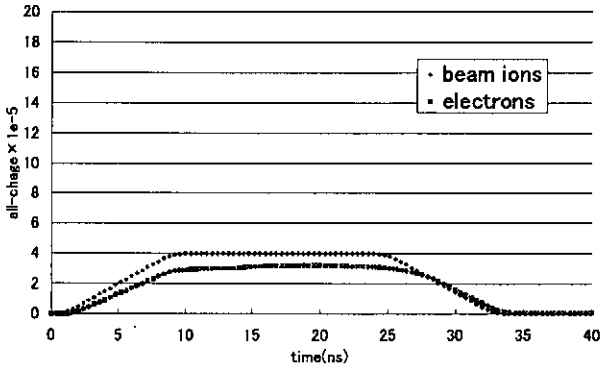

Fig.7 History of the total space charges of ion beam and electrons in the entire transport region. The emitted electrons neutralize the beam net-charge efficiently. The charge neutralization is self-regulated.

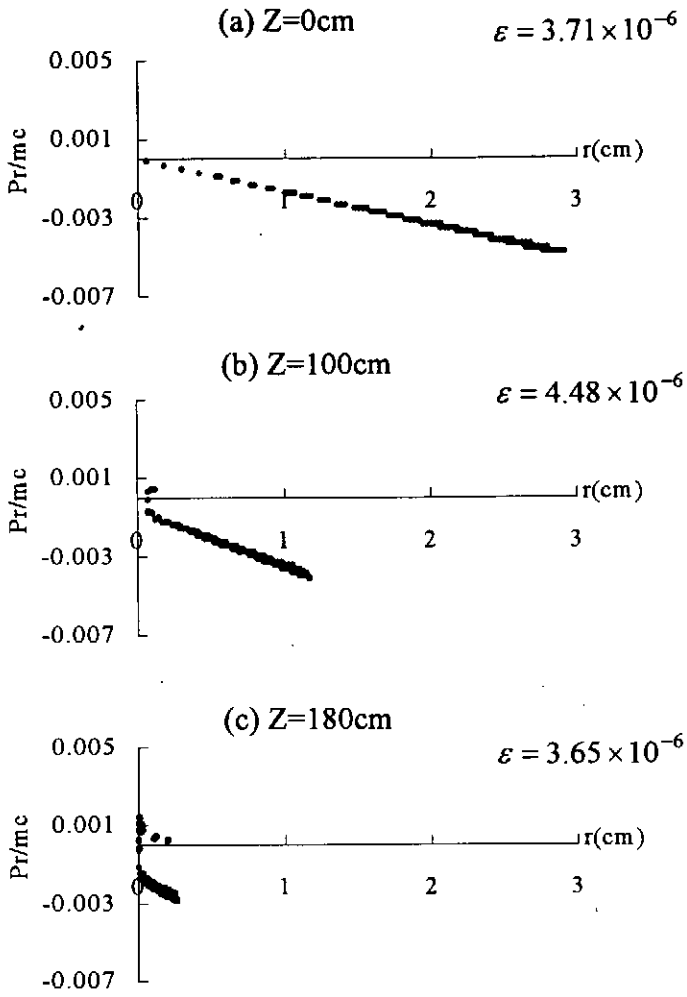

Fig.8 Pb^{+} distribution in the phase space and the normalized emittance. The particle distribution passing through Z=0[cm], Z=100[cm], and Z=150[cm] are plotted in Fig (a), (b) and (c), respectively.

IV. Summary

In this work, we proposed the heavy ion beam transport and focusing through an insulator beam guide. Plasma electrons were emitted from the plasma generated on the insulator inner surface. The electrons moved with the heavy ion beam, and the beam charge

was neutralized effectively by the electrons. By the PIC simulation, it is confirmed that the heavy ion beam propagated efficiently and was focused well through the insulator beam guide. We also confirmed that the heavy ion beam was in a high quality and an emittance growth was suppressed. The self-regulated charge neutralization is a unique feature of the simple insulator transport system.

References

1) D.Claude, S.Kawata and T.Nakamura, *Journal of Plasma and Fusion Research*, Vol.77, No.1, pp.33-39. (2001).
2) M.Tabak and D.Callahan-Miller, *Phys.Plasmas*, **5**,1895 (1998).
3) S.Kawata, S.Kato, S.Hanamori, S.Nishiyama, K.Naito, and M.Hakoda, *Jpn.J.Appl.Phys.*, **35**,L1127 (1996).
4) S.Hanamori, S.Kawata, S.Kato, T.Kikuchi, A.Fujita, Y.Chiba, and T.Hikita, *Jpn.J.Appl.Phys.*, **37**,L471 (1998).
5) T.Kikuchi, T.Nakamura, J.Sasaki, S.Kato and S.Kawata, *Proceedings of 13th international conference on high power particle beams (BEAMS2000), Niigata*, in press (2000).
6) A.B.Langdon and B.F.Lasinski, *Meth.Comp.Phys.*, **16**,327 (1976).

CALCULATION OF SURFACE TEMPERATURE DURING AN INTENSE PULSED ION BEAM IRRADIATION

Yoshiyuki Hashimoto

Department of Electronic Engineering, Kobe City College of Technology,
8-3 Gakuen-Higashimachi Nishiku, Kobe, Hyogo 651-2194

ABSTRATC

The temperature rise of a pure titanium sample induced by irradiation of the intense pulsed ion beam was calculated. When H^+ beam and C^+ beam with energy of 300 keV, current density of 100 A/cm^2, and pulse width of 50 nsec were irradiated to the sample, the temperatures of surface regions within about 1.7 μm and 1.2 μm were increased above melting point of the sample, respectively. Both cases of using H^+ beam and C^+ beam, the maximum cooling rate of the sample was calculated to be 7.7 x 10^8 K/sec. When the ion beam with a same pulse width was used, the cooling rate was in inverse proportion to the power density of the ion beam. A melting depth of the sample was increased to the beam pulse width; however, the cooling rate was decreased.

§1. Introduction

Recently, it was found that ion implantation of metal surfaces could improve their wear, friction and corrosion resistance. Ion implantation of specific tools is now preferred over other types of coating technologies because the ion implanted layer doesn't delaminate. In the world, various experiments on this topic have been performed.[1-5] In our laboratory, production of nanostructured crystallites on a pure titanium surface and an amorphous layer on a nickel alloy by an intense pulsed ion beam (IPIB) irradiation was succeeded.[6-10] Processes like phase transitions strongly depend on the attained temperatures of a target sample. Besides the maximum temperature also the temperature gradients of the sample are of crucial importance. The cooling rate of the sample determines if the phase transformations occur conformable the equilibrium phase diagram and it influences the refinement of the microstructure as well. Additionally thermal stresses will be induced in the modified layer, as a consequence of the thermal gradient. The temperature of a sample can be measured in several ways. In principle a distinction can be made in which way the

detection occurs, namely by direct contact or contactless. The first mentioned method, where the thermocouple is a well-known tool, has the disadvantage of a low response time. The other method determines the temperature of a target surface by measuring its emitted radiation. However, these methods are not suitable to measure locally high temperature gradients. Therefore, we calculate a temperature rise of a sample induced by irradiation of the IPIB. In this paper, we describe on the calculation results of temperature rise during the IPIB irradiation and estimation of the cooling rate of a pure titanium sample.

§2. Calculation Model

The temperature rise of a sample body induced by irradiation of the intense pulsed ion beam is calculated. Whenever a temperature gradient exists within a body, transport of energy takes place by means of heat transfer. The flow of heat in a rigid isotropic medium can be described by the heat conduction equation

$$\rho c_p \frac{\partial T(x,y,z,t)}{\partial t} = K\nabla^2 T(x,y,z,t) + Q(x,y,z,t), \tag{1}$$

where $T(x, y, z, t)$ is the sample temperature at position (x, y, z), at time t, K is the thermal conductivity, ρ is the density, c_p is the specific heat of sample materials and $Q(x, y, z, t)$ is the quantity of heat per unit volume and per time. If it is assumed that the beam is uniformly irradiated to the target, the thermal diffusion in the target is expressed one-dimensional equation as follows,

$$\rho c_p \frac{\partial T(z,t)}{\partial t} = K\nabla^2 T(z,t) + Q(z,t), \tag{2}$$

where

$$Q(z,t) = (dE/dz) \times I - H(z,t). \tag{3}$$

In equation (3), I is an ion beam current, dE/dz is the stopping power of an ion and $H(z, t)$ is corrective term for latent heat of the sample at position z, at time t. Phase transformations and temperature dependent physical properties are included in this model. To estimate the change of the target temperature with time and depth, we solve equation (2) by using the finite difference method.

We estimate the cooling rate of the sample surface from the result of above temperature profile. The cooling rate R_C was defined as followed,

$$R_c(z) = \frac{T_M - T_T}{\Delta t_c(z)}, \tag{4}$$

where T_M and T_T are the melting point and the transition point of the sample, respectively. $\Delta t_c(z)$ is time for decreasing the sample temperature from T_M to T_T.

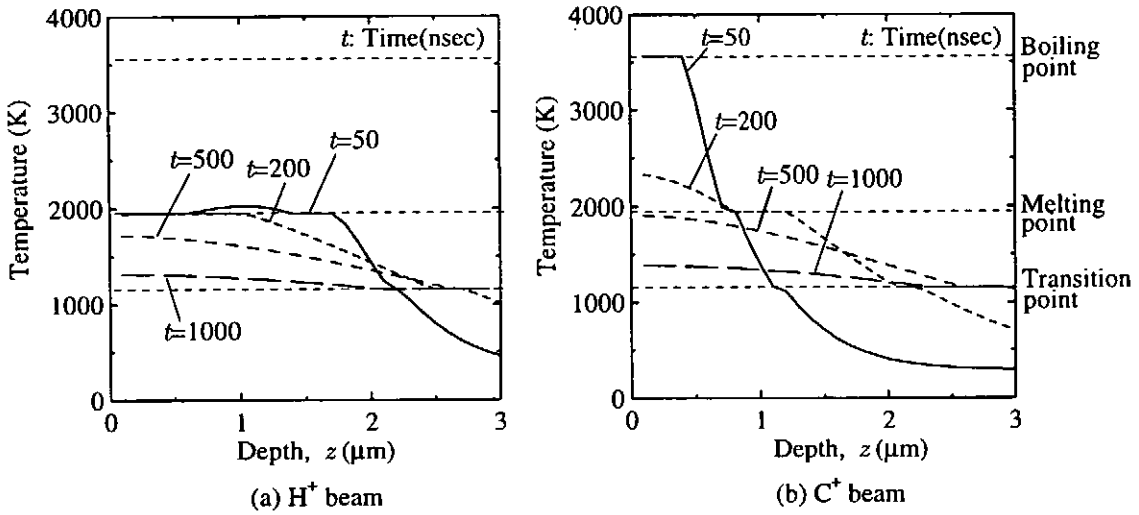

Fig.1 Profile of the calculated temperature rise (a) H^+ beam and (b) C^+ beam. The absorbed beam energy, current density and pulse width are 300 keV, 100A/cm^2 and 50 nsec, respectively. The thermophysical properties of Ti are used for this calculation.

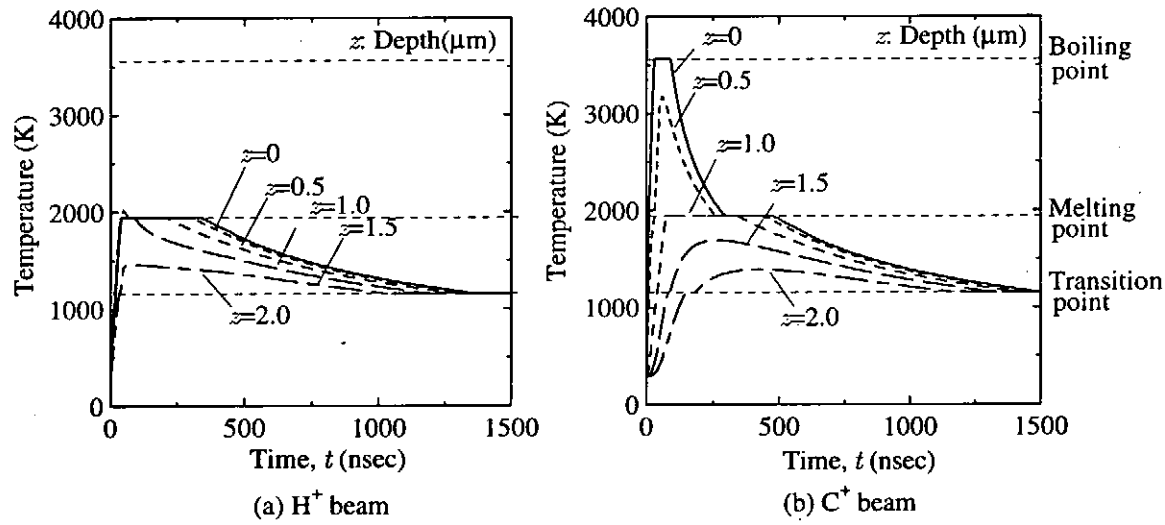

Fig.2 Profile of the calculated temperature rise (a) H+ beam and (b) C+ beam. The absorbed beam energy, current density and pulse width are 300 keV, 100A/cm^2 and 50 nsec, respectively. The thermophysical properties of Ti are used for this calculation.

§3. Calculation Results

The temperature rise of a pure titanium sample induced by irradiation of the intense pulsed ion beam is calculated from equation (2). Figure 1 shows the temperature of the sample as a function of depths, where (a) and (b) indicate in the case of H^+ and C^+ IPIB irradiation, respectively. When H^+ beam with energy of 300 keV, current density of 100 A/cm^2, and pulse width of 50 nsec is irradiated to the sample, the temperature of surface

regions within about 1.7 μm is increased above melting point of the sample. In case of C^+ beam with energy of 300 keV, current density of 100 A/cm^2, and pulse width of 50 nsec, the temperature of surface regions within about 0.4 μm is reached to boiling point of the sample and the temperature of surface regions within about 1.2 μm is increased above melting point of the sample. However, since the latent heat for evaporation of the target is very large, the temperature of the target can't exceed its boiling point in this calculation condition.

Figure 2 depicts the temperature of the sample as a function of time for various depths, where (a) and (b) indicate in the case of H^+ and C^+ IPIB irradiation, respectively. As seen in Fig. 2, it is found that the surface temperature is reached to the melting point within 50 nsec and reduced to the transition point within 1μsec. Both cases of using H^+ beam and C^+ beam, the maximum cooling rate of the sample is calculated to be 7.7 x 10^8 K/sec.

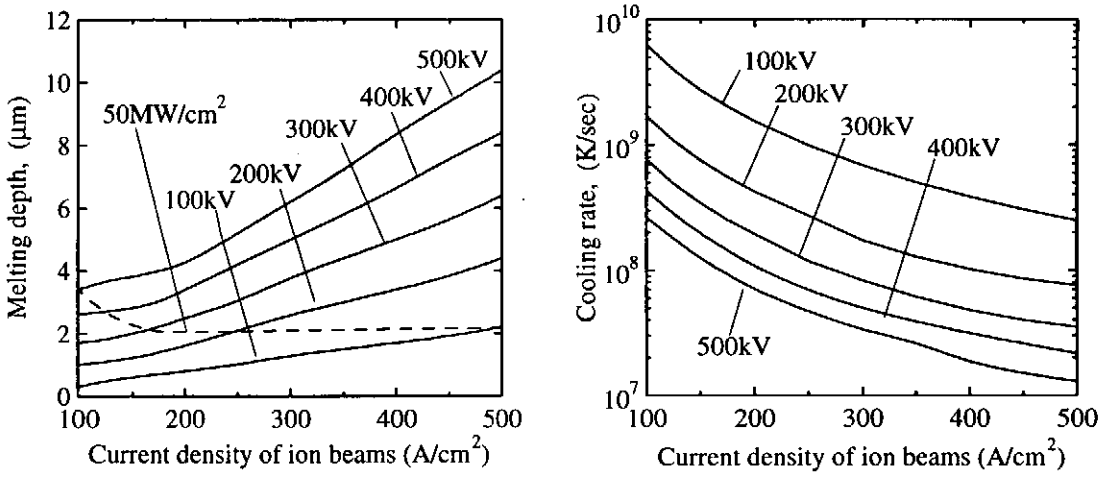

(a) Melting depth (b) Cooling rate

Fig. 3 Melting depth and a cooling rate of the titanium sample after irradiation of the intense pulsed ion beam with 50 nsec and H^+.

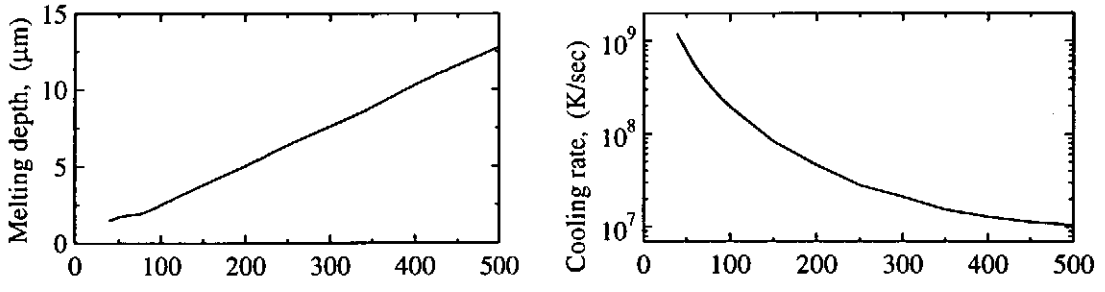

(a) Melting depth (b) Cooling rate

Fig. 4 Melting depth and a cooling rate of the titanium sample after irradiation of the intense pulsed ion beam with 300 keV, 100 A/cm^2 and H^+.

Figure 3 shows (a) melting depth and (b) a cooling rate of the titanium sample surface (z=0) after irradiation of a proton beam with pulse width 50 nsec. From Fig. 3(a), it is found that melting depth of the sample increases with beam current density or beam energy. As a result, the melting depth depends on the power density of the ion beam. From Fig. 3(b), the cooling rate of the sample decreases with increasing the current density of the ion beam. This result indicates an excess energy of the IPIB prevent rapid cooling of the target. However, the target melting by the IPIB irradiation is necessary for surface modification.

Figure 4 shows (a) melting depth and (b) a cooling rate of the titanium sample surface (z=0) after irradiation of a proton beam with 300 keV and 100 A/cm^2. It is found that melting depth of the sample is increased to the beam pulse width in Fig.4(a); however, the cooling rate is decreased in Fig.4(b).

§4. Summary

The temperature rise of a pure titanium sample induced by irradiation of the intense pulsed ion beam was calculated. When H^+ beam with energy of 300 keV, current density of 100 A/cm^2, and pulse width of 50 nsec is irradiated to the sample, the temperature of surface regions within about 1.7 μm was increased above melting point of the sample. In case of C^+ beam with energy of 300 keV, current density of 100 A/cm^2, and pulse width of 50 nsec, the temperature of surface regions within about 0.4 μm was reached to boiling point of the sample and the temperature of surface regions within about 1.2 μm was increased above melting point of the sample. Both cases of using H^+ beam and C^+ beam, the maximum cooling rate of the sample was calculated to be 7.7 x 10^8 K/sec. When the ion beam with a same pulse width was used, the cooling rate was in inverse proportion to the power density of the ion beam. A melting depth of the sample was increased to the beam pulse width; however, the cooling rate was decreased.

References

1) G.E.Remnev and V.A.Shulov: Laser and Particle Beams **11**(1993)707.

2) E. L. Neau, IEEE Trans. Plasma Sci. **22** (1994) 2.

3) R.W.Stinnett, D.C.McIntyre, R.C.Buchheit, E.L.Neau, J.B.Greenly, M.O.Thompson, G.P.Johnston and D.J.Rei: Proceedings of 10th International Conference on High-Power Particle Beams (1994) 94.

4) H.Akamatsu, Y.Tanihara, T.Ikeda, K.Azuma, E.Fujiwara and M.Yatsuzuka: Jpn. J. Appl. Phys. **40** (2001) 1083.

5) H.Akamatsu, Y.Tanihara, T. Ikeda, K. Azuma, E. Fujiwara, and M. Yatsuzuka: Proceedings of 13th International Conference on High-Power Particle Beams (2000) 94.

6) M.Yatsuzuka, T.Yamasaki, H.Uchida and Y.Hashimoto: Appl. Phys. Lett., **6** (1995) 206
7) M.Yatsuzuka, Y.Hashimoto, H.Uchida and T.Yamasaki: Jpn. J. Appl. Phys. **35** (1996) 1857.
8) M.Yatsuzuka, Y.Hashimoto, H.Uchida and T. Yamasaki: Proceeding of ISAPS'97 (1997) 165.
9) Y. Hashimoto and M.Yatsuzuka: Proceedings of ISAPS'99 (1999) 375.
10) Y.Hashimoto and M.Yatsuzuka: Proceedings of 13th International Conference on High-Power Particle Beams (2000) 361

PREPARATION OF POLYCRYSTALLINE SILICON THIN FILMS BY PULSED ION-BEAM EVAPORATION

Sung-Chae Yang, Ali Sharoon, Toshiaki Suzuki*, Weihua Jiang and Kiyoshi Yatsui

Extreme Energy-Density Research Institute, Nagaoka University of Technology
1603-1 Kamitomioka, Nagaoka, Niigata 940-2188, Japan
** Product Development Laboratory, Meidensha Corporation,*
515 Kaminakamizo, Numazu, Shizuoka 410-8588, Japan

ABSTRACT

By intense pulsed ion beam evaporation, we have succeeded in the preparation of polycrystalline silicon thin films on silicon substrate. High crystallinity and deposition rate have been achieved without heating the substrate. The crystallinity of poly-Si film has been improved with increasing the density of the ablation plasma, where the grain size of the film has been found to be much smaller. To enhance the crystallinity and density of poly-Si thin film, bias voltage was applied to the substrate, where the quality of poly-Si film has been improved by the ion bombardment.

I. Introduction

The preparation of polycrystalline silicon (poly-Si) thin films has received much attention due to their wide application potential for a semiconductor in thin film transistors (TFTs), solar cells, peripheral circuits of liquid-crystal displays, and electrodes in Si-integrated circuits. Conventionally, poly-Si films were prepared by a plasma-enhanced chemical vapor deposition (PECVD) method with post annealing (~800 °C) of a-Si:H films or substrate heating (200 - 400 °C).[1-4] This technique requires high processing temperatures and a long processing time. Since such a high temperature limits substrate materials or fabrication process, the deposition of poly-Si films at low temperatures has been desired, which will lead to the improvement of the throughput and the feasibility.

For practical engineering applications, in addition, the very low deposition rate is a serious problem for achieving higher throughput of electronic devices, such as solar cells. For this purpose, several types of low-pressure and high-density plasma sources have been applied to increase the crystallinity and the deposition rate of poly-Si thin films such as inductively coupled plasma (ICP), surface wave plasma (SWP), ultra high-frequency (UHF) plasma, and

electron cyclotron resonance (ECR) plasma.[2-7)]

In the present paper, we report the deposition of poly-Si thin films at room temperature, i.e., without heating the substrate, by using a high density ablation plasma produced by the intense, pulsed, ion beam, which was named as pulsed ion-beam evaporation (IBE). The crystallization and the deposition rate of poly-Si thin films prepared at different substrate positions are investigated. Furthermore, to improve the crystallinity, the bias voltage was applied to the substrate.

II. Experimental Apparatus and Method

If the pulsed proton beam irradiates solid targets, high-density ablation plasma can be produced due to short range of protons in targets. Using such the plasma, it has been found out to prepare thin films very efficiently. After the first demonstration of the preparation of thin films of ZnS in 1988,[8)] various kinds of thin films, e.g., YBCO, ITO, $BaTiO_3$, BN, SiC, TiO_2, ZrO_2, AlN, have been successfully prepared by IBE.[9-11)]

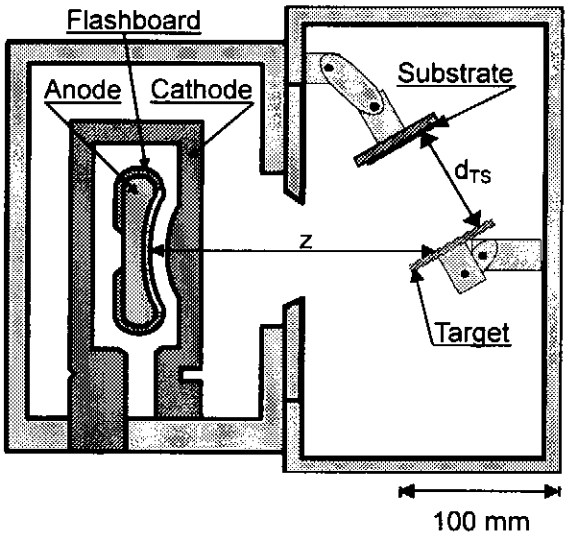

Fig. 1 Experimental setup.

Figure 1 shows the schematic of the experimental arrangement. The light ion beam (LIB) is produced by a geometrically focused, magnetically insulated diode (MID). A polyethylene sheet (flashboard) is attached on the anode (aluminum), which acts as the ion source. From the measurement by energy spectrometer, the ion species has been found to be mostly protons (approximately 75%), being the rest carbons.

Table I. Typical experimental conditions.

ion species	protons (H^+)
beam voltage (peak)	1 MV
beam current	70 kA
energy density on target	50 J/cm^2
z (anode-target distance)	180 mm
d_{TS} (target-substrate distance)	70 mm
target angle	45°
substrate	Si (200)
pressure	10^{-4} Torr
substrate temperature	R. T.
number of shots	5 or 10

The energy density of the ion beam was observed up to be ~100 J/cm^2 at the geometrically focusing point. The beam spot size on the target was 20 mm in diameter. As a target, a single crystal silicon was used with 50 mm in diameter, and 10 mm in thickness. As a substrate, we used Si wafer (200). The substrate (20 × 80 mm) was kept at room temperature and the ablation plasma directly hits the substrate. The chamber pressure was ~10^4 Torr. Typical experimental conditions are presented in Table I.

The crystal structures and the properties were characterized by X-ray diffraction (XRD), Auger electron spectroscopy (AES), Raman spectroscopy and scanning electron microscopy (SEM). The grain size for a certain crystal plane (*nkl*) was estimated from the full width at half-maximum (FWHM) values of the XRD spectra by use of Scherrer's formula. The film thickness was measured by a roughness meter.

III. Experimental Results and Discussions

In our previous paper,[12] we have investigated the behavior of the ablation plasma by high-speed camera. It was found that the ablation plasma is produced by the irradiation of the ion beam, and that the plasma expands in the direction perpendicular to the target surface. The substrate is surrounded by the ablation plasma for 20 μs after the start of the beam irradiation.

Figure 2 shows XRD spectra of poly-Si films deposited on Si substrate by 5 shots of ion beam. From Fig. 2, diffraction peaks of (111), (220) and (311) axes can be observed at d_p = 20 mm, where d_p is the distance from the plasma center. The most intense XRD peak appears for the (111) axis, followed by (220) and (311) axes. However, any diffraction peaks cannot be observed at d_p = 60 mm. These results mean that the crystallinity of the film is significantly improved near the center because the plasma density is much higher than that at the periphery.

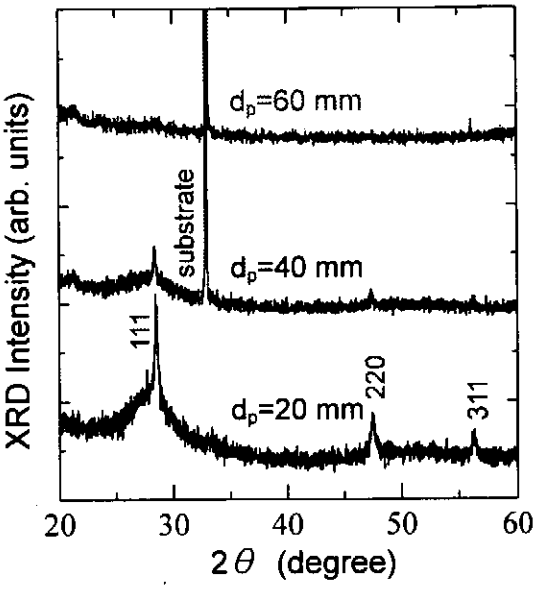

Fig. 2. XRD spectra of poly-Si films by 5 shots of ion beam irradiation.

Figure 3 shows XRD spectra of poly-Si films. In this experiment, the bias voltage, V_{bias} = -50 V, is applied to the substrate. From Fig. 3, diffraction peaks of (111), (220) and (311) axes can be observed at all substrate positions. The intensity of these peaks increases if approaching the center of the ablation plasma. The most intense XRD peak appears at (111) axis. These results suggest that it is possible to prepare the large-area of poly-Si thin films with high

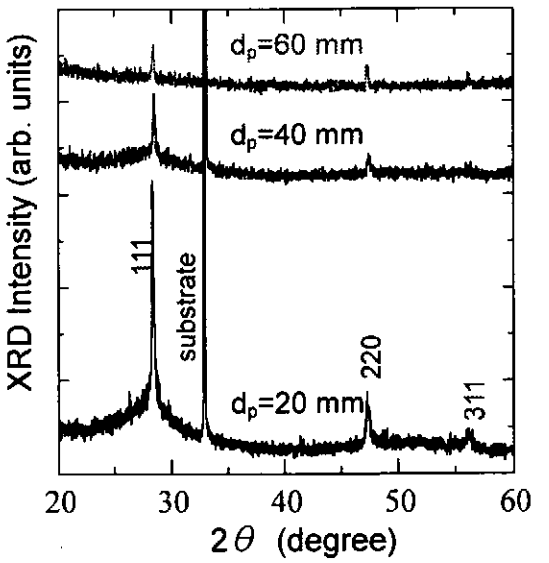

Fig. 3. XRD spectra of poly-Si films by 5 shots of ion beam irradiation and the substrate bias voltage V_{bias} = -50 V.

crystallinity by the bias voltage supplied on the substrate, where the ion bombardment affects the crystallization.

From the XRD data, the grain size of the nanocrystalline silicon films was calculated using Scherrer's formula:

$$d = 0.9\lambda / \beta \cos\theta, \qquad (1)$$

where d is the grain size, λ the X-ray wave length, β the FWHM, and θ the Bragg angle. Using eq. (1), the grain size of poly-Si films deposited under the conditions of Fig. 3 is estimated to be 30, 37 and 43 nm at d_p = 20, 40 and 60 mm, respectively. The deposition rate of preparing silicon films was estimated to be about 200 nm/shot near the center by the measurement of the roughness meter.

Figure 4 shows AES of poly-Si thin film prepared at dp = 35 mm. From Fig. 4, it is found that only the surface of the film is oxygenated. There are no impurities such as carbon and oxygen etc. in poly-Si thin film.

Figure 5 shows (a) peak intensity of (111) and (b) the film thickness as a function of distance from the plasma center, d_p, with the substrate bias voltage, V_{bias}, as a parameter. From Fig. 5(a), it is found that the XRD peak intensity increases with increasing the substrate bias voltage. The increment of the peak intensity certainly increases if approaching the center. The most intense peak is obtained at the substrate bias voltage V_{bias} = -100 V. This result means that the crystallinity of the film is improved if approaching the center because the plasma density is much higher than that near the periphery. Furthermore, the crystallinity of the film increases by (-) bias voltage supplied on the substrate, where the ion bombardment affects the

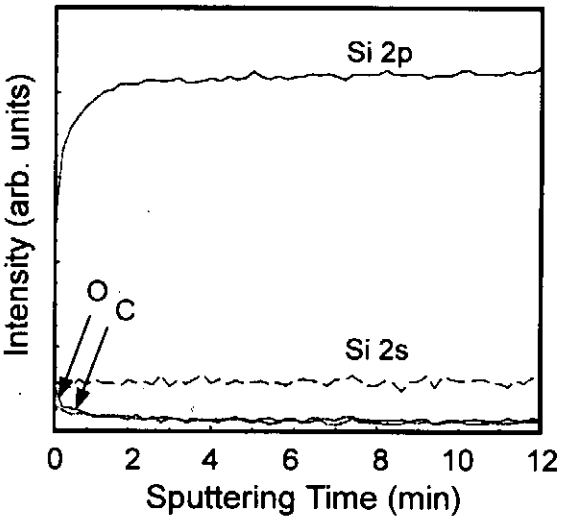

Fig. 4. AES depth profile of poly-Si thin film prepared at dp = 35 mm.

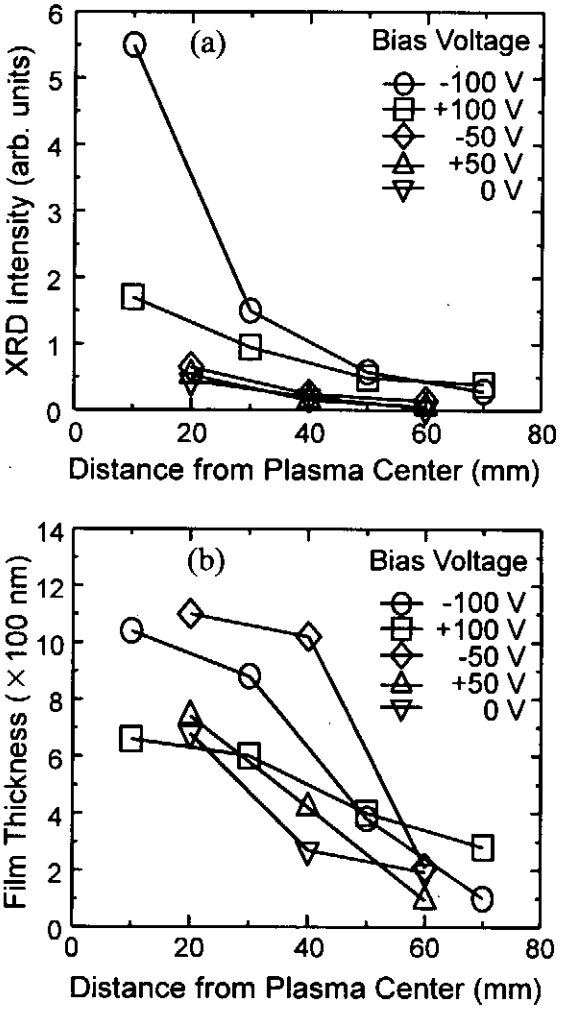

Fig. 5. (a) peak intensity of (111) and (b) the film thickness as a function of d_p and V_{bias}.

Microcrystalline Silicon Using High-Density SiH_4 Microwave Plasma", Jpn. J. Appl. Phys., **38**, 6629-6635 (1999).

5) R. Nozawa, H. Takeda, M. Ito, M. Hori and T. Goto, "Substrate Bias Effects on Low Temperature Polycrystalline Silicon Formation Using Electron Cyclotron Resonance SiH_4/H_2 Plasma", J. Appl. Phys., **81**, 8035-8039 (1997).
6) S. Hasegawa, M. Sakata, T. Inokuma and Y. Kurata, "Structural Change of Polycrystalline Silicon Films with Different Deposition Temperature", J. Appl. Phys., **85**, 3844-3849 (1999).
7) K. Murata, Y. Mizutani, E. Iwasaki, S. Takashima, M. Hori, T. Goto, S. Samukawa and T. Tsukada, "Growth of Preferentially Oriented Microcrystalline Silicon Film Using Pulse-Modulated Ultrahigh-Frequency Plasma", Jpn. J. Appl. Phys., 40, L4-L6 (2001).
8) Y. Shimotori, M. Yokoyama, H. Isobe, S. Harada, K. Masugata and K. Yatsui, "Preparation and Characteristics of ZnS Thin Films by Intense Pulsed Ion Beam", J. Appl. Phys. **63**, 968-970 (1988).
9) K. Yatsui et al., Phys. of Plasmas, "Applications of Intense Pulsed Ion Beam to Materials Science", 1, 1730-1737 (1994).
10) K. Yatsui, C. Grigoriu, K. Masugata, W. Jiang and T. Sonegawa, "Preparation of Thin Films and Nanosize Powders by Intense, Pulsed Ion Beam Evaporation", Jpn. J. Appl. Phys., **36**, 4928-4934 (1997).
11) W. Jiang, N. Hashimoto, H. Shinkai, K. Ohtomo and K. Yatsui, "Characteristics of Ablation Plasma Produced by Pulsed Light Ion Beam Interaction with Targets and Applications to Materials Science", Nucl. Instr. & Methods, **A415**, 533-538 (1998).
12) S.-C. Yang, R. Iwashita, T. Suzuki, W. Jiang, K. Yatsui, N. Uchitomi and T. Suzuki, "Preparation of Polycrystalline Silicone Thin Films by Pulsed Ion-Beam Evaporation", Proc. International Symposium on Pulsed Power and Plasma Applications, Chang-Won, Korea, 2000, pp. 215-220.

PREPARATION OF $YBa_2Cu_3O_{7-\delta}$ EPITAXIAL THIN FILMS BY PULSED ION-BEAM EVAPORATION

S. Sorasit, G. Yoshida, T. Suzuki, H. Suematsu, W. Jiang and K. Yatsui

Extreme Energy-Density Research Institute, Nagaoka University of Technology
Nagaoka, Niigata 940-2188, Japan

ABSTRACT

Thin films of $YBa_2Cu_3O_{7-\delta}$ (Y-123) grown epitaxially have been successfully deposited by ion-beam evaporation (IBE). The c-axis oriented $YBa_2Cu_3O_{7-\delta}$ thin films were successfully deposited on MgO and $SrTiO_3$ substrates. The Y-123 thin films which were prepared on the $SrTiO_3$ substrates were confirmed to be epitaxially grown, by X-ray diffraction analysis. The instantaneous deposition rate of the Y-123 thin films was estimated as high as 4 mm/s.

I. Introduction

After the discovery of the first high T_c superconductor, $La_2Cu_4O_{4+\delta}$ [1], many superconductors have been found. $YBa_2Cu_3O_{7-\delta}$ (Y-123) is one of the superconductors and has a peak in the characteristics of critical current density (J_c) as a function of applied magnetic field (H) [2]. This phenomenon is called the peak effect. Many works have been reported on the peak effect in Y-123. The reason of the peak effect, however, has not been clarified.

In order to study the peak effect, Y-123 samples which are epitaxially grown thin films with thickness of $\sim$ 10 μm are required. Numerous thin films preparation techniques, such as sputtering [3], molecular beam epitaxy (MBE) [4], electron beam evaporation [5] and pulsed laser ablation methods [6] have been developed to prepare the epitaxailly grown Y-123 thin films. However, the deposition rate of Y-123 thin films by these methods was slow and it is difficult to prepare 10 μm thick films.

Ion-beam evaporation (IBE) method has been developed to prepare various kinds of thin films with high deposition rates. The preparation of the films was carried out with a intense pulsed ion beam generator, which produces an ion beam with a kinetic energy of 1 MV (peak) and a current of 60 kA for a pulse width of ~50 ns [7]. Then the ion beam is irradiated on a target. Since the *range* of the ion beam in the target is very short, the surface is heated according to the delivered energy density by the ion beam. This causes the production of high-density ablation plasma which deposits on substrates with a rate of

~1μm / shot [8].

In the present work, the Y-Ba-Cu-O thin films are prepared by the ion beam evaporation (IBE) method. The crystallinity of the Y-123 thin films is characterized by various X-ray diffractometries.

II. Substrate Materials

Single crystals of MgO are known as substrate materials which do not react with Y-123 thin films at growth temperatures [9]. The preparation of high quality c -axis oriented Y-123 thin films have been reported on the MgO substrates [10], despite more than 9 % lattice mismatch between a-parameters of Y-123 and MgO.

Lattice mismatch between $SrTiO_3$ and Y-123 (1%) is better than that of Y-123 and MgO. Utilizing this advantage, epitaxially grown Y-123 thin films were prepared on $SrTiO_3$ substrates. Moreover, the thermal expansion coefficient of $SrTiO_3$ is close to that of Y-123. From these reasons, single crystals of MgO and $SrTiO_3$ were selected as substrates on which Y-123 thin films were deposited by IBE.

III. Experimental Arrangement

Figure 1 shows the schematic of the ion beam source and the sample deposition chambers in the pulsed power generator "ETIGO-II". The ion beam was produced by a magnetically insulated ion diode (MID) with geometrically focused configuration. A polyethylene sheet (flashboard) was attached on the anode (aluminum). The ion species were mainly protons. The cathode, which also worked as a one-turn theta-pinch coil, produced a transverse magnetic field, by which electrons emitted from the cathode are prevented from reaching the anode. The obtained ion beam was focused on the sintered Y-Ba-Cu-O target. After the ion beam irradiation, ablation plasma is produced on the surface of the target and thin films were deposited on the single crystal substrates facing toward the target. For each substrate, thin film was deposited by a single shot of ion beam

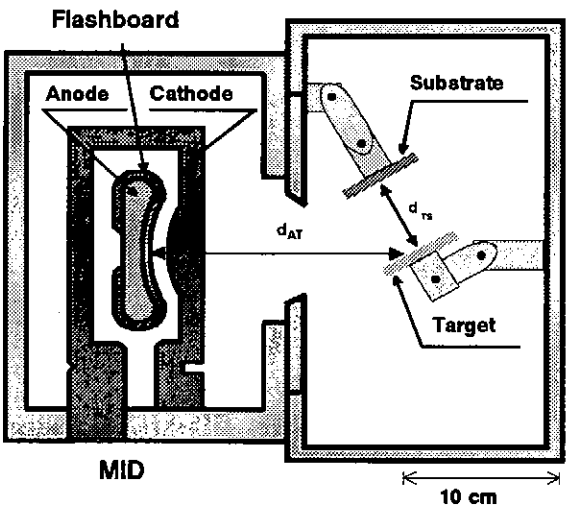

Fig. 1 Schematic of the ion beam source and the sample deposition chambers.

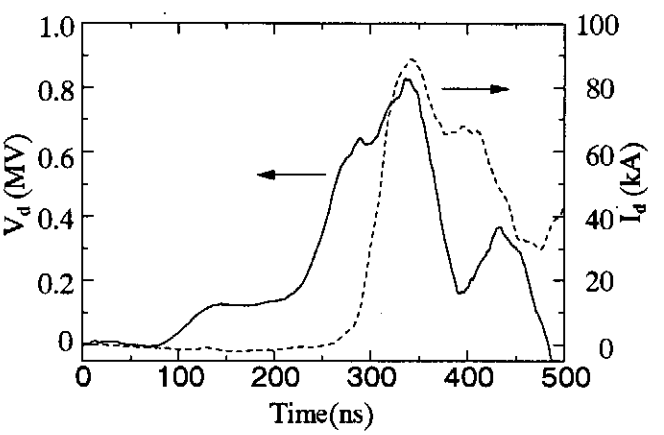

Fig. 2 Typical waveforms of V_d and I_d.

bombardment. Table I summarizes the deposition conditions.

Table I. Experiment conditions.

Accelerating Voltage	1 MV
Pulse width	50 ns
Ion type	H^+
Fluence	25 J/cm^2
Target	$YBa_2Cu_3O_{7-\delta}$
Target size	ϕ 50 mm, 5 ^{t}
Substrate	$SrTiO_3$ and MgO (100)
Distance (Anode- Target: d_{AT})	200 mm
Distance (Target-Substrate: d_{TS})	70 mm
Substrate temperature	RT.
Shot number	1 shot
Pressure	10^{-4} Torr

Table II. Annealing conditions.

900 ℃	5 hours
600 ℃	5 hours
400 ℃	40 hours

*These processes have been done in flowing oxygen gas

Figure 2 shows typical waveforms of V_d (diode voltage) and I_d (diode current). From Fig. 2, we see that V_d ~1 MV and I_d ~80 kA (peak) with τ (pulse width) ~ 70 ns (FWHM). Figure 3 shows the evolution of the ablation plasma which is formed on the Y-Ba-Cu-O target. These photographs were taken by a high-speed camera (Ultra NAC FS501). From these photographs we see that the Y-123 thin film was deposited in a period of 72 μs.

The as-deposited films were annealed in flowing oxygen gas. The annealing conditions are shown in Table II. The thin films were characterized with an X-ray diffractometer. The thickness of the thin films was measured by a roughness tester (Surfcom 130A, Tokyo Seimitsu). The cation composition of the target and the Y-123 grains in the thin films was determined by X-ray fluorescence spectrometry and energy dispersive X-ray analysis (EDX), respectively. A specimen for EDX was prepared by scratching the surface of a thin film on a $SrTiO_3$ substrate by a piece of glass. The powders from the film were collected on a carbon microgrid supported by a molybdenum mesh. The EDX spectra for the thin films was determined with an energy dispersive X-ray spectrometer attached on a transmission electron microscope (JEM-2010, JEOL) operated at 200 kV. The intensity of the characteristic X-ray from the specimen was calibrated by those from a standard sample of Y-123 powder. Thin film approximation which ignored absorption of the emitted X-ray in the films was assumed for quantifying the composition.

IV. Results and Discussions

The XRD patterns for the annealed Y-123 thin films on the MgO and $SrTiO_3$ substrates are shown in Fig. 4. The peaks of Y-123 thin films on both substrates exactly correspond

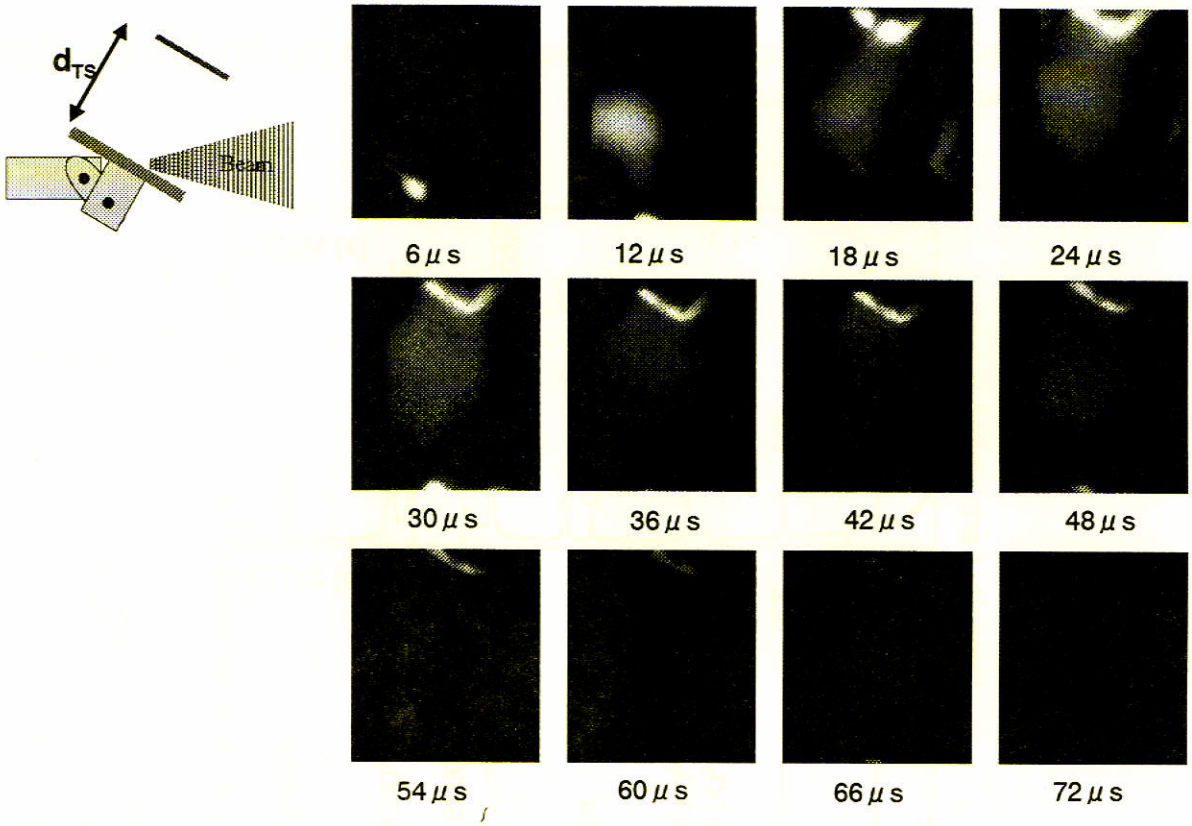

Fig. 3 High-speed photographs of the ablation plasma from the Y-Ba-Cu-O target.

to the reflections for Y-123 or substrates phases. The films were essentially single-phase. Although the peak for the 103 reflection is also found in the pattern for the Y -123 thin films on the MgO substrate, most of the peaks for Y-123 are matched to the 00 *l* reflections. This indicates that the c-axis for the Y-123 thin films was perpendicular to the (100) surface of the substrates.

The rocking curve of the 002 reflection has been taken to characterize the c-axis orientation. The full-width of half maximum (FWHM) value of 002 rocking curve are given in the Table III. From the results, we see that the Y-123 thin films on both substrates are less than 1° . This indicates that Y-123 thin films prepared by IBE method were c-axis oriented. Then, the intensity change of the (102) reflection for Y-123 thin films due to ϕ scanning have been taken to characterize the in-plane orientation, which are shown in Fig. 5. Since four-fold symmetry is clearly seen in the pattern for the thin films on the $SrTiO_3$ substrate, but not seen in the pattern for the Y-123 thin films on the MgO substrate, the Y-123 thin films are concluded to be epitaxially grown on the $SrTiO_3$ substrate.

The cation composition of Y-123 grains which was measured by EDX is shown in Table IV. From the result, the cation composition of the Y-123 thin films is almost the same as that of the Y-Ba-Cu-O target. This confirms the previously concluded character of the IBE method [11], i.e. the composition of the films is as same as that of target.

The thickness of the epitaxially grown Y-123 thin films was measured with the roughness tester, yielding 0.3 μ m with a single shot of ion beam bombardment. According to the ablation plasma photographs which was shown in Fig. 2, the Y-123 thin

films were deposited in a period of 72 μ s. Thus, the instantaneous deposition rate of the films was calculated to be ~ 4 mm/s.

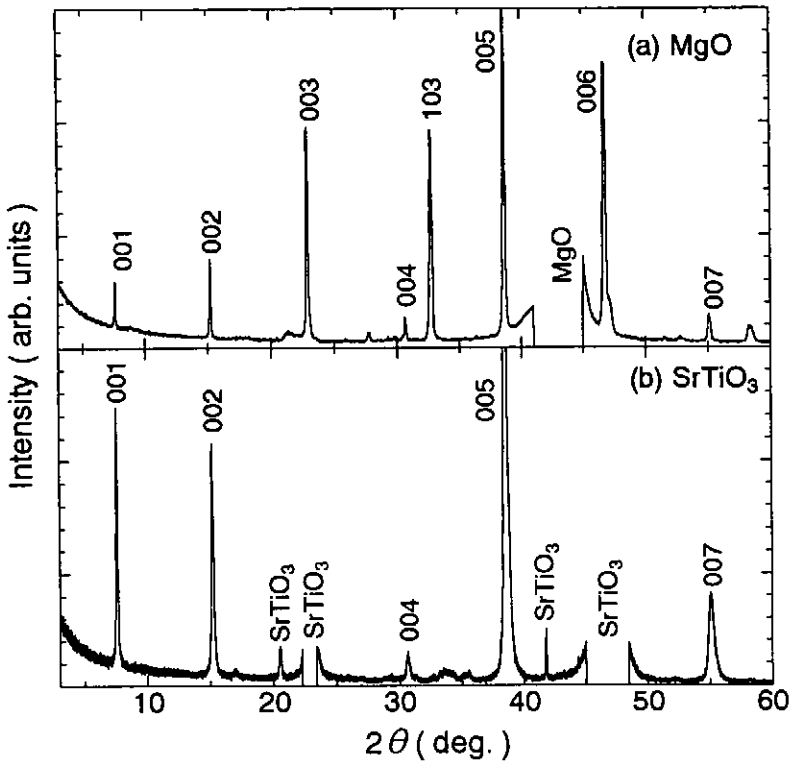

Figure 4 XRD patterns of the Y-123 thin films on (a) MgO and (b) $SrTiO_3$.

Table III. FWHM values of rocking curves of 002 reflections for Y-123 thin films.

Substrate	FWHM (deg.)
MgO	0.18
$SrTiO_3$	0.73

Table IV. Cation composition of the target and Y-123 thin film.

	Y	Ba	Cu
Target	1.0	2.0	3.0
Sample	1.0	2.0	2.9

V. Conclusions

The c-axis oriented Y-123 thin films have been deposited on the MgO and $SrTiO_3$. The epitaxial Y-123 thin films were successfully achieved on the $SrTiO_3$ substrate by IBE method. The composition of the films is found to be in good agreement with that of the target. Utilizing the high-density ablation plasma which was formed by this method, Y-123 thin films have been prepared by the fast deposition rate of $\sim$ 4 mm/s.

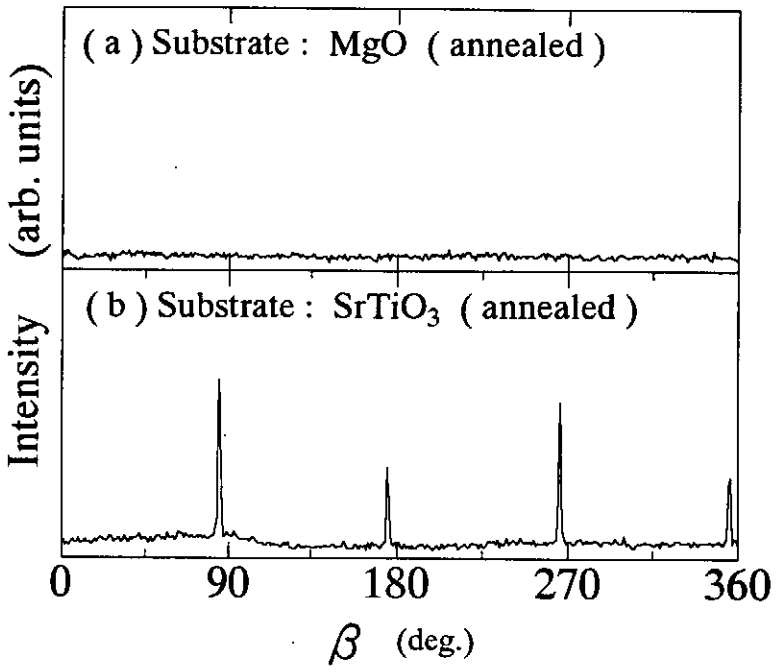

Figure 5 Intensity change of the (102) reflection due to β scan for Y-123 on (a) MgO and (b) $SrTiO_3$.

References

1) J.G. Bednorz and K. A. Muller, "Possible High T_c Superconductivity in the Ba-La-Cu-O system", Z. Phys., B.**64** 189-193 (1986).
2) M. Daeumling, J. M. Seuntjens and D. C. Larbalestier, "Oxygen-Defect Flux Pinning, Anomalous Magnetization and Intra-grain Granularity in $YBa_2Cu_3O_{7-d}$s", Nature, **346** 332-345 (1990).
3) H. Adachi, K. Setsune, T. Mitsuyu, K. Hirochi, Y. Ichikawa, T. Kamada and K. Wasa, "Preparation and Characterization of Superconducting Y-Ba-Cu-O Thin Films", Jpn. J. Appl. Phys., **26** L709-L710 (1987).
4) J. Kwo, T. C. Hsieh, R. M. Fleming, M. Hong, S. H. Liou, B. A. Davidson and L. C. Feldman, "Structural and Superconducting Properties of Orientation-Ordered $Y_1Ba_2Cu_3O_{7-x}$ Films Prepared by Molecular-Beam Epitaxy", Phys. Rev. B, **36** L4039-L4042 (1987).
5) B. –Y. Tsaur, M. S. Dilorio and A. J. Strauss, "Preparation of Superconducting $YBa_2Cu_3O_x$ Thin Films by Oxygen Annealing of Multilayer Metal Films", Appl. Phys. Lett., **51** 858-860 (1987).
6) D. Dijkkamp, T. Venkatesan, X.D. Wu, S.A. Shaheen, N. Jis rawi, Y.H. Min-Lee, W.L. McLean and M. Croft, "Preparation of Y-Ba-Cu Oxide Superconductor Thin Films using Pulsed Laser Evaporation from high T_c Bulk Material", Appl. Phys. Lett., **51** 619-621 (1987).
7) Y. Shimotori, M. Yokoyama, S. Harada, K. Masugata and K. Yatsui , "Quick Deposition of ZnS:Mn Electroluminescent Thin Films by Intense, Pulsed, Ion Beam Evaporation", Jpn. J. Appl. Phys. **28**, 468-472 (1989).
8) K. Yatsui, "Industrial Applications of Pulse Power and Particle Beams", Laser and Particle Beams., **7** 733-741(1989).
9) L. A. Tietz, et al., J. Mater. Res., **4** 1072 (1989).
10) Q. Li, O. Meyer, X. X. Xi, J. Geerk and G. Linker, "Growth Characterization of $YBa_2Cu_3O_{7-x}$ Thin Films on (100) MgO", Appl. Phys. Lett., **55** 310-312 (1989).
11) K. Yatsui, T. Sonegawa, K. Ohtomo and W. Jiang: "Preparation of Thin Films of Dielectric Materials using High-Density Ablation Plasma produced by Intense Pulsed Ion Beam", Mater. Chem. Phys., **54**, 219-223 (1998).

THE RELATIONSHIP BETWEEN THE HARDNESS AND THE POINT-DEFECT-DENSITY IN NEUTRON-IRRADIATED $MgO \cdot 3.0Al_2O_3$ AND AlN

H. Suematsu[1], K. Yatsui[1] and T. Yano[2]

1 Extreme Energy-Density Research Institute, Nagaoka University of Technology, Nagaoka 940-2188, Japan
2 Research Laboratory for Nuclear Reactors, Tokyo Institute of Technology Tokyo 152-8550, Japan

ABSTRACT

$MgO \cdot 3.0Al_2O_3$ single crystals and sintered AlN polycrystals were irradiated with fast neutrons in various conditions and the hardness of the irradiated and unirradiated samples was measured with a Vickers hardness tester. The hardness of as-irradiated $MgO \cdot 3.0Al_2O_3$ and AlN samples increased by 23 and 51 %, respectively. After isochronal annealing, the hardness gradually decreased and mostly recovered to that of the unirradiated one up to 1400 °C. Volume of the sample also increased after the irradiation and changed in the same way as the hardness by annealing. A relationship between the hardness and the density of point defects is proposed and the experimental results agree with the relationship. It implies that the point defects pin down dislocations generated by the indentation and increase the hardness of neutron irradiated $MgO \cdot 3.0Al_2O_3$ samples.

I. Introduction

Most of ceramic materials are known to be stable under neutron irradiation. Among the ceramics, $MgO \cdot nAl_2O_3$ spinel shows unique characters under neutron irradiation. The volume change after the irradiation was much smaller than most of oxides[1]. In the irradiated $MgO \cdot nAl_2O_3$ samples, it is believed that knock-on atoms fill open spaces in the crystal structure rather than become interstitial atoms causing volume change. Furthermore, the fracture toughness of $MgO \cdot nAl_2O_3$ spinel samples increases after neutron irradiation[2]. However, the mechanism to the increase is not certain. The change in other mechanical properties of $MgO \cdot nAl_2O_3$ samples due to the irradiation was also paid attentions, however, few works have been reported.

We have reported that hardness of neutron irradiated $MgO \cdot 3Al_2O_3$ single crystals and AlN polycrystals increased by 23 and 51 %, respectively[3-6]. At the same time, the hardness change of the samples was similar to the volume change, which is related to the density of the point defects. It was likely that the hardness change in the neutron irradiated samples was related with the change in the point defects. However, detailed mechanism of the hardness increase was not certain. In the present work, $MgO \cdot 3.0Al_2O_3$ single crystals and sintered AlN polycrystals were irradiated by neutrons in a various conditions. Hardness of the irradiated crystals was measured with a Vickers hardness tester. A relationship between hardness and the density of point defects is proposed and the

mechanism of the hardness increase in neutron irradiated $MgO{\cdot}3.0Al_2O_3$ single crystals and AlN polycrystals is discussed.

II. Experimental

Pressureless sintered AlN polycrystals and $MgO{\cdot}3.0Al_2O_3$ single crystals were cut into rectangular parallelepiped samples with a size of 2 x 4 x 25 mm^3. All of the surfaces of the single crystals were designed to be parallel to {100}. The surfaces for both samples were polished with a diamond paste. Neutron irradiation of the samples was carried out in the Japan Material Testing Reactor at temperatures between 100 and 785 °C up to fluences between 8.3 x 10^{22} and 5.2 x 10^{24} n/cm^2 (E > 1MeV). After the irradiation, hardness of the samples were measured at room temperature with a Vickers hardness tester. The indentation load (P) was 0.3 kg for $MgO{\cdot}3.0Al_2O_3$ and 5 kg for AlN and the indenter was loaded for 15 seconds on the surface of a sample. Hardness of the sample (H) was calculated from the diagonal of the indentation($2a$ (mm)) with the following standard equation:

$$H = 1.854\, P/(2a)^2. \qquad (1)$$

Macroscopic length of the sample was measured at room temperature with a point-type micrometer, which was firmly attached with a sample holder. The holder allowed reproducible alignment of the sample and the reading error of th e length was within 1 μm. Assuming isotropic volume change by the introduction of defects, the volume change was calculated to be three times of the length change. Then, the samples were annealed in a vacuum of 1 Pa at temperatures between 100 and 1000 °C for 1 hour and in a vacuum of 10^{-4} Pa at temperatures between 1100 to 1400 °C for 1 hour. After annealing at a certain temperature, hardness and macroscopic length was measured again at room temperature. The samples were annealed at a higher temperature. This annealing-measurement cycle was conducted repeatedly.

III. Results and Discussion

Hardness of irradiated and unirradiated $MgO{\cdot}3.0Al_2O_3$ sample is shown in Fig. 1. After the neutron irradiation, the hardness of a sample irradiated at 100 °C up to 8.3 x 10^{22} n/m^2 is increased by 23%, while the hardness of a sample irradiated at 470 °C up to 2.4 x 10^{24} n/m^2 is comparable to that of the unirradiated one. After annealing up to 1000 °C, the hardness of the unirradiated sample stays almost constant. Hardness of the sample irradiated at 470 °C up to 2.4 x 10^{24} n/m^2 is also unchanged. On the other hand, the hardness of the sample irradiated at 100 °C up to 8.3 x 10^{22} gradually decreases. After the sample annealing above 600 °C, the hardness of the sample is mostly recovered to that of the unirradiated one.

Macroscopic volume change due to the sample annealing is shown in Fig. 2. For the sample irradiated at 470 °C up to 2.4 x 10^{24} n/m^2, the volume change is comparable to that of the unirradiated one and unchanged due to sample annealing up to 1000 °C. On the other hand, the volume of the sample irradiated at 100 °C up to 8.3 x 10^{22} n/m^2 is 0.17 % larger than that before the irradiation. After annealing between 100 and 600 °C, the volume of the sample gradually decreases. The volume change of the sample is almost 0.03 % at 600 °C and less than 0.02 %, which is close to the detection limit of the present

apparatus, above 900 °C. For these irradiated samples, the hardness and volume change as function of annealing temperature are quite similar.

Hardness and macroscopic volume change for neutron irradiated AlN were also shown in Figs. 3 and 4, respectively. For an AlN irradiated at 470 °C up to 2.4 x 10^{24} n/m^2, hardness change is 51 % which is the highest value among the samples. Similar to the curves for $MgO{\cdot}3.0Al_2O_3$ samples (Figs. 1 and 2), hardness and macroscopic volume was almost constant after annealing below the irradiation temperatures. After annealings above the irradiation temperatures, the hardness and the macroscopic volume change values gradually decrease in a similar manner. The similarity of the hardness and macroscopic volume changes due to annealing is also observed for the other two neutron irradiated AlN samples

During the irradiation, a number of de fects should be introduced. In $MgO{\cdot}3.0Al_2O_3$ and AlN, dislocation loops were observed by transmission electron microscopy and point defects and their small clusters which are responsible for the macroscopic volume change must be present[5,6]. Since the hardness and volume change exhibit similar manner, it is natural to think that point defects should affect the hardness increase.

Assuming that strain field around point defects pin down dislocations which are moved by the stress applied by the indentation and this cause hardening in irradiated spinel samples. In metals, solution hardening from asymmetric point defects had been known and the yield stress change is described by the following empirical equation:

$$\tau_h = \tau_0 + \frac{1}{3}\mu\Delta\varepsilon c_i^{\frac{1}{2}} \qquad (2)$$

where τ_h is the yield stress of the hardened material, τ_0 is the yield stress of the control sample, μ the shear modulus, $\Delta\varepsilon$ transverse strain of the tetragonal distortion and c_i the concentration of solute atoms. Following Eq. (2), we have proposed that the hardness increase after neutron irradiation should be given by:

$$H_i = H_0 + Ac_d^{\frac{1}{2}} \qquad (3)$$

where H_i and H_0 are Vickers hardness values after and before the neutron irradiation, c_d the concentration of point defects and A a constant[7]. Since the volume change of the irradiated sample may be proportional to c_d, Eq. (3) can be derived as follows:

$$H_i - H_0 = B\left(\frac{\Delta V}{V}\right)^{\frac{1}{2}} \qquad (4)$$

where B is a constant, $\Delta V/V$ the volume change. From the results in Figs. 1 and 2, values of $H_i - H_0$ for irradiated $MgO{\cdot}3.0Al_2O_3$ samples are plotted against the volume change in Fig. 5. The slope of the straight line, which is a least square fit of the plots, is 0.57, i.e. almost equal to 1/2. Values of $H_i - H_0$ for irradiated AlN samples are also plotted against the volume change in Fig. 6. Similar to the plots for the $MgO{\cdot}3.0Al_2O_3$ samples, the slope of the line was 0.53, which is also close to 1/2. Moreover, plots from the differ ent samples fall on a single line. These results indicates that irradiation hardening can be explained by dislocation pinning at point defects and their small clusters, which is described in Eq. (3).

IV. Conclusions

Hardening of neutron irradiated $MgO \cdot 3.0Al_2O_3$ single crystals and AlN polycrystals were observed. A relationship between the concentration of point defects and the hardness change was proposed and the experimental results agree well with the relationship. This indicates that the hardness change in neutron irradiated $MgO \cdot 3.0Al_2O_3$ single crystals and AlN polycrystals can be explained as the dislocation pinning by the irradiation-induced point defects.

References

1) G. F. Hurley, J. C. Kennedy, J. F. W. Clinard, R. A. Youngman, and W. R. McDonell, "Structural Properties of MgO and $MgAl_2O_4$ after Fission Neutron Irradiation near Room Temperature", J. Nucl. Mater **103-104,** 761-65 (1981).
2) J. F. W. Clinard, G. F. Hurley, R. L. Youngman, and L. W. Hobbs, "The Effect of Elevated-Temperature Neutron Irradiation on Fracture Toughness of Ceramics", J. Nucl. Mater. **133-134,** 701-704 (1985).
3) H. Suematsu, T. Iseki, T. Yano, T. Saito, T. Suzuki, and T. Mori, "Point Defect Hardening in $MgO \cdot 3Al_2O_3$", J. Am. Ceram. Soc. **75,** 1742-47 (1992).
4) T. Yano, M. Ikari, T. Iseki, E. Farnum, F. Clinard Jr., and T. E. Mitchell, " Effect of Neutron Irradiation on Knoop Microhardness Anisotropy in $MgO \cdot 3Al_2O_3$ Single Crystals", J. Am. Ceram. Soc. **78,** 1469-1474 (1995).
5) T. Yano, "Effects of Neutron Irradiation on the Mechanical Properties of Magnesium Aluminate Spinel Single Crystals and Polycrystals", J. Am. Ceram. Soc. **82,** 3355-3419 (1999).
6) T. Iseki, M. Tezuka, C-. S. Kim, T. Suzuki, T. Suematsu and T. Yano, "Hardening by Point Defects in Neutron Irradiated AlN and SiC", J. Nucl. Sci. Technol., **30**, 68-77 (1993).
7) H. Suematsu, T. E. Mitchell, T. Iseki, and T. Yano, " Hardening in AlN Induced by Point Defects" Mat. Res. Soc. Symp. Proc. **235,** 445-450 (1992).

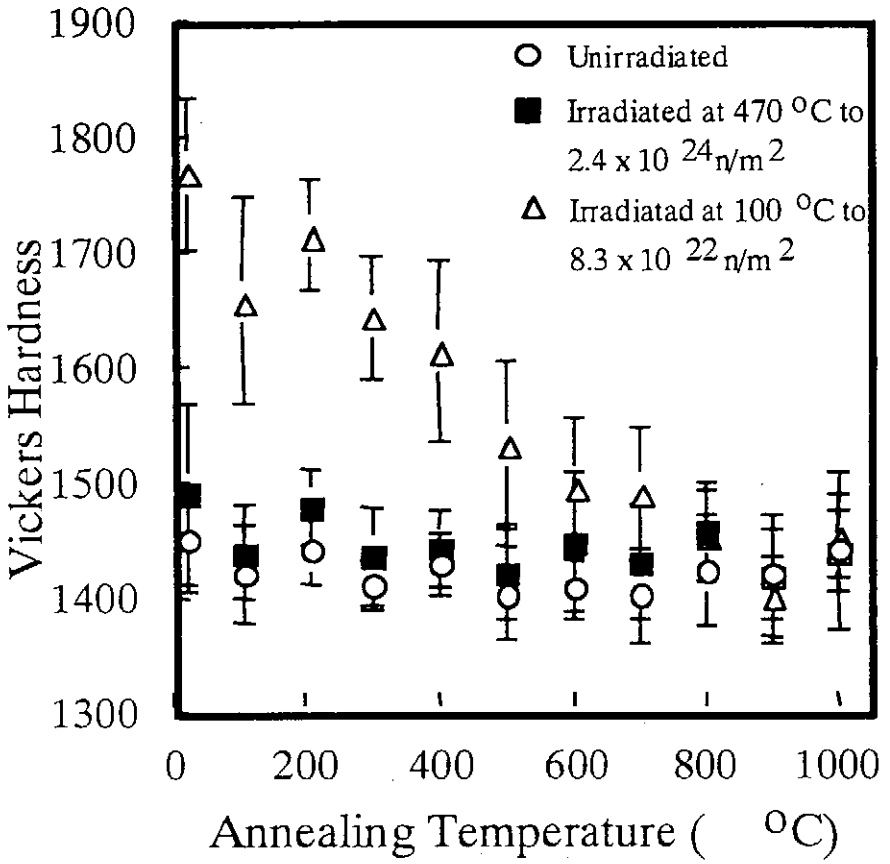

Fig.1 Hardness of unirradiated and irradiated $MgO3.0Al_2O_3$ single crystals after isochronal annealing.

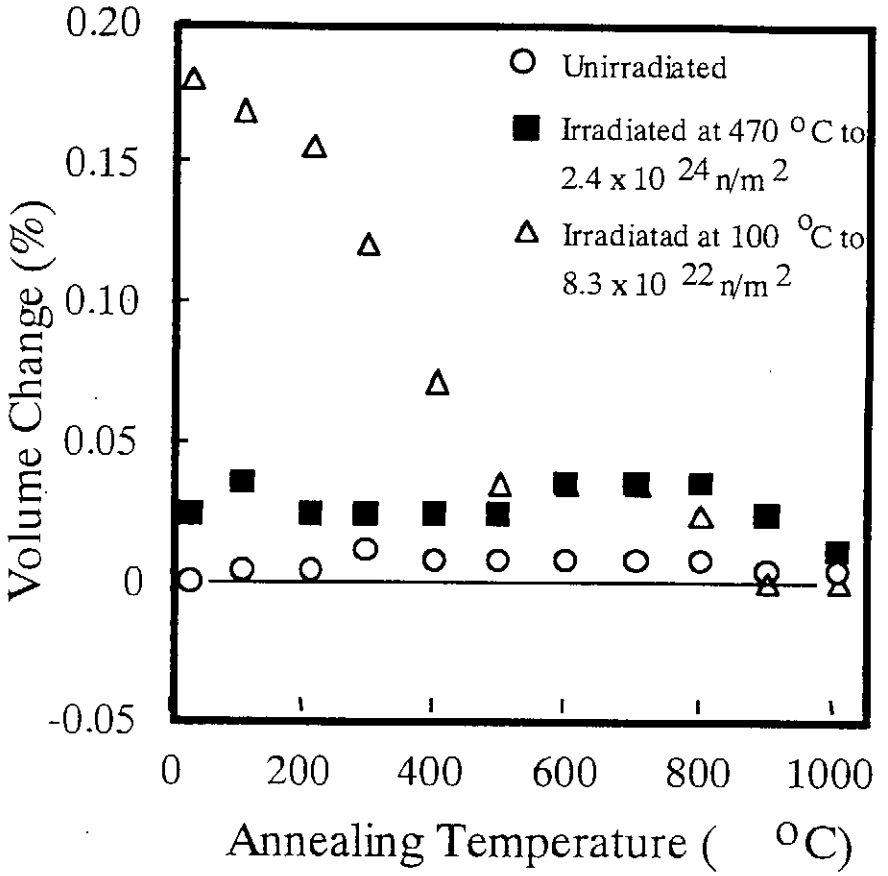

Fig.2 Volume change in unirradiated and irradiated MgO3.0Al_2O_3 single crystals after isochronal annealing.

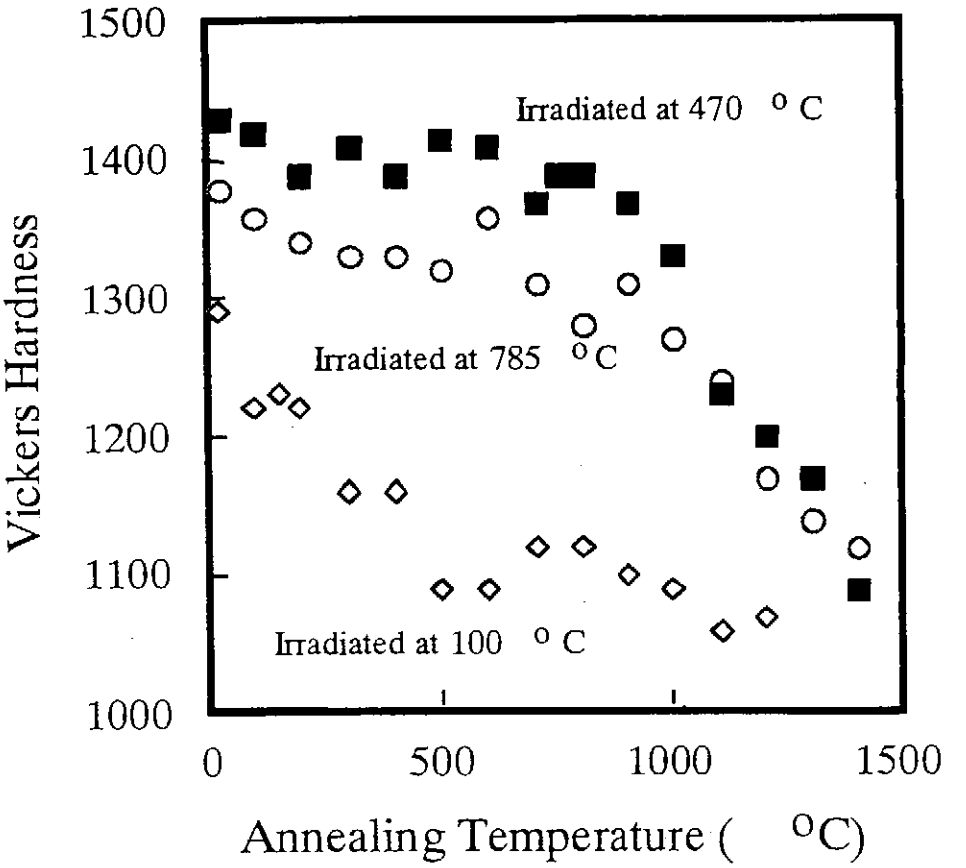

Fig.3 Hardness of unirradiated and irradiatedAlN polycrystals after isochronal annealing.

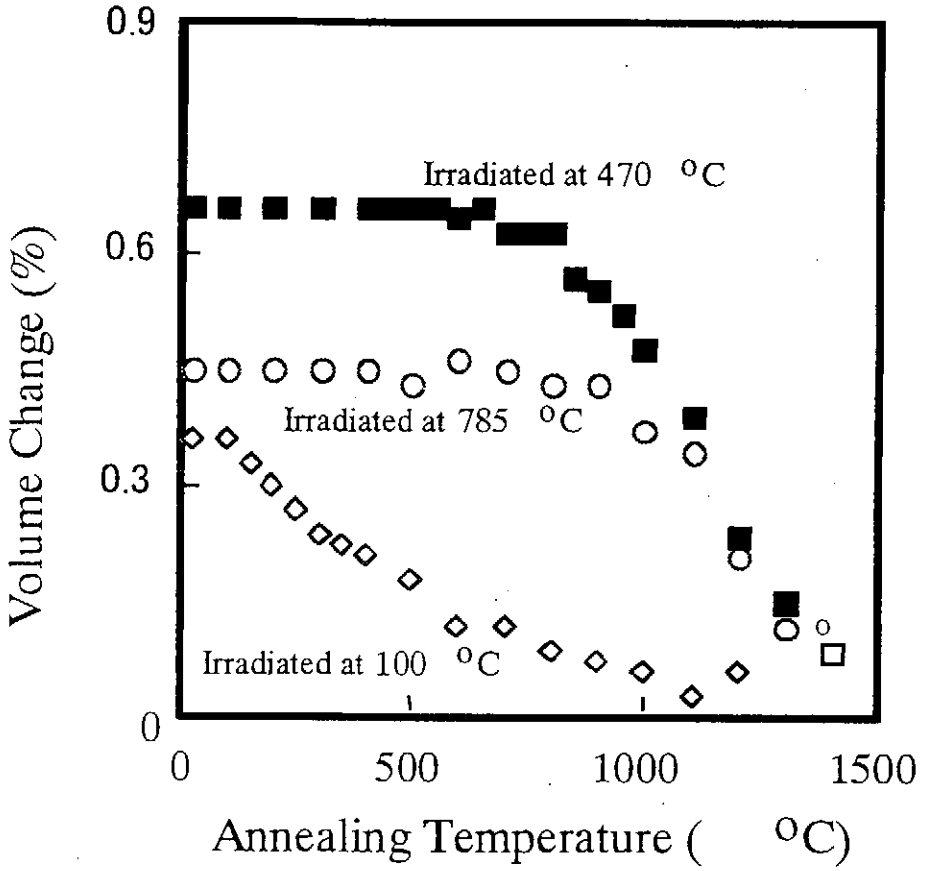

Fig.4 Volume change in unirradiated and irradiatedAlN polycrystals after isochronal annealing.

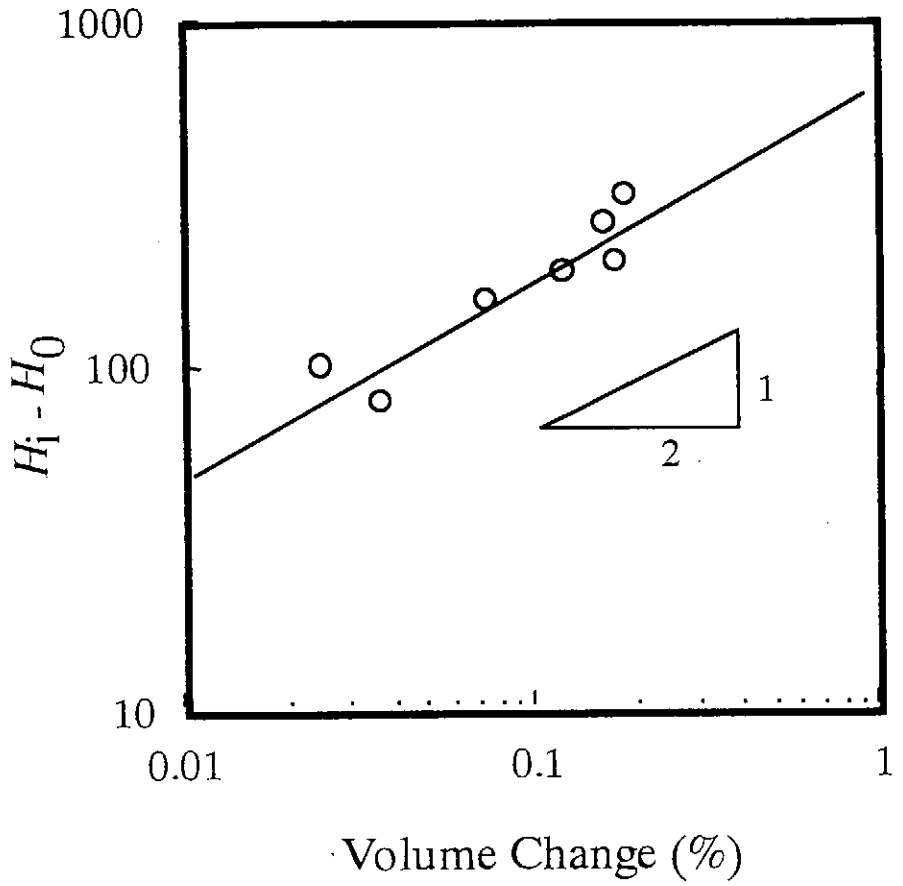

Fig.5 Plots of H_i - H_0 -vs.- volume change for neutron irradiated MgO3.0Al_2O_3 single crystals.

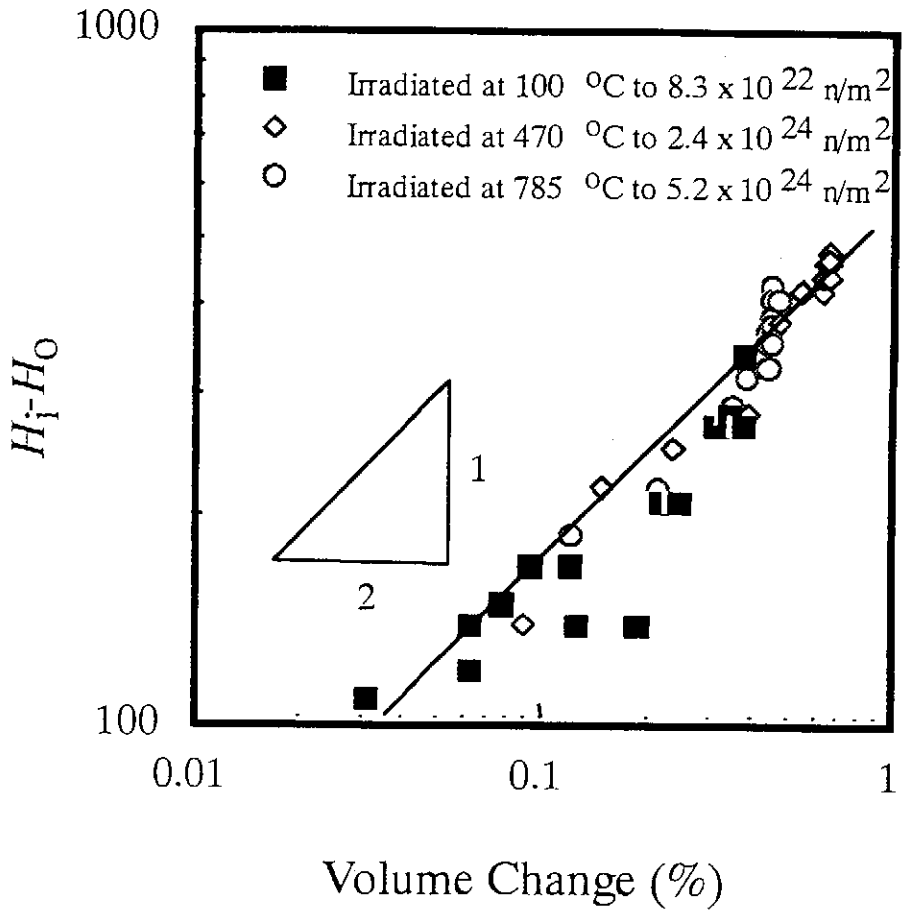

Fig.5 Plots of H_i - H_0 -vs.- volume change for neutron irradiatedAlN polycrystals.

AUTOMODULATION OF AN INTENSE RELATIVISTIC ELECTRON BEAM USING DECREASING LENGTH CAVITIES

Masaki Kamada, Michiya Mori, Keiichi Kamada, Ritoku Ando,
Cha-Yeol Lee and Masaru Masuzaki

Department of Physics, Faculty of Science, Kanazawa University,
Kanazawa 920-1192, Japan

ABSTRACT

Automodulation of an intense relativistic electron beam was reexamined experimentally to obtain trains of subnanosecond electron bunches. An electron beam with energy of 550 keV, current of 3.5 kA and duration of 10 ns was utilized. The rise time of the beam current was about 2 ns. One cavity was used to investigate the relation between the level of current fluctuations and the cavity length. The length of a coaxial cavity was changed from 75 mm to 300 mm. The higher-level current fluctuations were observed when the longer cavity was utilized, as expected by the transmission line theory. Poor current fluctuations were obtained by a 75 mm cavity which was expected to generate subnanosecond bunches. These results indicated that the rise time of the beam current should be improved to obtain trains of subnanosecond electron bunches. A series of cavities with decreasing length was employed. The first cavity was adjusted to 300 mm which caused the IREB high-level current fluctuations. High-level current fluctuations with frequency of 1 GHz was obtained when the cavity lengths were adjusted to 300,150,75 and 75 mm.

1 Introduction

The physics of propagation of an intense relativistic electron beam (IREB) with strong self- and induced field was not only interesting but also important for many applications. Autoacceleration[1] and automodulation[2] of IREB's are remarkable phenomena in which the self- and induced field are effectively harnessed. The energy of an IREB increases twice in the expense of its duration using only a coaxial passive cavity[3] in the one-stage autoacceleration. In the automodulation, a series of coaxial passive cavities modulates

an IREB with power of more than 10^{10} W and no external oscillator is needed. The modulation frequency depends on the round trip time for light of the cavity. Moreover, we reported that an IREB with duration of less than 1 ns was attainable with multi-stage autoacceleration using decreasing length cavities[4],[5]. An IREB with energy of 1.1 MeV, current of 1 kA and duration of 0.8 ns was obtained by 4-stage autoacceleration from that with energy of 500 keV, current of 5 kA and duration of 12 ns. It is technically difficult for conventional pulse-forming-line systems to generate an IREB with duration of less than 1 ns and current of more than order of 1 kA. While the multi-stage autoacceleration was useful to generate one pulse of subnanosecond IREB, automodulation is a potential approach to generate trains of subnanosecond electron bunches. An IREB with subnanosecond duration is an interesting subject of study for an application to high-power, short pulse millimeter-wave generation called superradiance [6]. Trains of subnanosecond IREB should expand the abilities of IREB's.

Automodulation was intensively studied by M. Friedman, et al.[7]. They reported that electron beams with voltage varying from 0.25 MeV to 1 MeV, current from 1 to 8 kA, and pulse duration from 20 to 300 ns were modulated to a depth of nearly 100 %. According to their reports, we started an automodulation experiment to obtain trains of electron bunches with duration of 1 ns for superradiation. However, only a poorly modulated electron beam was observed. We considered that our IREB with current rise time longer than the round trip time for light in the 1 GHz cavity resulted in the poor modulation. We report here the experimental results of the 1 GHz automodulation using decreasing length cavities.

2 Experimental Setup

A Pulserad 105A produced by Physics International, which utilized a conventional Blumlein line, was used as a beam source. A 650 kV, 16 kA, 10 ns pulse is available to a matched load.

Two types of experiments were carried out. One cavity whose length was changeable was utilized to examine that the cavity length affected the quality of modulation of an IREB. The cavity length was changed from 75 mm to 300 mm. The experimental setup of this experiment is shown in Fig. 1. Another experiment employed a series of decreasing length cavities, as shown in Fig. 2. Two serieses of cavities with lengths of 300-75-75 mm and 300-150-75-75 mm were utilized.

In both experiments, foilless diode consisted of a carbon cathode with hollow knife-

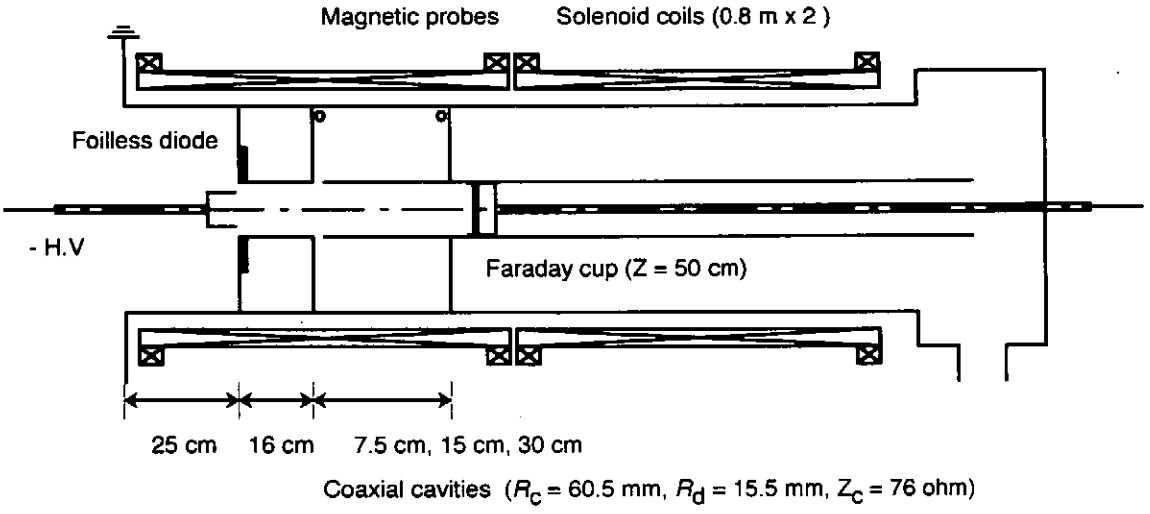

Figure 1: Schematic of one cavity experiment.

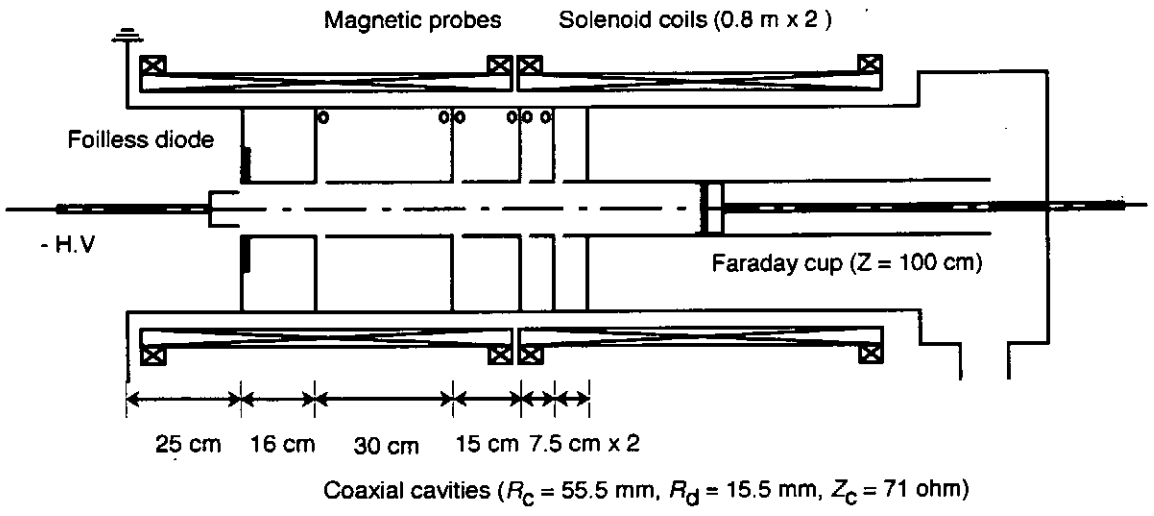

Figure 2: Experimental arrangement for decreasing length cavities.

edge of 20 mm diameter and a carbon anode with 29 mm diameter aperture. The anode-cathode spacing in the diode was 7 mm. An annular electron beam with diameter of 22 mm and thickness of 1 mm was injected from the diode into a conducting drift tube with length of 2.0 m and inner diameter of 31 mm. Typical waveforms of the diode voltage and the current are shown in Fig. 3(a) and (b), respectively. As shown in Fig. 3(b), the FWHM of the pulse duration of the measured beam current was 12 ns, and the rise time was 2 ns. An axial magnetic field of 1 T was applied by two solenoid coils with total length of 1.6 m. Each coil had compensating magnetic field coils at the both ends to hold the magnetic field strength constant at the joint of coils. The first cavity was connected to the drift tube via gap at $z = 16$ cm, where z is the distance from the anode. The gap spacing in any cavity was 2.5 cm and the impedance of cavities was typically 76 Ω. The base pressure in the system was maintained below 1×10^{-5} Torr.

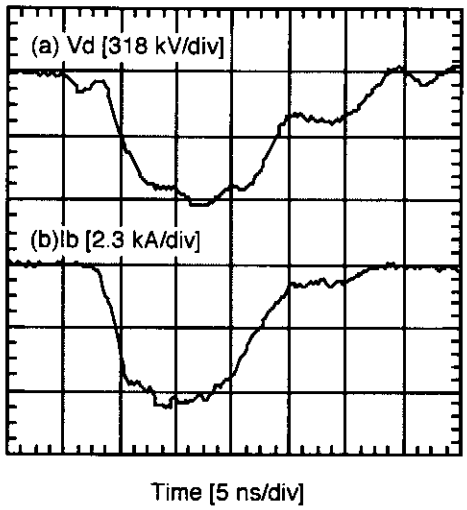

Figure 3: Typical waveforms of (a) diode voltage and (b) beam current.

A Faraday cup was used to measure the beam current at various locations along the axis in the drift tube and to estimate the kinetic energy of beam electrons. The Faraday cup consisted of a carbon disk collector, a 0.042 ohm shunt resistor composed of chip resistors and a 51 ohm chip resistor for matching. Aluminum foils of various thickness were placed in front of the Faraday cup and a transmitted current through aluminum foils was measured. Using the ratio of the transmitted current to the current detected without foil and the range-energy relations [7], the kinetic energy of beam electrons was estimated. A magnetic analyzer located at the end of the drift tube was used to check the

electron kinetic energy obtained by the range-energy relations. And the measured energy was in good agreement with the estimated one.

Magnetic probes shown in Fig. 1 and 2 were used to measure the beam current at each gap and the current at the end of cavity. The differentiated currents detected by magnetic probes were integrated numerically.

The signals were monitored by Tektronix TDS 684A digitizing oscilloscope (1 GHz, 5 GS/s).

3 Experimental Results and Discussion

3.1 One cavity experiment

One cavity whose length was changeable was utilized. The cavity length was adjusted to 75, 150, 300 mm. The Faraday cup waveforms detected at z=50 cm for each cavity length are shown in Fig. 4. No fluctuations in beam current was observed for IREB propagation through a smooth drift tube [Fig. 4 left(a)] When one cavity whose length adjusted to 75 mm was inserted in the drift tube, low-level current fluctuations were observed [Fig. 4 left (b)]. High-level current fluctuations were observed when the cavity lengths were adjusted to 150 and 300 mm [Fig. 4 left (c),(d)]. The Fast Fourier transform of the Faraday cup waveforms showed that the fundamental frequencies of fluctuations were 0.5 and 0.25 GHz for 150 and 300 mm cavities, respectively, as shown in Fig. 4 [right]. These frequencies corresponded to the round trip time for light in each cavity. However, the expected frequency of 1 GHz for the 75 mm cavity was not observed clearly because of its low-level fluctuations. The waveforms of the magnetic probes in the cavity corresponded to those of the Faraday cup. Poor fluctuations were also observed with frequency of 1 GHz by the magnetic probe in the 75 mm cavity, though high-level fluctuations were detected in the150 and 300 mm cavities.

It was reported in ref [8] that the fluctuations of beam current in one cavity experiments were strongly dumped when $LdI/dt < V$; where L was the cavity inductance, V was the diode voltage and I was the beam current. In our case, LdI/dt's were caliculated to be 50, 120 and 250 kV for 75, 150 and 300 mm cavities, respectively, while the V was 500 kV. Strong dumping was observed only when the cavity length was 75 mm. Our experimental results indicated that the the strong dumping occurred when $LdI/dt << V$. However, as a trains of subnanosecond electron bunches was expected in our experiments, high-level current fluctuations with less than 75 mm cavity was necessary. In this context,

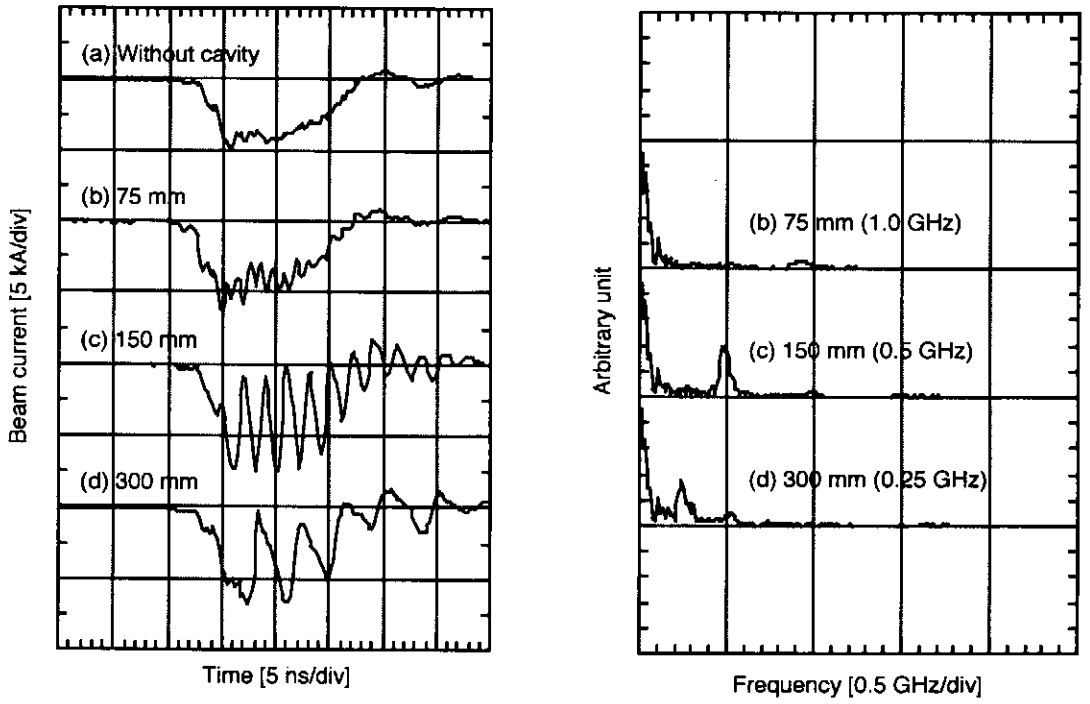

Figure 4: Beam current passing through the smooth drift tube or one cavity (left) and their FFT waveformes (right), (a) without cavity, (b) 75 mm, (c) 150 mm and (d) 300 mm.

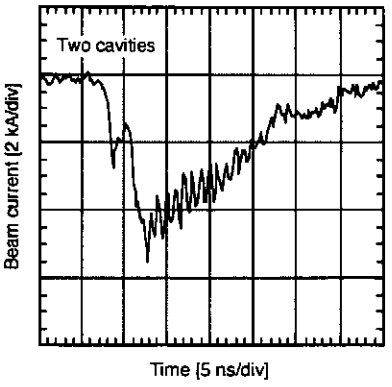

Figure 5: Beam current passing through two 75 mm cavities.

as the inductance of the cavity was difficult to increase, dI/dt must be increased to obtain high-level current fluctuations with a short cavity.

It was also reported in ref [8] that the presence of two or more cavities caused the appearance of high-level fluctuations in the beam current. A series of cavities with lengths of 75 mm were utilized. Though the number of cavities was changed from two to four, levels of fluctuations in the beam current were a little increased as shown in Fig. 5. The reason why the high-level of fluctuations did not appear was not clear. It was considered that the beam current was not enough to obtain high-level current fluctuations with a series of cavities.

Return to one cavity experiments, we calculated LdI/dt's from the inductance of the 75 mm cavity and the currents fluctuated by 150 and 300 mm cavities. LdI/dt's were increased to100 and 120 kV for fluctuated currents of150 and 300 mm cavities, respecrively. The rise time of the beam current was improved by one cavity modulation. Therefore, we tried to utilize the 150 and/or 300 mm cavities in front of 75 mm cavity to increase dI/dt.

3.2 Decresing length cavities experiment

Two serieses of cavities with lengths of 300-75-75 mm and 300-150-75-75 mm were utilized to obtain high-level current fluctuations with frequency of 1 GHz. The Faraday cup waveforms as shown in Fig.6 indicated that the levels of current fluctuations were increased. The level of current fluctuations of the 300-150-75-75 mm cavities were higher than those of the 300-75-75 mm cavities. The fundamental frequencies of the current fluctuations were about 1 GHz for both cases.

In order to obtain the kinetic energy of the accelerated electrons by the range-energy relation method, aluminum foils were attached in front of the Faraday cup. As the current fluctuations were still observed in the current waveforms passing through aluminum foils as shown in Fig. 7, parts of beam electrons were accelerated and the rest of electrons were decelerated. The increases of the energy of the accelerated parts were 150keV and 250 keV for the 300-75-75 mm and the 300-150-75-75 mm cavities, respectively. These results indicated that the length of the $(n+1)$ th cavity should be adjusted to half of the (n) th cavity length for high-level current fluctuations. The appropriate numbers and lengths of the cavities at each stage for high-level current fluctuations must be exmined. The use of decreasing length cavities should make high-frequency and high-level current fluctuations possible for the IREB with low current and low dI/dt.

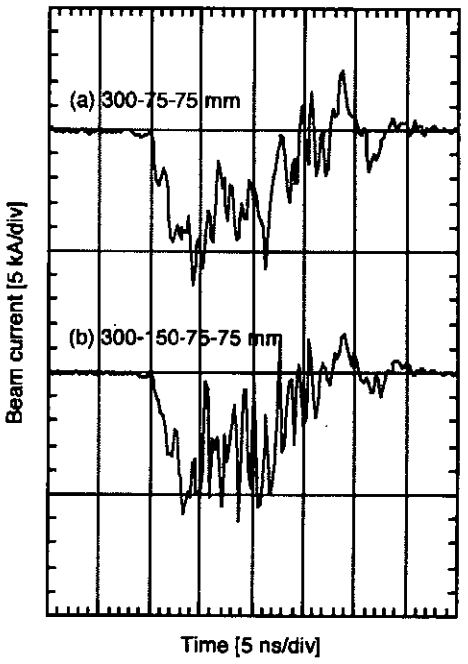

Figure 6: Beam current passing through a series of decreasing lengths cavities, (a) 300-75-75 mm and (b) 300-150-75-75 mm.

4 Conclusion

A series of cavities with decreasing length was found to be effective to obtain trains of subnnanosecond electron bunches by the automodulation scheme. Developments of cavity structure and arrangements of the cavities had just started experimentally to obtain higher-level current fluctuations and shorter bunch duration.

Acknowledgement

The authors gratefully acknowlege Dr. D. Hasegawa for helpful discussions and technical supports and Mr. M. Nakashima for helpful assistances.

A part of this work is supported by a Grant-in-Aid for Scientific Research from Ministry of Education, Science, Sports and Culture, Japan.

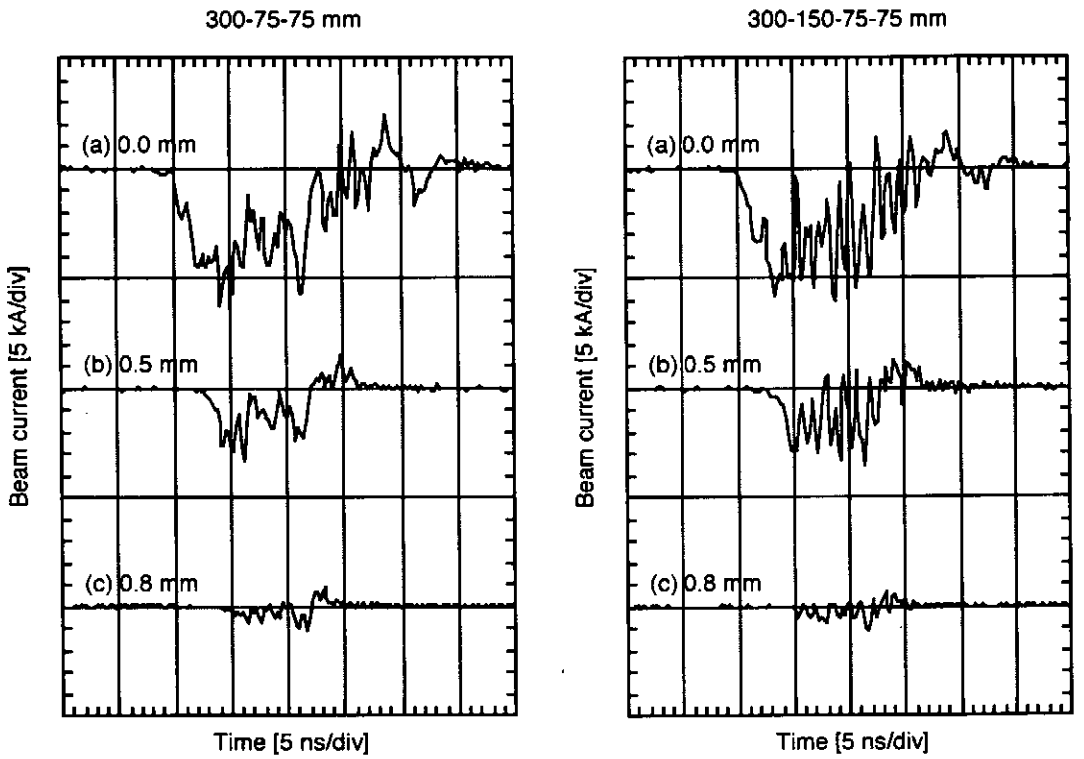

Figure 7: Typical waveforms of Faraday cup with alminum foil of various thickness, (a) 300-75-75 mm and (b) 300-150-75-75 mm.

References

[1] A. Kisletsov L. N. Kazanski and A. N. Lebedev, "Selfacceleration in intense electron beams," *At. Energ.*, vol. 30, pp. 27–31, 1971.

[2] M. Friedman, "Automodulation of an intense relativistic electron beam," *Phys. Rev. Lett.*, vol. 32, pp. 92–940, 1974.

[3] M. Friedman, "Autoacceleration of an intense relativistic electron beam," *Phys. Rev. Lett.*, vol. 31, pp. 1107–1110, 1973.

[4] K. Kamada, D. Hasegawa, K. Shimizu, R. Andou and M. Masuzaki, "Two-stage autoacceleration using decreasing length cavities," *IEEE Trans. Plasma Sci.*, vol. 27, pp. 1609–1610, 1999.

[5] D. Hasegawa, K. Kamada, K. Shimizu, R. Andou and M. Masuzaki, "Four-stage autoacceleration for a subnanosecond intense relativistic electron beam," *IEEE Trans. Plasma Sci.*, vol. 28, pp. 1648–1651, 2000.

[6] N. S. Gintburg, I. V. Zotovan A. S . Sergeev I. V. Konoplev A. D. R. Phelps A. W. Cross S. J. Cooke, V. G. Shpak, M. I. Yalandin, S. A. Shunalinov, and M. R. Ulmaskulov, "Experimental observation of cyclotron superradiance under group synchronism conditions," *Phys. Rev. Lett.*, vol. 78, pp. 2365–23680, 1997.

[7] H. H. Seliger, "Transmission of positrons and electrons," *Phys. Rev.*, vol. 100, pp. 1029–1037, 1955.

[8] M. Friedmn, V. Serlin, A. Drobot and L. Seftor, "Self-modulation of an intense relativistic electron beam," *J. A ppl. Phys.*, vol. 56, pp. 2459–2474, 1984.

2.5-D Analysis of Intense Relativistic Electron Beam propagation in an unmagnetized plasma

Norio Toyosugi, Ritoku Ando, Cha-Yoel Lee, Keiichi Kamada and Masaru Masuzaki

Department of Physics, Faculty of Science, Kanazawa University, Kanazawa, 920-1192, Japan

Abstract

Interactions between an unmagnetized plasma and an injected intense relativistic electron beam are simulated by 2.5-dimensional particle-in-cell code KARAT. The ratio of the beam electron density (n_b) to the plasma electron density (n_p) is taken as a parameter. The ratio, n_b/n_p, is found to affect the beam propagation window and the two-stream instability. When the two-stream modes are excited strongly (n_b/n_p = 0.01 ~ 0.1), the beam electrons diverge radially and the beam propagation is disturbed. When the two-stream modes are excited weakly (n_b/n_p = ~ 1), the beam electrons are focused and the beam propagates through the plasma.

I. Introduction

When an intense relativistic electron beam (IREB) is injected into an unmagnetized plasma, the plasma develops into a strong Langmuir turbulence state originated from the two-stream instability between beam and plasma electrons.[1-3] In this state, density depressions in which the high frequency electric field is trapped (caviton) are created,[4] and the background Langmuir wave also exists.[4] It is found experimentally that the n_b/n_p affects the microwave radiation and the beam propagation. It was observed that a suitable plasma density exists for the IREB propagation[6]. The radius of the IREB is observed by a phospher plate . The beam radius when the n_b/n_p is between 0.005 and 0.1 is larger than that observed when n_b/n_p is 0.1 and 1.[6] This result shows the effective electron beam propagation is achieved when the n_b/n_p is 0.1 and 1. Microwave spectrum is measured experimentally with spectrometers covering 18-140 GHz.[5] When the n_b/n_p is between 0.005 and 0.1, the strong broadband microwave radiation from the plasma is observed.[6] When the n_b/n_p is between about 0.1 and 1, no radiation is observed.[6] The mechanism of the high-power microwave radiation is considered to be originated from the interaction of the modulated IREB with the electric field of the cavitons. The IREB modulation is considered to occur by the interaction of the IREB with the background Langmuir wave. Therefore, the high-power microwave radiation is suspected to relate with the strong Langmuir turbulence plasma. The Langmuir wave is originated from the two-stream instability.

When an intense relativistic electron beam (IREB) is injected into an unmagnetized plasma, it is expected that the two-stream instability occur. Analysis of the two-stream instability was studied extensively[7-11]. The question of interest was the ratio of the maximum electric field energy density at saturation to the initial beam energy W. The parameter $S \equiv \beta_0^2 \gamma_0 \left(n_b / 2n_p\right)^{1/3}$ was defined by Thode and Sudan[7,8], where β_0 is the normalized initial beam velocity by the speed of light, γ_0 is the initial relativistic mass factor of the beam. Based upon a single wave approximation, a semiquantitative analytic solution for the fraction of beam energy converted into electric filed energy was predicted to be[8]

$$W \equiv \varepsilon |E|^2 / 4 n_b \gamma_0 mc^2 = 0.5 S (1+S)^{-5/2},$$

where ε is the permittivity of free space, m is the electron mass. When the W is large, the strong two-stream instability occurs. When the beam energy is fixed, the W is a function of the n_b/n_p. And W is maximized by an appropriate n_b/n_p.

It is not clear whether the one-dimensional result is applicable to explain our experimental results or not. Then we have carried out 2.5-dimensional simulations of the beam propagation in an unmagnetized plasma to study the beam propagation in an unmagnetized plasma and the two-stream instability. There are little theoretical reports for the interaction between an IREB and an unmagnetized plasma in 2.5-dimension. In 2.5-dimensional simulations, radial electric field is observed, which is not considered in 1-d case. The result of 2.5-dimensional simulation is reported here.

II.Simulation

We have carried out computer simulations using 2.5-D code KARAT[12]. KARAT is a fully electromagnetic code based on the particle-in-cell (PIC) method. It is aimed primarily at the solution of non-stationary electrodynamic problem having complicated geometry and involving dynamic of relativistic electrons and non-relativistic ions. In particular, KARAT is well suited to the simulation of high-current electron devices such as vircators, free-electron lasers, gyrotrons, etc. It is also appropriate for modeling of physical phenomena in labolatory and space plasmas.

In our simulations for changing the density ratio n_b/n_p, the beam electron density is varied for a fixed plasma density. The drift tube is a cylinder and both ends of that has thin foils. The cylindrical wall and the foil are perfectly conducting. The radius, r_d, is 1.9 cm and the length, L_d, is 40 cm. When the particles enter into the cylindrical wall and both ends of the drift tube during the calculation, they escape form the simulation region. A cold unmagnetized neutral argon plasma with radius, r_p, of 1.7 cm and length, L_p, of 40 cm is initially loaded along the axis. The plasma density is

fixed at $n_p = 2\times10^{11}$ cm^{-3} initially. To avoid non-physical instability, the plasma electrons and ions are introduced some initial temperature. A cold electron beam with radius, r_b, of 1.5 cm is injected into the plasma from the left side boundary. Both the rise time and the fall time of the beam current are 1ns and the duration of the beam is 25 ns. The initial beam energy is 1.0 MeV. The density ratio of the beam electrons to the plasma electrons n_b/n_p is changed from 0.001 to 0.5. When the n_b/n_p is 0.5, the beam current has the maximum value of 3.2 kA.

III. Simulation results

1. The high density ratio case

When the beam density is high, i.e. the initial density ratio $n_b/n_p = 0.5$, the simulation results are as follows. The positions of the beam and plasma electrons at $t = 8.0$ ns is shown in Fig. 1 (a) and (b), respectively. As the volume element varies like r^2, the beam electron density near the axis is more than inferred from the Fig. 1 (a). Figure 1(a) shows that the electron beam has radial oscillation and the beam density is high near the drift tube axis. Figure 1(b) shows the plasma electrons are forced out from the axis because of the repulsion for the injected beam electrons and an ion channel is created.

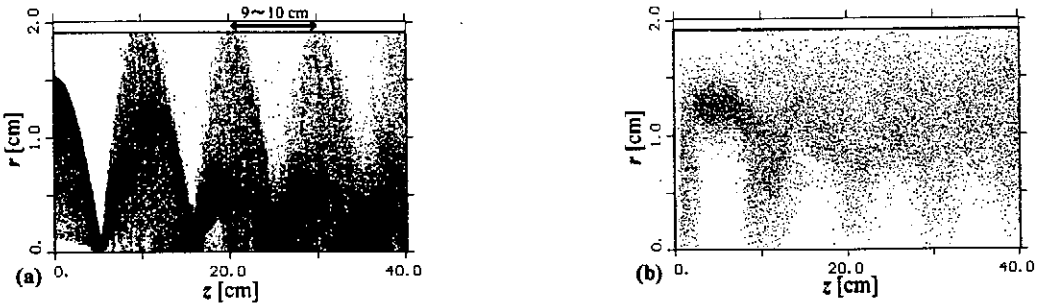

Figure 1: Electron positions at $t = 4$ ns ($n_b/n_p = 0.5$). (a) Beam electrons. (b) Plasma electrons.

Figure 2 shows the Fourier transform of the longitudinal electric field excited in the plasma at $z = 35$ cm and $r = 0.2$ cm. The time interval of the Fourier transform is between $t = 0$ ns and $t = 4$ ns. The plasma frequency of 4 GHz corresponding to the initial plasma density is not observed. The observed oscillation wavelength along the axis in the beam envelope is 9 ~ 10 cm as shown in Fig. 1 (a). This is half of the betatron wavelength. The effective beam

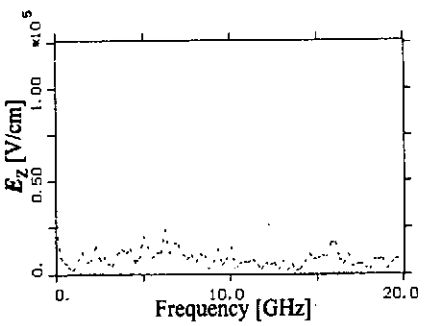

Figure 2: The Fourier transform of the longitudinal field ($n_b/n_p = 0.5$).

transport in the ion-focused regime is reported.[13] The betatron wavelength is derived for the case of the beam propagation in the ion focused regime ($n_b / n_p \approx 1$). Therefore, in the high density ratio case, the beam propagation is explained by the theory of the ion-focused regime. And the two-stream instability is suppressed by the escape of the plasma electrons. The radial oscillation is produced by imbalances in the beam's transverse pressure and the radial force of the ion channel.[13] When the n_b/n_p is high, the effective beam propagation continues in the simulation time.

2. The intermediate density ratio range

The simulation results of the case of $n_b/n_p = 0.1$ initially are as follows. The positions of the beam and plasma electrons at $t = 4.0$ ns is shown in Fig. 3 (a) and (b), respectively. Figure 3 (a) shows that the injected electron beam is focused in radial direction at $z = 10$ cm then the beam electrons begin to oscillate radially. Some beam electrons have large amplitude of transverse oscillation and escape from the cylindrical wall. Figure 3 (b) shows that some plasma electrons near the drift tube axis are also forced out between $z = 20$ cm and 40 cm as seen in Fig 3 (b).

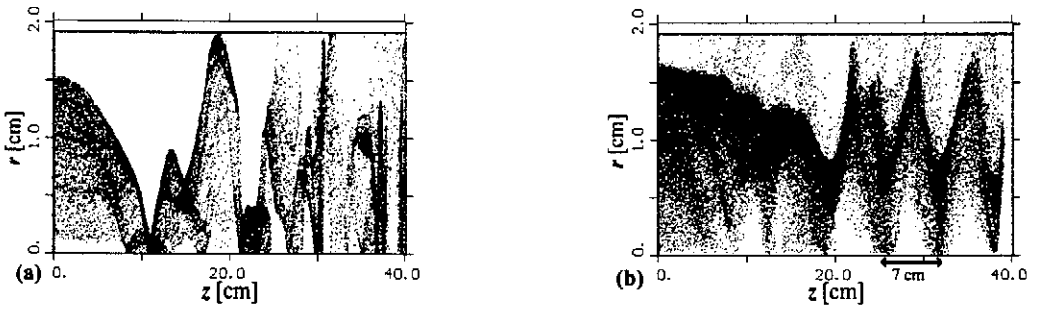

Figure 3: Electron positions at $t = 4$ ns ($n_b/n_p = 0.1$). (a) Beam electrons. (b) Plasma electrons.

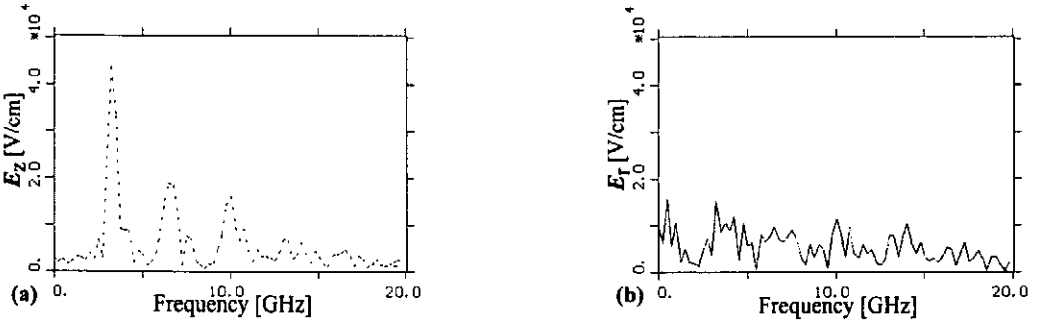

Figure 4: The Fourier transform of the electric field ($n_b/n_p = 0.1$).
(a) The longitudinal field. (b) The radial electric field.

In Figure 3 (b) plasma electrons still remains compared with Fig. 1 (b) of the high density ratio case. The radial electric filed is observed in our 2.5-dimensional simulations, which is not included in 1-dimensilnal simulations. Figure 4 (a) and (b) shows the Fourier transform of the longitudinal and radial electric field excited in the plasma at z = 35 cm and r = 0.2 cm. The time interval of the Fourier transform is between t = 0 ns and t = 4 ns. The plasma frequency of 4 GHz corresponding to the initial plasma density and frequencies corresponding to higher harmonics are observed. From the one-dimensional linear theory, the most unstable wave excited by the two-stream instability has a wave number $k \cong \omega_p / V_{b0}$, where ω_p is the plasma frequency and V_{b0} is the beam velocity. In this case the wave number is about 90 m^{-1}, that is, the wavelength is 7 cm. This wavelength agrees with the wavelength observed in Fig. 3(b). The distributions of the beam electrons and plasma electrons in the phase space at t = 4 ns are shown in Fig. 5. The beam electrons are trapped and rotate in the phase space. Therefore, the two-stream instability is found to be observed in the simulation. The ratio of the maximum electric field energy density at saturation to the initial beam energy W is calculated to be 0.06. To evaluate W, we use the value of the electric field strength observed at z = 30 cm and r = 0.2 cm. And we assume that the electric field has the Bessel functional radial dependence and the longitudinal dependence of the fields is ignored (i.e. the wave strength value z = 30 cm and r = 0.2 cm is uniform in z direction.).

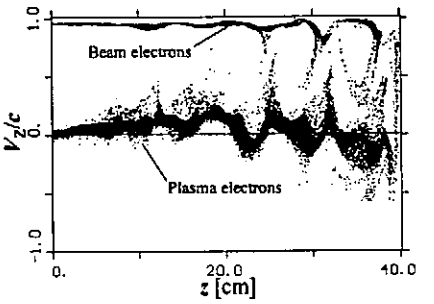

Figure 5: The distributions of the beam electrons and the plasma electrons in the phase space at t = 10 ns (n_b/n_p = 0.1).

When t = 2 ns ~ 10 ns, the most unstable wave of 4 GHz excited by the two-stream instability is dominate. After $t \approx 10$ ns, the results of the simulation are changed. The positions of the beam and the plasma electrons at t = 12.0 ns are shown in Fig. 6 (a) and (b), respectively.

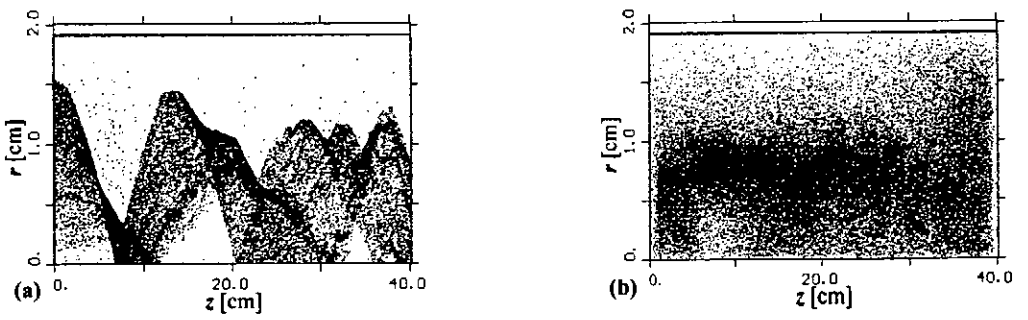

Figure 6: Electron positions at t = 12 ns (n_b/n_p = 0.1). (a) Beam electrons. (b) Plasma electrons.

In Figure 6 (a) the electron beam has radial oscillation. But little beam electrons reach at the cylindrical wall in contrast with Fig. 3 (b). The maximum amplitude of the oscillating beam radius decreases slightly (slightly focused in the radial direction). In Fig. 6 (b) the plasma electrons have no bunch like Fig. 3 (b). Figure 7 (a) and (b) show the wave spectrum of the longitudinal and radial electric field at z = 35 cm and r = 0.2 cm. The time interval of the Fourier transform is between t = 8 ns and t = 12 ns.

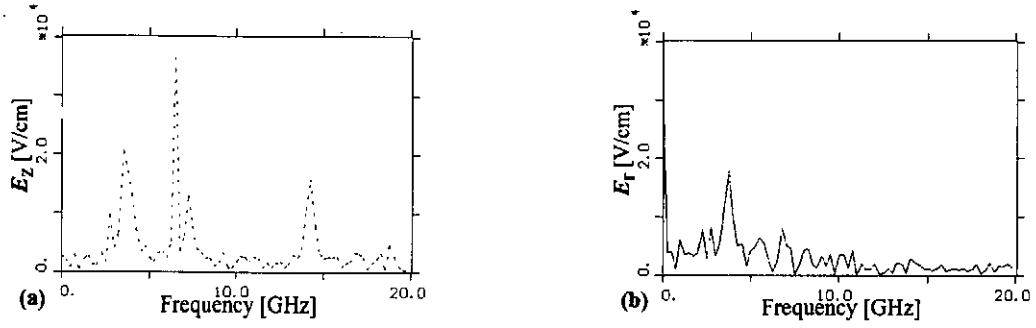

Figure 7: The Fourier transform of the electric field (n_b/n_p = 0.1).
(a) The longitudinal field. (b) The radial electric field.

In this time interval, the averaged plasma electron density decreases from $n_p \approx 5\times10^{10} cm^{-3}$ to $n_p \approx 4\times10^{10} cm^{-3}$ because of the escape of the electrons from the cylindrical wall (r_d =1.9cm). Plasma frequencies 2.0 GHz and 1.8 GHz corresponding to these densities are not observed. The distributions of the beam and the plasma electrons in the phase space at t = 10 ns are shown in Fig.8. Little beam electrons are trapped.

In the intermediate density ratio, the most unstable wave excited by the two-stream instability of wave number $k \cong \omega_p / V_{b0}$ dominates at 0 < t < 10 ns. And the wave becomes weak at t > 10 ns.

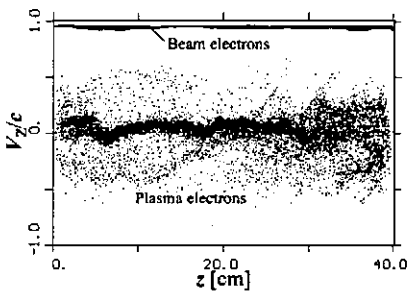

Figure 8: The distributions of the beam electrons and the plasma electrons in the phase space at t = 10 ns (n_b/n_p = 0.1).

3. The lower density ratio case

The simulation results of the case of n_b/n_p = 0.001 initially are as follows. The positions of the beam and the plasma electrons at t = 8.0 ns is shown in Fig. 9 (a) and (b), respectively. In

Fig. 9 (a) the electron beam keeps its radius with 1.5 cm. Figure 9 (b) shows the plasma electrons are not disturbed. Figure 10 (a) and (b) shows the Fourier transform of the longitudinal and radial electric field excited in the plasma at z = 35 cm and r = 0.2 cm. The time interval of the Fourier transform is between t = 4 ns and t = 8 ns. The plasma frequency of 4 GHz corresponding to the initial plasma density is observed. And radial oscillation of the electron beam is observed as shown in Fig. 10 (b).

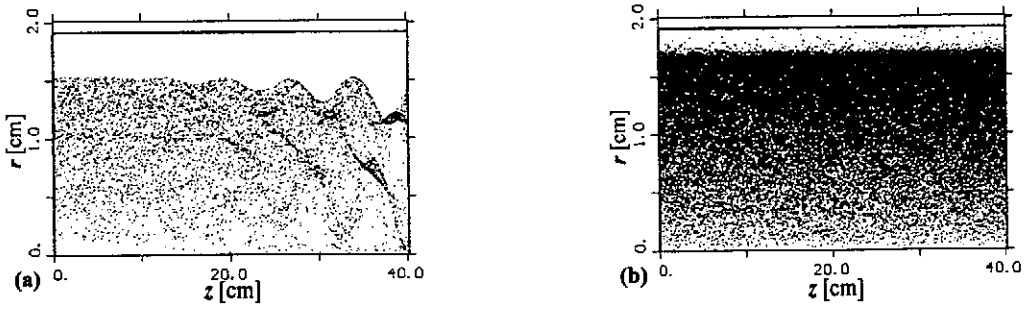

Figure 9: Electron positions at t = 8 ns (n_b/n_p = 0.001). (a) Beam electrons. (b) Plasma electrons.

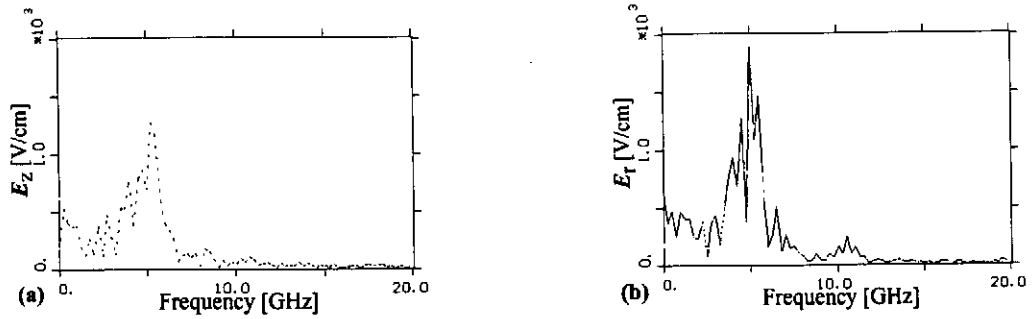

Figure 10: The Fourier transform of the electric field (n_b/n_p = 0.001).
(a) The longitudinal field. (b) The radial electric field.

The two-stream instability may be excited weakly. In the low density ratio simulation, the most unstable wave of 4 GHz excited by the two-stream instability continues during the beam pulse length. The distributions of the beam electrons and the plasma electrons in the phase space at t = 8 ns is shown in Figure 11. No beam electrons are trapped. The strength of the wave is too weak to trap the beam electrons though the injected electron beam current is

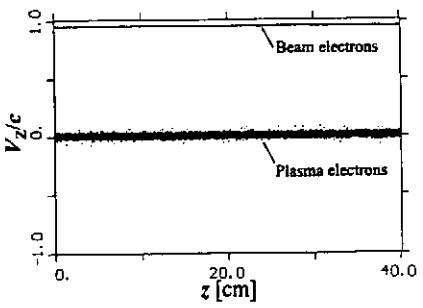

Figure 11: The distributions of the beam electrons and the plasma electrons in the phase space at t = 8 ns (n_b/n_p = 0.1).

enough to excite the two-stream instability. The ratio of the maximum electric field energy density at saturation to the initial beam energy, W, is calculated about 0.01. This value is smaller than that observed in the intermediate density ratio cases. When the W is small, the two-stream instability is excited weakly. The dependence of the two-stream instability on the density ratio qualitatively agrees with Thode and Sudan's study.

VI. Discussion and concluding remarks

We have carried out the beam-plasma interaction by the PIC 2.5-dimensional simulations with non-periodic boundary conditions and with no external magnetic field. The simulation results show the two-stream instability between the beam electrons and the plasma electrons has the dependence on the density ratio n_b/n_p. And the beam propagation window has also the dependence on the density ratio. When the density ratio n_b/n_p is ~ 0.5, the two-stream instability is suppressed because of escape of the plasma electrons. The beam propagation is explained by the theory of the ion-focused regime. When the density ratio n_b/n_p is 0.01 ~ 0.1, the two-stream instability is strongly excited. The radial electric field is observed in the 2.5 dimensional simulations. The longitudinal electric field traps the beam electrons. And the radial electric filed disturbs the beam propagation. When the density ratio n_b/n_p is small (~ 0.001), the two-stream instability is excited weakly. However, the strength of the excited waves is too small to trap beam electrons.

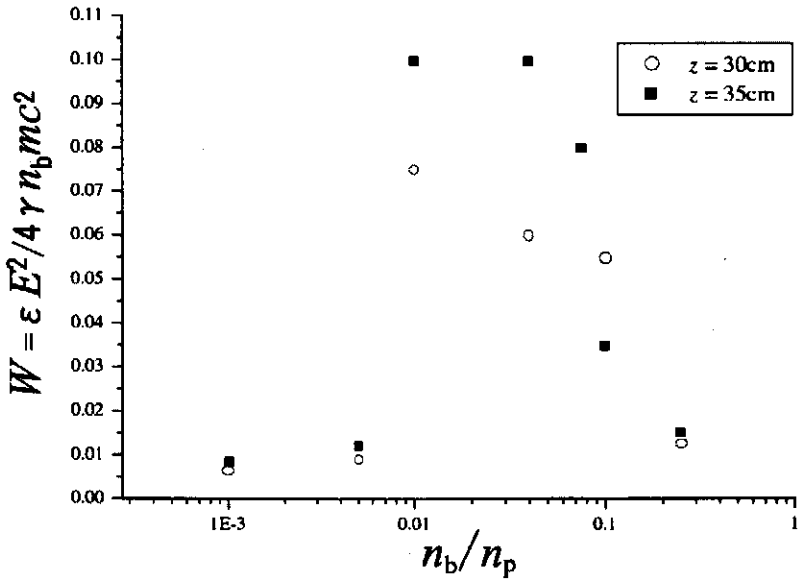

Figure 12: The calculated W as a function of n_b/n_p.

Figure.12 shows the calculated maximum energy transfer efficiency from the beam to the excited wave. We have calculated the W with assumptions as mentioned above. The

calculated W have maximum values when the n_b/n_p is 0.01~0.04, respectively. The dependence of the two-stream instability on the n_b/n_p seen in Fig. 12 is qualitatively agree with the prediction in 1-dimensional theory, in which the W has also the maximum value for the appropriate value of n_b/n_p. When the W is large, the two-stream instability is excited strongly. When the W is small, the two-stream instability is excited weakly. In our experiments, when the n_b/n_p is between 0.005 and 0.1, the radiation occurs and the beam propagation is disturbed. When the n_b/n_p is between 0.1 and 1, no radiation occurs and the effective beam propagation is achieved. The observed relation between the beam propagation and the two-stream instability in our simulations is qualitatively consistent with these experimental results. And the simulation results show the possibility of the beam modulation by the two-stream instability. The relation between the strong Langmuir turbulence plasma and the beam propagation will be studied.

References

1) G. C. M. Janssen, E. H. A. Granneman, and H. J. Hopman, Phys. Fluids, 27 (1984) 736.
2) D. Levron, G. Benford, and D. Tzach, Phys. Rev. Lett., 58 (1987) 1336.
3) M. Yoshikawa, M. Masuzaki, and R. Ando, J. Phys. Soc. Jpn., 64 (1994) 3303.
4) P. A. Robinson, Rev. Mod. Phys., 69 (1997) 507.
5) H. Yoshida, M Masuzaki, S. Ooyama, R. Ando, and K. Kamada, IEEE Trans. Plasma Sci. 27 (1999) 682.
6) R. Ando, M. Masuzaki, H. Morita, K. Kobayashi, M. Yoshikawa, H. Koguchi and K. Kamada, J. Phys. Soc. Jpn., 65 (1996) 2518.
7) L. E. Thode and R. N. Sudan, Phys. Rev. Lett., 30 (1973) 732.
8) L. E. Thode and R. N. Sudan, Phys. Fluids 18 (1975) 1552.
9) Ya. B. Fainberg, V. D. Shapiro, and V. I. Shevchenko, Zh. Eksp. Teor. Fiz. 57 (1969) 966 [Sov. Phys. JETP 30, (1970) 528].
10) R. I. Kovtun and A. A. Rukhadze, Zh. Eksp. Teor. Fiz. 58, (1970) 1709 [Sov. Phys. JETP 31, (1970) 915].
11) N. G. Matsiborko, I. N. Onishchenko, V. D. Shapiro, and V. I. Shevchenko, Plasma Phys. 14 (1972) 591.
12) V. P. Tarakanov, Users Manual for Code KARAT ver. 7.09 (1999).
13) S. B. Swanekamp, J. P. Holloway, T. Kammash and R. M. Gilgenbach, Phys. Fluids B4 (1992) 1332.

Spectrum Analysis of Hydrogen Plasma in Spherically Convergent Beam Fusion

Kazuki Ogasawara, Kunihito Yamauchi, Masato Watanabe,
Akitoshi Okino*, Yoshitaka Sunaga and Eiki Hotta

Department of Energy Sciences,
Tokyo Institute of Technology,
Nagatsuta, Midori-ku, Yokohama, Kanagawa 226-8502, Japan.
**Department of Electrical and Electronic Engineering,*
Tokyo Institute of Technology,
O-okayama, Meguro-ku, Tokyo 152-8552, Japan.

ABSTRACT

Spectroscopic analysis of spherical glow discharge fusion device was carried out using hydrogen gas. Effects of the discharge current and cathode voltage on spectrum profiles of hydrogen Balmar lines were measured. The profiles of all hydrogen lines were broadened with the cathode voltage. From the relationship between the maximum broadening width and the cathode voltage, it was indicated that the broadening was caused by the Doppler effect. From the spatial distribution of emission intensity, it was found that plasma core size became larger with discharge current and smaller with cathode voltage.

I. Introduction

Spherically convergent beam fusion (SCBF) is a scheme for accelerating deuterium ions, which are generated between electrodes by a glow discharge, toward the spherical center and giving rise to fusion reactions. As the SCBF device is very simple and compact unlike other fusion devices, it is applicable to a portable neutron source.

In 1994, G. H. Miley *et al.* confirmed a steady-state D-D neutron production over 10^6 s^{-1} using a simple fusion device[1]. However, the detailed mechanism of SCBF has not been made clear yet. In this report, the visible emission from the device was investigated using hydrogen discharge.

II. Experimental setup

The schematic of an experimental SCBF device is illustrated in Fig.1. The device consists of 45 cm diameter, 31 cm high stainless steel cylindrical chamber and a spherical mesh-type anode of 30 cm diameter. A spherical grid cathode of 7 cm diameter located at the center of the anode is connected to a 0–60 kV, 0–20 mA constant current dc power supply through a ballast resistor of 1 kΩ and a stabilization capacitor of 0.15 μF. The cylindrical chamber is evacuated by a turbo-molecular pump and a base pressure of 10^{-5}

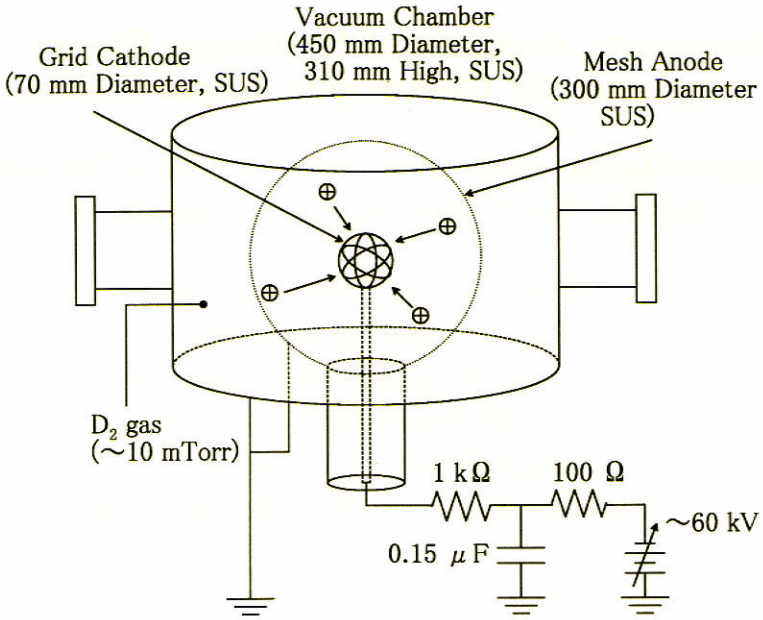

Fig.1. Schematic of an experimental device

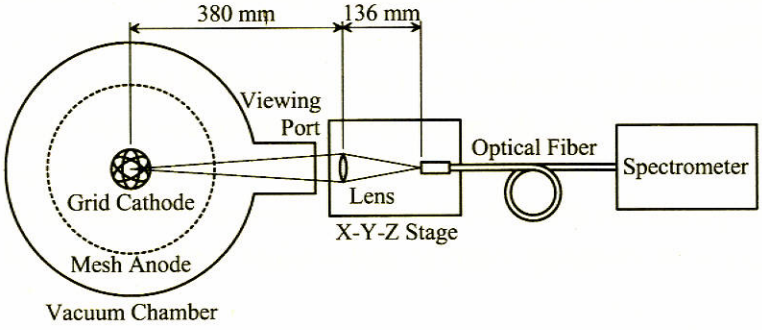

Fig.2. Schematic of an optical measurement system

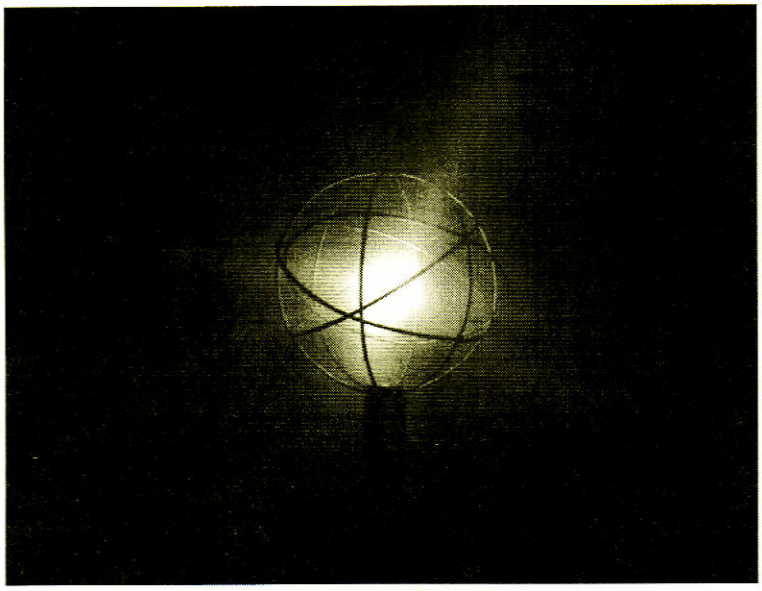

Fig.3. Photograph of a discharge plasma

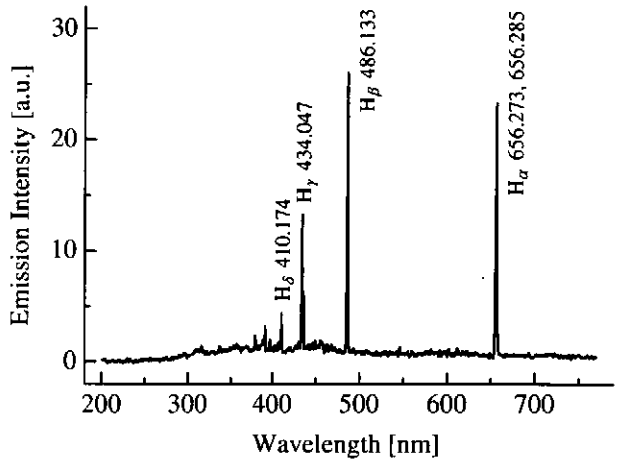

Fig.4. Emission spectrum of hydrogen discharge

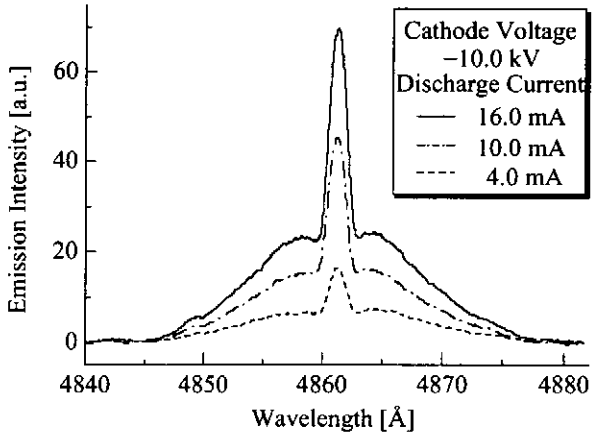

Fig.5. Profiles of H_β line spectra at discharge currents of 4.0–16.0 mA with a fixed cathode voltage of 10.0 kV

Torr is achieved. The system is maintained at a constant pressure of 1–15 mTorr by feeding hydrogen gas through a leak valve.

A schematic of an optical measurement system is illustrated in Fig.2. The visible and ultraviolet lights emitted from the SCBF device are focused by a lens (f=100 mm, D=50 mm) on an end of optical fiber and guided to a spectrometer. The spectrometer is a Czerny-Turner type and the resolution is 0.0270 nm. A spectrum intensity is measured with a photomultiplier. The spatial resolution in the direction of optical axis is low ($\sim$ 10 cm) because the distance from the spherical center to the lens, which is made as short as possible, is rather long and the acceptance angle of the fiber is small. Therefore, the detected intensity is integrated over the device in the direction of optical axis.

III. Experimental results and discussion

Figure 3 shows a photograph of a hydrogen discharge plasma. The remarkable feature of the SCBF called " Star Mode " [1], the formation of a bright plasma core inside the grid-type cathode and the some beams of light through each hole of the grid cathode, is

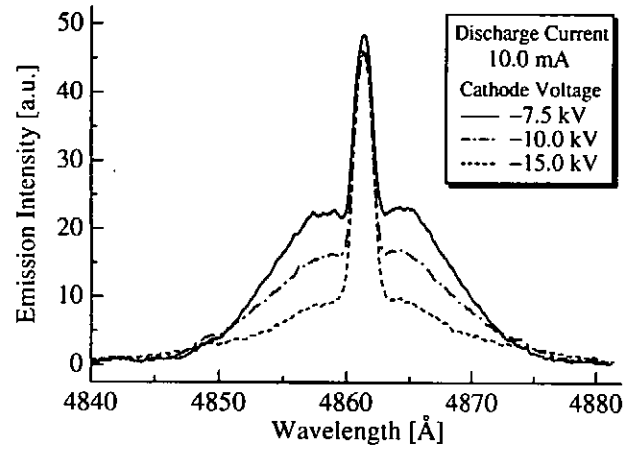

Fig.6. Profiles of H_β line spectra at cathode voltages of 7.5–15.0 kV with a fixed discharge current of 10.0 mA

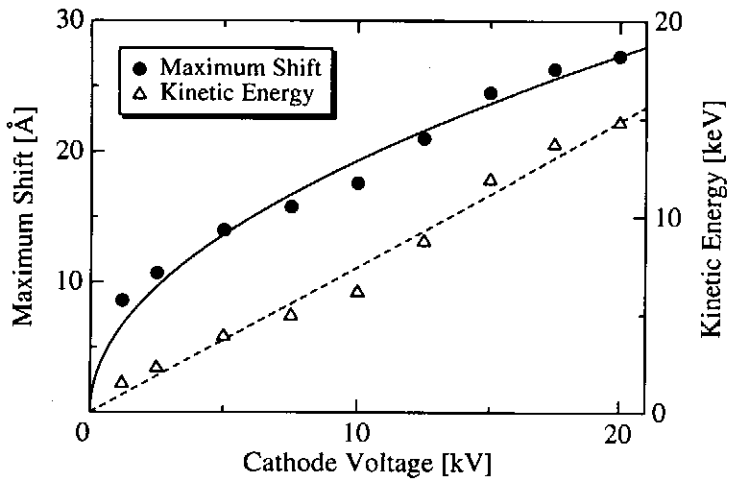

Fig.7. Maximum shift and kinetic energy vs. cathode voltage at a constant current of 10 mA

observed. An emission spectrum of a hydrogen discharge from 200 nm to 770 nm is shown in Fig.4. From this figure, strong hydrogen Balmar lines are observed and H_β line (486.133 nm) has the largest intensity. Therefore, H_β line is used in the following spectroscopic measurements.

Profiles of H_β line spectrum at discharge currents of 4.0–16.0 mA with a fixed cathode voltage of 10.0 kV are shown in Fig.5. The remarkable broadening of spectrum which has secondary peaks on both sides of the central peak is observed, and all other hydrogen lines are also broadened similarly. As shown in Fig.5, emission intensity increases with discharge current and the profiles are much the same.

Profiles of H_β line spectrum at cathode voltages of 7.5–15.0 kV with a fixed discharge current of 10.0 mA are also shown in Fig.6. Emission intensity of the central peak is nearly constant. However, intensity of the side spreads decreases and the maximum broadening width increases with increasing cathode voltage. The relationship between the maximum shift and cathode voltage is shown in Fig.7. Here, the maximum shift is defined as half

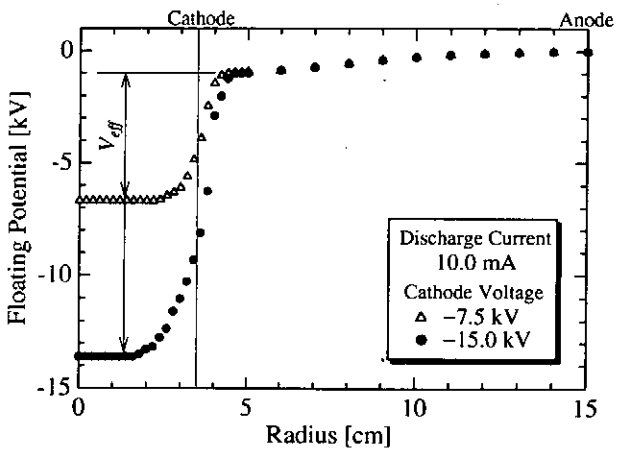

Fig.8. Profiles of floating potential

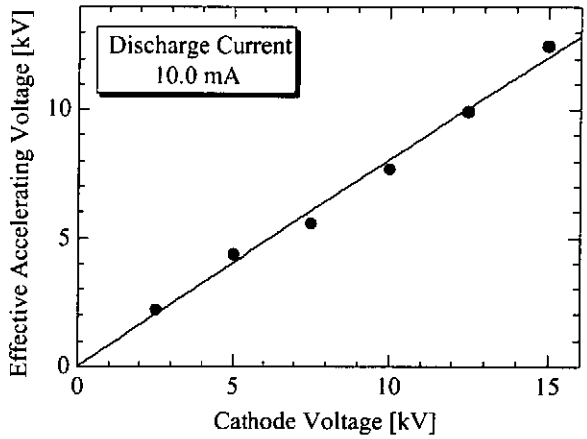

Fig.9. Effective accelerating voltage vs. cathode voltage

the maximum broadening width of the profile. Assuming that the side spread is caused by Doppler shift, the shifted wavelength is given by the following expression,

$$\lambda = \frac{c \pm v}{c}\lambda_0 = \lambda_0 \pm \frac{v}{c}\lambda_0 \tag{1}$$

where λ_0 is the wavelength of unperturbed line, v is the velocity of ion, c is the velocity of light in vacuum. Using Eq.(1), the kinetic energies are calculated from the data of maximum shift as shown in Fig.7. The curves in Fig.7 are derived from experimental results by using least-square fittings of the data. It seems that kinetic energy is approximately proportional to cathode voltage. Hence the shift is expressed as a function of square root of cathode voltage. To discuss this result further, the floating potential profiles are measured with an electrostatic probe. The probe has an electrode, which is made of 1.0 mm diameter, 1.0 mm long copper wire, and is inserted through a grid hole of the cathode. The results is shown in Fig.8, which shows that the floating potential decreases remarkably around the cathode and is nearly constant well inside and outside the cathode. Figure 9 shows the relationship between effective accelerating voltage and cathode voltage. Here, the effective accelerating voltages V_{eff} is defined as the effective

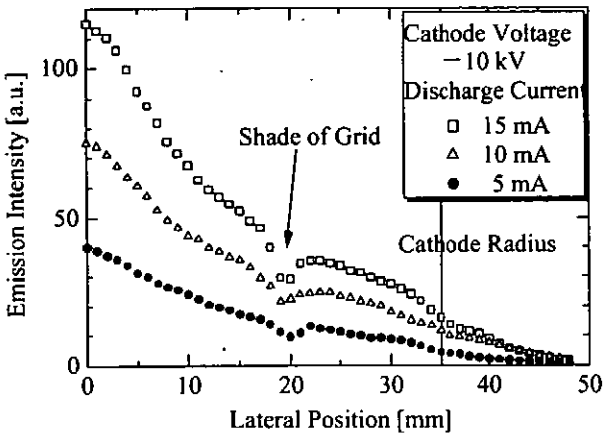

Fig.10. Emission intensity vs. lateral positions at discharge currents of 5.0–15.0 mA with a fixed cathode voltage of 10.0 kV

Table 1. HWHM vs. discharge currents at a constant voltage of 10.0 kV

Discharge current	HWHM
5.0 mA	12.5 mm
10.0 mA	13.6 mm
15.0 mA	13.8 mm

potential difference between the floating potential inside and outside of the cathode as shown in Fig.8. V_{eff} is 20 percent lower than cathode voltage as shown in Fig.9. Compared with Fig.7, it seems that the side spread is caused by the Doppler effect because V_{eff} corresponds to the kinetic energies.

The spatial distribution of H_β line intensity at discharge currents of 5.0–15.0 mA with a fixed cathode voltage of 10.0 kV are shown in Fig.10. The spatial distribution is measured from 0 mm to 50 mm in the lateral direction. Partial decreases of emission intensity in Fig.10 indicate the shade of the grid cathode wire. Table 1 shows half width at half maximum(HWHM) of emission intensity at discharge currents of 5.0–15.0 mA with a fixed cathode voltage of 10.0 kV. From the results of HWHM, it is found that plasma core becomes larger with discharge current. The spatial distribution of H_β line intensity at cathode voltages of 5.0–15.0 kV with a fixed discharge current of 10.0 mA are also shown in Fig.11. It is found that plasma core becomes smaller with cathode voltage as tabulated in Table 2.

IV. Conclusion

The visible emission from the SCBF device was measured using spectroscopic method. Strong emission lines of hydrogen were observed, and all hydrogen lines were broadened remarkably. The broadening of the profile was independent on discharge current and depended on cathode voltage. The side spread of spectrum was caused by the Doppler effect. Plasma core size became larger with discharge current and smaller with cathode

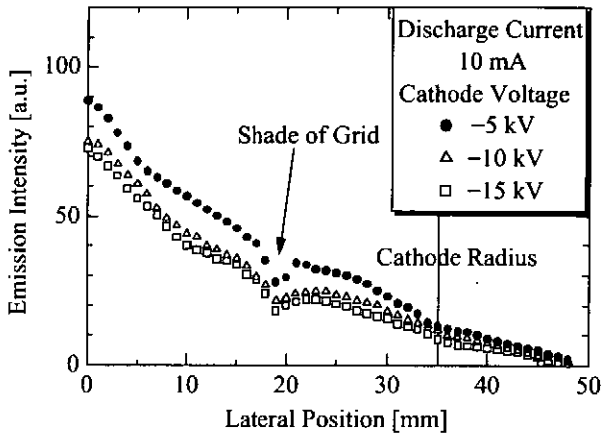

Fig.11. Emission intensity vs. lateral positions at cathode voltages of 5.0–15.0 kV with a fixed discharge current of 10.0 mA

Table.2. HWHM vs. cathode voltage at a constant current of 10.0 mA

Cathode voltage	HWHM
5.0 kV	15.5 mm
10.0 kV	13.6 mm
15.0 kV	12.6 mm

voltage.

Acknowledgement

This work is partly supported by The Sumitomo Foundation.

Reference

1) George H. Miley *et al.*, "Inertial-Electrostatic Confinement Neutron/Proton Source", Proc. of 3rd Int. Conf. on Dense Z-pinches, AIP Press, New York, pp.675–688, 1994.

REMOVAL OF NO_x BY PULSE ELECTRON BEAM IN COMBINATION WITH PHOTOCATALYST

Y. Nakagawa, A. Mannami, and H. Natsuno

Department of Electrical Engineering, Faculty of Engineering, Osaka City University, 3-3-138, Sugimoto, Sumiyoshi-Ku, Osaka 558-8585, Japan

ABSTRACT

NO_x in the oxygen mixed NO(=200ppm)/N_2 gas was removed efficiently with a synergistic effect of oxidization by the pulse electron beam and the photocatalyst (TiO_2 containing several % of water of crystallization). The photocatalyst was activated mainly by the plasma and radicals produced by the electron beam rather than UV light from the diode. NO_x removal efficiency in the oxygen 5% mixed NO(=200ppm)/N_2 gas was as high as 1010 nmol/J at removal ratio 83%. Without any radiation on the photocatalyst, NO_x was gradually decreased to 22.6% of the initial NO_x after 28 min in the oxygen 20% mixed NO(=200ppm)/N_2 gas. Concentration of NO_2 was below a few ppm during all process and it was expected that NO_2 was immediately oxidized to HNO_3 on the photocatalyst after NO was oxidized to NO_2.

1. Introduction

Recently, dry processes for flue gas treatment using gas discharge have been investigated and its potentiality has been demonstrated.[1-4] However, improvement of energy efficiency for these gas treatment devices operating by electrical power is still a key issue to develop a practical gas treatment device. Several achievements were reported in improvement of energy efficiency by radical shower or shorten the discharge voltage pulse.[3, 5] New approach to this subject is to use catalyst with the gas discharge. [6, 7] The maximum removal efficiency for the flue gas weight using non-thermal plasma combined with the Cu-ZSM-5 or three way catalysis was 100 J/g. Very recently, photocatalyst (TiO_2) was used with the surface discharge in gas discharge treatment device.[8, 9] It is reported that the photocatalyst was driven by the discharge plasma and significant improvement of the performance of NO_x removal adding hydrogen peroxide.[8] Energy consumption for NO_x removal in the unit of the ratio of input energy to gas mass flow achieved was 125 J/g at removal rate 92% with 1000 ppm of H_2O_2.

On the other hand, gas treatment device using pulse intense electron beam injection has been investigated for a candidate of gas treatment method having many advantages and an efficient removal of NO_x, VOCs and CS_2 by pulse intense electron beam injection was demonstrated. [10-13] Recently, flue gas treatment by pulsed relativistic electron beam having energy of 2 MeV or 8 MeV has been studied.[14] Up to now, effects on the NO_x removal by the pulse electron beam injection co-operation with the photocatalyst (TiO_2) have not yet been tested. The photocatalyst has a merit that can be operated as an oxidation catalyst at room temperature in the presence of molecular oxygen in contrast with that nearly all-heterogeneous catalyst function at elevated temperatures. On the other hand, NO_x adsorption on surface of TiO_2 with water of crystallization without any radiation was observed by Nishikata et al.[15] Same amount of NO and NO_2 was simultaneously removed in this process.

In this paper, it is reported that high efficiency of NO_x removal is achieved by the pulse

electron beam injection combined with the photocatalyst ("anatase" TiO_2).

2. Experimental apparatus and procedure

Experimental apparatus of NO_x removal using pulse electron beam combined with photocatalyst is shown in Fig.1. The pulse electron beam of about 95keV, 120A, 900ns was produced by a electron beam diode having an active plasma cathode and a stainless anode similar to that developed ourselves.[16] The electron beam was injected through holes of the stainless anode and an aluminized PET film of 25 μ m thickness into atmospheric pressure NO(=200ppm)/N_2 gas or oxygen mixed NO(=200ppm)/N_2 gas. The pulse electron beam was injected in a rate of one shot in 10~15 s. The electron beam energy injected in one pulse measured by a Faraday cup was 4.8 J to 3.7 J depending on the experimental conditions, when the stored energy in the Marx generator was 10.9 J. A gas chamber of 16 cm internal diameter and 27 cm of length was made of stainless steel tube and its capacity was 6.2 l. The inner wall of the gas chamber and surface of a gas mixer were covered by a photocatalyst sheet of 0.5 mm thickness. The sheet was prepared by Fuji Electric Co., Ltd. by rolling down a mixture of 70% of hydrous TiO_2 powder(ST-01 made by Ishihara Industry Co., Ltd.) and 30% of Teflon powder. NO(=200ppm)/N_2 gas and O_2 were introduced into the gas chamber by measuring partial pressure with a mercury manometer and the gas mixture was prepared by three strokes of the gas mixer and waiting for three minutes of diffusion time. NO_x(=NO_2+NO) or NO was measured using the NO_x-O_2 gas analyzer(NOA-7000 made by Shimadzu Co., Ltd.) introducing N_2 from opposite side of the gas chamber after the same process as the preparation of the mixture gas.

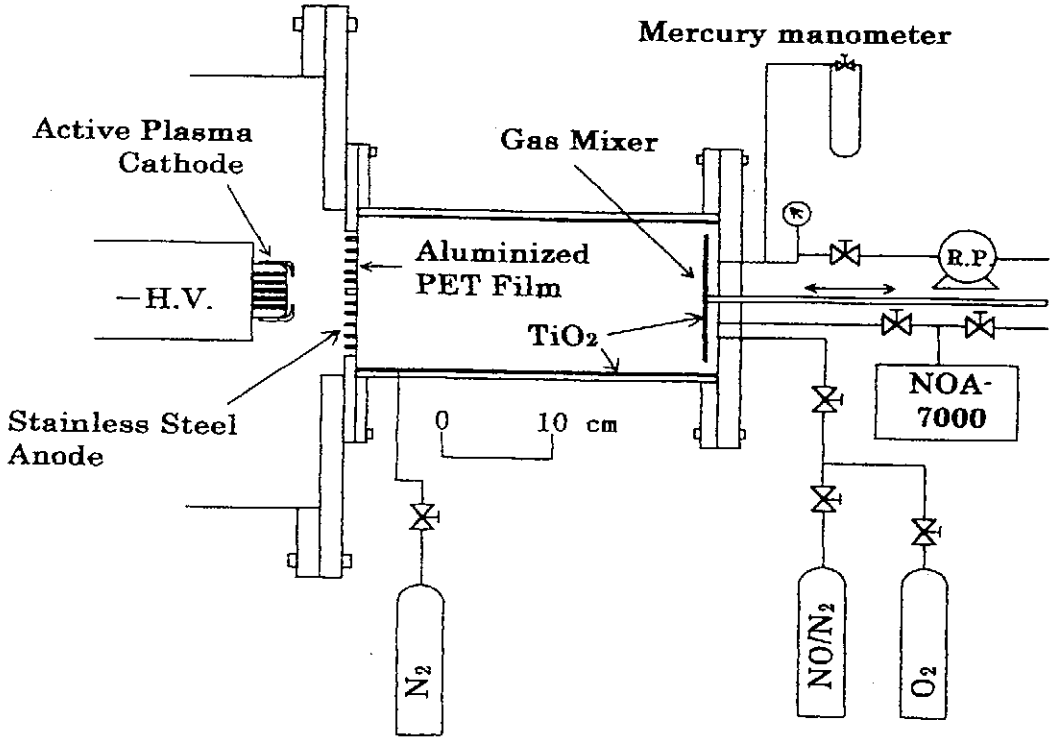

Fig.1. Experimental apparatus.

3. Experimental results and discussion

3-1. Observation of light from the electron beam diode and the plasma

Open shutter photograph taken from the side of electron beam diode shows that the electron beam produced plasma and radicals are radially expanded and contacted with the chamber wall. The light from the electron beam diode including plasma light produced by electron beam was measured by a pin-photo diode with a quartz window placed in the front of the electron beam diode. Temporal shape of signal was composed of a large peak with 500 ns pulse width from the start of electron beam pulse followed by comparatively small signal until the end of the electron beam pulse. It is expected that X-ray, UV and visible light from the diode, the plasma and radicals irradiate on the surface of the photocatalyst sheet on the chamber wall.

3-2. NO_x removal in NO(=200ppm)/N_2 gas by the pulse electron beam with photocatalyst

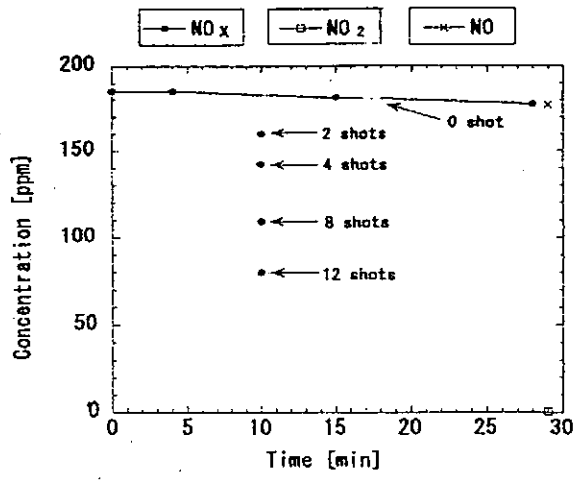

Fig.2. Temporal change of NO_x, NO_2 and NO concentrations and NO_x concentration after electron beam injection at 10 min in NO(=200ppm)/N_2 gas.

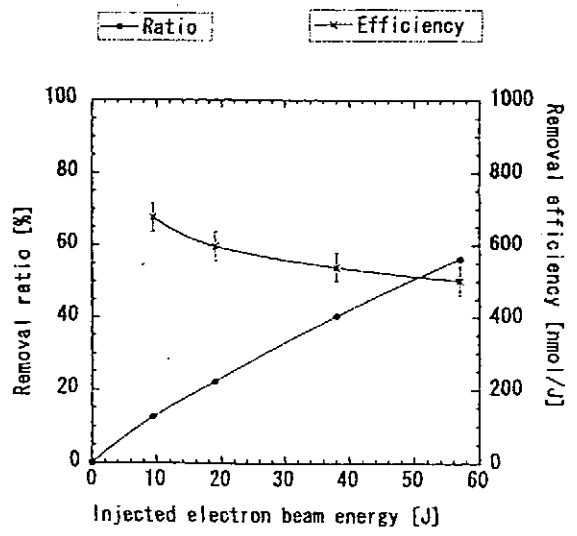

Fig.3. The removal ratio and the NO_x removal efficiency in NO(=200ppm)/N_2 gas depending on the injected electron beam energy.

Temporal change of NO_x, NO_2, NO concentrations and NO_x concentration after electron beam injection in NO(=200ppm)/N_2 gas at 10 min were shown in Fig.2. NO_2 was not detected and NO= NO_x was only slightly decreased after 28min. NO_x decreased by the electron beam injection into the gas chamber at 10 min. In Fig.3, the removal ratio and the removal efficiency depending on the total injected electron beam energy were shown. The total injected electron beam energy of 19 J is corresponding to four electron beam shots. NO_x of 40% was removed by the electron beam injection of 38 J and the energy efficiency was 540 nmol/J at this removal ratio. This value can be compared with the efficiency 400 nmol/J at same removal ratio without the photocatalyst by injecting same electron beam in the same gas chamber. Removal process in this case is reduction of NO by N radicals in the gas phase and it is collected that reduction reaction is enhanced by the photocatalyst excited by the plasma collision and UV irradiation. However, the improvement of the energy efficiency of NO_x removal was not so high enough.

3-3. NO_x removal in oxygen mixed NO(=200ppm)/N_2 gas without any radiation

Temporal change of NO_x, NO_2, NO concentrations in the oxygen 5% mixed NO(=200ppm)/N_2 gas and in the oxygen 20% mixed NO(=200ppm)/N_2 gas were shown in Fig.4 and Fig.5, respectively. One of significant character of NO_x removal is that NO_2 is below a few ppm (2.6 ppm) in the process. In our previous experiment,[13] we observed that 50% of NO_2 and NO at 25 min after mixing 20% of oxygen to NO(=200ppm)/N_2 gas without decreasing NO_x(=NO+NO_2), when the photocatalyst was not used in dry conditions. We have also observed that NO_2 of 22ppm for NO_x of 100ppm was remained in the gas chamber at 10 min after gas mixing in the case, which the inner wall was covered by a wet cloth.

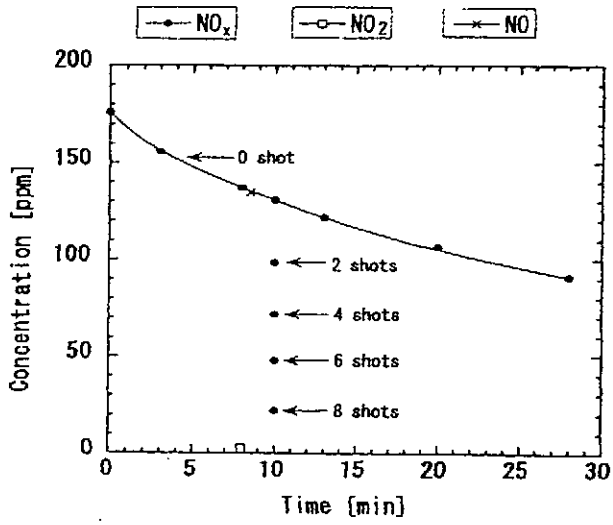

Fig.4. Temporal change of NO_x, NO_2 and NO concentrations and NO_x concentration after electron beam injection at 10 min in the oxygen 5% mixed NO(=200ppm)/N_2 gas.

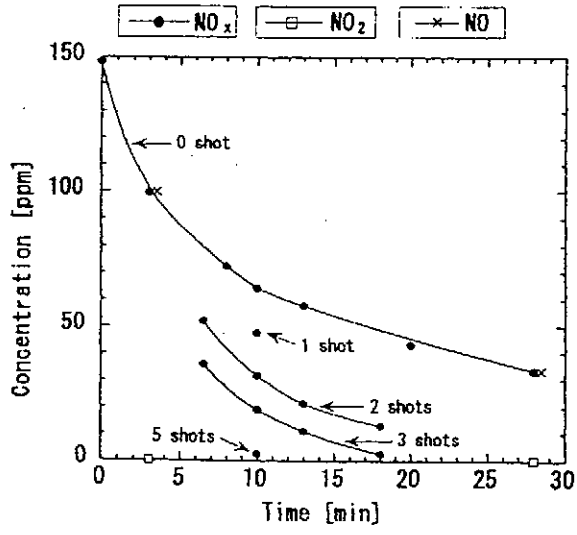

Fig.5. Temporal change of NO_x, NO_2 and NO concentrations and NO_x concentrations after electron beam injection at 10 min in the oxygen 20% mixed NO(=200ppm)/N_2 gas.

Without any radiation on the photocatalyst, NO_x was gradually decreased to 22.6% of the initial value after 28 min in the oxygen 20% mixed NO(=200ppm)/N_2 gas and 52% in oxygen 5% mixed NO(=200ppm)/N_2 gas. A tendency to saturate absorption capability was also observed. It is clear that NO_2 is strongly absorbed by the photocatalyst without any radiation. Similar NO_x removal without any radiation was observed by Nishikata et al using the same photocatalyst sheet.[15] They proposed the mechanism of NO_x removal that NO_x was dissolved into the water adsorbed on TiO_2 and $NO+NO_2+H_2O \rightarrow 2HNO_2$. This shows a possibility to use the photocatalyst (TiO_2) for the NO_x removal without the light source.

3-4. NO_x removal in oxygen mixed NO(=200ppm)/N_2 gas by the pulse electron beam irradiation with the photocatalyst

Change of NO_x concentration after electron beam injection in the oxygen 5% mixed NO(=200ppm)/N_2 gas at 10 min and in the oxygen 20% mixed NO(=200ppm)/N_2 gas were

also shown in Fig.4 and Fig.5, respectively.

In Fig.4, NO_x was removed by the consequence of the pulse electron beam injection into the gas mixture at 10min. In Fig.5, NO_x was removed by the electron beam injection at 10 min and 6, 13 and 18 min after the preparation of gas mixture. The removal ratio and the removal efficiency depending on the injected electron beam energy at 10 min in both cases were shown in Fig.6. NO_x removal efficiency in the oxygen 5% mixed NO(=200ppm)/N_2 gas was as high as 1200 nmol/J at the removal ratio 25% and 1007 nmol/J at large removal ratio of 83%. In the oxygen 20% mixed NO(=200ppm)/N_2 gas, largest efficiency of 1006 nmol/J by two pulse of the electron beam injection was obtained at the removal ratio 62% and 13 min. The largest efficiency of 872 nmol/J at the removal ratio 80% by three beam pulse was obtained at 13 min. These efficiencies can be compared with our previous results described in Ref.13. When oxygen of 20% was mixed to NO(=200ppm)/N_2 gas, NO was oxidized to NO_2 resulting in NO=NO_2 at 24 min after the mixing without changing NO_x(=NO+NO_2). The pulse electron beam injection clearly promoted the oxidization of NO and its efficiency was about 200 nmol/J. When the pulse electron beam was injected into the same gas in the gas chamber, which internal surface was covered by a wet cloth, NO_x was removed with total efficiency of 570 nmol/J at removal ratio 40% by formation of HNO_3 with OH radical in the gas phase and by dissolving NO_2 into the water in the wet cloth at the wall. However, the removal efficiency by the electron beam injection only was 150~200 nmol/J. The NO_x removal efficiency was increased 4~6 times compared with these efficiency by using the photocatalyst sheet.

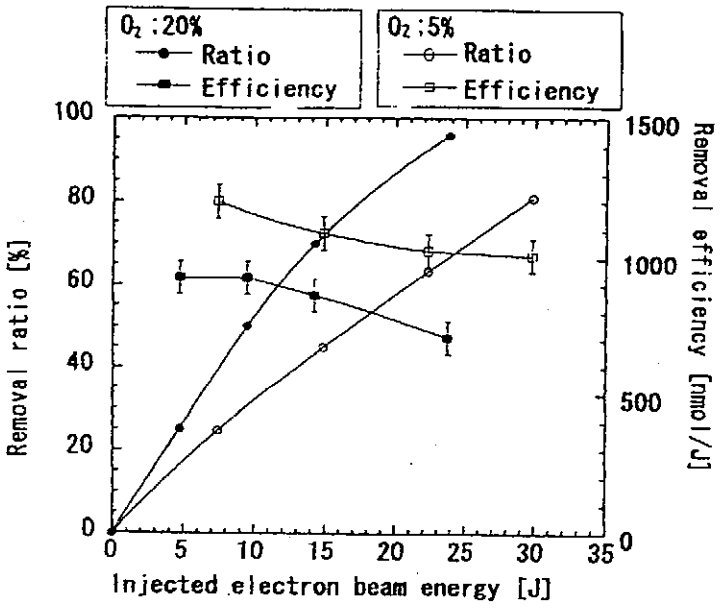

Fig.6. The removal ratio and the NO_x removal efficiency in oxygen mixed NO(=200ppm)/N_2 gas depending on the injected electron beam energy at 10 min.

Above-mentioned efficiency was estimated by dividing the removed amount of NO_x in [nmol] unit by the injected electron beam energy [J]. The efficiency for the stored energy in the Marx generator (10.9J) was about 350~380 nmol/J at the removal ratio 70 to 80%.

In spite of difficulty on direct comparison of efficiency with other NO_x removal experiment used the catalyst, we will try to compare the results described in Ref. 7 using the Cu-ZSM-5 and three-way catalyst and Ref. 9 using the photocatalyst(TiO_2) with our result converting the unit [J/g] to [nmol/J]. In both experiment, the energy efficiency is the ratio of input energy including discharge power and energy loss in the power source to gas mass flow. The efficiency about 100 J/g converted to the efficiency about 120 nmol/J in our unit. Our efficiency was three times higher than that but they removed NO_x in flowing gas in contrast with our treatment of the stagnated gas in the gas chamber.

The light from the electron beam diode were measured by the pin-photo diode when Mylar film of 200 μ m thickness was added to the aluminized PET film to prevent the electron beam

injection in the gas chamber. The waveform and peak height of the light signal were almost the same as that for the case without the Mylar film on the contrary the pulse electron beam signal was decreased to less than 1/10. A small attenuation of UV light by the Mylar film of 200 μ m thickness was examined using another surface flashover light source. When the electron beam diode was operated in this conditions, NO_x was not removed at all. This means that the photocatalyst is activated by the plasma, radicals and plasma light rather than UV light from the electron beam diode. Activated TiO_2 induced chemical reaction of oxidization producing active radicals (OH, O, O^-), which OH came from the water of crystallization and O from mixed O_2, on TiO_2 catalyst. These radicals effectively oxidized NO and NO_2 forming HNO_3 and keeping it on the surface of the photocatalyst.

4. Conclusion

NO_x removal by the pulse electron beam in combination with the photocatalyst was examined. Removal efficiency of NO_x in oxygen mixed NO(=200ppm)/N_2 gas was highly enhanced by the synergistic effect of oxidization with the pulse electron beam and the photocatalyst (TiO_2). The photocatalyst was activated by the bombardment by the plasma, radicals and plasma light rather than UV light from the electron beam diode.

ACKNOWLEGEMENT

Author would like to express his sincere thanks to Mr. Nishikata of Fuji Electric co. Ltd. for supplying the photocatalyst (sheet made by TiO_2 and Teflon).

References

1) S.Masuda and H.Nakao: IEEE Trans. Ind. Applicat., **26**(1990)374.
2) M.Higashi, S.Uchida, N.Sizuki and K.Fujii: IEEE Trans. Plasma Sci., **20**(1992)1.
3) T.Ohkubo, S.Kanazawa, Y.Nomoto, J.S.Chang and T.Adachi: IEEE Trans. Ind. Applicat., **32**(1996)1058.
4) G.E.Vogtlin and B.M.Penetrante: *in Non-Thermal Plasma Techniques for Pollution Control, Part B. Oxford, U.K.: Springe-Verlag,* 1993, p.187.
5) T.Namihira, S.Tsukamoto, D.Wang, S.Katsuki, R.Hacam, H.Akiyama, Yuchida and M.Koike: IEEE Trans. Plasma Science, **28**(2000)434.
6) T.Oda, T.Kato, T.Takahashi and K.Shimizu: J.Electrostatics, **42**(1997)151.
7) K.Shimizu and T.Oda: IEEE Trans. Ind. Applicat., **35**(1999) 1311.
8) A.Mizuno, Y.Kisanuki, M.Noguchi, S.Katsura, S.H.Lee, Y.K.Hong, S.Y.Shin and J.H.Kang: IEEE Trans. Ind. Appl., **35**(1999)1284.
9) H.H..Kim, K.Tsunoda, S.Katsura and A.Mizuno: IEEE Trans. Ind. Appl., **35**(1999)1306.
10) Y.Nakagawa, S.Adachi, A.Kohchi and J.Nagasawa: Jpn. J. Appl. Phys., **34**(1995)L793.
11) Y.N. Novoselov, G.V.Denisov and A.I.Suslov: *Proc. 12th Int. Conf. High- Power Particle Beams, Haifa,-Israel,* 1998, IEEE Catalog NO. 98EX103, p.1020.
12) Y.Nakagawa and H.Kawauchi: Jpn. J. Appl. Phys., **37**(1998)5082.
13) Y.Nakagawa and H.Kawauchi: Jpn. J. Appl. Phys., **39**(2000)4231.
14) T.Ikegaki, S.Seino, Y.Oda, T.Matsuda, G.Imada, W.Jiang and K.Yatsui: Jpn. J. Appl. Phys. **40**(2001)1104.
15) S.Nishikata, T.Nishimura, H.Takeuchi and A.Ibusuki: Photocatalysis, **1**(2000)95. (in Japanese)
16) Y.Nakagawa and R.Kodera: Jpn.J.Appl.Phys., **39**(2000)L1064.

CHARACTERISTICS OF FLUE GAS TREATMENT BY INTENSE, PULSED, RELATIVISTIC ELECTRON BEAM

Satoshi SEINO[1], Akihito INAGAWA[1], Go IMADA[1,2], Weihua JIANG[1], and Kiyoshi YATSUI[1]

[1] *Extreme Energy-Density Research Institute, Nagaoka University of Technology, 1603-1 Kamitomioka, Nagaoka, Niigata 940-2188, JAPAN*

[2] *Department of Electrical Engineering, Nagaoka University of Technology, 1603-1 Kamitomioka, Nagaoka, Niigata 940-2188, JAPAN*

ABSTRACT

Treatment of NO_x has been demonstrated using an intense, pulsed, relativistic electron beam (IREB). The short (20 cm long) and elongate (180 cm long) chamber are filled with N_2-balanced NO or N_2/O_2-balanced NO gas mixture with the pressure of 120 kPa, and are irradiated by the IREB energy of 2 MeV with the pulse width of 50 ns (full width at half maximum). With the initial NO concentration of 100 ppm in N_2-balanced NO gas mixture filled in the elongate chamber, ~ 95 % of NO_x is removed by firing 10 shots of IREB. We have obtained NO_x removal efficiency of 20-200 nmol/J. Removal of NO_x by the IREB has been also simulated by a numerical calculation code in N_2/O_2-balanced NO gas mixture filled in the short chamber.

1. Introduction

The flue gases produced by the electric power plants, ironworks and diesel engines have caused serious environmental problems in the earth. For example, a large amount of NO_x may result in the acid rain or the photochemical smog. The injection of an intense, pulsed, relativistic electron beam (IREB) into a flue gas is expected to be effective for pollutant removal. In the removal of NO_x by IREB, NO_x reacts with the radicals, such as O, N, OH, HO_2 and so on. The radicals are formed by the collision of the electrons with the atoms or molecules. The IREB is able to produce a lot of radicals simultaneously due to the short pulse width and high current density. It is reported that the removal efficiency of NO_x can be improved by utilizing a pulsed electron beam.[1-3] The electrons of IREB have large kinetic energy, resulting in long *range* in the gas. The *range* of IREB at 2 MeV is calculated to be ~ 8.6 m in an atmosphere. Therefore, the IREB irradiation is believed to be a promising candidate for NO_x removal in the elongate chimney at electric power plants and in the tunnels for automobiles.

We have succeeded in the demonstration of NO_x removal by IREB of the beam energy of the order of MeV. In this study, the dependence of removal of NO_x on the length of reaction chamber, the flue gas composition and the initial concentration of NO_x have been investigated using a pulsed power generator, "ETIGO-III" (8 MV, 5 kA, 50 ns). Removal of NO_x by the IREB has been also simulated by a numerical calculation code.

2. Experimental Setup

Figure 1 shows the schematic diagram of the IREB generator, "ETIGO-III". It consists of a Marx generator, a pulse forming line, and induction acceleration cells in four stage. The output voltage of the pulse forming line is 670 kV, which is fed to the four cells. Three amorphous cores are installed in each cell, producing approximately 2 MV per cell (670 kV × 3). The electron beam with the energy up to 2 MeV is generated by an electron-beam diode set at the first acceleration cell. The field emission diode with a hollow cathode is used to generate the electron beam. The inner and outer diameters of the cathode are 59.5 mm and 60 mm, respectively. This electron beam is accelerated by each acceleration cell, and the maximum energy of the IREB increases up to 8 MeV.

Figure 2 shows the cross-sectional view of flue gas reaction chamber. The IREB generated by "ETIGO-III" is injected into the reaction chamber through a window. The window consists of a titanium foil with a thickness of 40 μm and a honeycomb flange with an optical transparency of ~ 50 %. The kinetic-energy loss of the IREB through the titanium foil is estimated to be ~ 26 keV. The length, diameter and volume of the reaction chamber are summarized in Table I. The reaction chamber is evacuated up to 10 Pa by a rotary vacuum pump. In this experiment, N_2-balanced NO or N_2/O_2-balanced NO gas mixture with the total pressure of 120 kPa have been used to simulate the flue gas. To confine the IREB in the elongate chamber, an external magnetic field is applied along the chamber axis. The concentrations of NO_x (= NO + NO_2) and NO are measured by a controlled potential-electrolysis gas analyzer (testo Co., Ltd., GSV-350) after mixing up the gas.

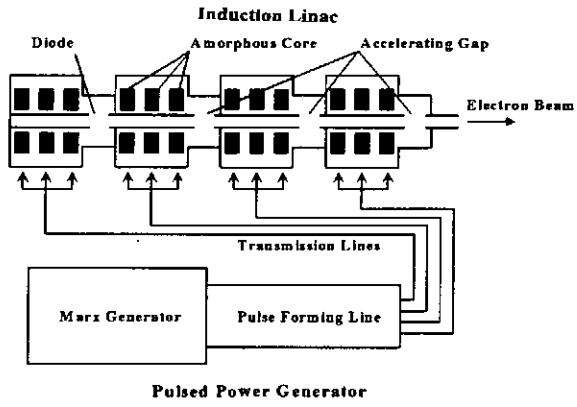

Fig. 1 Schematic diagram of "ETIGO-III".

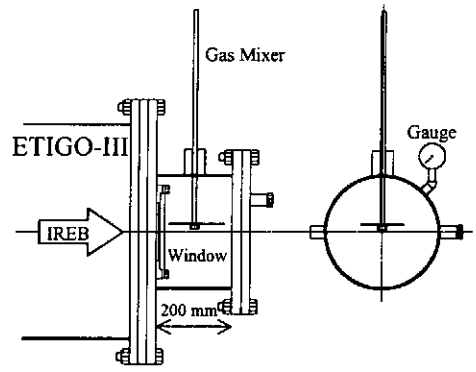

(a) Short type.

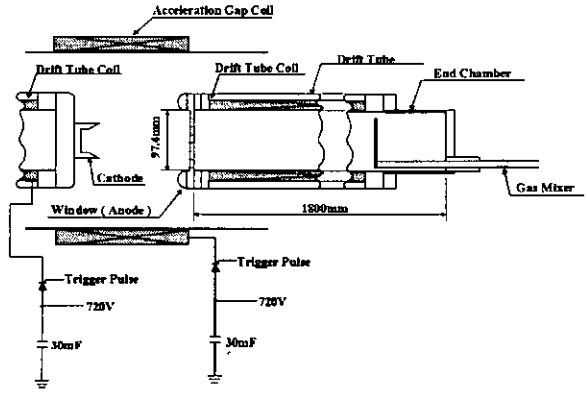

(b) Elongate type.

Fig. 2 Schematic of reaction chambers.

Table I Dimensions of reaction chambers.

	Short type	Elongate type
Length	200 mm	1800 mm
Diameter	259.4 mm	97.4 mm
Volume	10.6 ℓ	13.4 ℓ

3. Results and Discussion

3.1 Propagation of IREB in reaction chamber

Figure 3 shows the typical time evolution of the IREB diode voltage and IREB current, where the IREB current is measured by a Faraday cup placed close to the window in the reaction chamber. The peak IREB current is observed to be ~ 600 A and ~ 2200 A on the short and elongate chamber with the beam voltage of 2 MV, respectively. The pulse width of the IREB current is approximately 60-80 ns (FWHM).

Figure 4 shows the peak IREB current distribution along the chamber axis in the reaction chamber. The reaction chamber is filled with an atmospheric gas. In the short chamber, the IREB maintains a current of 600 A in the absence of external magnetic field. On the other hand, in the elongate chamber, the IREB current is reduced with decreasing the magnetic field at z ~ 1600 mm. The injected IREB energy into the chamber is estimated to be ~ 60 J and ~ 280 J on the short and elongate chamber, respectively.

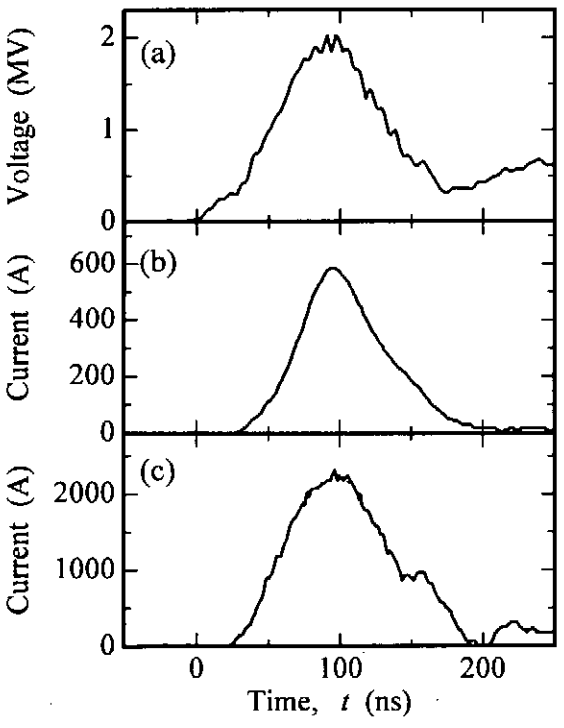

Fig. 3 Typical time evolution of voltage and current of "ETIGO-III". (a) IREB diode voltage, (b) IREB current in short chamber, and (c) IREB current in elongate chamber.

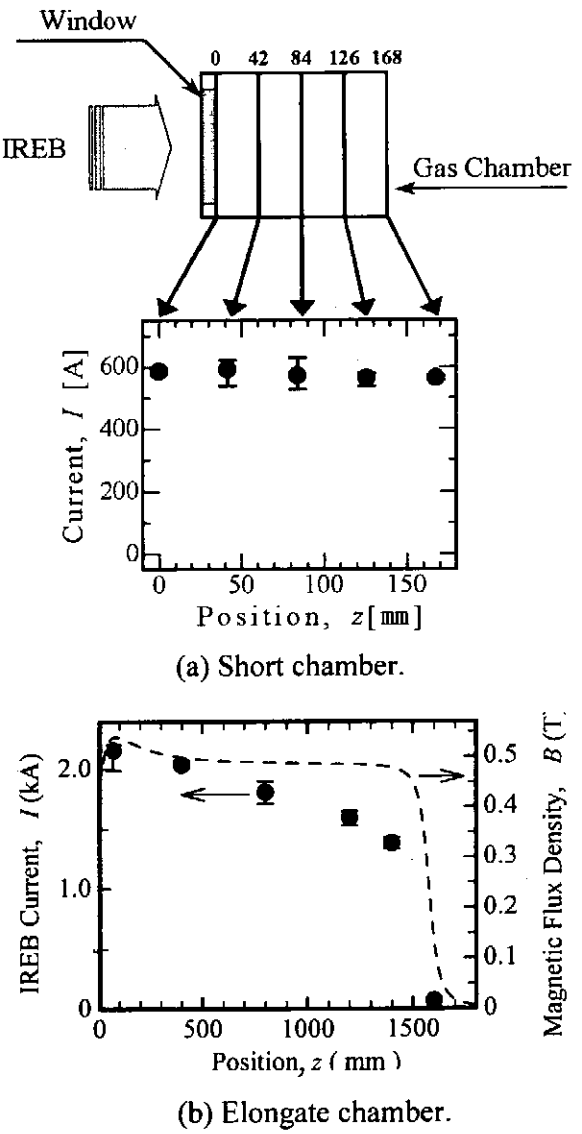

(a) Short chamber.

(b) Elongate chamber.

Fig. 4 IREB peak current after passing through window in reaction chamber. Magnetic flux density on chamber axis is also presented in (b).

3.2 Experimental and numerical results of flue gas treatment by IREB in short chamber

Figure 5 shows the NO_x concentration as a function of IREB shots for the initial NO concentration of 100 ppm in N_2/O_2-balanced NO gas mixture at the short chamber. The gas composition is $N_2:O_2 = 8:2$. Some NO is oxidized by ambient O_2 without firing the IREB, and the NO concentration equilibrates to ~ 62 ppm. It is found that NO is removed by the irradiation of IREB. Until the third shot of IREB, NO_2 is generated by the irradiation of IREB because of high NO concentration. The NO_2 concentration decreases in proportion to the number of IREB shots after the third shot of IREB when the reduction of NO may exceed the generation of NO.

We have developed a numerical calculation code for the flue gas treatment by pulsed IREB. This code consists of rate equations for the chemical reactions during and after the IREB irradiation. The chemical reactions and rate constants are summarized in Table II. The number density of electrons is estimated from the experimentally obtained IREB current (see Fig. 3(b)). The calculated concentrations of NO_2 and NO are presented in Fig. 5 as a solid and broken line, respectively. It is found that the numerical results well agree with experimental one in the NO_2 concentration. We see small deviation in the calculated concentration of NO from the experimental one because the rate constant of $2NO_2 \rightarrow 2NO + O_2$ is uncertain.

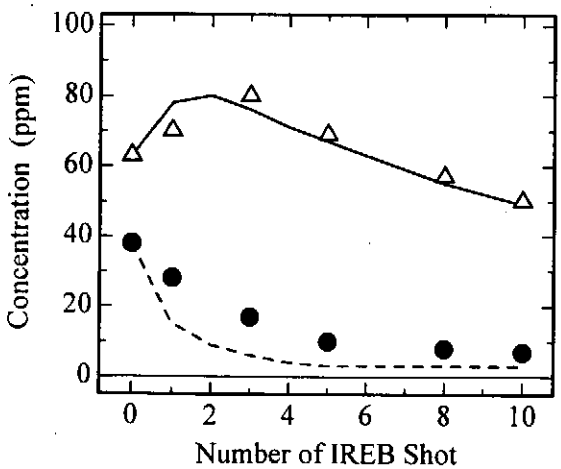

Fig. 5 NO_x concentration as a function of number of IREB shots for initial NO concentration of 100 ppm in N_2/O_2-balanced NO gas mixture. ●: NO, △: NO_2. Numerical results are shown by broken line (NO) and solid line (NO_2).

Table II Chemical reactions and rate constants.

During IREB irradiation

Reactions	Rates	Ref.
$N + NO \rightarrow N_2 + O$	5.9×10^{-11} cm^3/s	4)
$N + NO_2 \rightarrow 2NO$	9.0×10^{-12} cm^3/s	4)
$O + NO + N_2 \rightarrow NO_2 + N_2$	9.0×10^{-32} cm^6/s	5)
$N + N + N_2 \rightarrow N_2 + N_2$	4.0×10^{-33} cm^6/s	5)
$O + O + N_2 \rightarrow O_2 + N_2$	8.0×10^{-33} cm^6/s	5)
$NO + O_3 \rightarrow NO_2 + O$	1.8×10^{-14} cm^3/s	5)
$N + NO_2 \rightarrow N_2O + O$	3.0×10^{-12} cm^3/s	5)
$O + O_2 \rightarrow O_3$	1.0×10^{-14} cm^3/s	5)
$N + O_2 \rightarrow NO + O$	1.0×10^{-16} cm^3/s	5)
$N + O_3 \rightarrow NO + O_2$	1.0×10^{-16} cm^3/s	5)
$N_2O + O \rightarrow N_2 + O_2$	4.9×10^{-11} cm^3/s	5)
$N + O + N_2 \rightarrow NO + N_2$	3.9×10^{-32} cm^6/s	5)
$2NO + O_2 \rightarrow 2NO_2$	3.8×10^{-38} cm^6/s	5)
$N_2 + O \rightarrow N + NO$	7.0×10^{-12} cm^3/s	5)
$O + NO_2 \rightarrow NO + O_2$	6.5×10^{-12} cm^3/s	5)
$NO_2 + O_3 \rightarrow NO_3 + O_2$	3.0×10^{-17} cm^3/s	5)
$O + NO_2 + N_2 \rightarrow NO_3 + N_2$	9.0×10^{-32} cm^6/s	5)
$NO_3 + O \rightarrow NO_2 + O_2$	3.0×10^{-11} cm^3/s	6)
$N_2 + e \rightarrow N + N + e$	2.7×10^{-19} cm^2 *	7)
$O_2 + e \rightarrow O + O + e$	3.7×10^{-19} cm^2 *	7)

After IREB irradiation

Reactions	Rates	Ref.
$2NO + O_2 \rightarrow 2NO_2$	3.8×10^{-38} cm^6/s	5)
$2NO_2 \rightarrow 2NO + O_2$	5.8×10^{-19} cm^3/s	8)

*: Cross section, Ref.: Reference

3.3 Comparison of treatment properties between short and elongate chamber

Figure 6 shows the NO_x concentration as a function of IREB shots for the initial NO concentration of 100 ppm in N_2-balanced NO gas mixture for the short and elongate chamber. It is found that ~ 95 % of NO_x is removed by the IREB irradiation of 30 shots in the short chamber in spite of the absence of O_2. It is clear from Figs. 3 and 4 that the IREB current in the elongate chamber is ~ 3 times higher than that in the short chamber. Therefore, in the elongate chamber, ~ 95 % of NO_x is removed by the IREB irradiation of 10 shots.

3.4 Flue gas treatment by IREB in elongate chamber

Figure 7 shows the NO_x removal efficiency (ε) as a function of the number of IREB shots for the initial NO concentration of 100 and 900 ppm in N_2-balanced NO gas mixture at the elongate chamber. Here, ε is defined by the ratio of the NO_x removal amount over the injected IREB energy into the chamber. It is found that ε increases from ~ 70 nmol/J to ~ 200 nmol/J if the initial concentration of NO is increased from 100 ppm to 900 ppm, respectively. It may be understood by that the O radical, which originates from NO and useful for treatment of the flue gas, will increase the number density at the high initial NO concentration.

Figure 8 shows the NO_x concentration as a function of IREB shots for the various initial NO concentration in N_2/O_2-balanced NO gas mixture at the elongate chamber. The gas composition is $N_2 : O_2 = 8 : 2$. The NO_2 is generated by the irradiation of IREB into the atmosphere (See Fig. 8(a)). It is found that NO_x is successfully removed if the initial NO concentration is less than 200

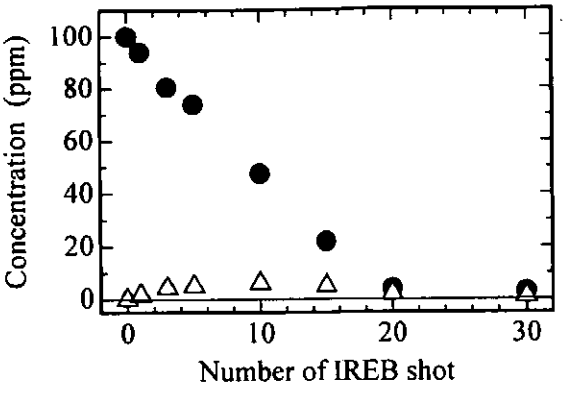

(a) Short chamber.

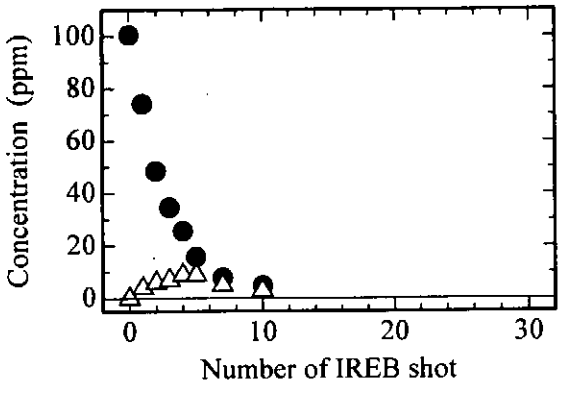

(b) Elongate chamber.

Fig. 6 NO_x concentration as a function of number of IREB shots for initial NO concentration of 100 ppm in N_2-balanced NO gas mixture. ●: NO, △: NO_2.

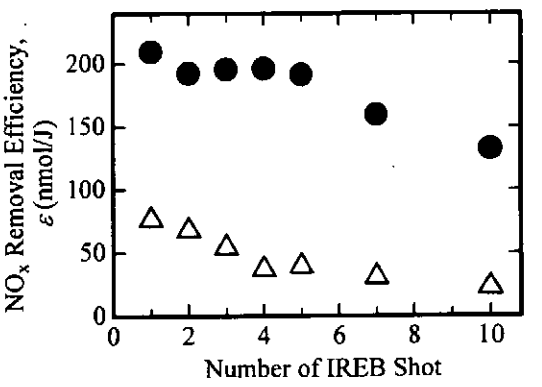

Fig. 7 NO_x removal efficiency as a function of IREB shots in elongate chamber filled with N_2-balanced NO gas mixture. Initial NO concentration, ●: 900 ppm, △: 100 ppm.

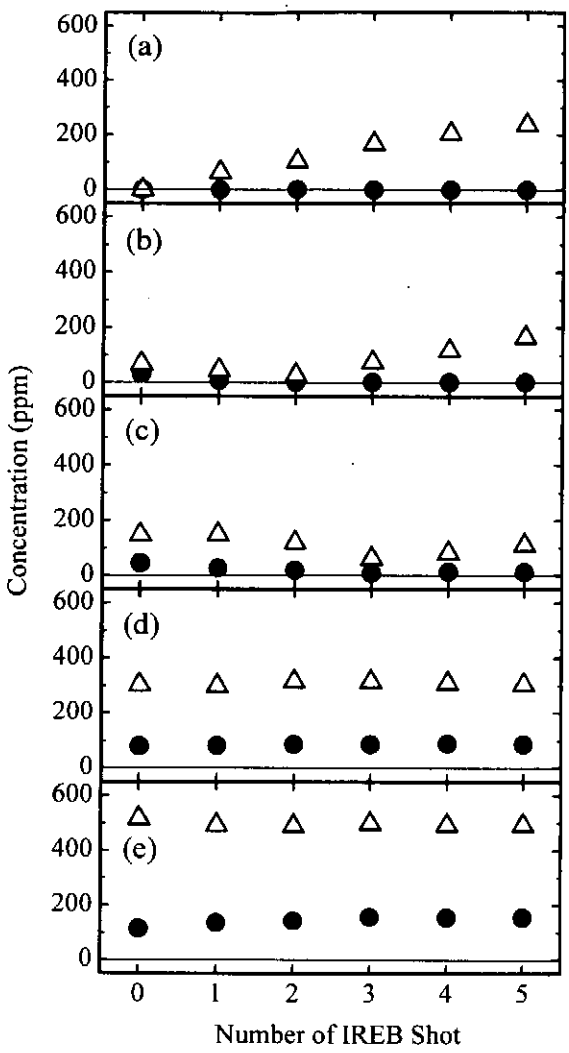

Fig. 8 NO_X concentration as a function of number of IREB shots for various initial NO concentration in N_2/O_2-balanced NO gas mixture. ●: NO, △: NO_2. Initial NO concentration: (a) 0 ppm, (b) 100 ppm, (c) 200 ppm, (d) 390 ppm, and (e) 640 ppm.

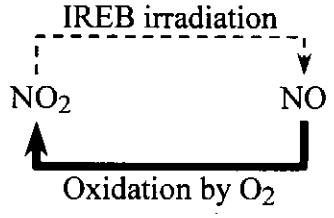

Fig. 9 Model of reduction and generation of NO_2 in O_2-rich gas mixture.

ppm. In this gas mixture, the oxidation of NO by ambient O_2 is dominant in comparison with the reduction of NO by IREB (See Fig. 9). In the high initial NO concentration, therefore, NO_X is hardly treated by the irradiation of IREB.

4. Conclusions

Treatment of the flue gas has been successfully demonstrated using pulsed IREB. The following results can be drawn from the present investigation.

1) We have developed a numerical calculation code for the flue gas treatment. The numerical results well agree with experimental one in the short chamber filled with N_2/O_2-balanced NO gas mixture.
2) With the initial NO concentration of 100 ppm in N_2-balanced NO gas mixture filled in the elongate chamber, ~ 95 % of NO_X is removed by firing 10 shots of IREB.
3) The NO_X removal efficiency of 20-200 nmol/J is obtained at the elongate chamber.

Acknowledgements

The authors would like to thank Mr. Y. Sekimoto for help with the mechanical design and experiment.

References

1) B. Penetrante: Proc. 2nd Int'l Symp. on Environmental Appl. of Advanced Oxidation Technol., UCRL-JC-123410 (1996).
2) B. Penetrante: Proc. 11th IEEE Pulsed Power Conf., **I**, 91 (1997).
3) H. Kawauchi and Y. Nakagawa: Trans. IEE Jpn., **118-A**, 1186 (1998) [in Japanese].
4) K. Kawamura, *et al.*: Trans. IEE Jpn., **117-A**, 956 (1997) [in Japanese].
5) B. Penetrante, *et al.*: IEEE Trans. on Plasma Sci., **23**, 679 (1995).
6) J. Lowke and R. Morrow: IEEE Trans. on Plasma Sci., **23**, 661 (1995).
7) F. Rieke and W. Prepejchal: Phys. Rev., **A6**, 1507 (1972).
8) T. Ikegaki, *et al.*: Jpn. J. Appl. Phys., **40**, 1104 (2001).

NOx Decomposition Utilizing Pulsed Discharge in Porous Honeycomb Ceramics

S. Ibuka, T. Nakamura, T. Murakami, H. Kondo, K. Yasuoka and S. Ishii

Tokyo Institute of Technology, 2-12-1 O-okayama, Meguro-ku, Tokyo, 152-8552, JAPAN

ABSTRACT

Pulsed discharges in porous honeycomb ceramics of alumina were investigated to discuss the feasibility of a new type non-thermal plasma reactor for decomposition of air pollutants. Using rod-cylinder electrodes configuration with a PET sheet as an insulator, the barrier discharge type reactor was fabricated with the honeycomb ceramics. A fast framing image converter camera was used to observe the temporal development of discharges. The uniform discharges in the honeycomb ceramics were successfully obtained by a high voltage pulse generator utilizing a fast SI-thyristor. NO removal experiment in N2 was carried out with the reactor. The results suggest that the surface condition of the ceramics greatly influence the NO removal characteristic. The NO removal efficiency of the reactor is estimated to be 295 eV/molecule at the maximum NO removal rate.

I. Introduction

Non-thermal plasma produced by a pulsed power generator has attracted the attention of researchers for air pollution control. Although many kinds of reactors have been proposed, no clear conclusion is obtained on the most suitable one for the pollution control. A key factor in the selection of the reactor is the energy efficiency for decomposing the pollutants. To achieve a breakthrough leading to high decomposition efficiency, we proposed to utilize a fast pulsed discharge in honeycomb ceramics. The honeycomb ceramics are one of the most common carrier materials to support various catalytic processes because of their large surface area that is highly active for chemical reactions. There is a possibility that the non-thermal plasma produced by the fast pulsed discharge enhances the chemical reactions on the ceramics surface. To establish highly efficient decomposition of the pollutant gases, not only the volume reaction in the non-thermal plasma but also the surface reaction on the ceramics surface should be utilized simultaneously.

II. Structure of honeycomb ceramics reactors

We prepared three types of discharge reactors with/without the honeycomb ceramics as shown in Fig.1. In this paper, reactor of each structure shall be called (a) surface discharge type, (b) coaxial type, (c) glass tube type, as illustrated in Fig. 1.

For (a) surface discharge type, the honeycomb ceramics for the flue filter of small incinerator was cut into the 15mm thickness, and electrode was installed on the cut section. According to our previous reports[1][2][3], the electric field concentration near the anode electrodes is necessary to obtain uniform surface streamer discharges. In order to promote the electric field concentration, asymmetric electrode configuration of the stainless steel mesh cathode and the tungsten wire anode electrodes was utilized. In the case of surface discharge

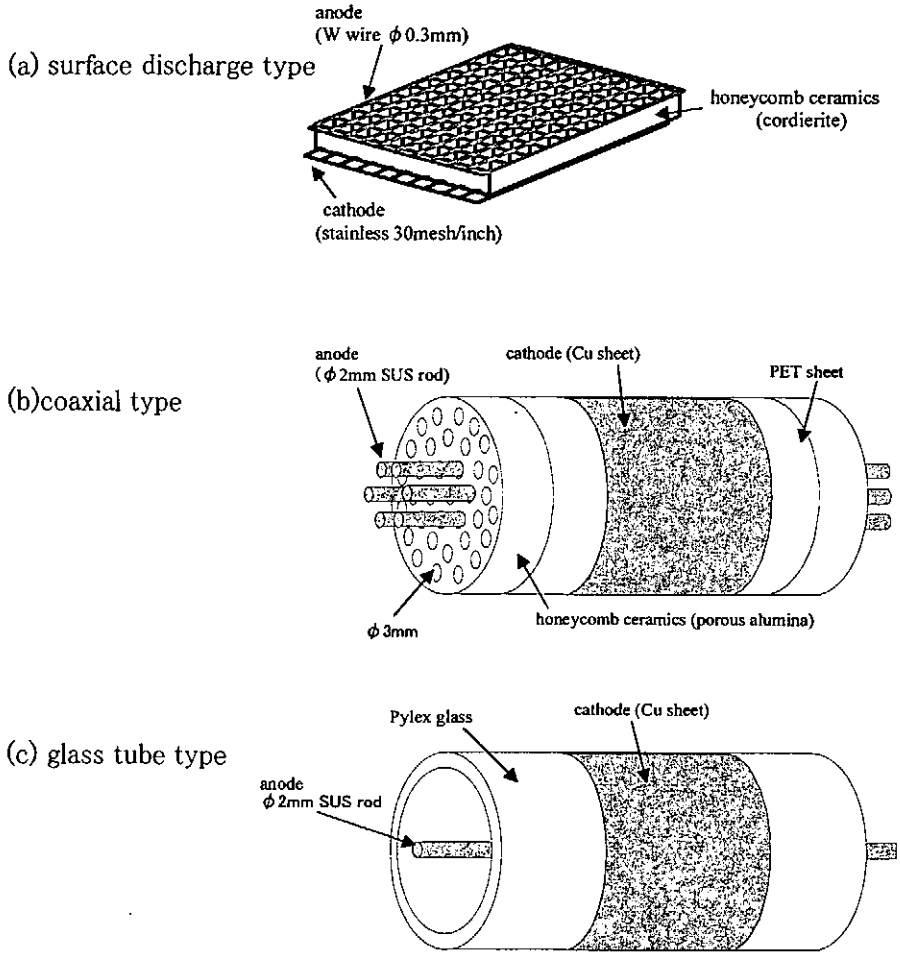

Fig.1 Schematics of the reactors.

type reactor, the discharge develops in parallel to the direction of the gas flow.

In the case of (b) coaxial type reactor, honeycomb ceramics of the lotus root shape, called monolith type, for the solid-liquid separation filter was used. This ceramics was made from porous alumina with great number of micron seize holes as shown in Fig.2[4]. In addition, the inner surface of the monolith ceramics was specially treated to create micropore layer of several tens of nm. The stainless rod electrodes were inserted to the axial holes as anode electrodes. The copper sheet electrode was installed on the outer surface of the monolith ceramics and was grounded. In order to change the electric field distribution of the reactor inside, the number of the anode rod electrodes could be varied. To suppress the generation of arc discharges, the barrier discharge configuration was adopted inserting the PET sheet between the copper sheet electrode and the ceramics. It was noted that (c) glass tube type reactor using Pyrex glass tube (26mm of inner and 30mm of outer diameter) alternative to the monolith ceramics was also prepared to clarify the effect of the ceramics.

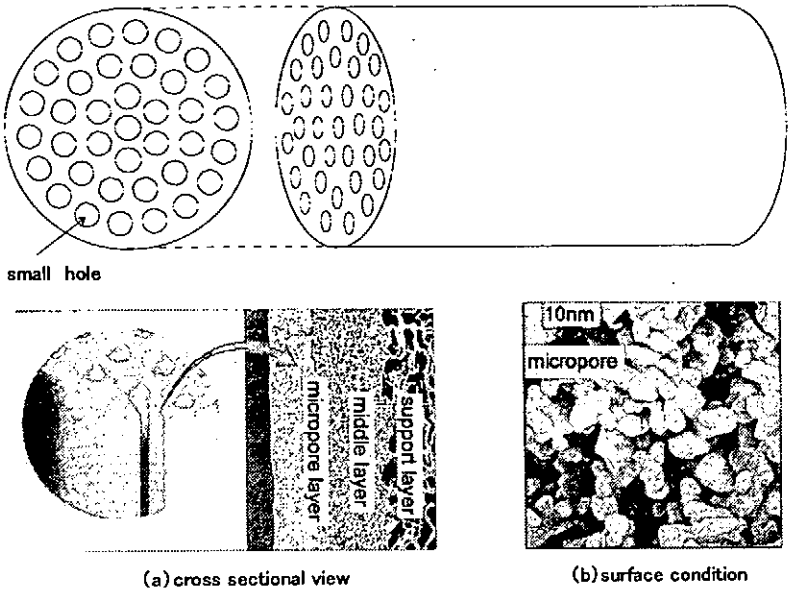

Fig.2 The porous honeycomb ceramics.

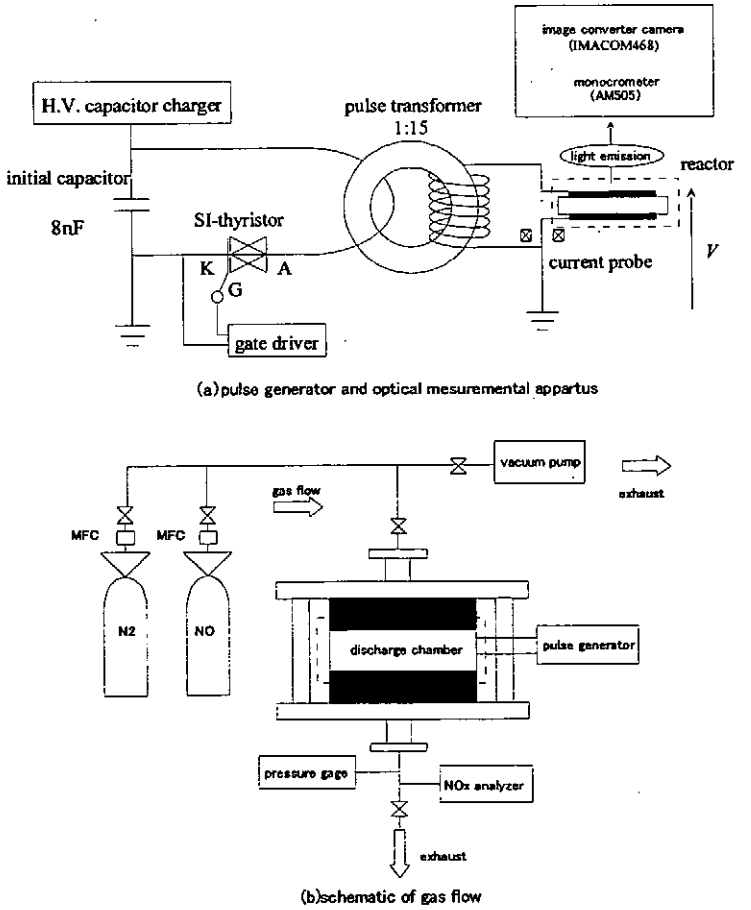

Fig.3 Experimental apparatus

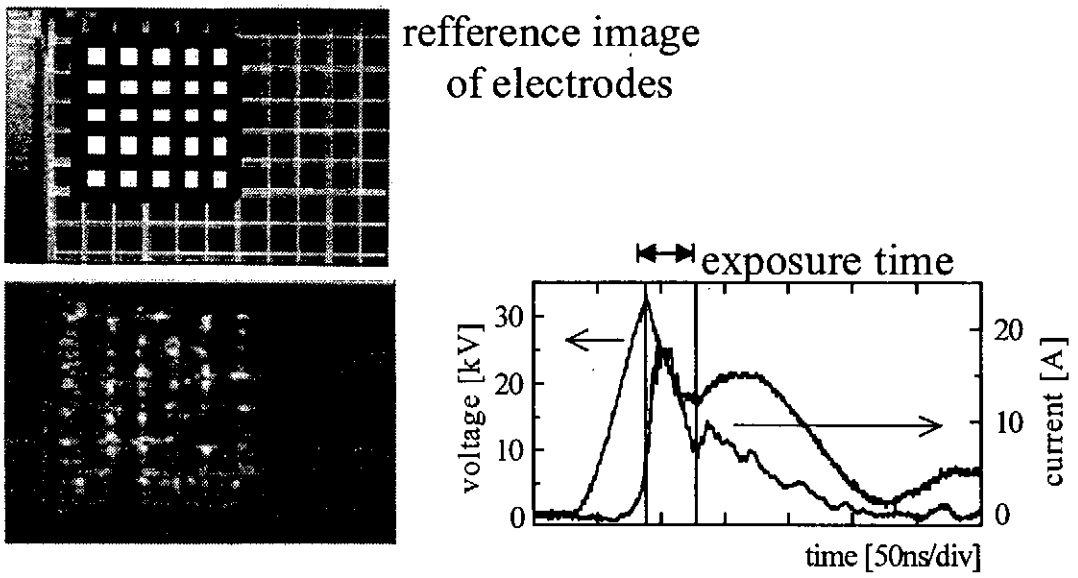

Fig.4 photograph of the discharge of the surface discharge type reactor.

III. Experimental apparatus

Fig.3 shows the set up of the experimental apparatus. A high voltage pulse generator utilizing a fast SI-thyristor and a ferromagnetic step up transformer produces high voltage pulses with 40kV amplitude and 200ns pulse width. The generator can be used with the repetition rate of up to 2kHz. An image converter camera (IMACON468) was used for observation of the discharge phenomena. For gas decomposition experiments, NO of the nitrogen dilution was used. The NO initial concentration and the gas flow rate were set to be 200ppm and 1slpm, respectively, by mass flow controllers. All the experiments were carried out under room temperature and atmospheric pressure. A NOx analyzer was utilized for the mesurement of NO and NO_2 concentration.

IV. Pulsed discharges in the honeycomb ceramics

(a) *Surface discharge type reactor*

Fig.4 shows the photograph of the discharge taken by the image converter camera. Uniform discharges, which were considered to be surface streamers, in each cell of the honeycomb ceramics were obtained. However, according to our previous results, it became clear that the following problems prevented the effective utilization of the ceramics surface.

(1) The size of the reactive plasma was limited by the electrode separation (about 15mm).
(2) The electrode construction becomes complexity, and it is difficult to form the uniform plasma.

(b) *Coaxial type reactor*

Fig.5 shows the photograph of repetitive discharges with the repetition rate of 800Hz taken by the image converter camera. Exposure time of each frame was set to be 50ns and the gate timing was illustrated with voltage and current waveform in Fig.5. First of all, the discharge appeared near the stainless rod electrodes, and it developed to the outer cells of the ceramics. Intense light emission was observed after the voltage peak. The uniform discharges were successfully obtained around outer cells of the ceramics. According to the reference [5], the

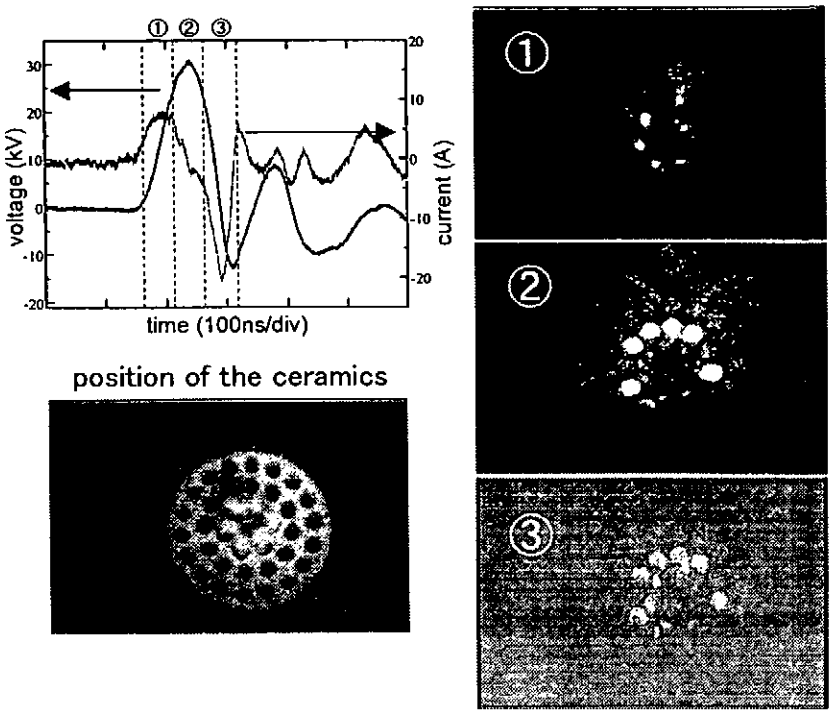

Fig.5 photograph of the discharge of the surface discharge type reactor.

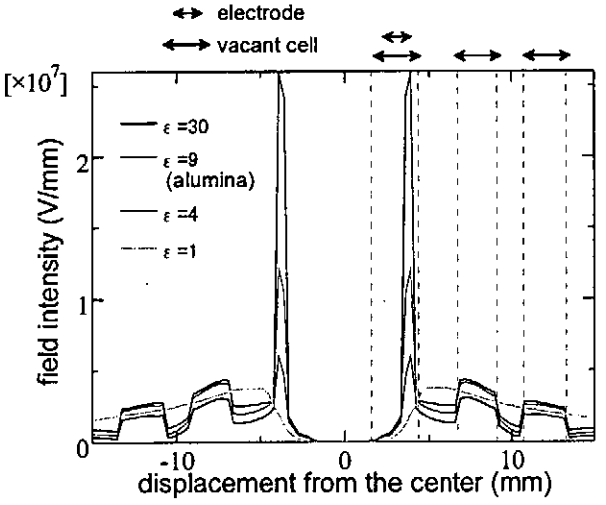

Fig.6 Calculated electric field distribution in the coaxial type reactor.

discharge arises only in the small region near the anode electrodes. However, in this experiment, uniform discharge was observed even in the outer cells of the honeycomb ceramics.

The discharges in the vacant cells were caused by the effect of increasing the field intensity. To investigate the electric field distribution, the numerical analysis of electric field in the lotus shape honeycomb ceramics was carried out. Fig.6 shows the electric field distribution in the case of the applied voltage of 30kV. In Fig.6, the relative dieletctric constant of the ceramics

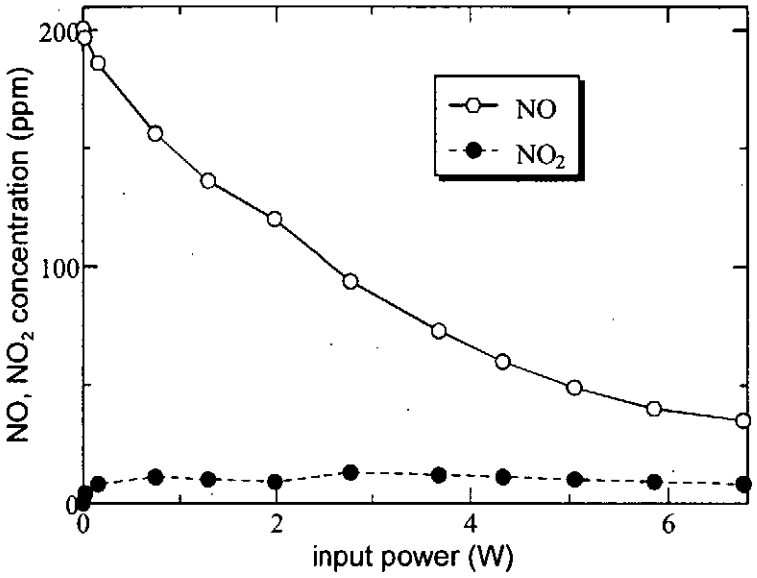

Fig.7 NOx decomposition characteristics of the coaxial type reactor.

was varied from 1 to 30. Generally, higher dielectric constant is advantageous for the discharge formation because the electric field increases in the vacant cells. However, in Fig.6, the lower field intensity is obtained in the outer cells when the dielectric constant is higher value. This is because the electric field concentration near the rod electrode was promoted excessively. Consequently, it is advantageous to use material with the relative dielectric constant of about 9 from 4 in order to obtain uniform discharge. However, the detailed analysis of the effect of the electric field concentration is necessary because the electric field distribution in the honeycomb ceramics depends on not only the dielectric constant but also the electrode configuration and the reactor shape.

V. NOx decomposition experiment

(a) *Characteristics of the coaxial type reactor*

The NOx decomposition characteristics of the coaxial type reactor are shown in Fig.7. The reactions in the NO of the nitrogen dilution are considered to progress through the following processes. At first, the nitrogen radical is created in dissociation of nitrogen by the electron collision.

$$N_2 + e \rightarrow 2N + e \qquad (1)$$

Then the radical-molecule reactions occur.

$$NO + N \rightarrow N_2 + O \qquad (2)$$

$$NO + O + N_2 \rightarrow NO_2 + N_2 \qquad (3)$$

$$O + NO_2 \rightarrow NO + O_2 \qquad (4)$$

The reduction of NO mainly bases the reductive reaction (2), and the O radical produced by this reaction contributes generation of NO_2. The effect of the reaction (4) increases, when the NO concentration becomes lower. Consequently, the concentrations of NO and NO_2 saturate to be certain value.

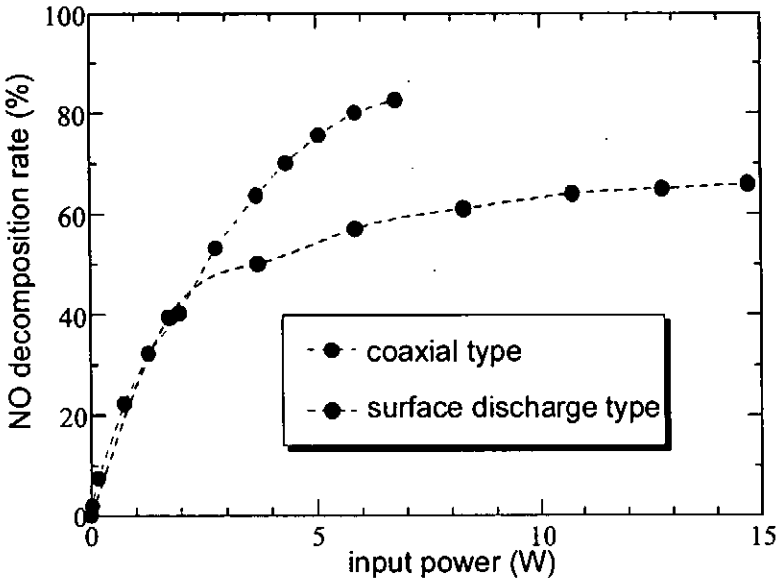

Fig.8 NO decomposition rate.

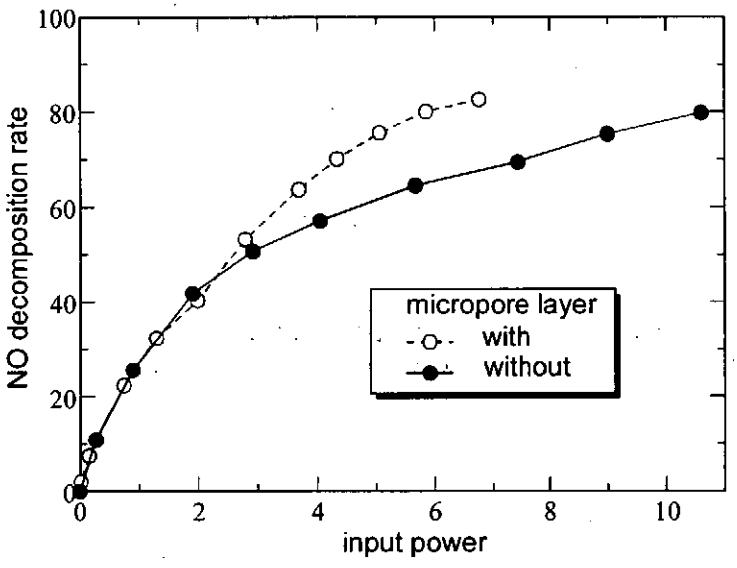

Fig.9 NO decomposition characteristic using the two kinds of ceramics.

(b) *Comparison with the surface discharge type reactor*

Fig.8 shows the NO decomposition rate for the injected electric power into the discharge. In the case of the coaxial type rector, the largest NO decomposition rate of 82% was obtained for comparatively low injected electric power. According to this result, it can be said that the coaxial type reactor utilizing the porous honeycomb ceramics improves the characteristics of NO decomposition in comparison with the surface discharge type reactor.

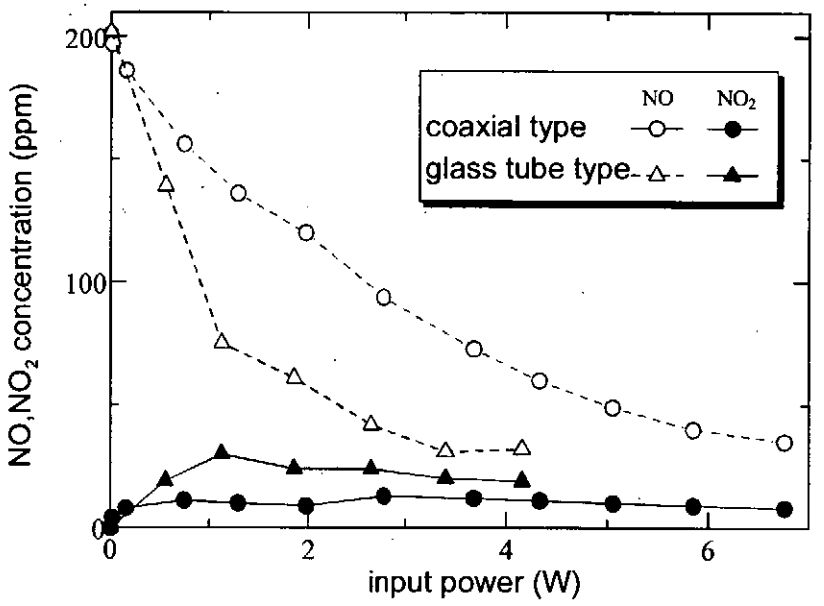

Fig.10 Comparison of the two types of the reactors.

(c) *Effect of the surface condition*

As it is mentioned above, not only the volume reaction in the honeycomb ceramics but also the surface discharge on the ceramics can play the important role of the NO decomposition in the case of coaxial type reactor. To clarify the effect of the surface discharge, we examined two types of the porous honeycomb ceramics. One had the micropore layer of several tens of nm on the inner surface produced by the special surface treatment, the other did not have. The result of the gas decomposition characteristic using the two kinds of ceramics is showed in Fig.9. The improvement of the gas decomposition characteristic was confirmed in the case of the ceramics with the micropore layer. This result indicates that the surface condition greatly influences the discharge characteristics. According to this result, the improvement of the NO decomposition characteristics seems to be possible sufficiently by controlling the surface condition of the ceramics.

(d) *Comparison with the glass tube type reactor*

To clarify the effect of the honeycomb ceramics, the comparison experiment with the glass tube type reactor was carried out. Because of the difficulty of assimilating the experimental condition between the two types of reactors, the experimental conditions were set to be as followings. (1)The size of the reactors was set to be almost the same. (2)The NO decomposition characteristics were only investigated under the condition in which the uniform discharges were obtained. Fig.10 shows the experimental results comparing the two types of the reactors. In the case of the coaxial reactor using the porous honeycomb ceramics, the NO_2 formation is suppressed drastically, even though the NO decomposition efficiency remained lower value. Although detailed investigation on this phenomenon is required, possible explanation is as followings.

In the case of the coaxial type reactor using the porous ceramics, chemical reactions on the ceramics surface affect the gas decomposition characteristics. In literature [6] and [7], the radical reactions on the ceramics surface are reported. In the paper of [6], the light emission from the excited state of NO molecule was observed from the discharge in pure nitrogen atmosphere. This phenomenon was explained by the reactions of O radical adsorbed in SiO_2

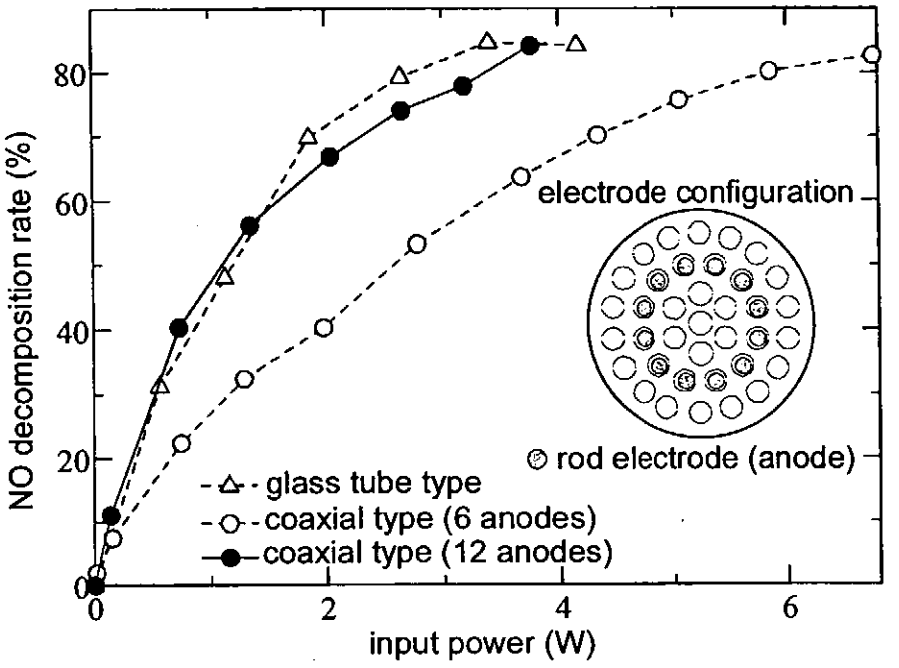

Fig.11 NO decomposition with the reactor using twelve anode rod electrodes.

as followings.

$$e + N_2 \rightarrow N + N + e \quad (5)$$

$$N + O(SiO_2) \rightarrow NO + SiO_2 \quad (6)$$

$$e + NO \rightarrow NO^* \rightarrow NO + h\nu \quad (7)$$

NO was produced by the reaction of absorbed O radical and N radical generated by electron collision. Since the porous ceramics has superior absorptive characteristics, the adsorption phenomena of such O radical may have happened in our experiment. Consequently, NO_2 generation could be possibly suppressed by the adsorption of O radicals. In the literature [7], it is explained that adsorbed O radical becomes oxygen through the recombination reaction. Though such phenomenon is able to arise even in the glass tube type reactor, the large surface area of the honeycomb ceramics promotes the surface reactions and makes difference in the NO_2 yield.

(e) *Effect of the number of the anode rod electrodes*

Fig.11 shows the experimental results of the NO decomposition with the reactor using twelve anode rod electrodes. The NO decomposition characteristic was improved to almost the same performance of the glass tube type reactor in comparison with the case of six rod electrodes. This can be explained by the increase of the electric field intensity caused by narrowing of the electrode separation. The results indicated the possibility of improving the NO decomposition efficiency raising the applied voltage to the reactor.

(f) *Discussion on the energy efficiency*

The energy efficiency for the NO decomposition rate of the each types of the discharge reactor is showed in Fig.12. The energy efficiency was evaluated as the energy required for decomposing a NO molecule (eV/molecule). In the case of the coaxial type reactor with twelve anode rod electrodes, the energy efficiency of 294.5(eV/molecule) was obtained at the

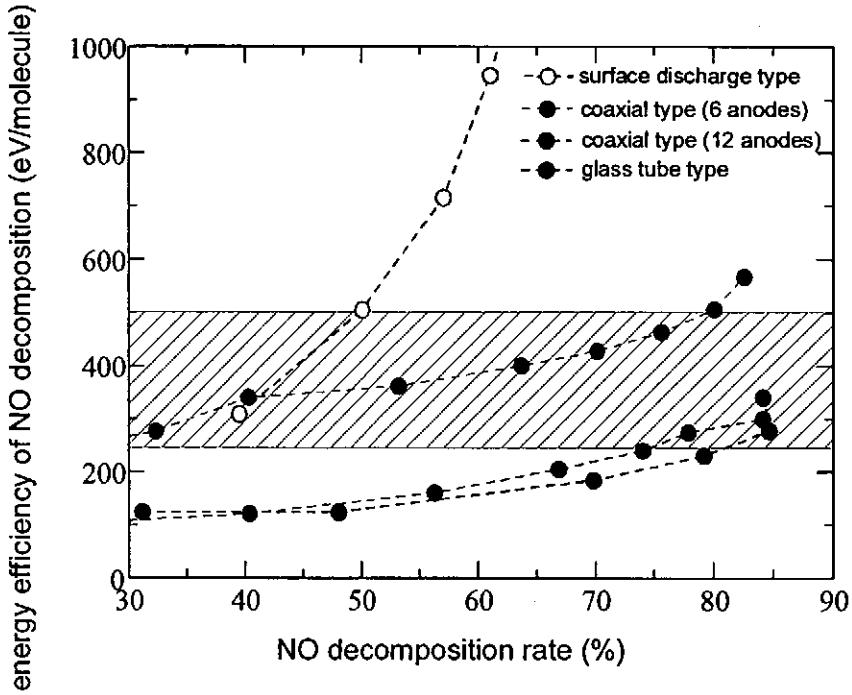

Fig.12 NO decomposition rate of the each types of the discharge reactor.

maximum NO decomposition rate of 84%. The reported value of the energy efficiency is form 250 to 500 (eV/molecule) as it was showed in the hatched region of Fig.12 [8][9]. The efficiency of the reactor of our proposing remains to be in this range.

VI. Summary and conclusions

The coaxial type reactor using the porous honeycomb ceramics, which was not utilized for discharge applications so far, was proposed and the generation of the uniform discharge in atmospheric pressure required for gas decomposition applications was successfully obtained. Comparing with our conventional rector of surface discharge type, the new reactor drastically improved the NO decomposition characteristics. According to the experimental results of NO decomposition, the surface condition of the ceramics had remarkable effect on the characteristics of the reactor utilizing the porous honeycomb ceramics. This effect can be advantageous point of the reactor, because there is large possibility to improve energy efficiency of NO decomposition utilizing the control of the surface conditions. Moreover, the utilization of the surface chemical reactions, namely combined use of catalysts, may realize drastic improvement of the efficiency. It can be possible to conclude that the application to the gas decomposition is practicable for electrical discharge method using the porous honeycomb ceramics.

VII. Acknowledgments

The honeycomb ceramics and the SI thyristor used in this study variously received were supplied from NGK INSULATORS Co., Ltd..

References

[1] S.Masuda, "Report on novel dry DeNOx/DeSOx technology for cleaning combution gases

from utilty thermal power plant boilers," Nontermal plasma techniques for pollution control, Part B, pp.131-138, (1993)
[2] S. Ibuka et al., "Optical investigation of fast pulsed discharge on surface of ceramics for environmental applications," 13th International Conference on High-Power Particle Beam (BEAMS 2000).
[3] T. Nakamura et al., "Pulsed surface discharge in honeycomb ceramics and its environmental applications" International Symposium on Pulsed Power and Plasma Applications (ISPP-2000), PPT-00-68, pp.73-78, (2000)
[4] "NGK Techno-Contents," NGK INSULATORS Co., Ltd.
[5] Oda, Tetsuji, et al., "Decomposition of dilute trichloroethylene by using non-thermal plasma processing - frequency and catalyst effect," Conference Record - IAS Annual Meeting vol.3, pp. 1871-1876, (1998)
[6] I.P.Vinogradov et al., "Classical absorption and emission spectroscopy of barrier discharge in N_2/NO and O_2/NOx mixtures," Plasma Sources Sci. Tech. Vol.6, pp. 307-316, (1997)
[7] B.Goedies et al., "Surface kinetics of N and O atoms in N_2-O_2 discharges," J. Phys. D: Appl. Phys., 29, pp. 1021-1031, (1996)
[8] B.M.Penetrante et al., "Comparison of electrical discharge techniques for nonthermal plasma processing of NO in N2," IEEE Trans. on Plas. Sci., Vol.23, No.4, pp.679-687, (1995)
[9] B.M.Penerrante et al, "Kinetic analysis of non-thermal plasma used for pollution control," Jpn. J. Appl. Phys., Vol.36, pp.5007-5017, (1997)

MEDICAL APPLICATIONS USING PULSED POWER TECHNOLOGY

T. Namihira, H. Hori*, K. Shinozaki*, S. Tsukamoto*, S. Katsuki, R. Hackam**,
H. Akiyama* and K. Okamoto***

The Department of Electrical and Computer Engineering, Kumamoto University, Kurokami 2-39-1, Kumamoto 860-8555, Japan.
**The Graduate School of Science and Technology, Kumamoto University, Kurokami 2-39-1, Kumamoto 860-8555, Japan.*
***The Department of Electrical and Computer Engineering, University of Windsor, 401 Sunset Avenue, Windsor, Ontario N9B3P4, Canada.*
****The School of Medicine, Kumamoto University, Honjo 1-1-1, Kumamoto 860-8556, Japan.*

ABSTRACT

Recently, nitric monoxide (NO) has began to be widely used in medical treatments of acute respiratory distress syndrome (ARDS), relaxation of blood vessels to treat high blood pressure and mitigate against the difficulty of breathing as NO is an endothelium derived relaxing factor (EDRF). Currently a gas cylinder of N_2 mixed with a high concentration of NO is used for medical treatment in a hospital setting. This arrangement is potentially risky due to the possibility of accidental leak of NO from the cylinder. The presence of NO in air leads to the formation of nitric dioxide (NO_2), which is toxic to the lungs. Therefore an on site generation of NO would be very desirable for patients with ARDS and other related illnesses.

We have recently reported on the production of NO using a pulsed arc discharge. In the present work the discharge reactor was made simpler and smaller. NO was generated using a pulsed arc discharge in dry air and in mixtures of oxygen and nitrogen. Before a further treatment of the produced mixture of gases by passing it over a heated molybdenum converter, Maxim concentrations of NO of 455 ppm (parts per million) and NO_2 of 138 ppm were obtained. NO_2, ozone (O_3) and solid particles of brass estimated from the electrodes by the action of the arc discharge, must be emitted from the gas before inhalation. NO_2 produced in the discharge was decomposed to NO by passing it over a heated molybdenum. The concentration of O_3 was found to be zero as determined by UV absorption measurements. The density of the brass particles, which had diameters over 0.3 μm, was less than 1.39 μg/L. A filter could readily capture and thus remove the brass particles. The composition of the gas

mixture after treatment with an arc discharge followed by exposure to heated molybdenum was 540 ppm of NO, 48 ppm of NO_2 and the balance N_2 at 0.1 MPa and 300 ± 3 K.

I. Introduction

For medical treatment, inhaled nitric oxide (iNO) has been used since NO was identified as an effective treatment involving endothelium-derived relaxing factor (EDRF) in 1987[1]. Currently iNO is being widely used as a cure for acute respiratory distress syndrome (ARDS), acute lung injury, persistent pulmonary hypertension of the newborn and other related illnesses[2, 3]. iNO is also used in surgery and heart transplantation[4]. Extensive medical research and development have been carried out on inhalation systems to be used by patient[5-8]. However all current inhalation systems have a common feature in which a gas cylinder of N_2 is mixed with a high concentration of NO. The concentration of NO in the gas cylinder is typically between about 500 ppm[6] to 800 ppm[7]. This arrangement is potentially risky due to the possibility of accidental leak of NO from the cylinder. If a leak is present, it would produce NO_2 by mixing NO with oxygen present in the air. A high concentration of NO_2 has a toxic effect on the lungs and this has been well established[8]. Therefore an on site generation of NO would be very desirable for patients with ARDS and other related illnesses. In the present work, the characteristics of a laboratory system for the production of NO which incorporates the latest improvements in the design of the discharge reactor[9, 10] is reported.

II. Experimental setup and procedure

Figure 1 shows a schematic diagram of the system for generating NO. This system consisted of gas cylinders, NO discharge reactor, NO_2 converter, a gas analyzer and gas pressure monitors. Gas cylinders of nitrogen (N_2), oxygen (O_2) and dry air were used. The proportion of O_2 in the mixtures of O_2 and N_2 was changed from 6 to 93 %. The gas cylinder of dry air included 80 % of N_2, 20 % of O_2 and traces of carbon monoxide (<1 ppm, parts per million), carbon dioxide (<1 ppm) and water vapor (<5 ppm). The gas inlet pressure (P_1) to the reactor was changed from 0.22 to 0.35 MPa. The gas outlet pressure (P_2) from the reactor was changed from 0.12 to 0.25 MPa. Both pressures (P_1 and P_2) were controlled using two valves, which were placed, respectively at the inlet and outlet of the reactor. The difference between P_1 and P_2 was fixed at 0.1 MPa. The flow rate of the gas mixture and dry air were varied from 2.0 to 5.0 L/min at 273 K and 0.1 MPa using a mass flow controller (SEC-440J, ESTEC, Japan).

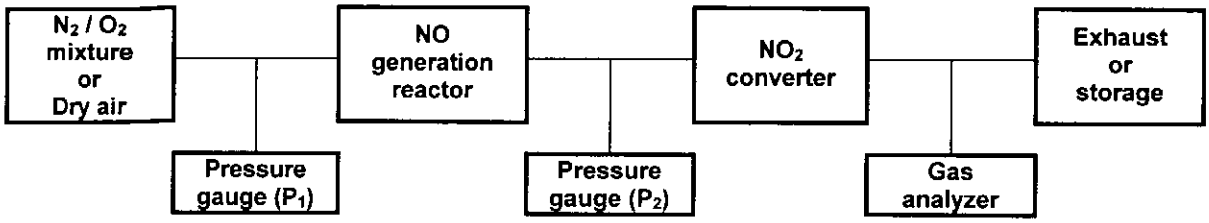

Fig. 1. Schematic diagram of the experimental set up.

Figure 2 shows a cross section of the NO discharge reactor, a charging capacitor C (0.4 to 2.0 nF), a dc power supply (50 kV, 3 mA, HDV-50K3US, Pulse Electronic Engineering, Japan), a limiting resistor (2 MΩ), a spark plug and a trigger pulse circuit. The trigger pulse circuit consisted of a capacitor (0.22 μF), a thyristor and a pulse transformer (1:200, HFT1009, Sanyo, Japan). This reactor is made simpler and smaller than that used previously[9, 10]. The rod and the plate electrodes were made of brass. The brass rod ending with a hemisphere had a diameter of 10 mm. The distance between the rod and the plate was 5 mm. The charging voltage to the capacitor was increased from 15 to 30 kV with increasing outlet pressure (P_2) from the reactor. The charging voltage for all gas pressures was set at a level of about 80 % of the self-breakdown of the gas. The pulse arc discharge between the rod and the plate was initiated by the ultra violet radiation from the discharge between spark plug and the plate electrode[11-15]. The pulse repetition rate was changed from 10 to 220 pps. The applied voltage to the rod electrode was measured using a voltage divider (EP-100K, Pulse Electronic Engineering, Japan), which was connected between the rod and the ground. The current to the reactor was measured using a Rogowski coil (Pearson current monitor, Model 110A, Pearson Electronics, USA). The gas analyzer is based on the method of potentiostatic electrolysis[9, 16].

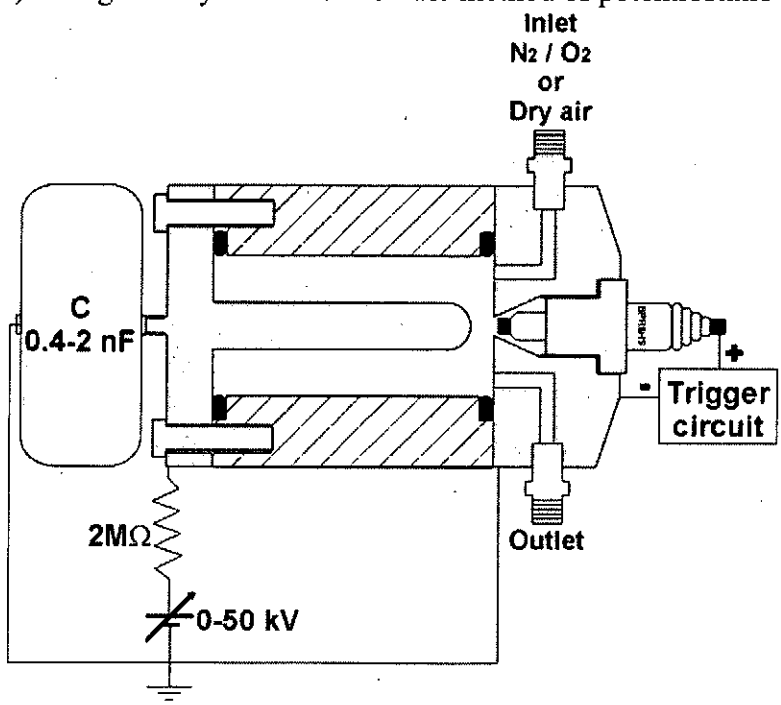

Fig. 2. A cross section of the NO discharge reactor and electrical circuit.

The NO_2 converter consisted of a stainless steel vessel enclosing a molybdenum (Mo) wire and a nickel-chrome wire heater. The molybdenum wire diameter was 0.1 mm and had a length of 100 m. The vessel was heated to about 670 K. Above 600 K NO_2 is converted to NO through the following reaction[9, 17],

$$Mo + 3NO_2 \rightarrow MoO_3 + 3NO \qquad (1)$$

An assessment of the NO production system, which also included the NO_2 converter, was performed. The concentration of O_3 was measured using an ultra violet absorption measurement (Ubest V-570DS, JASCO, Japan) at the same location of the gas analyzer (figure 1). The concentration of the brass particles in the gas mixture produced by the pulsed arc discharge was determined by passing the gas through a Whatman silica filter (0.3 μm) with a combination of a sensitive electronic balance (10^{-3} g, MJ-300, YMC co., Japan). Table 1 shows the conditions of all experiments.

Table 1. Experimental conditions.

	Proportion of O_2 in the mixture of O_2 and N_2 [%]	Concentration of NO_2 [ppm]	Inlet pressure to reactor (P_1) [atm]	Outlet pressure from reactor (P_2) [Mpa]	Charging voltage to capacitor [kV]	Gas flow rate (reduced 273 K and 1 atm) [L/min]	Capacitance of capacitor [nF] C	Pulse repetition rate [pps]	Temperature of vessel [K]
Expt. #1	6-93 (Mixture)	-	2.2	0.12	15	2.0	2.0	30	300
Expt. #2	20 (Dry air)	-	2.2-3.5	0.12-0.25	15-30	2.0	2.0	20	300
Expt. #3	20 (Dry air)	-	2.2	0.12	15	2.0-5.0	2.0	50	300
Expt. #4	20 (Dry air)	-	2.2	0.12	15	2.0	0.4-2.0	10-220	300
Expt. #5	20 (Dry air)	-	2.2	0.12	15	2.0	0.4	220	670

III. Experimental results and discussions

a. Applied voltage to and discharge current in the reactor

Figure 3 shows typical waveforms of applied voltage to and discharge current in the reactor for two discharge capacitors of 0.4 and 2.0 nF (Expt. #4 of Table 1). The trigger pulse voltage was applied to the spark plug at time t=0 and it took about 0.45 μs for the discharge current to fully develop. Both voltage and current waveforms show damped oscillations. The oscillation frequency decreased from about 10 MHz to about 5 MHz when the external capacitance C was changed from 0.4 to 2.0 nF. This is consistent with $\omega^2 = 1/LC_t$, where ω is the radian frequency, L the total inductance and C_t the total capacitance which includes that of the external circuit and the discharge.

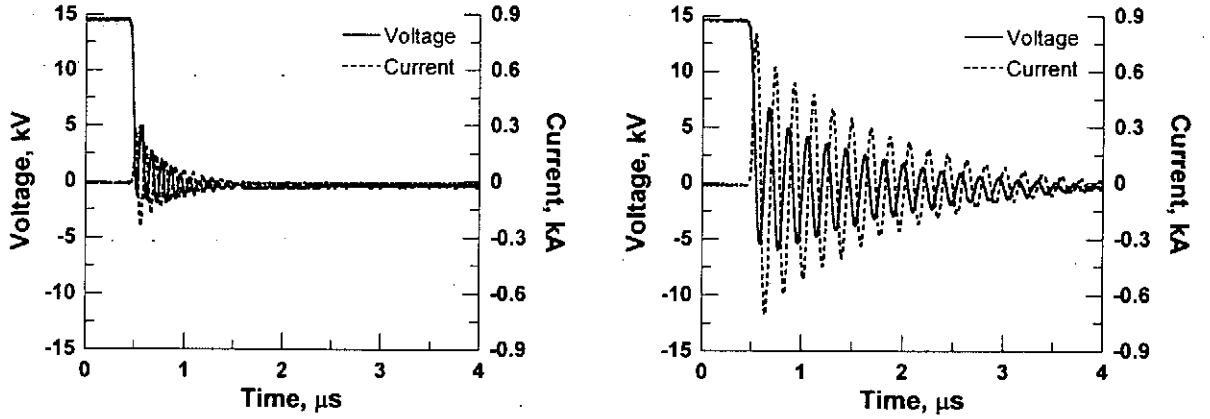

Fig. 3. Voltage and arc discharge current waveforms in the reactor in dry air for different charging capacitors. Conditions: Expt. #4. Table 1: (a)0.4 nF; (b)2.0 nF

b. Characteristics of NO generation reactor

Figure 4 shows the concentrations of NO and NO_2 as a function of the proportion of O_2 in the mixture of O_2 and N_2 (Expt. #1 of Table 1). It can be seen from Fig. 4 that the concentrations of NO and NO_2 had peaks when the proportion of O_2 in the mixture was about 35 and 60 %, respectively. The maximum concentrations of NO and NO_2 reached 282 and 153 ppm, respectively. Figure 5 shows the ratio of $NO/(NO+NO_2)$ as a function of the proportion of O_2 in the mixture of O_2 and N_2 (Expt. #1). It is desirable that the ratio of $NO/(NO+NO_2)$ should have a high value because NO_2 is toxic to humans. Medical practitioners suggest that a ratio of 1.0 should be used. The ratio of $NO/(NO+NO_2)$ had a peak, which had value of 0.74 when the proportion of O_2 in the mixture of O_2 and N_2 was 20 % (Fig. 5). At this mixture proportion the production of NO can be made in dry air. Therefore this choice of gas mixture would be most economical.

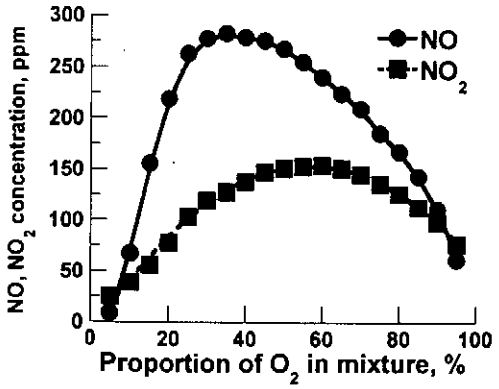

Fig. 4. Concentrations of NO and NO_2 as a function of the percentage of O_2 in a mixture of O_2 and N_2. Conditions: Expt. #1 of Table 1.

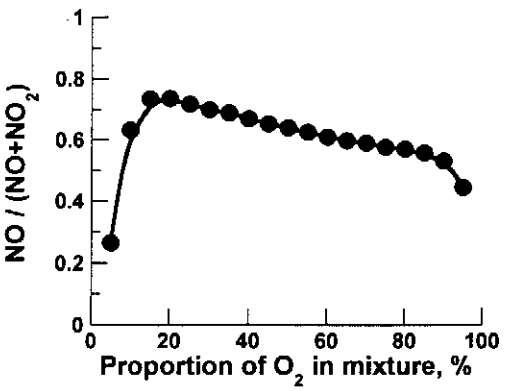

Fig. 5. Ratio of $NO/(NO+NO_2)$ versus percentage of O_2 in a mixture of O_2 and N_2. Conditions: As in Fig. 4.

Figure 6 shows the concentrations of NO and NO_2 as a function of the exhaust pressure (P_2) in dry air. The concentrations of NO and NO_2 increased with increasing the outlet

pressure and therefore with increasing charging voltage and increasing discharge energy. The ratio of $NO/(NO+NO_2)$ had a constant value of 0.74 in the range of 0.12 to 0.25 MPa of outlet pressure (Fig. 7).

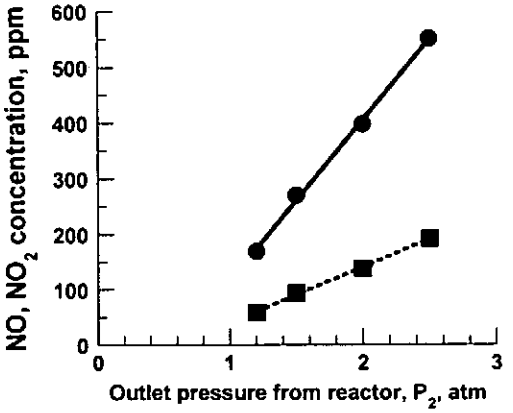

Fig. 6. Concentrations of NO and NO_2 versus P_2. Conditions: Expt. #2 of Table 1.

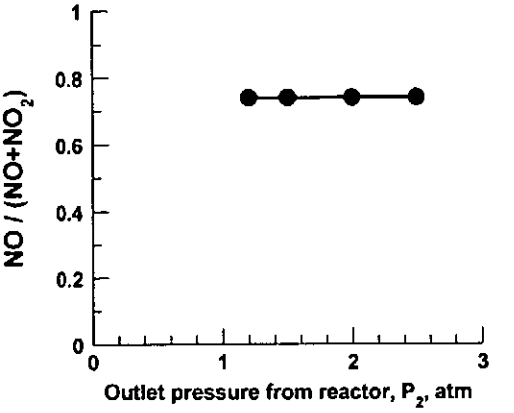

Fig. 7. Ratio of $NO/(NO+NO_2)$ as a function of P_2 in dry air. Conditions: As in Fig. 6.

Figure 8 shows the concentrations of NO and NO_2 as function of the gas flow rate in dry air (Expt. #3). The concentrations of NO and NO_2 decreased with increasing the gas flow rate due to decreasing residence time of the gas in the reactor. The ratio of $NO/(NO+NO_2)$ decreased slightly from 0.76 to 0.73 with increasing the gas flow rate from 2 to 5 L/min (Fig. 9).

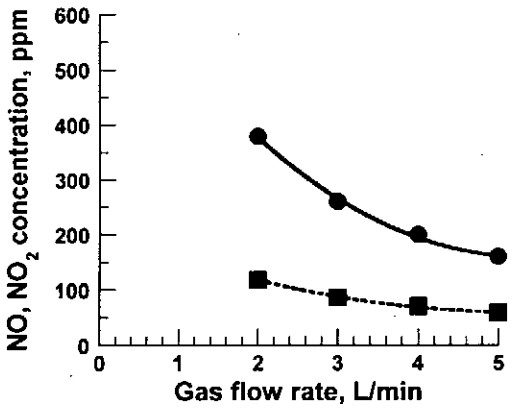

Fig. 8. Dependence of NO and NO_2 concentrations on the gas flow rate. Conditions: Expt. #3 of Table 1.

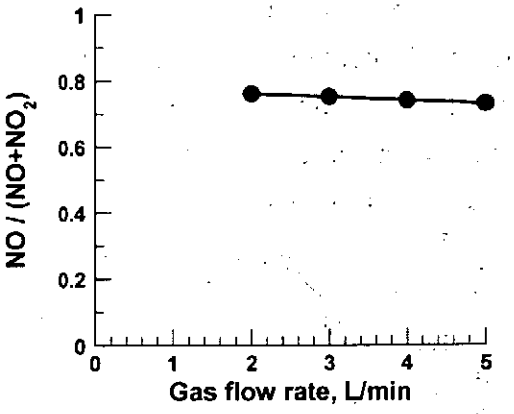

Fig. 9. Dependence of $NO/(NO+NO_2)$ on the gas flow rate. Conditions: As in Fig. 8.

Figure 10 shows the concentrations of (a) NO and (b) NO_2 as a function of the pulse repetition rate for different capacitances (Expt. #4 of Table 1). The maximum pulse repetition rate was limited by relationship a capacitor and a dc power supply (3 mA) used. The concentrations of NO and NO_2 increased linearly with pulse repetition rate (Fig. 10). The concentrations of NO and NO_2 were higher for higher values of the charging capacitance (higher input energy) at a fixed pulse repetition rate. Figure 11 shows the ratio of $NO/(NO+NO_2)$ as function of the pulse repetition rate for different capacitances. This ratio

initially increased with increasing pulse repetition rate until it saturated at 0.77 for all capacitors.

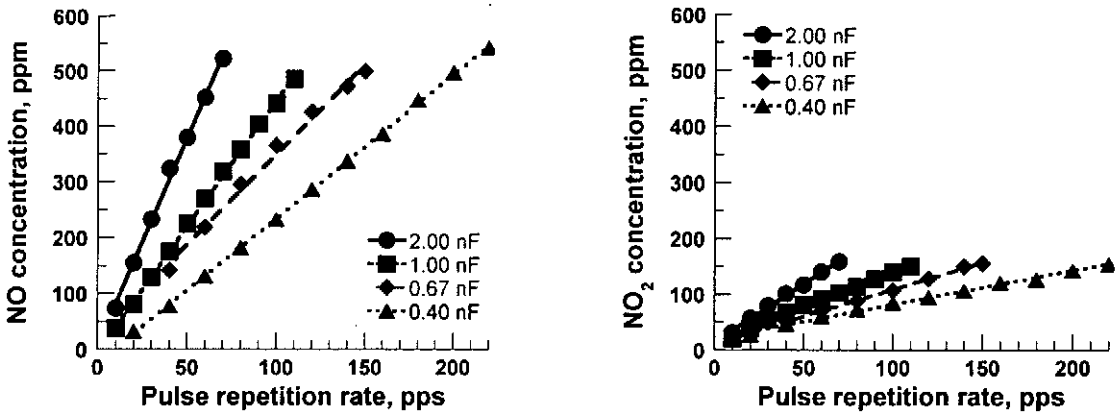

Fig.10. Dependence of the concentrations of (a)NO and (b)NO_2 on pulse repetition rate. Conditions: Expt. #4 of Table 1.

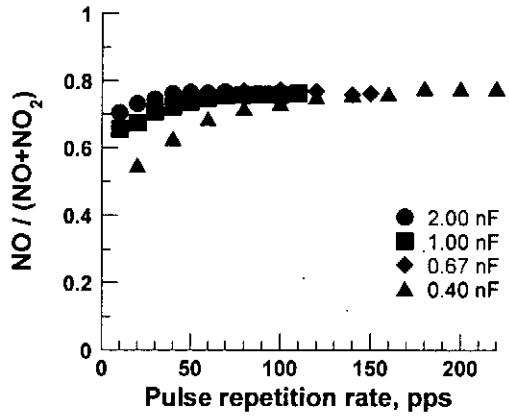

Fig.11. Dependence of NO/(NO+NO_2) on the pulse repetition rate for different charging capacitance. Conditions: Expt. #4 of Table 1.

Figure 12 shows the dependence of the concentrations of (a) NO and (b) NO_2 on the consumption of average power of the dc supply for different capacitances (Expt. #4 of Table 1). The consumption power (*P, in W*) was obtained from,

$$P = \frac{1}{2} \times C \times V^2 \times f \qquad (2)$$

where V and f are the charging voltage to the capacitor (in kV) and the pulse repetition rate (in pps).

It will be observed from Fig. 12 that for a given concentration of NO the power requirement decreased with decreasing capacitance. Therefore a smaller capacitance led to higher energy efficiency for NO production system. The ratio of NO/(NO+NO_2) increased with increasing the consumption power from about 0.55 at 0.9 W to 0.77 at 7.0 W and higher (Fig. 13).

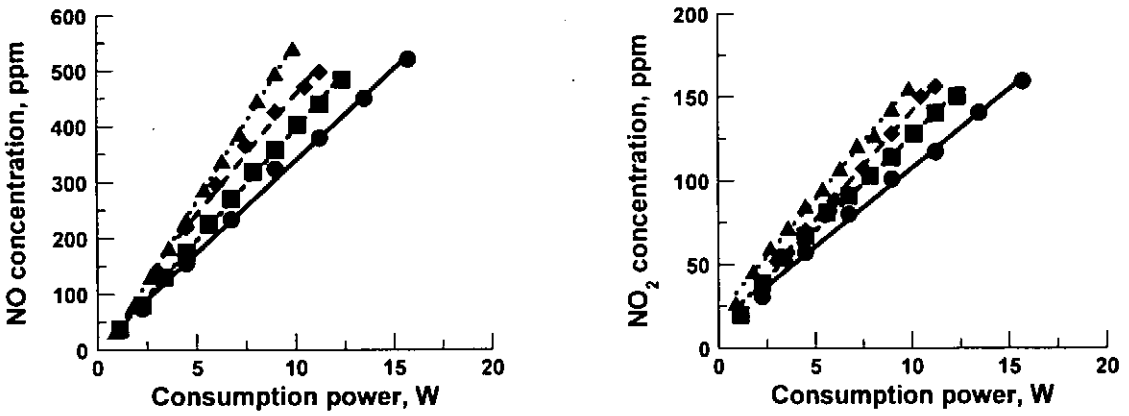

Fig. 12. Dependence of (a)NO and (b)NO_2 concentrations on the consumption of average power of the dc supply for different capacitance. Conditions: Expt. #4 of Table 1.

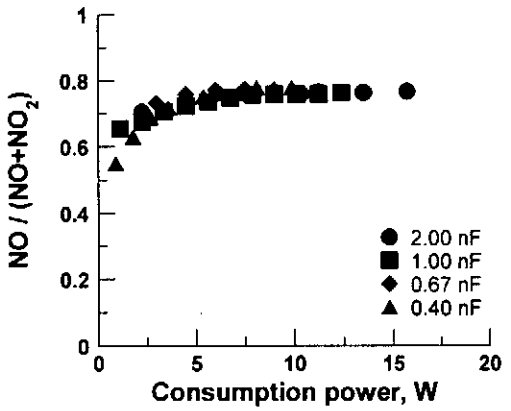

Fig. 13. NO/(NO+NO) against W. Conditions: As in Fig. 12.

c. Assessment of the NO reactor system

Figure 14 shows the dependence of the concentrations of NO and NO_2 on time subsequent to the application of the pulsed power to the reactor including the passage of the gas mixture over a heated Mo. (Expt. #5 of Table 1). The condition of this experiment was chosen due to yield the highest concentration and energy efficiency of NO. It will be observed from Fig. 14 that the concentrations of NO and NO_2 increased rapidly following the starting of the pulsed discharge and soon became constant. In the next step, the gas was passed over a heated molybdenum (NO_2 converter) and the concentration of NO increased while that of NO_2 decreased. The concentrations of NO increased from 455 to 540 and that of NO_2 decreased from 138 to 48 ppm. The concentration of O_3 and brass particle having diameters over 0.3 μm were zero and less than 1.39 μg/L, respectively measured at the location of the gas analyzer. The brass particles could be removed using a filter. The final ratio of NO/(NO+NO_2) was 0.92. This ratio might be made to reach 1.0 by having a longer contact time between the gas mixture and the heated molybdenum.

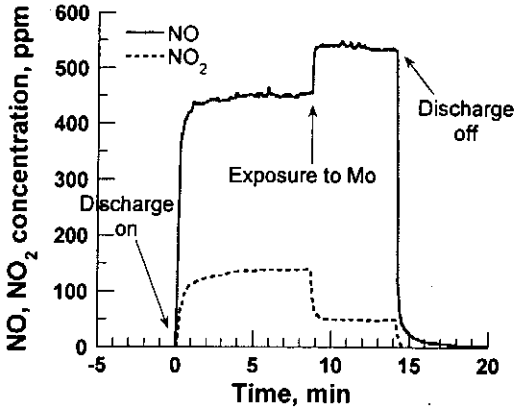

Fig. 14. Dependence of the concentrations of NO and NO_2 on time of application of pulsed power including the flow of the gas over heated Mo. Conditions: Expt. #5 of Table 1.

IV. Conclusions

NO discharge reactor system suitable for medical applications which uses a pulsed arc discharge was studied. The results are summarized as follows:

1) The present NO reactor system was more compact than earlier systems.
2) The concentration of NO was controlled by adjusting the outlet pressure of the gas mixture, the gas flow rate and the discharge energy (the charging capacitance and the pulse repetition rate).
3) The concentrations of O_3 was zero.
4) The highest concentration of NO obtained was 540 ppm in dry air.
5) The lowest concentrations of NO_2 obtained passing the gas over the Mo converter was 48 ppm in dry air.

References

[1] R.M. Palmer, A.G. Ferrige and S. Moncada, "Nitric oxide release accounts for the biological activity of endothelium-derived relaxing factor", Nature, Vol.327, pp.524-556, 1987.

[2] K. Okamoto, M. Hamaguchi, I. Kukita, K. Kikuta and T. Sato, "Efficiency of inhaled nitric oxide in children with ARDS", Chest, Vol.114, No.3, pp.827-833, 1998.

[3] K. Okamoto, I. Kukita, M. Hamaguchi, T. Motoyama, H. Muranaka and T. Harada, "Combined effect of inhaled nitric oxide and positive end-expiratory pressure during mechanical ventilation inacute respiratory distress syndrome", Artificial Organs, Vol.24, No.5, pp.390-395, 2000.

[4] W. Steudel, W.E. Hurford and W.M. Zapol, "Inhaled nitric oxide –Basic biology and clinical applicatios-", Medical Intelligence Article, Vol.91, No.4, pp.1090-1121, 1999.

[5] J.S. Dhillon, J.B. Kronick, N.C. Singh and C.C. Johnson, "A portable nitric oxide scavenging system designed for use on neonatal transport", Crit Care Med, Vol.24, No.6,

pp.-1068-1071, 1996.

[6] O. Stenqvist, B. Kjelltoft and S. Lundin, "Evaluation of a new system for ventilatory administration of nitric oxide", Acta Anaesthesiologica Scandinavica, Vol.37, pp.687-691, 1993.

[7] I. Kukita, K. Okamoto, T. Sato, Y. Shibata, K. Shiihara and K. Kikuta, "Evaluation of Mapleson systems for administration of inhaled nitric oxide", Journal of Anesthesia, Vol.10, pp.44-48, 1996.

[8] K. Miyamoto, A. Aida, M. Nishimura, T. Nakao, Y. Kawakami, Y. Ohmori, S. Ando and T. Ichida, "Effects of humidity and temperature on nitrogen dioxide formation from nitric oxide", The Lancet, Vol.343, No.8905, pp.1099-1100, 1994.

[9] T. Namihira, S. Tsukamoto, D. Wang, S. Katsuki, R. Hackam, K. Okamoto and H. Akiyamma, "Production of nitric monoxide using pulsed discharges for a medical application, IEEE Transactions on Plasma Science, Vol.28, No.1, pp.109-114, 2000.2.

[10] T. Namihira, S. Tsukamoto, D. Wang, S. Katsuki, H. Akiyama, R. Hackam and K. Okamoto, "Production of nitric monoxide in dry air using pulsed discharge, 12th IEEE International Pulsed Power Conference, Vol.2, pp.1313-1316, 1999.

[11] J.D. Craggs, M.E. Haine and J.M. Meek, "The development of triggered spark gaps for high power modulators", J. Inst. Elec. Eng., vol.93, part IIIa, p.963, 1964.

[12] S.L. Moran and L.W. Hardesty, "High-repetition-rate hydrogen spark gap", IEEE Transactions on Electron Devices, vol.38, no.4, pp.726-730, 1991.

[13] S.J. MacGregor, S.M. Turnbull, F.A. Tuema and O. Farish, "Factor affecting and methods of improving the pulse repetition frequency of pulse-charged and dc-charged high-pressure gas switches", IEEE Transactions on Plasma Science, vol.25, no.2, pp.110-117, 1997.

[14] S.J. MacGregor, F.A. Tuema, S.M Tutnbull and O. Farish, "The influence of polarity on trigatron switching performance", IEEE Transactions on Plasma Science, vol.25, no.2, pp.118-123, 1997.

[15] M. Hara and H. Akiyama, "High-voltage pulsed power engineering", Morikita Shuppan Co., 1994 (in Japanese).

[16] C. Iwakura, Y. Fukumoto, H. Inoue, S. Ohashi, S. Kobayashi, H. Tada and M. Abe, "Electrochemical characterization of various metal foils as a current collector of positive electrode for rechargeable lithium batteries", J. Power Sources, vol.68, no.2, pp.301-303, 1997

[17] Manual for NO_X-NO_2-NO auto analyzer, Model 42, Thermo Electron Co., 1993. (In Japanese)

A STUDY OF TRANSIENT CARRIER MEASUREMENTS IN PIN POWER DIODES BY INFRARED LASER PROBING

K.Yasuoka, N.Maeda, H.Matumoto, S.Ibuka, and S.Ishii

Dept. Electrical and Electric Engineering, Tokyo Institute of Technology, 2-12-1O-okayama Meguro-ku, Tokyo,152-8552, Japan

ABSTRACT

A measuring system has been developed for evaluating the distribution of excess carrier density in silicon power-devices. This system is based upon measurements of free carrier absorption transients in a silicon wafer by an infrared laser beam. Fast, precise and direct measurement is possible during the turn-on process of devices. The time resolution is estimated to be 5.1nsec through the measurement of the excess carrier density generated by a pulsed YAG laser beam. The spatial resolution is calculated to be 35μm by a ray-tracing method. A small portion of a high voltage PiN diode is used as a sample for evaluating the behavior of excess carrier density during the turn-on and turn-off periods. The pulsed YAG laser beam of 6.0mJ turns the diode on within 50ns at the reverse voltage of 35V. The uniformly formed excess carrier of about $10^{18}cm^{-3}$ is observed. The measured distributions of carrier density both in turn-on and off periods show almost similar behavior to the profiles calculated by a 2D simulation code.

I. Introduction

Because of the reliability, compactness and long lifetime, power semiconductor devices are widely used in a field of pulsed power technology. [1] Required current-switching ability is over 100kA/μsec. In such condition, the switching characteristics of the power semiconductor devices are greatly influenced by the carrier lifetime, carrier distribution, carrier number density, and carrier drift phenomena in the depletion layer. The 3D simulator to analyze the carrier behaviors is now available, however, the experimental results on temporal and spatial carrier behavior will give important information for developing semiconductor power devices. We have developed the measuring system for analyzing the transient carrier distribution in semiconductors using a free carrier absorption method (FCA). [2]

II. Free Carrier Absorption Method

The probing of the excess carrier density generated within silicon wafer is achieved by using a semiconductor laser beam at 1.55μm wavelength. The schematic drawing of the principle of FCA (Free Carrier Absorption) method is shown in Fig.1. The photon energy of the beam is smaller than the Si band-gap (1.12eV). In Fig.1(a), the probe beam intensity I decays within the sample due to absorption from free carriers according to equation (1).

$$I_0 = I \exp\{-\alpha_0 \cdot d\}, \tag{1}$$

where I_0 is the incident beam intensity, d the sample thickness and α_0 is a constant

absorption coefficient related to doping density.
The excess carriers are generated within the sample by an optical pulse that has the photon energy above band-gap energy of Si, or a current pulse flowing through the device. The incident beam decays with equation (2). α_{FCA} is the absorption coefficient which related to

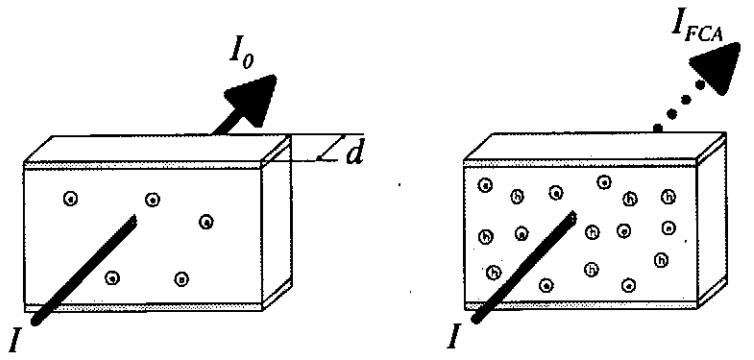

(a) (b)

Fig. 1. The decay of probing beams by the dopant induced free carriers (a) and by the excess carriers generated by external optical beams or current (b).

the density of free excess carriers generated in the wafer.

$$I_{FCA} = I \exp\{-(\alpha_0 + \alpha_{FCA}) \cdot d\} \tag{2}$$

From equation (1) and (2), the absorption coefficient is obtained :

$$\alpha_{FCA} = \ln\left(\frac{I_0 / I_{FCA}}{d}\right). \tag{3}$$

Usually, a linear dependence is assumed between α_{FCA} and excess carrier density Δn with constant σ

$$\Delta n = \sigma \cdot \alpha_{FCA} . \tag{4}$$

We have adopted a value $8.14 \times 10^{-18}\,\mathrm{cm}^2$ at 1.55μm wavelength. [3)]

III. Measurement system

The carrier density in a power device varies rapidly within a few nano second in a pulsed operation. To understand the phenomena on the turn-on process a fast and high precision system for measuring the temporal carrier density is required. Figure 2 shows the experimental setup for the FCA method. Fast InGaAs photo detector (G3476, Hamamatsu Photonics) which has 5.0nsec time-response at 1.55μm and oscilloscope (TDS3052, Tektronix) are used for measuring the intensity of probing beam. The overall response-time of this system is calculated to be 5.1nsec, which is enough to evaluate the turn-on phenomena of power devices.

The measured samples are silicon wafers and silicon PiN diodes. For the silicon wafers, the excess carrier is generated by irradiating an yttrium-aluminum-garnet (YAG) laser at the fundamental wavelength of 1.06μm. A pulsed voltage is applied to the PiN diode. The fundamental wavelength of YAG laser almost coincides in photon energy with the Si band gap. The calculated carrier distribution in the sample suggests that the sample is homogeneously excited by the laser beam.

Typical waveform of the YAG laser pulse is shown in Fig.3 with the measured and calculated excess carrier densities. The beam energy at the silicon wafer is 18mJ. The calculated carrier density is obtained by the integral of the output voltage from the photo detector-2 by equation (5). The constant A in equation (5) is adjusted to fit the calculated curve to the measured curve.

$$\Delta n = A \times \int_0^t V(t) \cdot dt \tag{5}$$

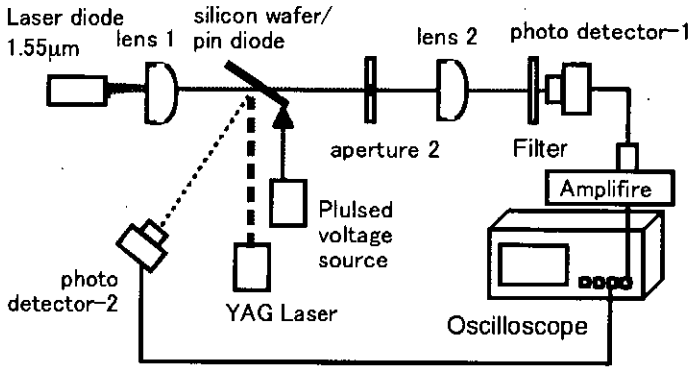

Fig. 2. Experimental setup for FCA technique.

The both curves agreed well by time 120nsec, because the attenuation term by the recombination is not contained. The carrier density reaches maximum at time 130 nsec after the irradiation of YAG laser with pulse width of 50nsec FWHM. The carrier slowly decreases for about 10μsec. In the build up time, the decrease of carrier by the recombination could be disregard by the comparison to the formation. From these results, the high-speed measurement is possible to carry out using the system.

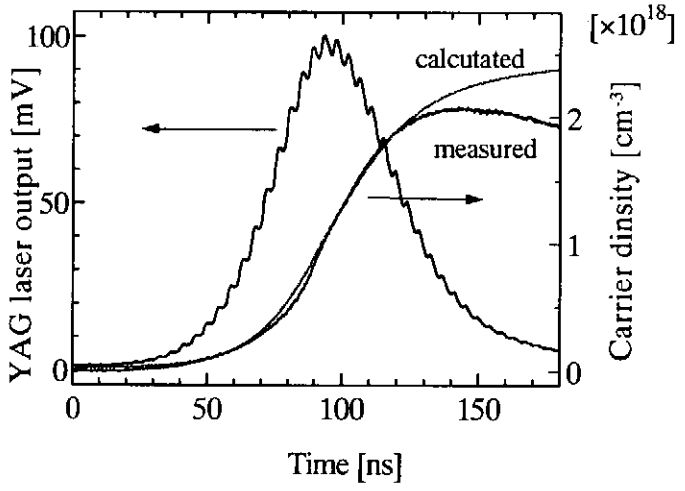

Fig. 3. YAG laser waveform, calculated and measured carrier density in a silicon wafer by FCA method.

IV. Experimental Results

The carrier number density is measured in a PiN diode of 2mm width 1mm length 0.47mm height, which is cut off from a power diode. The sample is shown in Fig.4.

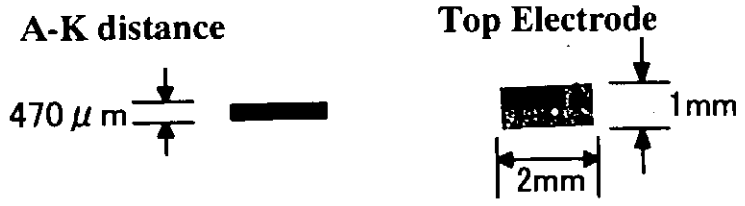

Fig. 4. Sample Diode

The A-K distance of 470μm is smaller than the beam size of probing laser which has a beam shape of ellipse with 4.3 mm × 2.0mm. Beam trajectories at 90° incident angle for a probe beam are calculated as a function of the distance of traveling direction for three different focal lengths of lens as shown in Fig.5. The Gaussian beam is assumed in the calculations.

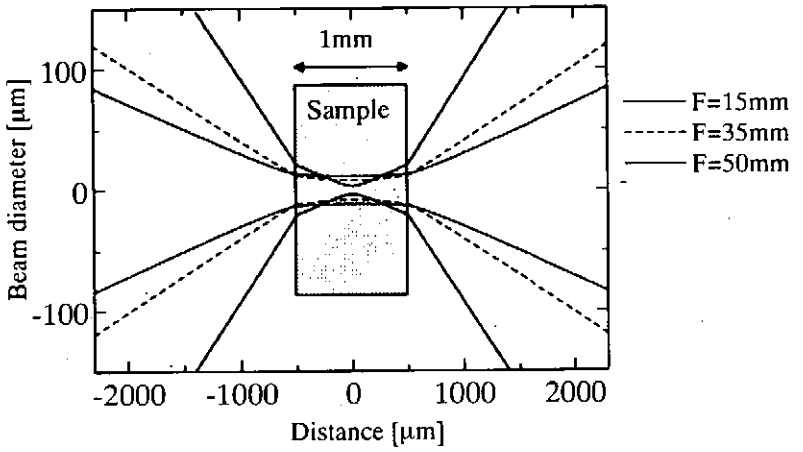

Fig. 5. Calculated beam trajectories at 90° incident angle for a probe beam.

Inside the silicon wafer, the beam profile seems to be nearly uniform with the focal length of 35 or 50mm. The lens with shorter focal length diminishes the beam waist only at the focal point but shows non-uniform profile. From Fig.5, the beam size in the silicon is estimated to be 35 × 16μm with f=35mm lens.

Figure 6 shows the applied square pulse current of 30μs in forward direction for generating excess carrier in PiN diode. The diode seems to be filled with excess carriers within 5μsec. However, the measured temporal change of the excess carrier density shows the lack of excess carriers especially near the p^+ layer at 5μsec. Carriers gradually increase and saturate at 30μsec as shown in Fig.7. Figure 8 shows the simulation results by 2D simulator calculated with the same doping profile of sample diode. Experimental and simulation results show the equal tendency that the carrier density is high near the p^+ and n^+ layers and low at the center part of n^- region. The increasing behavior is almost same in both rsults. However, there are some differences between experimental and simulation results. The increasing velocity of excess carriers especially in p^+ side of the diode is much lager in experiment and the excess carrier-distribution at both sides of PiN diode is almost same for experimental data but different for simulation results.

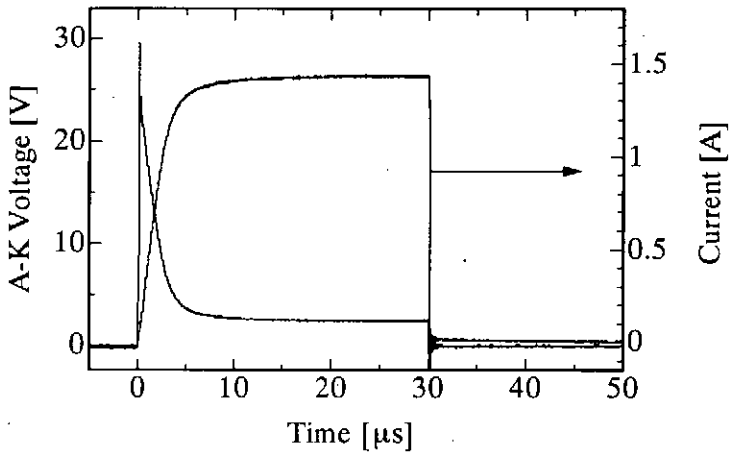

Fig.6. Voltage and Current waveforms applied to the sample PiN diode.

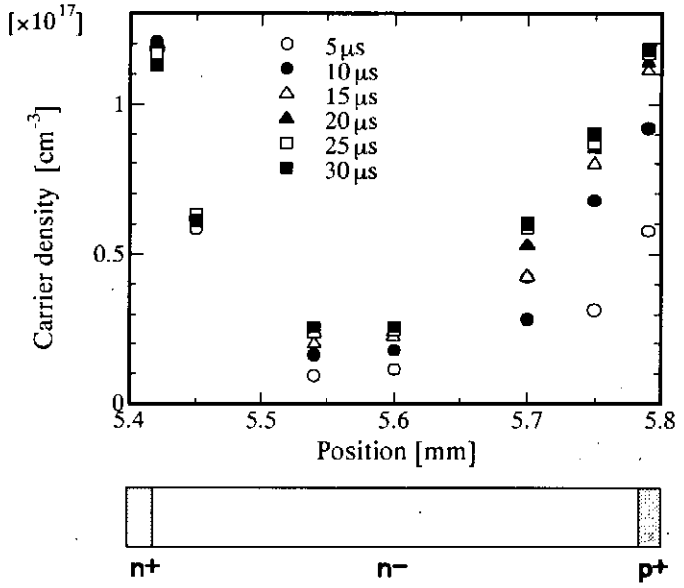

Fig.7. Measured temporal carrier distribution within PiN diode.

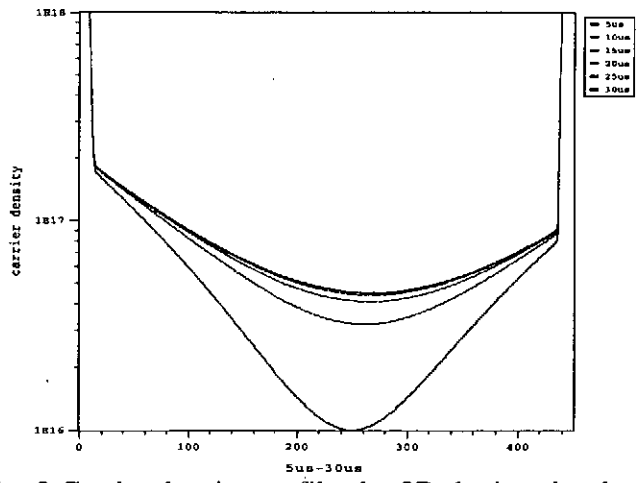

Fig. 8 Carrier density profiles by 2D device simulator.

The PiN diode used in this study is not a fast switching type but a high voltage resistance type so that the fast generation of the excess carrier is simulated by a photo excitation with YAG laser. Such method is equal to make an optically triggered semiconductor switches which have the very fast turn-on characteristics. The fundamental wave of the YAG laser beam of 6mJ is irradiated on the sample diode which is inversely biased to 35V. The switching waveforms are shown in Fig. 9.

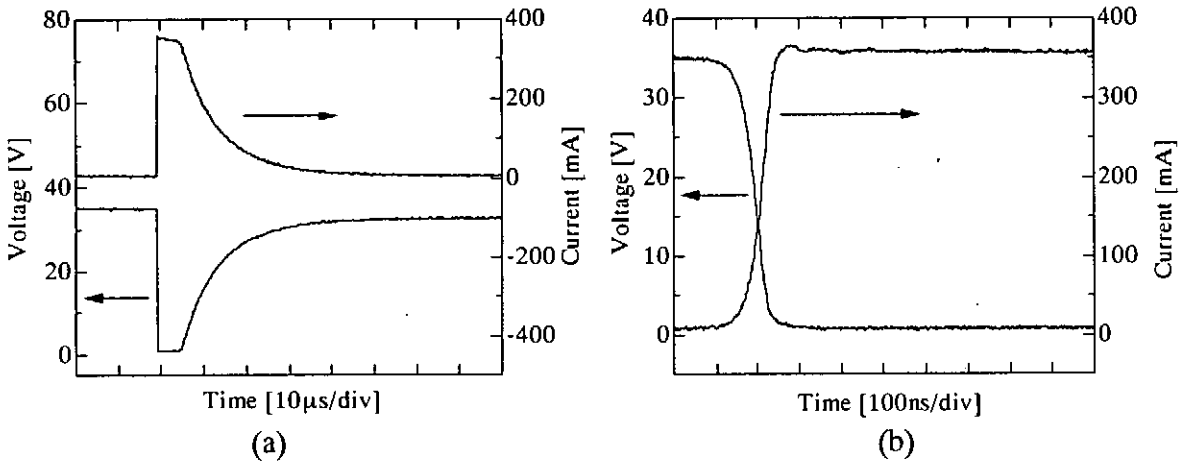

Fig.9 Voltage and current waveforms for photo triggered PiN diode.

The turn-on time is around 50ns after irradiation of laser beams as shown in Fig.9(b) which is a enlarged view of Fig.9(a). The turn on time is not influenced by the laser intensity of reversed voltage because the rise time of the laser beam is limited to be 50nsec. The turn-off time is a few tens μsec which is controlled in diffusion process. The carrier distribution after 200ns from a YAG laser irradiation is shown in Fig. 10. It is proven that the carrier of about $10^{18}cm^{-3}$ has been uniformly formed in PiN diode.

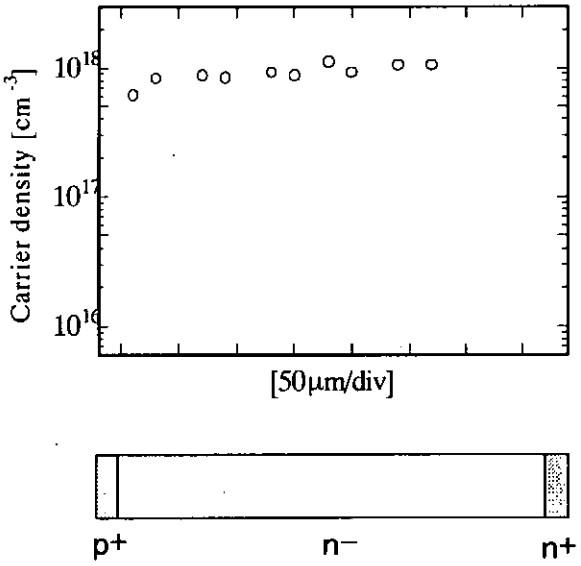

Fig.10 Carrier distribution in the turn-on process in optically excited PiN diode.

Figure 11 shows the carrier distribution in the turn-off process after irradiation of laser beam

at 0,1,3,9μsec. The rapid decreasing of carrier density is observed near the p^+ layer. In comparison with the steady state, the carrier distribution obtained by the simulator at reverse biasing 35V is shown in Fig.12, the low concentration part corresponds to the depletion layer around 80μm apart from the p^+ layer. Therefore, the turn-off process starts at the time in which the resistivity of depletion layer becomes high by the extinction of the carriers. The turn-off time depends on the carrier emission rate in depletion layer, and is possible to decrease by shortening the length of depletion layer by applying high reversed voltage.

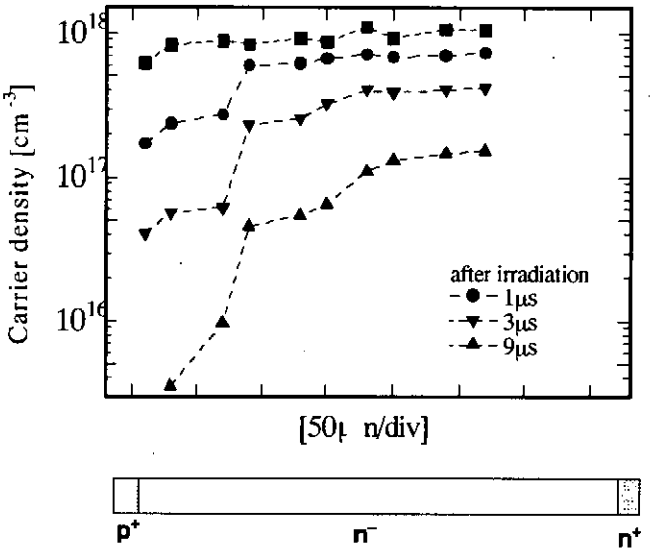

Fig.11 Measured carrier behavior during turn-off process.

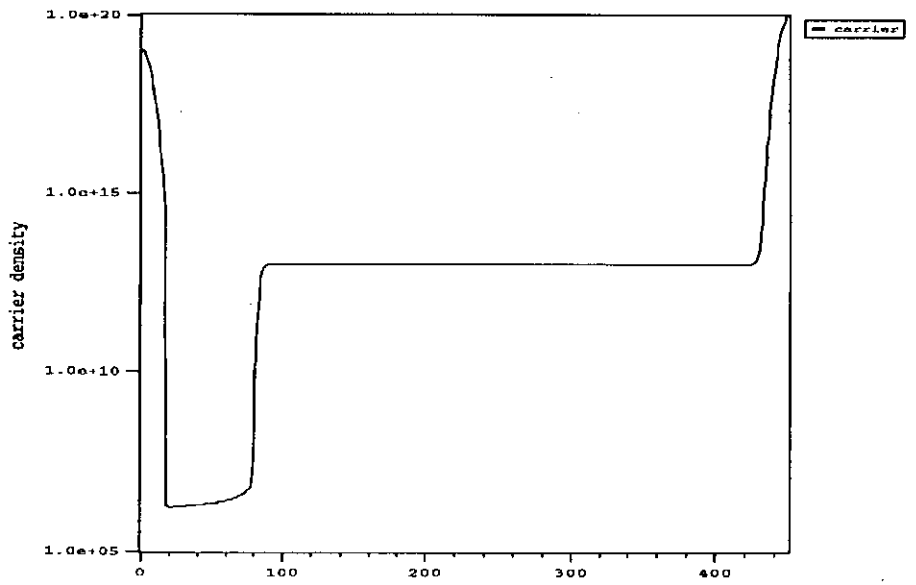

Fig.12 Simulated carrier density and depletion layer at reverse biased voltage.

V. Conclusion

The measuring system for the transient carrier in power devices has been developed by using a direct probing method with infrared laser. This system is based upon the FCA technique in which carrier density is obtained from the intensity ratio of output beam and incident beam. The time resolution is estimated to be 5.1nsec through the measurement of the excess carrier density generated in a silicon wafer that is irradiated by a pulsed YAG laser beam. The spatial resolution in a silicon wafer is calculated to be 35μm by a ray-tracing method that shows the beam profile in it. A small portion of high voltage PiN diode is used as a sample for evaluating the time dependences of excess carrier density during the turn-on and turn-off periods. The pulsed YAG laser beam of 6.0mJ turns the diode on within 50ns at the reverse voltage of 35V. The uniformly formed excess carrier of about $10^{18}cm^{-3}$ is observed. The measured distributions of carrier density both in turn-on and off process show almost similar behavior to the calculation results by a 2D simulator. The obtained date shows the usefulness of this direct measuring system for understanding fast switching process of power semiconductor devices.

Acknowledgement

The authors would like to thank NGK Insulators, LTD for providing the diode samples. This study was carried out of grant-in-aids for Scientific Research from the Ministry of education, Science, Sports and Culture, Japan.

References

1) S. Ishii, K. Yasuoka and S. Ibuka, "Pulsed Power Application assisted by Power Semiconductor Devices", he 13th International Symposium on Power Semiconductor Devices & ICs(ISPSD'01) (2001).
2) J. Linnros, "Carrier life time measurements using free carrier absorption transients", J. Appl. Phys. Vol. 84, pp.275-291(1998).
3) R. A. Soref and Brian R. Bennet, "Electrooptical effects in silicon", IEEE J. Auantum Elcetronics, Vol.QE-23, pp.123-129(1987).

SIMULATION OF NON-LINEAR COAXIAL LINE USING FERRITE BEADS

S.Furuya, H.Matsumoto, S.Takano and J.Irisawa

Nagaoka University of Technology, Niigata, 940-2188, JAPAN

ABSTRACT

A ferrite sharpener is a non-linear coaxial line using ferrite beads, which produces high-voltage, high-dV/dt pulses. We have been examining the characteristics of ferrite sharpeners experimentally, varying various parameters. In this report, we made the simulation of the ferrite sharpener and compared the predictions with the experimental results in detail to analyze the characteristics of the sharpener. As a result, the results of simulation are in good agreement with the experimental results.

1. Introduction

High-voltage, high-dV/dt pulses are necessary to drive pulsed laser, Pockels cell, pulsed radar and to control electron beam. There are various methods to produce high-dV/dt pulses; non-linear transmission line using ceramic capacitors[1], pn-junction diodes[2] and ferrite[3]. Among them non-linear coaxial line using ferrite beads is superior to the others with respect to low cost and simplicity of structure. Therefore, we have been examining the characteristics of ferrite sharpeners, non-linear coaxial lines using ferrite beads, experimentally, varying various parameters. We have obtained pulses which have high dV/dt of 12kV/ns and open-ended peak voltage of 45kV[4].

In this report, we made the simulation of the ferrite sharpener to analyze the characteristics of the sharpener along with Ref.5. Then we compared the predictions with the experimental results in detail. As a result, the results of the simulation are in good agreement with the experimental results.

In Sec.2, the experimental setup of the ferrite sharpener is described. In Sec.3, the equivalent circuit of the ferrite sharpener is presented. In Sec.4, the results of the simulation and discussion are described. Finally, the results of this report are summarized in Sec.5.

2. Experimental setup

Fig.1 shows the structure of a ferrite sharpener, which is a non-linear coaxial line using ferrite beads. A peace of ferrite bead is nickel-zinc ferrite bead TDK-HF70BB. The outer and inner diameter of a bead are 5.0mm and 2.0mm, respectively, and its length is 5.0mm. The impedance of the sharpener after ferrite saturation is designed to be approximately 50Ω. The principle of the sharpener is illustrated in Fig.2. As shown in the figure, an input voltage pulse dissipates its front, propagating in the sharpener. Then the input voltage pulse is steepened at the end of the sharpener. The rise time and peak voltage of the input pulse are approximately 40ns and 20kV, respectively. Typical output waveform of open-ended ferrite sharpener is shown in Fig.3. The rise time and peak voltage of the pulse are 2.4ns and 45kV, respectively, so high dV/dt of 12kV/ns is achieved. Voltages are measured by Tektronix high voltage probe: P6015A and Hewlett Packard digital oscilloscope: HP54510A.

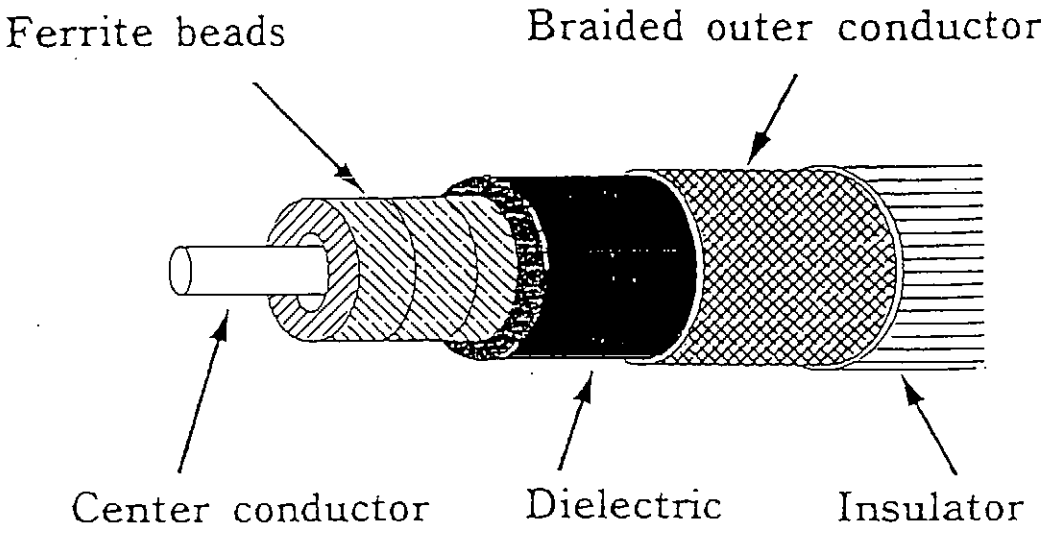

Fig.1 Structure of ferrite sharpener

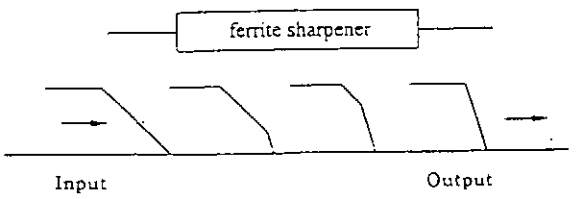

Fig.2 Principle of ferrite sharpener

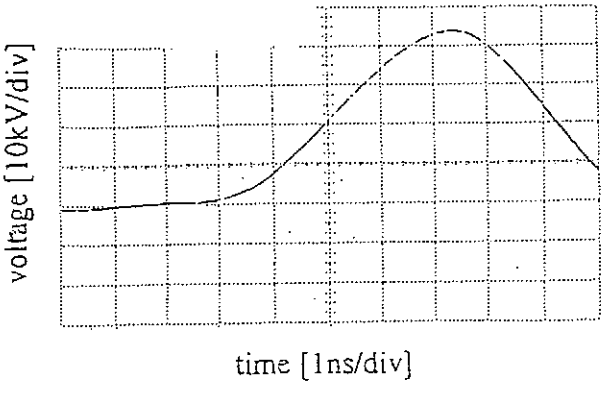

Fig.3 Output waveform of ferrite sharpener

3. Equivalent circuit of ferrite sharpener

Along with Ref.5, we made the simulation of the ferrite sharpener to analyze the characteristics of the sharpener. The equivalent circuit of the sharpener is derived as follows. Current equation of the sharpener is the same as a usual transmission line.

$$dI/dz = -C_0 dV/dt \tag{1}$$

where C_0 is the capacitance of the sharpener per unit length. The magnetic flux ϕ of the sharpener is

$$\phi = L_0 I + \int_n^{r_m} \mu_0 M(r) dr \tag{2}$$

where L_0 is the inductance of the sharpener per unit length after ferrite saturation. r_m and ri are the outer and inner radius of the ferrite bead, respectively, and M is the magnetization of the bead. If we assume that M is independent of the radius and is constant, eq.(2) becomes

$$\phi = L_0 I + \mu_0 M(r_m - r_i) \tag{3}$$

So voltage equation of the transmission line is

$$dV/dz = -d\phi/dt = L_0 dI/dt + \mu_0(r_m - r_i) dM/dt \tag{4}$$

From eq.(1) and (4) the equivalent circuit of the sharpener is derived, as shown in Fig.4. Voltage sources in the figure are respond to the product of Δz and the second term of eq.(4). dM/dt is obtained from Landau-Gilbert equation as below.

$$\frac{dM}{dt} = \frac{2}{S_W}\mu_0 H M_S\left(1 - \frac{M^2}{M_S^2}\right) \tag{5}$$

where S_W is a switching coefficient of the ferrite used and H is the magnetic field. M_S is the saturation magnetization of the ferrite used.

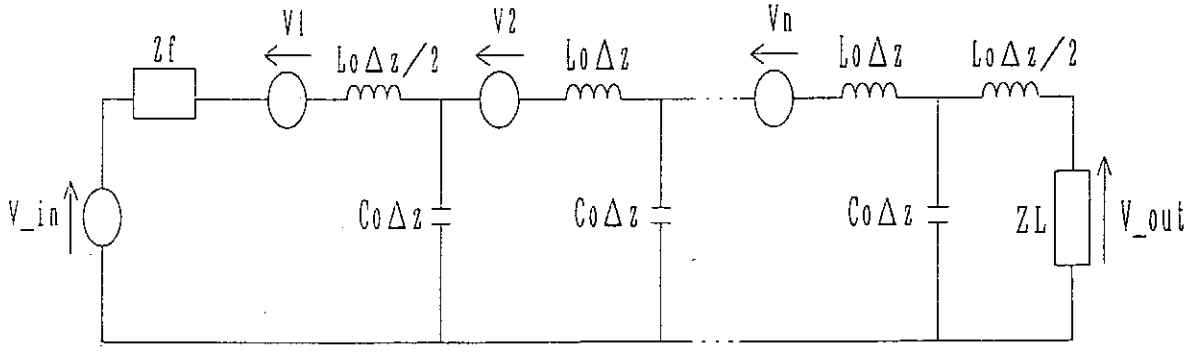

Fig.4 Equivalent circuit of ferrite sharpener

4. Results and discussion

. We assume B-H curve as shown in Fig.5. From the catalog, relative permeability at H=0 and saturation magnetic flux density are 1500 and 0.28T, respectively. According to Ref.6, the switching coefficient of nickel-zinc ferrite is 0.25 or 0.51 oe·μs. In simulation, time step Δt is 1ps and the sharpener is divided into 100 sections. The input voltage waveform of simulation is fitted to that of experiment. The output terminal is loaded with a 50Ω resistor.

Figure 6 shows the rise time of the output voltage pulse of the sharpener when the length of the sharpener is changed. The prediction with S_W=0.25 is in better agreement with the experimental results than that with S_W=0.51. The prediction agrees with the experimental results when the sharpener is long, however, neither it does when the sharpener is short.

Figure 7 shows the rise time of the output voltage pulse of the sharpener when the bias current to the ferrite beads is changed. The direction of the bias current is opposed to that of the input pulse. The prediction with S_W=0.25 is in better agreement with the experimental results than that with S_W=0.51, the same as Fig.6. The prediction agrees with the experimental results when the directions of bias current and input pulse are different, however, neither it does when the directions are same.

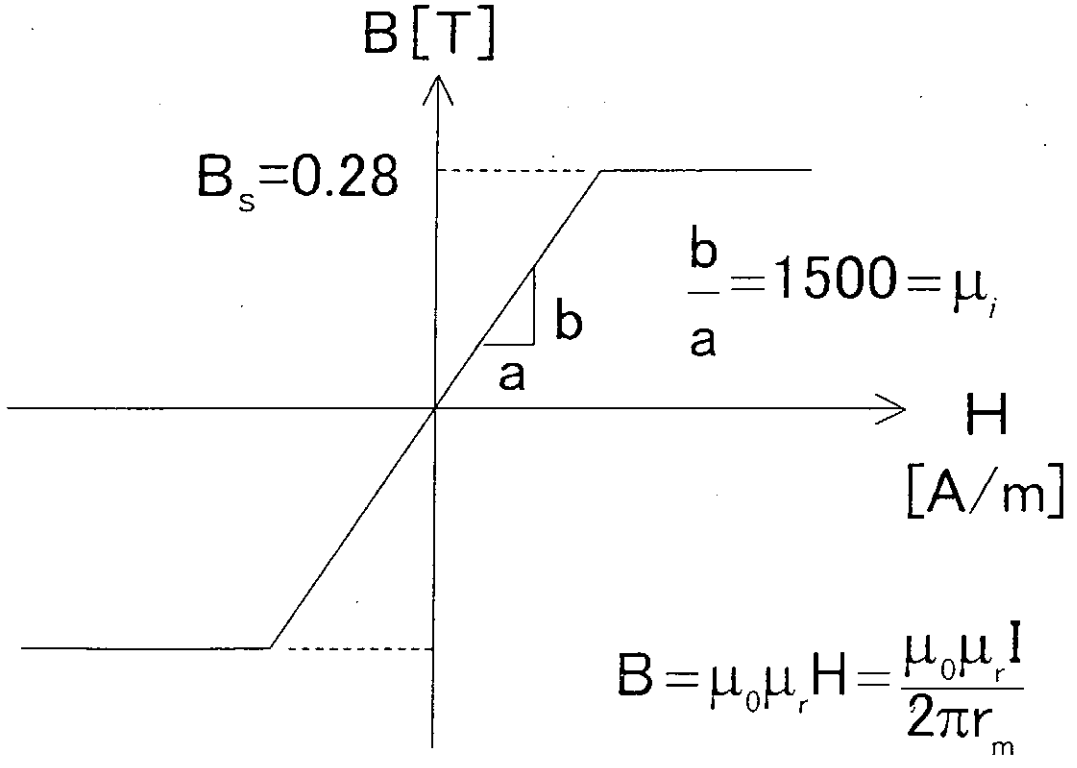

Fig.5 Modeling of B-H curve

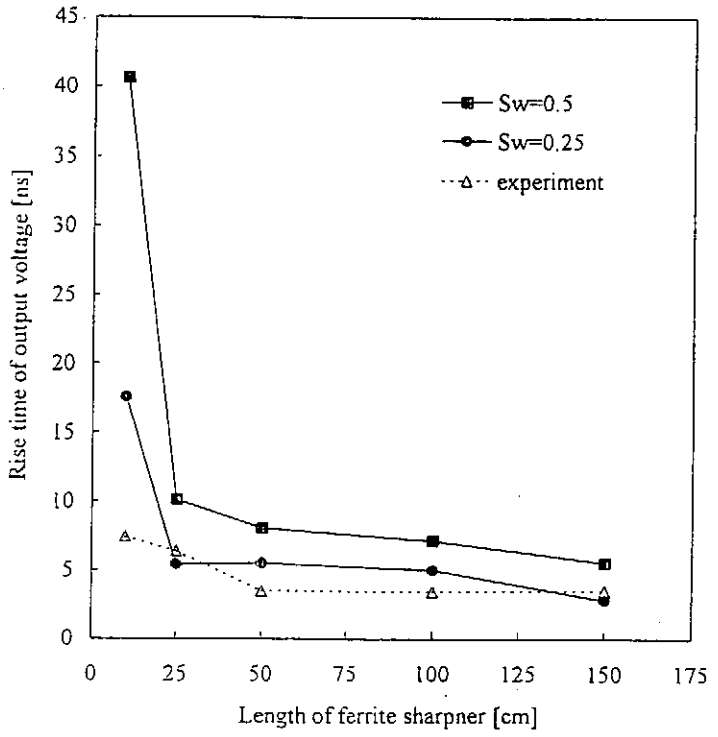

Fig.6 Rise time of output voltage vs. length of ferrite sharpener

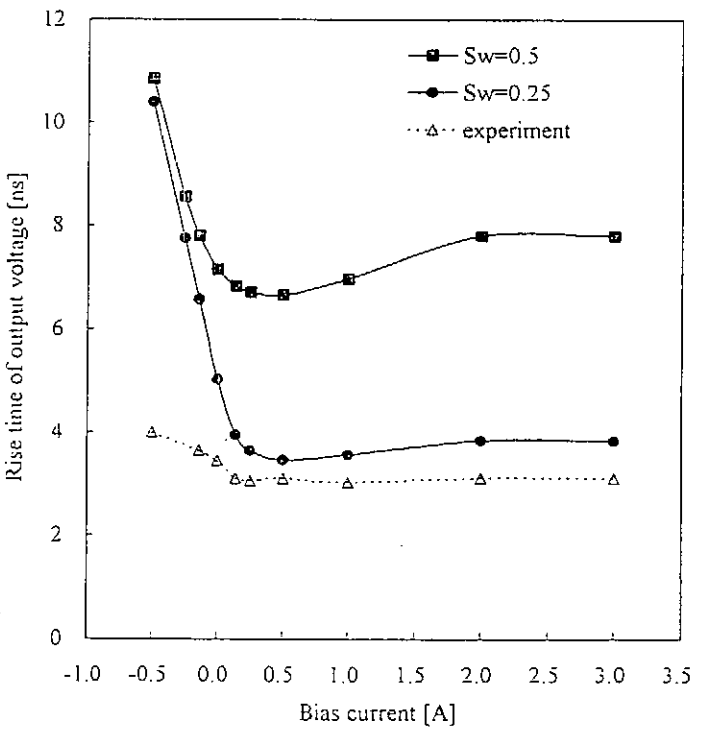

Fig.7 Rise time of output voltage vs. bias current

5. Conclusion

A ferrite sharpener is a non-linear coaxial line using ferrite beads, which produces high-voltage, high-dV/dt pulses. We have been examining the characteristics of ferrite sharpeners experimentally, varying various parameters. In this report, we made the simulation of the ferrite sharpener and compared the predictions with the experimental results in detail to analyze the characteristics of the sharpener. As a result, the results of simulation are in good agreement with the experimental results, however, neither it does when the length of the sharpener is short or the directions of the bias current and input voltage pulse are same.

Reference

(1) H.Ikezi, J.S.deGrassie and J.Drake, Appl. Phys. Lett., **58**(1988)986
(2) R.J.Baker et al., Meas. Sci. Technol., **4**(1993)893
(3) M.Weiner and L.Silber, IEEE Trans. Magn., **17**(1981)1472
(4) S.Takano et al., NIFS-PROC-26(1996)115
(5) J.E.Dolan, Electronics Lett., **29**(1993)762
(6) E.M.Gyorgy, J. Appl. Phys., **28**(1957)1011

ENERGY LOSS MECHANISM BEFORE PINCH IN PLASMA FOCUS DISCHARGE

M.A.M. Kashani, T. Miyamoto, K. Sato, A. Baba, R. Horiuchi, K.Takasugi
College of Science and Technology, Nihon University, Kanda-Surugadai, Chiyoda-ku, Tokyo,
S. Sasaki
High Energy research Institute, Tokyo, Japan
M. Lu
Hebei University, China
and V. Vikhrev
Kurchatov Institute, Russia

Abstract

The energy loss processes in the Mather-type plasma focus discharge, especially in the phase before pinch, were studied. In the previous plasma focus experiment using two types of cathode electrode -- sixteen copper-bars arranged along the envelope of cylinder and a conventional cylindrical tube, the neutron yield at the optimum pressure was three times higher in the former cathode than in the latter. The reason resulted from that the energy loss was enhanced in the latter cathode.

1. Introduction

The hot, dense plasma produced in plasma focus emits intensive X-ray and also neutron fluxes when deuterium gas was used. In devices with medium discharge energy, the scaling law on the neutron yields versus discharge energy and/or maximum current holds independently of details of devices under an optimum condition[1], [2] . The optimum condition depends on the discharge voltage, the capacitance, the gas pressure and the electrode parameters. It is well known that the anode length and diameter are important parameters that determine the pinch time and the neutron yield. On the other hand, the cathode parameter has been considered to have only minor influence on the plasma focus. In our previous experiment[3], however, it was shown that the bar cathode gave larger neutron yield than the tubular one.

The optimum condition for each device is, to speak roughly, obtained by pinching the plasma in front of the anode at the phase near the current maximum, in other words, by concentrating the discharge energy in the pinch region. When the strong focus occurs, the

impedance of the pinch region extremely increases, and the circuit energy concentrates there. This is the reason why the scaling law holds independently of the details of devices. The scaling laws obtained so far, however, include some ambiguities. They base on the results of different devices, and give only roughly the tendency, which spread around the scaling laws. The results obtained in our previous experiments, that is, the cathode structure dependence, are masked in the scaling laws. The purpose of the present paper is to clarify the cathode effects in plasma focus discharges.

2. Summary of Previous Experiments

2.1 Experimental Setup

The experiment was carried out using the Mather–type plasma focus device (see Fig.1. The capacitor bank (22.5 μF) was fired at 25 kV. Two types of cathode electrode were used: (I) the cathode consisted of sixteen bars arranged cylindrically and (II) the cylindrical tubular cathode. The anode was 35 mm in diameter and 120 mm in length. The cathode was 80 mm in inner diameter and 80 mm in length. The current I and dI/dt were measured by Rogowskii coil. The neutron yield was measured by the silver activation type detector. The detector was calibrated using Am neutron source to obtain the absolute value.

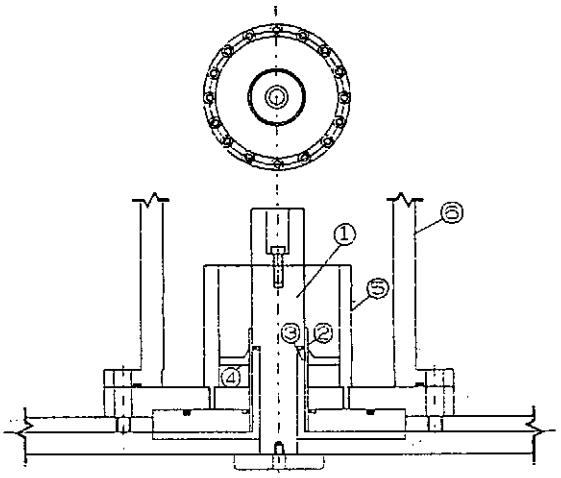

Figure 1. Schematic diagram of the device, ① Anode, ② Pyrex glass, ③ Polyethylene, ④ One part of Cathode, ⑤ Cathode and ⑥ Vacuum Chamber

2.2 Experimental Results

The typical signals of I and dI/dt are shown in Fig.2. The neutron yields versus filling pressure are given for both types of cathodes in Fig.3. Table 1 shows discharge parameters in the case that the anode was artificially short-circuited by a copper plate placed on the top of the cathode. The current reaches its maximum I_m at t_m, and $T_{1/4}$, L and R are the quarter period, the inductance and the resistance in this short-circuited discharge, respectively. When the circuit resistance is assumed to be zero, the maximum current should reach I_0. The discharge parameters for the focus discharge optimized by neutron yield are displayed in Table 2. The experimental results are summarized as the following:

(1) The neutron yield is higher in the bar cathode than in the tubular one.
(2) The short-circuited current is lower in the former.
(3) In spite of it, the maximum current in focus discharge (the current just before pinch) is higher in the former.
(4) The optimum pressure is higher in the former.

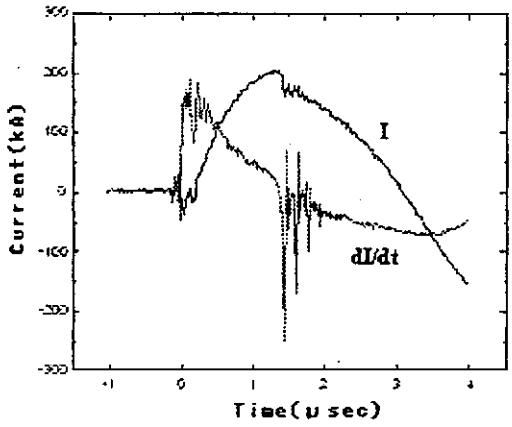

Fig.2 Typical current I and dI/dt signal in the bar cathode

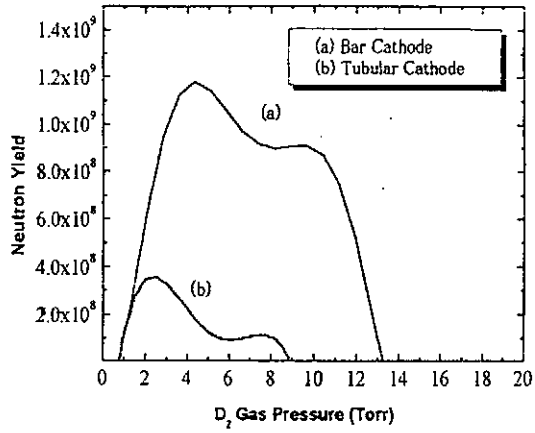

Fig.3 Neutron Yield vs. Gas pressure

Table 1. The discharge parameters at each optimum condition

Short-Circuited at Top of Anode	W (kJ)	U_0 (kV)	C (μ F)	I_m (kA)	I_0 (kA)	t_m (μ S)	$T_{1/4}$ (μ S)	L (nH)	R (m Ω)
Tubular Cathode	7.03	25	22.5	350	636	1.35	1.39	34.8	30.7
Bar Cathode	7.03	25	22.5	321	543	1.57	1.62	47.7	31.9

The inductances of discharge region in short-circuited discharge are given as

$$L_{Tubular} = \frac{\mu_0 \ell}{2\pi} \ln \frac{b}{a}$$

for the tubular cathode and

$$L_{Bar} \approx \frac{\mu_0 \ell}{2\pi} \left[\ln \frac{b}{a} + \frac{1}{N} \ln \frac{b}{d} - \frac{1}{2N} \left(\ln 2N + 3 \left(\frac{a}{b} \right)^{2N} - \cdots \right) \right]$$

for the bar cathode (see Appendix). They are 19.8 nH and 21.4 nH for the present

experimental parameter, respectively. This supports the above result (2). Zero inductance (when the cathode is connected to the anode at the bottom) is obtained subtracting this inductance of the discharge region from the short-circuited inductance of Table 1. The values derived by both tubular and bar cathodes should be the same with each other, but some discrepancy exists between them. This shows that the discharge was not carried out under completely same conditions. However, the discrepancy is too small to change the present considerations.

Table 2. The results of focus discharges at the optimum condition

Type	W(kJ)	U_0(kV)	C(μ F)	P (torr)	t_P (μs)	I_P(kA)	I_P/I_m	Yield Per shot
Tubular cathode	7.03	25	22.5	2.5	1.34	168	0.48	3.6×10^8
Bar cathode	7.03	25	22.5	4.5	1.62	211	0.67	1.2×10^9

The facts (2) and (3) show that the maximum plasma current, just before the radial pinch starts, was lower in the tubular cathode than in the bar cathode, in spite that the maximum current in the short-circuited discharge in Table 1 is higher in the former. These facts mean that the energy loss in the phase preceding the pinch is considerably high in both case (the ratios of the maximum plasma current to the short-circuited current were 0.67 and 0.48) and that it is higher in the latter. Most of previous papers did not give this ratio explicitly except the paper that gave the ratio $I_p / I_m = 0.44$ for the tubular cathode[4]. This ratio is consistent with the present results given in Table 2. The facts (1) - (3) show that the neutron yield does not correlate with the maximum short-circuited current or the bank energy, but with the plasma current just before pinch. The fact (4) means that high initial pressure in the bar cathode corresponds to low one of the tubular cathode, if a similarity holds between them.

3. Discussions

We are interested in why the energy is dissipated intensively in the phase traveling around the anode along the axis and also much more intensively in the tubular cathode, and why the optimum pressure is higher in the bar cathode. The ratios of the maximum plasma current to the short-circuited current give a measure of energy loss. We can consider that the inductance in the short-circuited discharge is

nearly same with that before pinch in the present case. When we suppose that all capacitor energy is concentrated on the circuit (or the inductance), the ratios of the energies lost before pinch to that of the short-circuited discharge result in about 0.23 for the tubular cathode and 0.45 for the bar one from Table 2. The ratios of the energy lost before pinch to the bank energy (the square of I_p/I_0) are about 0.070 (that corresponds to 0.49 kJ) for the tubular cathode and 0.15 (that corresponds to 1.1 kJ). Surprisingly most bank energy was lost before pinch in both cases. Especially, it is only about 0.5 kJ that contributed to plasma focus in the tubular cathode. It will be important to diminish this loss in order to improve the capability of plasma focus devices. The scaling law shows that neutron yield is nearly proportional to the square of the discharge energy. This means that the neutron yield increases to about 200 times in the tubular cathode, if no energy was lost before pinch.

Figure 4 shows a typical picture in the traveling phase that was obtained for the tubular cathode on the bases of the ideal MHD simulation. This picture shows that most gas around the anode is compressed to the inner surface of cathode after ionized and heated, and that the plasma contacts to the cathode in wide region. The energy to heat all the gas between the anode and the cathode to 10 eV is about or less than 100 Joule. Hence, most energy would be lost due to thermal conduction or due to ablation of the surface material of electrodes. The dissipation depends on resistance for a fixed total current. It seems that the increasing contact area makes the resistance (and the current density) decrease. However, the plasma temperature decreases in low current density, that is, the resistivity increases. The thickness of low temperature plasma near the cathode increases with decreasing current density. For the fixed total current, the increasing contact area does not necessarily make the resistivity decrease, but rather increase in some conditions.

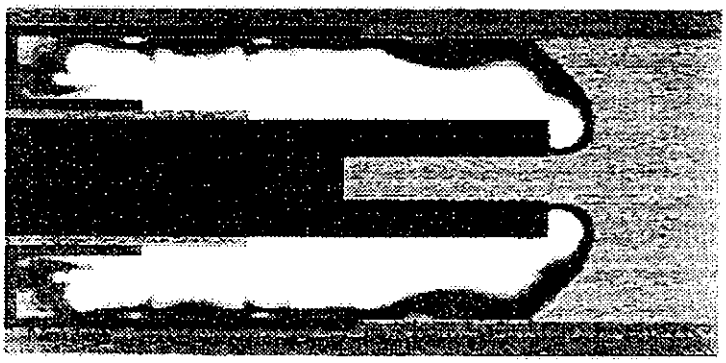

Fig. 4 Typical picture of the plasma motion obtained in the simulation based on the ideal MHD.

In the plasma sheet compressed near the cathode, the joule heating and the thermal conduction are estimated as

$$\eta i^2 = \bar{\eta} T^{-3/2} i^2 \sim \bar{\eta} T_{out}^{-3/2} i^2 \quad ,$$

$$\left| \frac{1}{r} \frac{\partial}{\partial r} r \kappa \frac{\partial T}{\partial r} \right| = \bar{\kappa} \left| \frac{1}{r} \frac{\partial}{\partial r} r n T^{5/2} \frac{\partial T}{\partial r} \right| \sim \bar{\kappa} n \frac{T_{in}^{7/2} - T_{out}^{7/2}}{\delta^2} \sim \bar{\kappa} n \frac{T_{in}^{7/2}}{\delta^2} \quad ,$$

where η $(= \bar{\eta} T^{-3/2})$, κ $(= \bar{\kappa} n T^{5/2})$, T_{in}, $T_{out} (<< T_{in})$, n and δ are the resistivity, the thermal conductivity, the temperatures of plasma sheet at both anode and cathode sides, the characteristic density and thickness of the sheet. In the quasi-steady state where the joule heating nearly equals the thermal conduction loss, we obtain the relation

$$(\frac{I\delta}{S})^2 \sim (i\delta)^2 \sim \frac{\bar{\kappa}}{\bar{\eta}} n T_{in}^{7/2} T_{out}^{3/2} \quad .$$

Therefore, the total dissipated energy is estimated as

$$RI^2 \approx \int \eta i^2 dV \sim \bar{\eta} \frac{\delta}{S} \frac{I^2}{T_{out}^{3/2}} \sim \bar{\kappa} \frac{S}{\delta} n T_{in}^{7/2} \quad .$$

This means that the total dissipated energy increases with the contact area and the density, if $Tin^{7/2}/\delta$ does not decrease so much.

No simulation was carried out for the bar cathode. We can expect that the plasma escapes through between bars on the way moving along the axis in this case. The plasma moves to the tip of anode, forming a thin sheet. Most current flows through this plasma sheet. The contact area and the plasma density near the cathode are smaller. As a result, the energy dissipation will be smaller in the bar cathode than in the tubular cathode.

When the contact area decreases extremely, however, the dissipation will increase as the ablation become dominate. As an example, we can cite the conventional anode structure of focus devices. The hole is bored at the tip of the anode in plasma focus devices to avoid the current concentration that ablates anode material from its surface, and that decreases neutron yield (see Fig 1). In order to minimize the dissipation, it is necessary to understand the interaction between plasma and electrodes.

4. Conclusions

The experimental result that the energy dissipation is lower in the bar cathode than in the tubular cathode is interpreted as the following:

(1) The dissipated energy increases with the contact area between the plasma and the cathode, and with the plasma density near the cathode.

(2) Both contact area and density are considerably smaller in the bar cathode than in the tubular cathode.

(3) This results from the fact that the plasma can escape through between the bars in the former.

(4) The result that the optimum pressure is higher in the bar cathode suggests the existence of escaping plasma, and seems to support the above considerations.

It is crucially important for improving the capability of a plasma focus device to decrease dissipation during the phase moving around the anode. If we eliminate this dissipation in a device with tubular cathode, we make the neutron yield increase more than an order.

On the basis of the experimental results in Sec.2 and the discussion in Sec.3, we conclude the following general guiding principles for improving plasma focus devices.

(1) To adapt electrode structures, such as the bar electrode, that decreases the energy dissipation. Especially, the cathode structure is important, because the plasma accumulates near the cathode.

(2) To decrease the length of electrodes for decreasing the interaction between the plasma and electrodes.

(3) To increase the optimum pressure without spoiling uniformity of discharge. Higher optimum pressure permits to decrease the electrode length.

(4) To increase the discharge voltage because of the same reason with (3).

(5) To decrease the resistance floating in the discharge circuit except the discharge region.

The number of bars, cathode length and diameter will also have some effects. It may also be useful to adapt a bar anode. The bar anode will hardly affect the energy dissipation before pinch (see Fig.4). However, the bar anode makes the plasma density on the anode surface decrease. In addition, the inductance between the anode and cathode decreases if the plasma escaped between the anode bars changes the path of return current to the vicinity of anode. As a result, they will be able to enhance the focus.

References

(1) L.Michel, K.H.Schonbach and H.Fisher, Appl. Phys. Lett. **24**, 57 (1974).

(2) H.Herold, A.Jerzykiewicz, M.Sadowski and H.Schmidt, Nucl. Fusion **29**, 1255 (1989).

(3) M.A.M.Kashani, K.Sato., T.Miyamoto, A.Baba, R.Horiuch, K.Takasugi, S.Sasaki, M.Lu and V.Vikhrev, Proc. of Int. Symp. On Pulsed Power and Plasma Applications (ISPP-2000), (Oct. 26, 2000 in Korea) p.243.

(4) B.H.Fishbine, J.W.Mather and D.W.Woodall, Phys. Fluid **B4**(10), 3344 (1992).

Appendix

The inductance of tubular cathode is easily given approximately by

$$L_{Tubular} = \frac{\mu_0 \ell}{2\pi} \ln \frac{b}{a}$$

where a, b and ℓ are the anode radius, the cathode radius and the length of anode. On the other hand, the inductance of bar cathode is a little troublesome.

The vector potential of a bar-cathode array consisted of N bars arranged with the angle $2\pi/N$ on the cylindrical surface of radius b is given by

$$A_b = \sum_{\nu=1}^{N} A_\nu = \frac{\mu_0 I_1}{4\pi} \sum_{\nu=1}^{N} \log\left[r^2 + b^2 - 2br\cos\left\{ \theta - \frac{2\pi\nu}{N} \right\} \right]$$

$$= \frac{\mu_0 I_1}{4\pi} \log\left[r^{2N} + b^{2N} - 2b^N r^N \cos N\theta \right]$$

$$= \begin{cases} \dfrac{\mu_0 I}{2\pi}\left[\log b - \displaystyle\sum_{n=1}^{\infty} \frac{1}{nN}\left(\frac{r}{b}\right)^{nN} \cos nN\theta \right] & \text{for } r < b \\ \dfrac{\mu_0 I}{2\pi}\left[\log r - \displaystyle\sum_{n=1}^{\infty} \frac{1}{nN}\left(\frac{b}{r}\right)^{nN} \cos nN\theta \right] & \text{for } r > b \end{cases}$$

where $I = NI_1$ is the total current. We have to add the contribution A_a of anode to the vector potential, and that A_{image} of image current obtained from the condition that the field should not exist inside of the anode

$$A_a = -\frac{\mu_0 I}{2\pi} \log r \quad \text{for} \quad r > a$$

$$A_{image} = \frac{\mu_0 I}{2\pi} \sum_{n=1}^{\infty} \frac{1}{nN}\left(\frac{a}{b}\right)^{nN}\left(\frac{a}{r}\right)^{nN} \cos nN\theta \qquad \text{for} \quad r > a^2/b$$

Thus, we obtain as the inductance of bar cathode configuration

$$A_{Bars} = A_b + A_{anode} + A_{image}$$

$$= \begin{cases} \dfrac{\mu_0 I}{2\pi}\left[\log\dfrac{b}{r} - \displaystyle\sum_{n=1}^{\infty} \frac{1}{nN}\left(\frac{r}{b}\right)^{nN} \left\{ 1 - \left(\frac{a}{r}\right)^{2nN} \right\} \cos nN\theta \right] & \text{for } a < r < b \\ -\dfrac{\mu_0 I}{2\pi} \displaystyle\sum_{n=1}^{\infty} \frac{1}{nN}\left(\frac{b}{r}\right)^{nN} \left\{ 1 - \left(\frac{a}{b}\right)^{2nN} \right\} \cos nN\theta & \text{for } r > b \end{cases}$$

The magnetic field is easily derived from $(B_r, B_\theta) = ((1/r)\partial A_{Bar}/\partial\theta,\ -\partial A_{Bar}/\partial r)$.

Integration of magnetic energy over whole space naturally diverges. The magnetic energy inside all bars is subtracted from this integration. We approximate it at the energy generated inside tube of radius d by a solitary straight wire. Then, the inductance of this system is approximated as

$$L_{Bar} = \frac{1}{I^2}\int \frac{B^2}{\mu_0} r dr d\theta dz$$

$$\approx \frac{\ell}{\mu_0 I^2}\lim_{\delta\to 0}\left[\int_a^{b-\delta} r dr \int_0^{2\pi} B^2 d\theta + \int_{b+\delta}^{\infty} r dr \int_0^{2\pi} B^2 d\theta - 2\pi N \int_{\delta}^{d}\left(\frac{\mu_0 I}{2\pi r N}\right)^2 r dr\right] .$$

After lengthy calculation, we obtain

$$L_{Bar} \approx \frac{\mu_0 \ell}{2\pi}\left[\ln\frac{b}{a} + \frac{1}{N}\ln\frac{b}{d} - \frac{1}{2N}\left(\ln 2N + 3\left(\frac{a}{b}\right)^{2N} - \cdots\right)\right] .$$

CHARACTERITICS OF ION BEAMS PRODUCED IN A PLASMA FOCUS DEVICE

K. Takao, M. Shiotani, S. Hirata and K. Masugata

Faculty of Engineering, Toyama University, 3190, Gofuku, Toyama 930-8555, Japan.

ABSTRACT

The characteristics of the nitrogen ion beam produced in a plasma focus device have been studied experimentally to apply the beam to material processing. In this application, the purity of the ion beam is very important. To clarify the mechanism of the production of impurity ions, two types of anode (rod type: type A, hollow type: type B) were used. In the experiment, a Mather type plasma focus device was used with a capacitor bank of 43.2μF. The bank was charged to 30 kV giving peak discharge current of 550 kA. To produce nitrogen ions, the device was pre-filled with N_2 at 5.5 Pa. Ion species and their energy spectra were evaluated using a Thomson parabola spectrometer (TPS). With type B anode, we have obtained a nitrogen ion beam of 90.5 %, whereas with type A anode the purity was 26.5 % and copper ion was observed as impurity.

I. Introduction

Plasma focus devices are known to produce high-energy, highly bright pulsed ion beams with energy of more than 1MeV[1]. Basically, ion species of the beam depend on the pre-filled gas. Therefore, the choices of the ion specie will be extended widely, and they are useful as a pulsed ion beam source.

The ion beams produced in the plasma focus device have been applied to material processing[2), 3)], and expected to be applied to a semiconductor process to implant dopant ions. When pulsed ion beams are applied to semiconductors, a high degree of purity of the ion beam is especially needed.

Pulsed ion beams produced in a plasma focus contain impurity ions[1), 4)]. These impurity ions seem to originate from the gas adhered on the electrodes. However, the physical mechanism of the production of these ions remains unclear.

In this study, we have evaluated the dependence of ion beam characteristics on the electrode shape to produce pure ion beams. Two- types of anode (rod type: type A, hollow type: type B) were used. Ion beams were measured by using an ion pinhole imaging system, a Thomson parabola spectrometer, and a biased ion collector. Pinhole images, ion current densities, energy spectra, and ion composition ratios have been compared on both of anodes.

II. Experimental apparatus

A. Plasma focus device

Figure 1 shows a schematic of the experimental system. The electrode chamber and the analyzer chamber were separated by a partition plate, which had a pinhole for introducing ions. In the experiment, we used a Mather-type plasma focus device. The device was operated by a capacitor bank of 43.2 μF. The charging voltage of the capacitor bank was 30 kV. The electrode chamber was evacuated below 1.5 x 10^{-3} Pa, and pre-filled with N_2 at 5.5 Pa to produce nitrogen ion beams. On the other hand, the analyzer chamber was differentially pumped to 1.0 x 10^{-3} Pa.

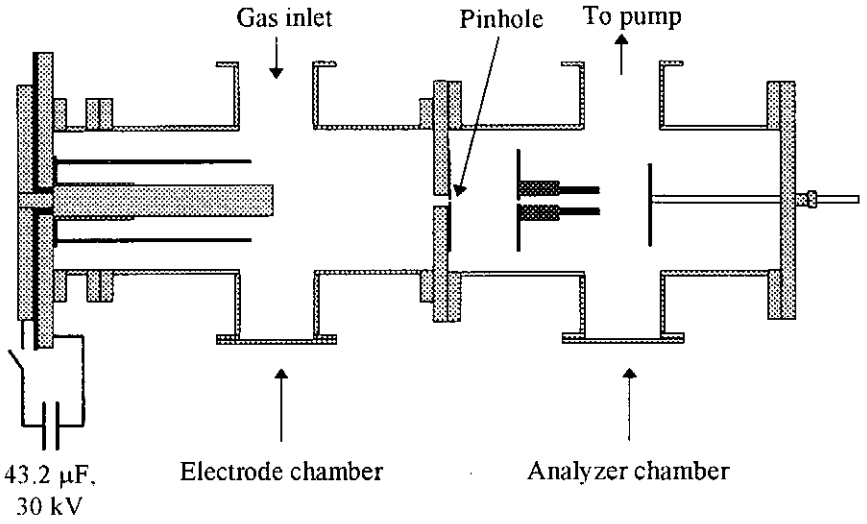

Fig. 1 Schematic of the experimental system.

B. Electrode

We used two-types of inner electrodes (anode) to evaluate the influence of the anode shape on the characteristics of ion beams. Figure 2 shows schematics of the top of anodes. Type A is a rod type. It has a rod of 14 mm in diameter and 13 mm in length on the hemispherical shape anode. This shape is expected to be enhanced the stability of the position of the focused plasma. Type B is a hollow type, and has a hollow of 40 mm in diameter and 20 mm in depth on the top of the electrode. The length and diameter of both anodes are 280 mm and 50 mm, respectively. The outer electrode (cathode) is squirrel-cage type and the length and the diameter are 250 mm and 100 mm, respectively.

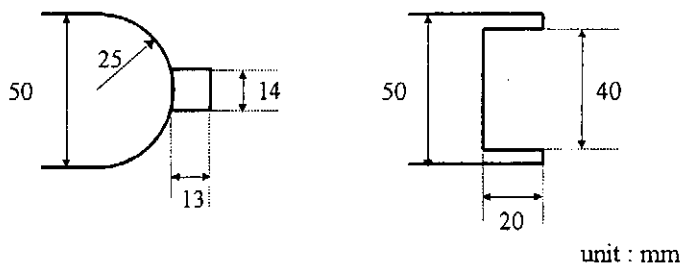

Type A (Rod type) Type B (Hollow type)

Fig. 2 Schematics of the top of anode.

C. Measurements

The biased ion collector (BIC) was used to measure the current density of the ion beams. The electrode of the BIC was made of brass, 45 mm in inner diameter and 40 mm in depth, and installed just behind the pinhole. Therefore, the BIC measured the ion current density at z = 218 mm from the top of the anode. As ion beams were neutralized, the BIC was biased at −1 kV to eliminate electrons.

The ion pinhole imaging system was used to obtain the radial distribution of ions and to evaluate the production pattern of the ion beams. We used the CR-39 track detector as an ion detector. The CR-39 was placed 100 mm downstream from a pinhole.

The Thomson parabola spectrometer (TPS) was used to measure ion species and their energy spectra. Figure 3 shows the schematic of the Thomson parabola spectrometer. It is constructed of a first pinhole, a second pinhole, a magnetic deflector, an electric deflector, and the CR-39. The diameters of the first and second pinholes were 0.21 and 0.1 mm, respectively. The ions irradiated onto the first pinhole (located on the electrode axis) are collimated and led into the magnetic and electric deflectors. The magnetic deflector comprises soft-iron pieces and a permanent magnet. The size of the magnetic field and the gap length are 50 x 50 mm^2 and 10 mm, respectively. The electric deflector comprises two plane electrodes (electric field area, 50 x 70 mm^2, gap length, 10 mm). The applied magnetic and electric fields were 0.65 T and 10 kV / cm, respectively.

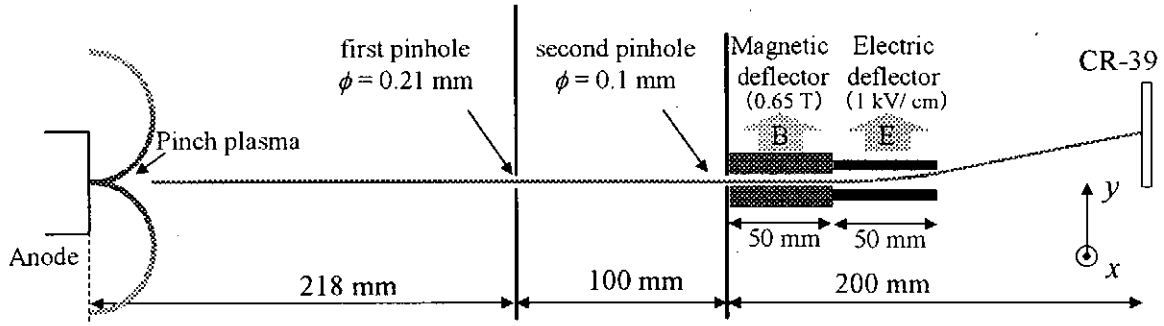

Fig. 3 Schematic of the Thomson parabola spectrometer

III. Results and Discussion

Figure 4 shows typical waveforms of the discharge current (I_d) and the ion current density (J_i). In type A anode, the discharge current reaches the peak value of 550 kA at 1.35 μs and drops to 400 kA at 1.6 μs suddenly. It suggests that the focused plasma is formed and collapsed within 250ns. J_i rises at 1.45 μs sharply and a peak value of 1150 A/cm^2 is observed with pulse width of 70 ns (FWHM). In type B anode, the discharge current reaches the peak value of 550 kA at 1.4 μs and drops to 450 kA at 1.65 μs. J_i rises at 1.5 μs sharply and the peak value of 900 A/cm^2 is observed with pulse width of 100 ns (FWHM). The difference of the pulse width between type A and type B seem to be due to the difference of the energy range (it will be showed later on) and affected by the time of flight effect.

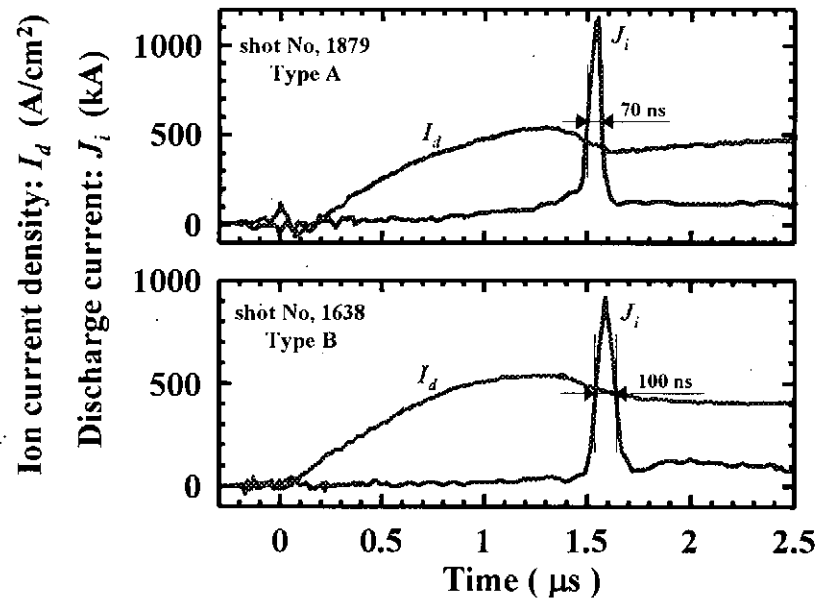

Fig. 4 Typical waveforms of the discharge current (I_d) and the ion current density (J_i).

Figure 5 shows typical pinhole image of ion beams. The scale written in the figures is converted at the top of the anode. As seen in the figures, production patterns are concentric circle type and contain small spots both of anodes.

Figure 6 shows the track pattern obtained using the TPS of type A (shot No. 1988). As seen in the figure, Cu^+, Cu^{2+}, O^+, N^+, C^+, O^{2+}, and N^{2+} were produced. We have not identified the trace next to Cu^{2+}, but it would be molecular ions. The energy range of nitrogen ion beams were distributed from 0.4 MeV to 0.15 MeV. On the other hand, the energy range of copper ion beams was distributed from 1 MeV to 0.5 MeV.

Figure 7 shows the energy spectrum of ion beams produced by type A anode (shot No. 1988). The vertical axis indicates the number of ions per unit energy (dE) per unit solid angle ($d\Omega$) at the second pinhole. In this case, dE is 0.1 MeV and $d\Omega$ is 7.85 x 10^{-7} Sr, respectively. As seen in the figure, N^+ and O^+ are almost same value at 0.2 MeV. On the other hand, the value of O^+ is larger than that of N^+ after 0.3 MeV. The values of C^+ are smaller than those of N^+ and O^+ at each energy. Values of doubly ionized ions of all ion species are less than those of singly ionized ions. The spectrum of Cu^+ has the peak value at 0.7 MeV. From fig. 7, an ion composition ratio for type A anode was estimated to be $N^{+,2+}$: $O^{+,2+}$: C^+: $Cu^{+,2+}$ = 26.5: 49.0: 12.5: 12.0 %.

Figure 8 shows the track pattern obtained with the TPS in case of type B anode (shot No. 1965). As seen in the figure, O^+, N^+, C^+, O^{2+}, N^{2+}, and N^{3+} were produced. However, oxygen and carbon ions were very low compared with type A anode, and copper ions were not observed. The energy range of nitrogen ion was distributed from 1 MeV to 0.2 MeV.

Figure 9 shows the energy spectrum of ion beams produced by the type B anode (shot No. 1965). As seen in the figure, the spectrum of N^+ has a peak around 0.4 and 0.5 MeV and decreases with increasing energy. On the other hand, the spectrum of N^{2+} monotonically decreases with increasing energy. The spectrum of N^{3+} is almost flat. The ion composition ratio

for type B anode was $N^{+,2+,3+}$: $O^{+,2+}$: $C^{+,2+}$ = 90.5: 7.8: 1.7 %. In type B anode, the production of nitrogen ion beams with high purity has been achieved.

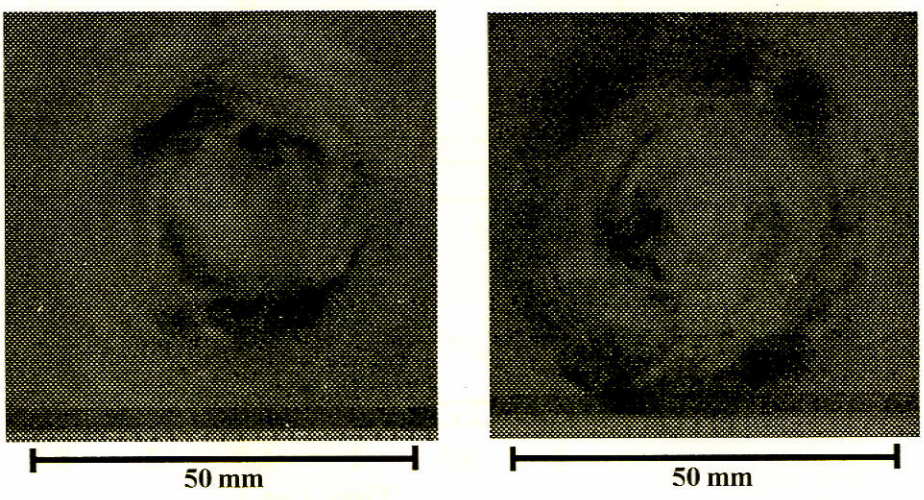

Fig. 5 Typical pinhole image of ion beams.

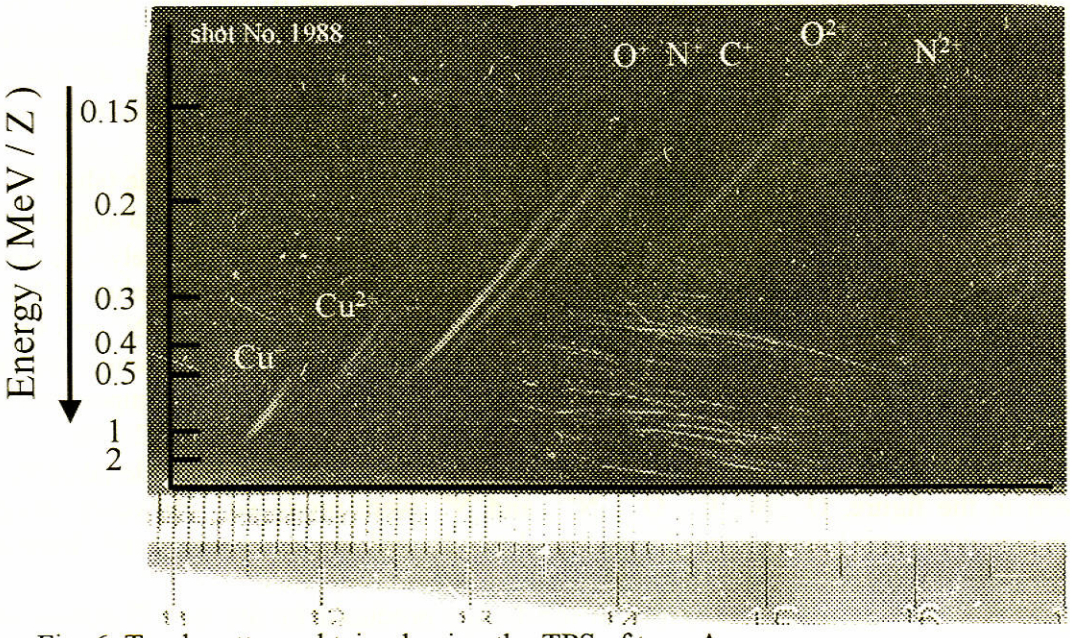

Fig. 6 Track pattern obtained using the TPS of type A.

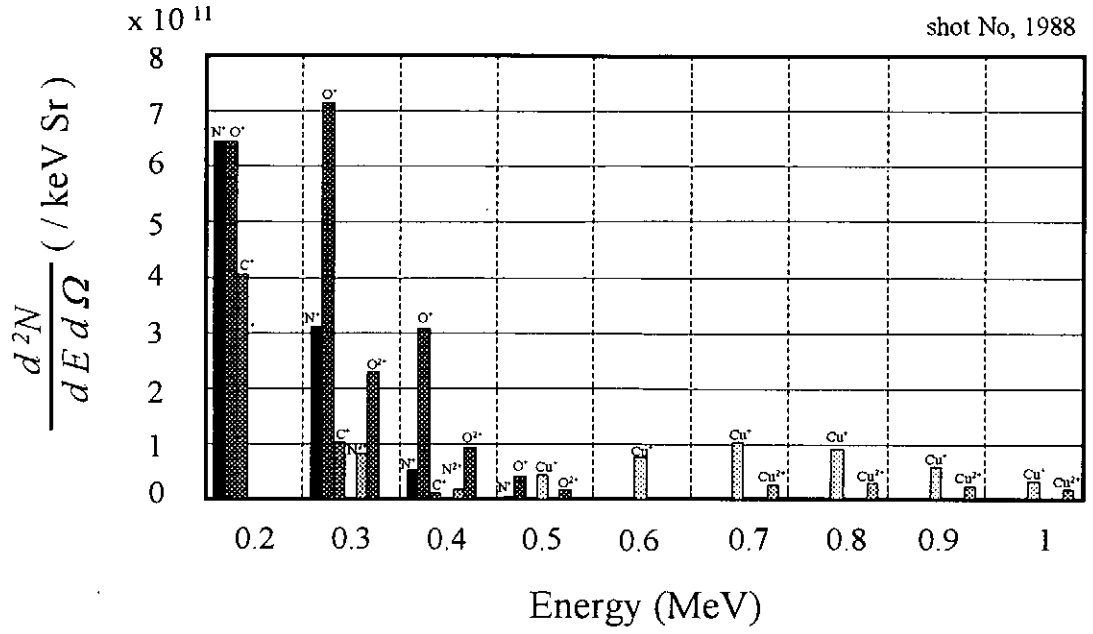

Fig. 7 Energy spectrum of ion beams produced by type A.

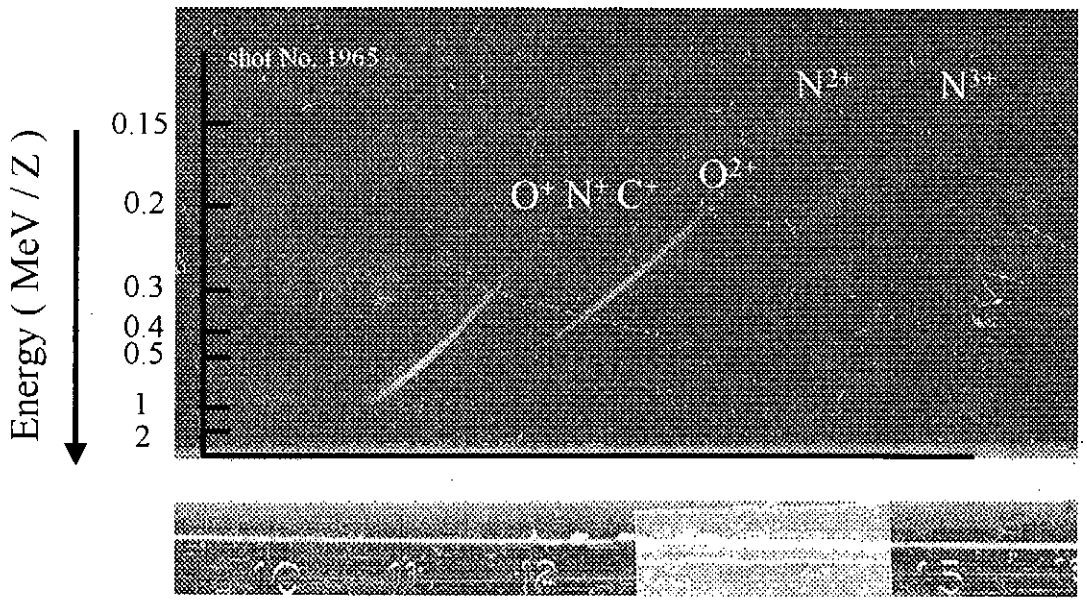

Fig. 8 Track pattern obtained using the TPS of type B.

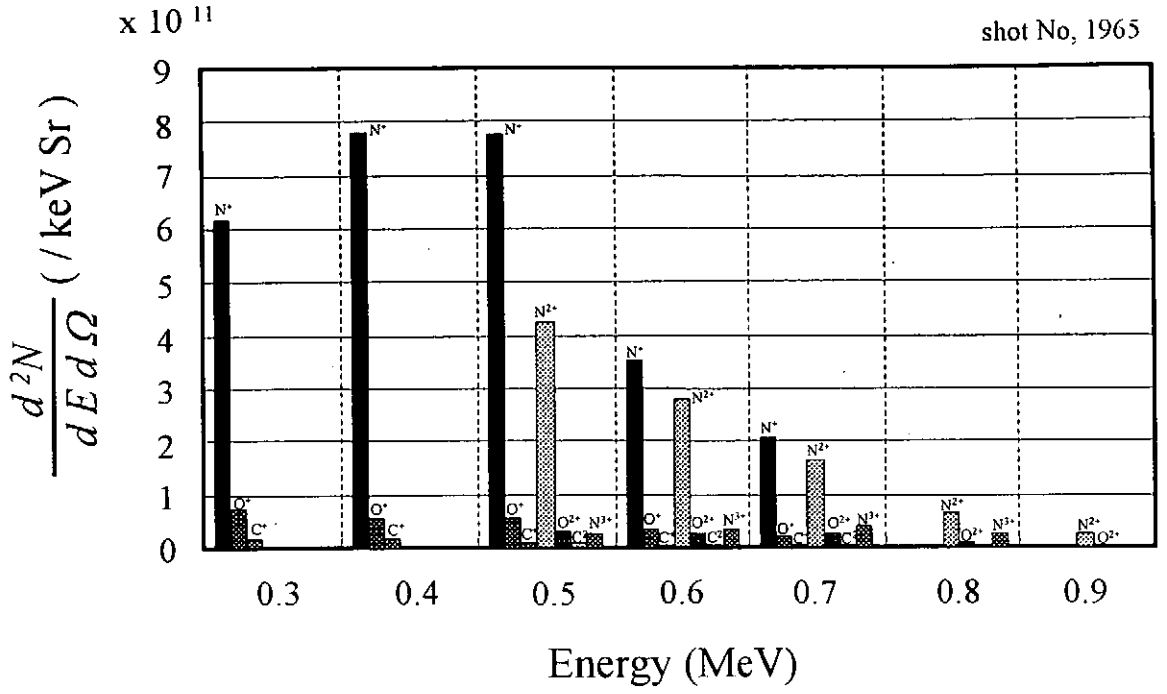

Fig. 9 Energy spectrum of ion beams produced by type B.

IV. Conclusion

The characteristics of the nitrogen ion beam produced in a plasma focus device have been studied experimentally to apply the beam to material processing. In this application, the purity of the ion beam is very important. To clarify the mechanism of the production of impurity ions, two types of anode (rod type: type A, hollow type: type B) were used. In the experiment, a Mather type plasma focus device was used with a capacitor bank of 43.2μF. The bank was charged to 30 kV giving peak discharge current of 550 kA. To produce nitrogen ions, the device was pre-filled with N_2 at 5.5 Pa. Ion species and their energy spectra were evaluated using a Thomson parabola spectrometer (TPS). With type B anode, we have obtained a nitrogen ion beam of 90.5 %, whereas with type A anode the purity was 26.5 % and copper ion was observed as impurity.

References

1) K. Takao, Y. Doi, S. Hirata, M. Shiotani, I. Kitamura, T. Takahashi, and K. Masugata: Jpn. J. Appl. Phys. **40** (2001) 1013
2) J. N. Feugeas, E. C. Llonch, C. O. de González, and G. Galambos: J. Appl. Phys. **64** (1988) 2648
3) H. Kelly, A. Lepone, A. Márquez, D. Lamas, and C. Oviedo: Plasma Sources Sci. Technol. **5** (1996) 704
4) H. Herold, A. Mozer, M. Sadowski, and H. Schmidt: Rev. Sci. Instrum. **52** (1981) 591

TIME RESOLVED MEASUREMENT OF SOFT X-RAYS GENERATED FROM PLASMA FOCUS DEVICE

H. Itano, N. Iwami, K. Shimoda and M. Sato

Department of Electronic Engineering, Gunma University,
1-5-1 Tenjin-cho, Kiryu, 376-8515, Japan

ABSTRACT

We newly constructed a small plasma focus device, and investigated the characteristics of it. Hydrogen gas was used as a working gas, and a small amount of neon gas was mixed to the working gas. A time-resolved X-ray pinhole camera was made, and was used to observe the pinched plasma. Several framing pictures of the soft X-ray images were obtained with the time-resolved X-ray pinhole camera, and one of them suggested occurrence of instability in the pinched plasma.

I. Introduction

The plasma focus device is well known as an inexpensive and compact source of intense soft X-rays. It has been used for number of applications: soft X-ray microscopy[1], soft X-ray lithography[2], X-ray backlighting for high-density plasmas[3]. The soft X-rays ranged from 2.33 to 4.37 nm (so-called water window) are required for the soft X-ray microscopy, because the soft X-rays ranged in these wavelengths are not absorbed by oxygen and are absorbed by carbon; those can be used to observe living cells. We tried generation of the soft X-rays ranged in these wavelengths by using a gas-puff Z-pinch device[4], but the intensities of the generated X-rays were very low. So we newly constructed a small plasma focus device as the soft X-ray source.

A time-resolved X-ray pinhole camera[5,6] usually consists of pinholes, a micro channel plate with strip lines and a camera. Pulsed high voltages of which pulse widths are approximately 1 nanosecond are applied to the strip lines. During the pulsed high voltages pass through the strip lines, pinhole images of soft X-rays on the strip lines are amplified and taken with the camera. This short shutter time is great advantage in investigations of the soft X-rays generated in the plasma focus device,

We newly constructed a small plasma focus device, and investigated the characteristics of it. Hydrogen gas was used as a working gas, and a small amount of neon gas was mixed to the working gas. A PIN diode, a convex crystal spectrometer, a streak camera were used to observe the pinched plasma. A time-resolved X-ray pinhole camera was made, and was used to observe the pinched plasma. Several framing pictures of the soft X-ray images were obtained with the time-resolved X-ray pinhole camera, and one of them suggested occurrence of instability in the pinched plasma. The results of preliminary experiments are presented in this paper.

II. Experimental Setup

Figures 1 show the schematic drawings of the experimental setup. Configuration of a plasma focus device and an external circuit are shown in Fig. 1 (a). The plasma focus device consists of an inner electrode, an outer electrode and an insulator. The outer electrode is

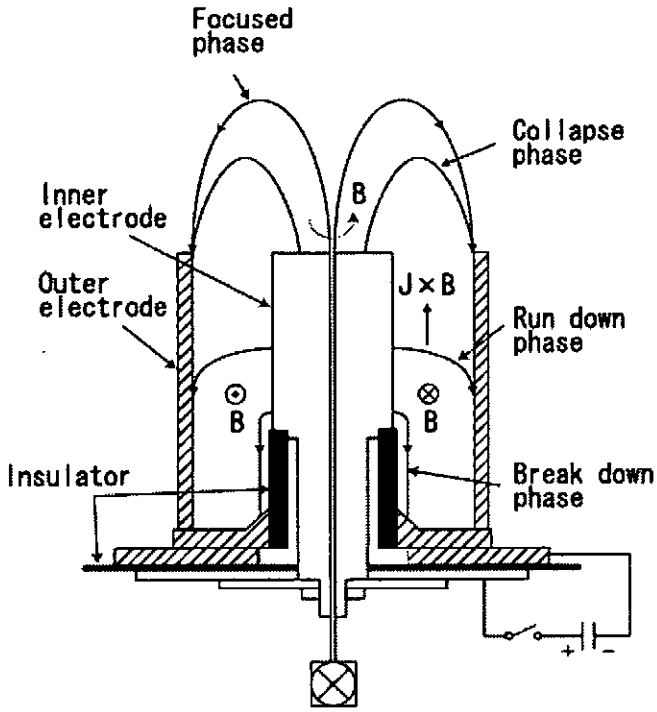

(a)

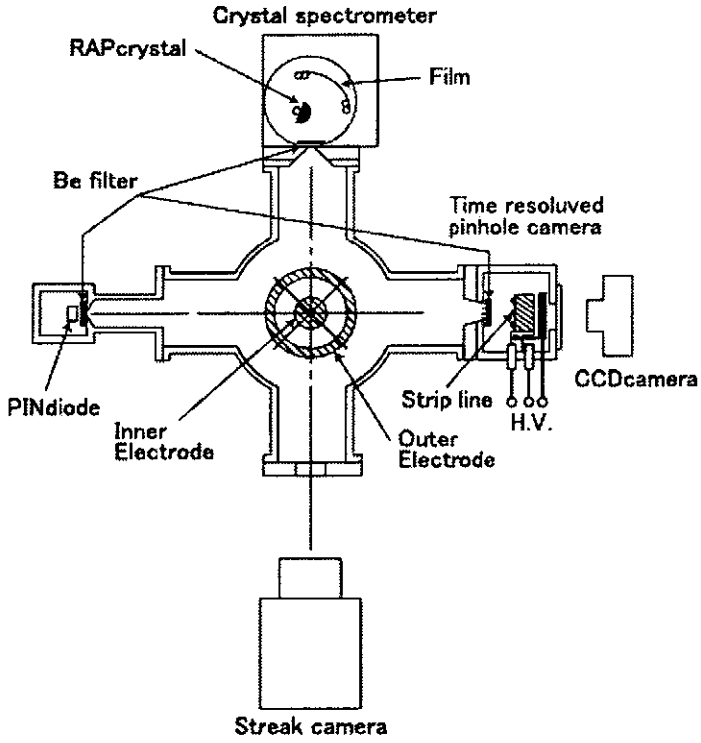

(b)

Fig. 1 Schematic drawings of experimental setup; configuration of plasma focus device (a), location of measurement tools (b).

constructed from 24-copper rods of which diameters are 8 mm; the geometry of the plasma focus device is like a square cage. The inner diameter of the outer electrode is 100 mm. In order to make discharge with gas-puff operation by a fast opening valve[6], a small hole is drilled along the centerline of the inner electrode. All the experiments reported here were performed without gas-puff operation by the fast opening valve. The outer diameter of the inner electrode is 50 mm. The lengths of the electrodes are 155 mm. The insulator is made of a Pyrex glass, and the outer diameter and the length of it are 55 and 51 mm, respectively. The maximum voltage and the maximum stored energy of a condenser bank are 30 kV and 25 kJ, respectively. In all the experiments reported here, the condenser bank was used with the charged voltage of 15 kV. Hydrogen gas was used as a working gas, and a small amount of argon or neon gas was mixed to the working gas.

In the experiments, a PIN diode, a crystal spectrometer, a streak camera (IMACON-700) and a time resolved X-ray pinhole camera were located as shown in Fig. 1 (b). The PIN diode was used to detect the soft X-rays, and appearance of its signal also suggested pinching of the plasma. In front of the PIN diode, the crystal spectrometer and a time resolved X-ray pinhole camera, the beryllium foils of which thickness were 20 micrometers were usually set as a filter. The crystal spectrometer consists of a slit, a convex rubidium acid phthalate (RbAP) crystal and a film (KODAK TRI-X). The spectrometer was used to analyze the wavelength of the soft X-rays, and its detail specification was reported in Ref. 7. A pinhole image by the soft X-rays was made on the film of the spectrometer. This image is usually used to calibrate the shits in wavelengths caused by change in the position of the pinched plasma. In our experiments the pinhole images were also used to verify the soft X-ray images obtained with the MCP which was operated in time-integrated mode.

Figure 2 shows the schematic drawing of a time resolved X-ray pinhole camera. This camera consists of a high voltage pulse generator, a micro channel plate (MCP) and a charge couple device (CCD) camera. The high voltage pulse generator is CPSS/1ns/N made by Kentech Instruments Ltd. in England, and the maximum value and the pulse width of the

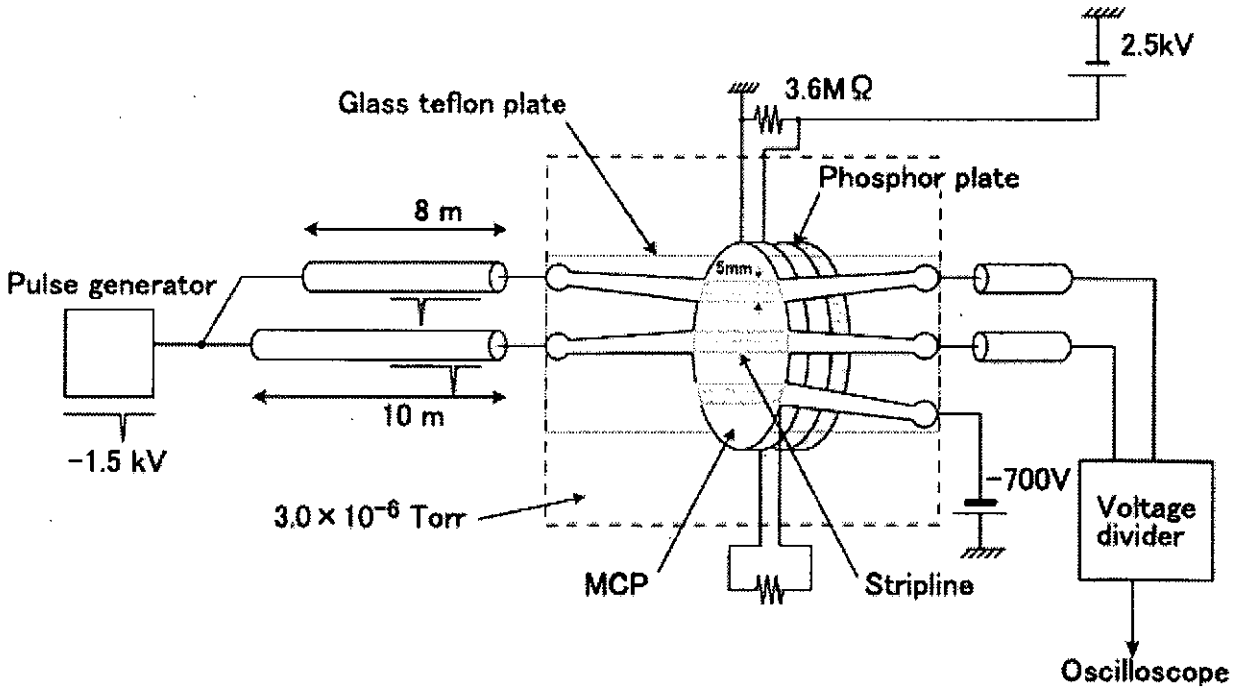

Fig. 2 Schematic drawing of time resolved X-ray pinhole camera with strip lines.

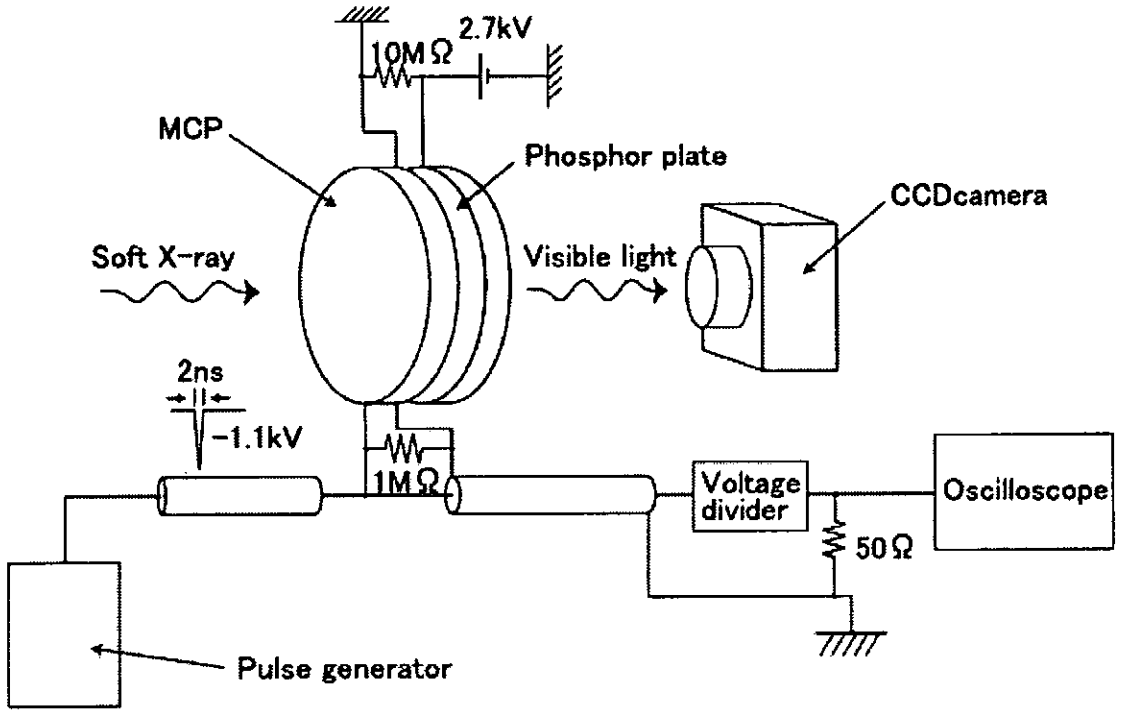

Fig. 3 Schematic drawing of time resolved X-ray pinhole camera.

output voltage are -1.5 kV and 1 ns, respectively. The pulsed voltage is divided in two 50 Ω coaxial cables, and put into the MCP. The delay time of 10 ns appears between the divided pulsed voltages, because the lengths of the two cables are 8 and 10 m, respectively. In front of the MCP, three strip lines are made, and are coated by gold to increase the sensitivity for the soft X-rays. Since the widths of the strip lines are 5 mm, the impedance is calculated by 20 Ω. In order to decrease reflection of the pulsed voltages, transmission lines from the wall of a vacuum chamber to the strip lines were made with taper shape. Two strip lines are used to time resolved observation of soft X-rays, and the other one is used to observe the time integrated image of soft X-rays. When the pulsed voltage pass through the strip line, the electrons generated by the soft X-rays are amplified and are accelerated to the phosphor plate. The visible images on the phosphor plate generated by bombardment of the accelerated electrons are taken with the CCD camera.

In the experiments, the high voltage of 2.5 kV was not able to apply between the MCP and the phosphor plate. The reason why the high voltage was not able to apply was due to the roughness on the surface of the phosphor plate. Therefore another time resolved X-ray pinhole camera was used in the experiments. The schematic drawing of this camera is shown in Fig. 3. This camera also consists of a high voltage pulse generator, a MCP and a CCD camera. This pulse generator was made in our laboratory, and the maximum value and the pulse width of the output voltage are -1.1 kV and 2 ns, respectively. Since this MCP has no strip line, one framing picture of a soft X-ray image is taken in time-resolved mode. When a high voltage of -700 V is applied to the MCP, one framing picture of a soft X-ray image is taken in time-integrated mode.

III. Experimental Result

The waveforms of a discharge current and the signal of the PIN diode are shown in Fig. 4. The waveforms shown in Fig. 4 were obtained by the experiment with 10 % admixture of

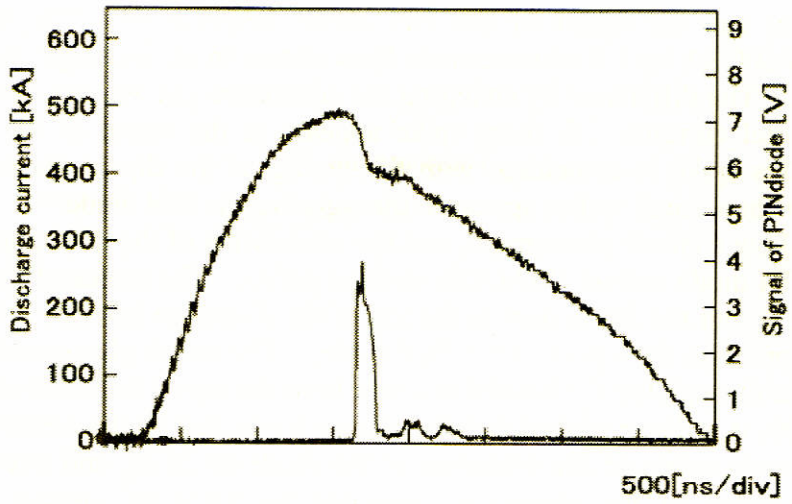

Fig. 4 Typical waveforms of discharge current and signal of PIN diode.

neon gas to hydrogen gas. The experiments were performed with changing the total gas pressure, and the maximum value of the signal of the PIN diode was obtained at the total gas pressure of 1.4 torr. Therefore the all experiments reported here were performed at the total gas pressure of 1.4 torr. In the figure, the upper and the lower trace correspond to the

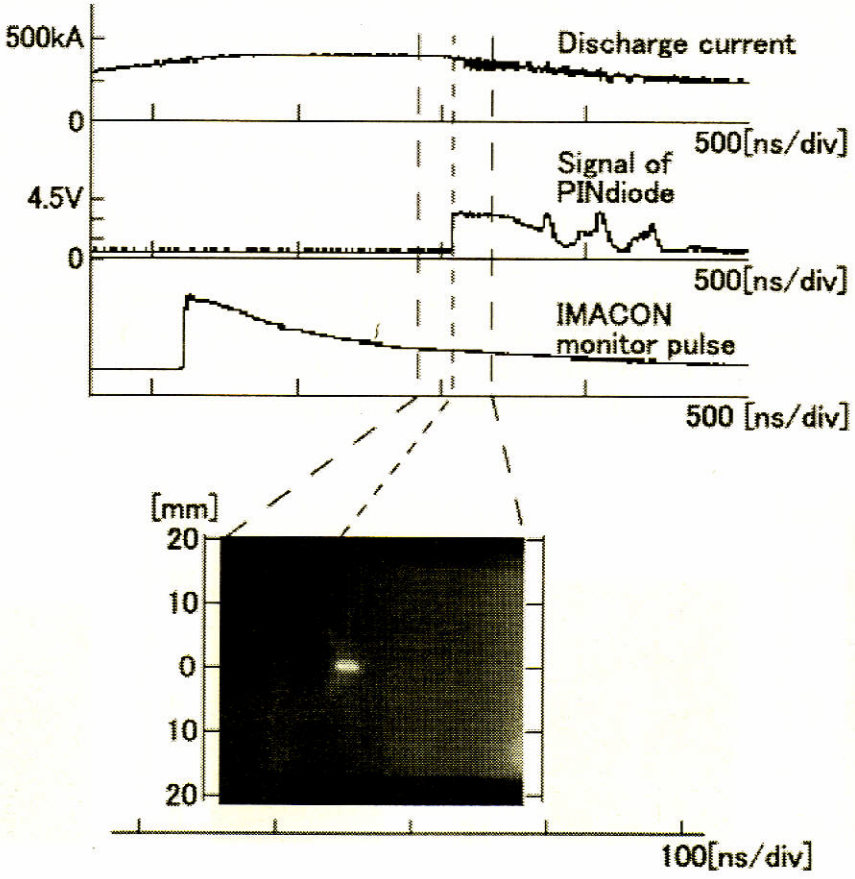

Fig. 5 Streak photograph and waveforms of the discharge current, and signals of PIN diode and IMACON monitor pulse.

discharge current and the signal of the PIN diode, respectively. The discharge current reaches to about 500 kA by 1.4 microseconds from initiation of discharge, and the dip is seen at the tops of it. The difference by changing the admixture gas was not distinguished in the signals of the total currents. A sharp spike appears in the signal of the PIN diode, and appearance of this spike is coincident with the timing of the dip in the discharge current. After that two or three small spikes appear in the signal of the PIN diode.

Figures 5 show a streak photograph, and the waveforms of the discharge current and the signals of the PIN diode and an IMACON monitor pulse. The scales of the waveforms are varied from Fig. 4, but the dip is seen at the top of the discharge current. At the same time, several spikes appear in the signal of the PIN diode. The streak photograph was taken with the streak camera through the slit located at 5 mm from the top of the inner electrode. In this streak photograph, it is distinguished that the plasma is pinched on the centerline of the diode. This pinched plasma exists on the centerline of the diode by 20 ns, and after that disappears. The pinched velocity of the plasma is estimated by 2.8×10^7 cm/sec from the streak photograph.

Pinhole photographs obtained in time-integrated mode are shown in Figs. 6. In Figs. 6 (a) and (b), the photographs shown in left side were taken with the film located in the crystal spectrometer. Another photographs were taken with the pinhole camera shown in Fig. 3. Figures 6 (a) and (b) were obtained by using 6 % admixture gas of neon and argon, respectively. Here the images shown in Figs. 6 (b) are slightly different; the numbers of the spot-like images are same, but the images tilt in opposite direction. The reason why the images tilt in opposite direction is caused by the difference in observation ports. As shown in Figs. 1 (b), the observation ports of the spectrometer and the pinhole camera are mounted in right angle. Therefore the images may tilt in opposite direction. In Figs. 6 (a) the soft X-ray images are cylindrical shape. On the other hand, the spot-like images are seen along the centerline of the diode in Figs. 6 (b). These features agree with the results reported in Ref. 3. In the pinhole photographs the bright areas also exist near the top of the inner electrode (I.E.). These areas may correspond to the electrode plasmas generated by bombardment of the pinched plasmas or high-energy electrons. From the results it is verified that the soft X-ray images are obtained with the pinhole camera shown in Fig. 3.

Figure 7 shows the line spectra obtained with the convex crystal spectrometer. These spectra were obtained by the experiments with 9 % admixture of neon gas to hydrogen gas, and the soft X-rays of the thirty-five shots were superimposed on the film. The three spectra

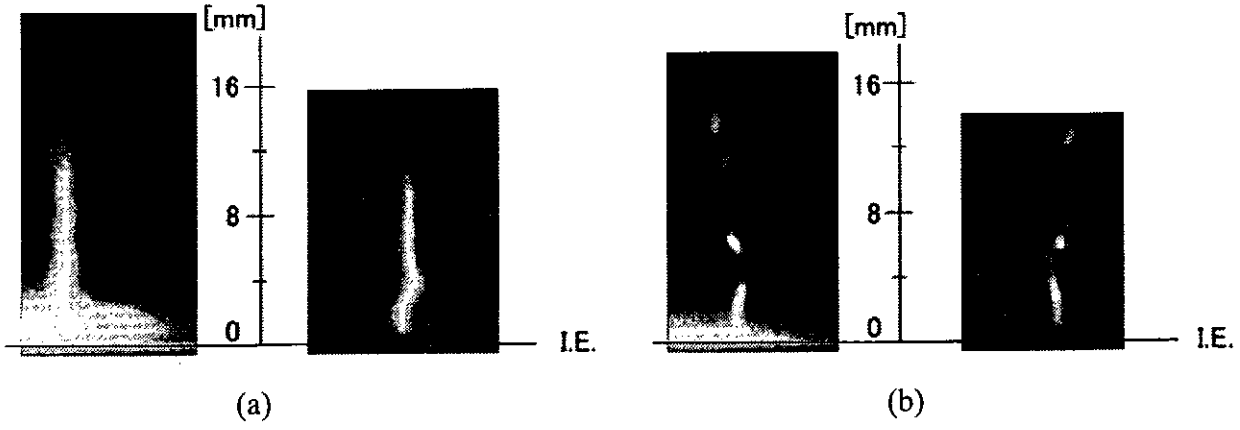

Fig. 6 Pinhole photographs obtained in time-integrated mode.

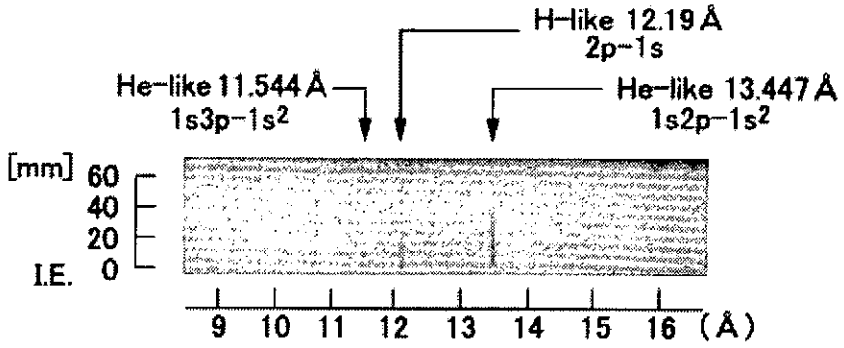

Fig. 7 Line spectra obtained with convex crystal spectrometer.

are distinguished in this figure, and its images expand from the top of the inner electrode along the centerline of the diode. The each spectrum corresponds the radiations by $1s3p\text{-}1s^2$ (11.544Å), 2p-1s (12.19Å) , $1s2p\text{-}1s^2$ (13.447Å). The number of the spectra reported in Ref. 7 was much larger than that obtained in our experiments. This result suggests that the electron temperature in our experiments might be relatively low. This fact is also verified that the spectra were not obtained in the case of argon gas; a higher electron temperature is required in K-shell radiation of argon gas. In order to make the plasma with higher electron temperature, we will try to the experiments with gas puff at the top of the inner electrode by the fast opening valve[6].

The three framing pictures of the soft X-ray images are shown in Figs. 8. These images were obtained by the experiments with 9 % admixture of neon gas to hydrogen gas. The waveforms are also shown in Figs. 8, and the upper and the lower traces correspond to the signals of the PIN diode and the attenuated pulsed voltage passed through the MCP, respectively. The time correlations of these traces show the times when the images are

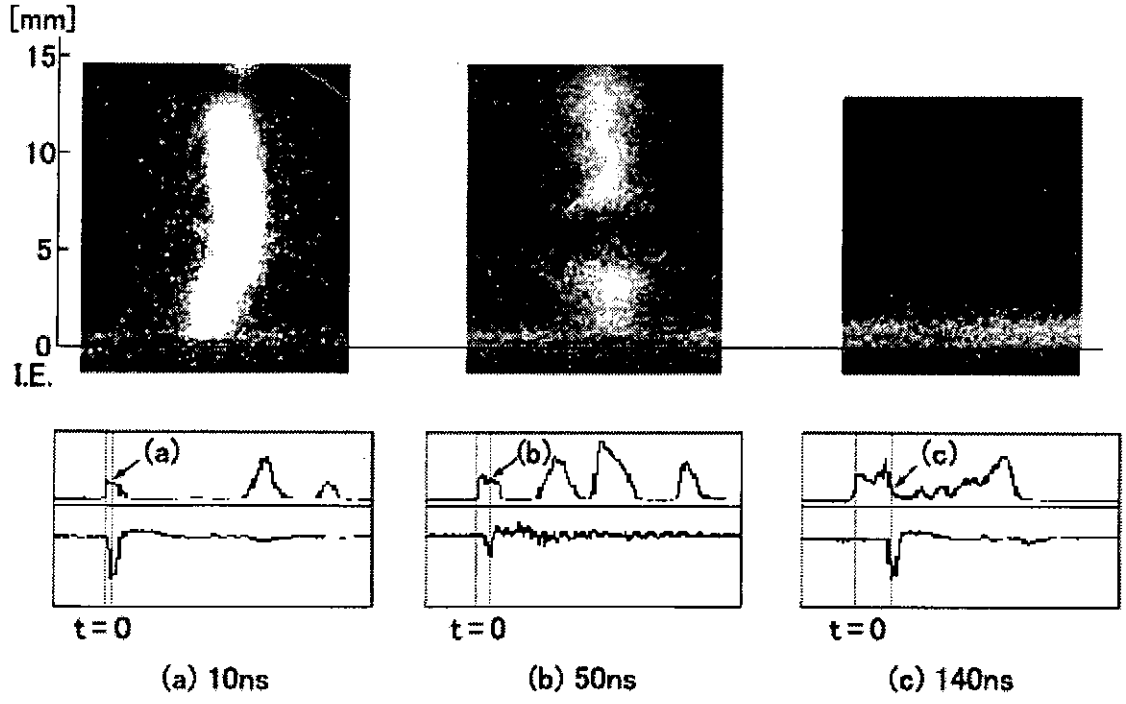

Fig. 8 Framing pictures of soft X-ray images obtained with the time-resolved pinhole camera.

taken. Since the origin of the time scale is defined as the onset of the signal of the PIN diode, each image is taken at 10, 50 and 140 ns. Although the time-resolved pinhole camera shown in Fig. 3 is able to take one framing picture in a shot, typical images are collected from several shots in Figs. 8. The image shown in Fig. 8 (a) is taken just after pinching, and the bright area is cylindrical shape. In Fig. 8 (b) the bright area in the image breaks into two areas. This result means occurrence of instability in the pinched plasma, and is only obtained by time-resolved measurement. The bright area is not seen along the centerline of the diode in the image shown in Fig. 8 (c), but expands near the top of the inner electrode. This bright area may correspond to the electrode plasma generated by bombardment of the pinched plasmas or high-energy electrons. In these images the thickness of the electrode plasma become thick with progress in time. This fact means that expansion of the electrode plasma is verified graphically by time-resolved measurement.

IV. Summary

We newly constructed a small plasma focus device, and investigated the characteristics of it. Hydrogen gas was used as a working gas, and a small amount of neon gas was mixed to the working gas. By measurement with the PIN diode and the streak camera, pinching of the plasma was verified. Three line spectra were distinguished by the image obtained with the convex crystal spectrometer. The time-resolved X-ray pinhole camera was made, and was used to observe the pinched plasma. Several framing pictures of the soft X-ray images were obtained with the time-resolved X-ray pinhole camera, and one of them suggested occurrence of instability in the pinched plasma. Adjustment of the time-resolved X-ray pinhole camera with the strip lines is under going, so two framing pictures in a shot will be obtained in a short time.

References

1) M. Howells, J. Kirz and D. Sayre, Sci. Am., **264** (1991) 42.
2) Y. Kato, I. Ochiai, Y. Watanabe and S. Murayama, J. Vac. Sci. Technol., **B6** (1988) 195.
3) F. Beg, I. Ross, A. Lorenz, J. Worley, A. Dangor and M. Haines, J. Appl. Phys., **88** (2000) 3225.
4) H. Maeda, K. Shimoda and M. Sato, NIFS-PROC-45 (2000) 58.
5) B. Shan, T. Yanagidaira, K. Shimoda and K. Hirano, Rev. Sci. Instrum., **70** (1999) 117.
6) P. Röwekamp, G. Decker, W. Kies, B. Lucas, F. Schmitz, G. Ziethen, D. Simanovskii and S. Bobashev, Proc. 11th Int. Conf. High Power Particle Beams, Prague, (1996) 174.
7) T. Yanagidaira, K. Shimoda, Y. Ono and K. Hirano, Rev. Sci. Instrum., **71** (2000) 88.

IMPLODING PROCESS AND X-RAY EMISSION OF SHOTGUN Z-PINCH PLASMA

Ryusuke Muto,[+] Keiichi Takasugi, and Tetsu Miyamoto

Atomic Energy Research Institute, Nihon University
[+]College of Science and Technology, Nihon University

ABSTRACT

Rayleigh-Taylor instability was observed on the surface of a contracting z-pinch plasma. Wavelength of the instability was analyzed from the envelope of the profile, and it increased with implosion. Analysis with finite Larmor radius effect shows that there is some acceleration of ions during the contraction process. A suggestion to obtain macroscopically uniform plasma is to increase plasma current without heating the plasma.

I. Introduction

The achievement of uniform implosion of z-pinch plasma is a key feature to z-pinch driven inertial confinement fusion rsearch. The uniform formation of hot spots is essential for the efficient and uniform radiation of x-ray. However, as z-pinch plasma is naturally unstable to MHD modes, it is a difficult objective to avoid instability. In the previous experiments it is pointed out that the formation of hot spots has a good correlation to the instability pattern that develops in the contraction [1 – 4]. Although the instability is unavoidable, we will be able to control the occurrence of hot spots if we find a method of controling the instability.

Here we investigated the development of Rayleigh-Taylor instability in the contraction phase of the SHOTGUN z-pinch plasma. Using a laser shadowgraphy a clear image of plasma envelope was obtained. The spatial profile of the instability was analyzed, and change of wavelength of the instability with implosion was observed.

II. Experimental Setup

Figure 1 shows the schematic view of the SHOTGUN gas-puff z-pinch device. The main storage section consists of high-speed capacitor bank of 24 μF (25kV, 7.5kJ). The gap width of the electrodes is 30 mm. Both electrodes are made of Al. A hollow gas distribution is intended to form between the electrodes using a hollow nozzle on the anode with a high speed gas valve. The diameter of the nozzle is 28 mm. Ar gas is used in this experiment, and the prenum pressure is fixed to 5 atm.

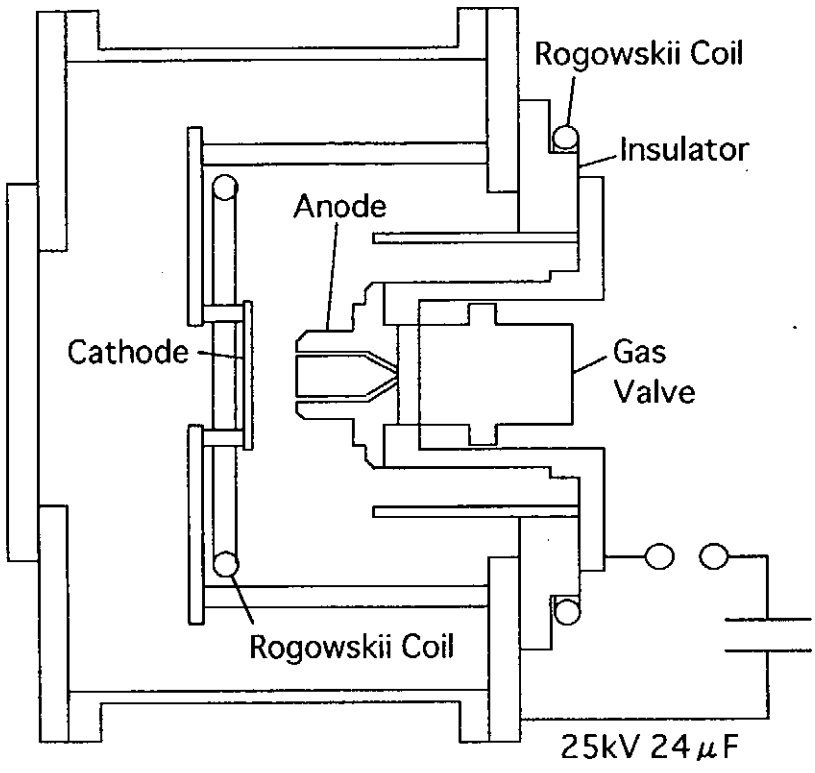

Figure 1: The SHOTGUN z-pinch device.

The electric currents of the anode and the cathodes are detected by Rogowski coils. The anode current shows the total input current, and the cathode current shows that goes through the z-pinch plasma.

X-ray measurement is important to monitor the maximum pinch. A scintillation probe is used to measure x-ray above 1 keV. K-shell radiations of Ar ion are in this region. A vacuum x-ray diode with Al cathode is used for XUV measurement (20 eV – 3 keV). L-shell and M-shell radiations of Ar ion are in this region. An x-ray pinhole camera is used to obtain space resolved image of hot spots of the plasma.

In order to observe contraction process of the plasma, shadowgraphy using a Nd:YAG laser is employed. Using a harmonics generator maximum output of 25 mJ is performed at the wavelength of 532 nm.

III. Experimental Results

Figure 2 shows sequential shadowgrams of the contracting z-pinch plasma. The anode current, x-ray and XUV signals are shown in the top frame. The moment of each shadowgram is shown in the current trace. In each shadowgram the anode is on the right and the cathode is on the left. The gas distribution is not quite uniform and the zippering effect is observed.

The motion of the plasma is slow until the current goes up to a certain level (1). The plasma boundary becomes more clear in the frame (2), which indicates the density increase. The plasma starts to shrink rapidly at (3), and the displacement from sinusoidal current becomes obvious. An axisymmetric ripple is found on the surface of the plasma, which is

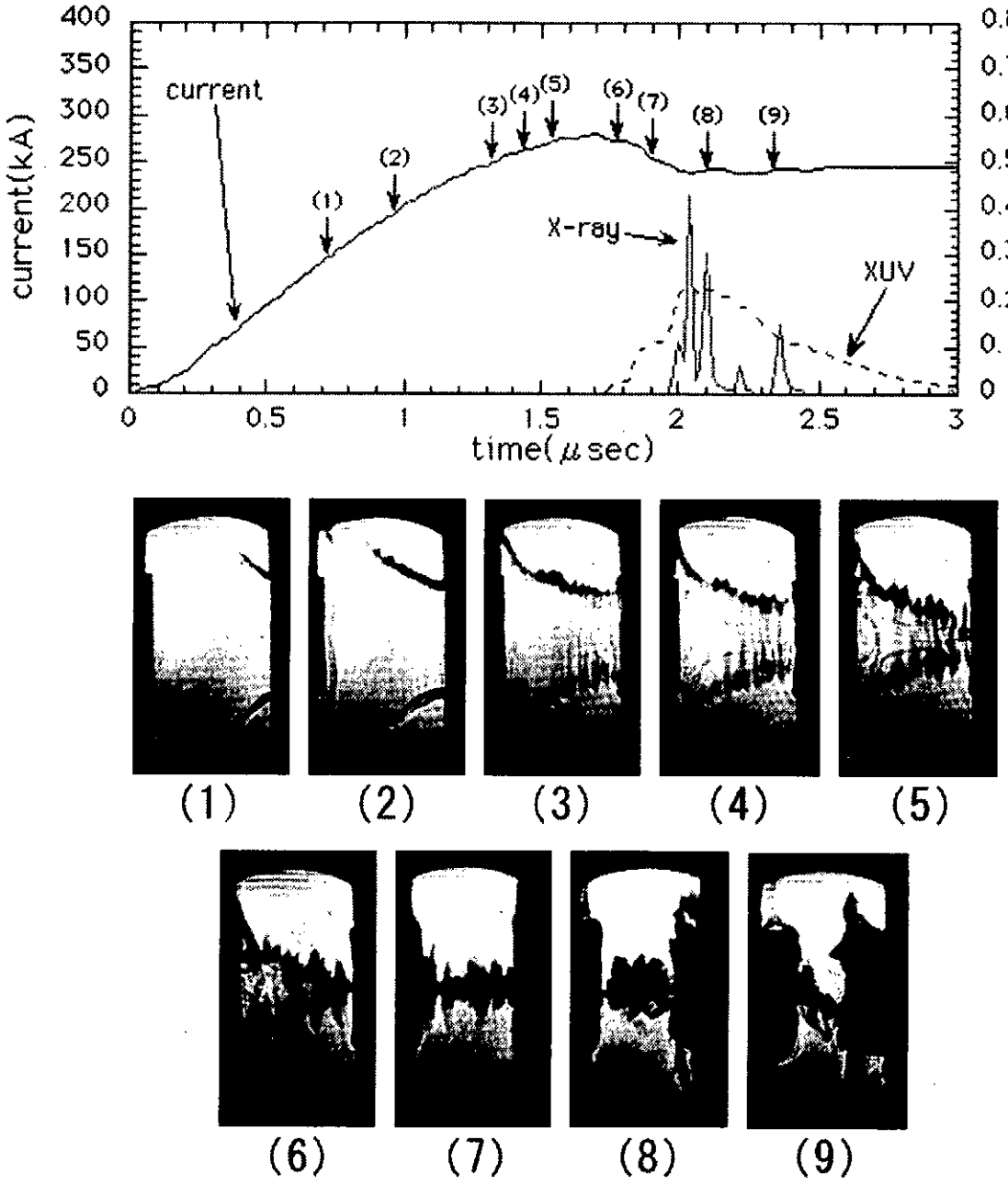

Figure 2: Sequential shadowgrams of the contracting z-pinch plasma. The moment of each frame is shown in the top trace.

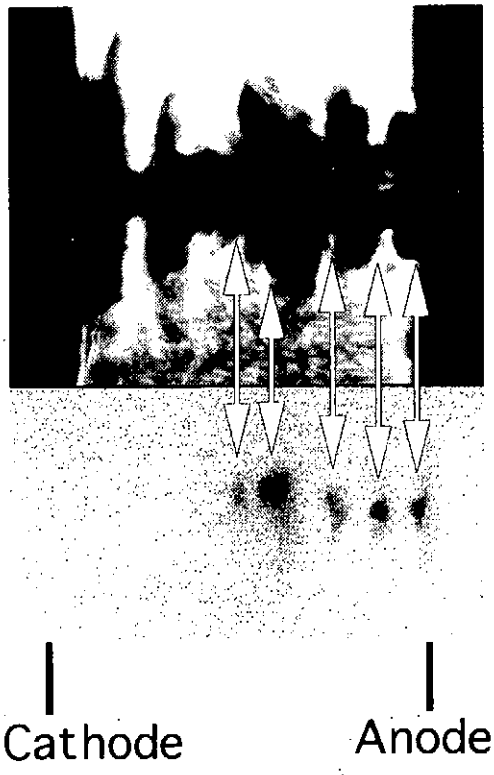

Figure 3: Simultaneous measurements of shadowgram and x-ray pinhole image of the z-pinch plasma.

the Rayleigh-Taylor instability caused by the implosion. The plasma continues to shrink at (4) – (5), and the instability also grows. The plasma contracts on the axis at (6) – (7), and the instability goes into nonlinear stage. The XUV signal increases here, which indicates the increase of electron temperature. Then the plasma reaches the local pinch ($m = 0$ mode) at (8), and x-ray pulses are emitted. Finally the plasma starts to expand hellically ($m = 1$ mode) at (9). Dense plasma flow from both electrodes is observed at (8) – (9). The observed instability is axisymmetric. As the magnetic field directs purely azimuthal direction, the wave number vector is perpendicular to the magnetic field $k_{\parallel} = 0$.

Figure 3 shows the shadowgram at maximum pinch and the x-ray pinhole photoraph taken in the same shot of discharge. The ripple observed in the shadowgram reaches the axis. This triggers $m = 0$ mode MHD instability which causes hot spots. Five hot spots are observed in the x-ray photograph. Each position of the hot spots is well corerated with spatial pattern of the $m = 0$ mode instability.

It was shown that the formation of hot spots has strong relation to the spatial pattern of the instability. The wavelength of the instability was observed to increase with implosion. In order to see the change of the wavelength numerically, the envelope of density profile is extracted, and the spatial pattern is analyzed by Fourier transformation.

Figure 4 shows changes of the wave number (open circle) and the wavelength (cross) of the instability with time. The lines in the figure show exponential fitting to the values. Here, the wave number is the number of waves in 3 cm. The wavelength is calculated from this value. It is clear that the wave number decreases and the wavelength increases with time.

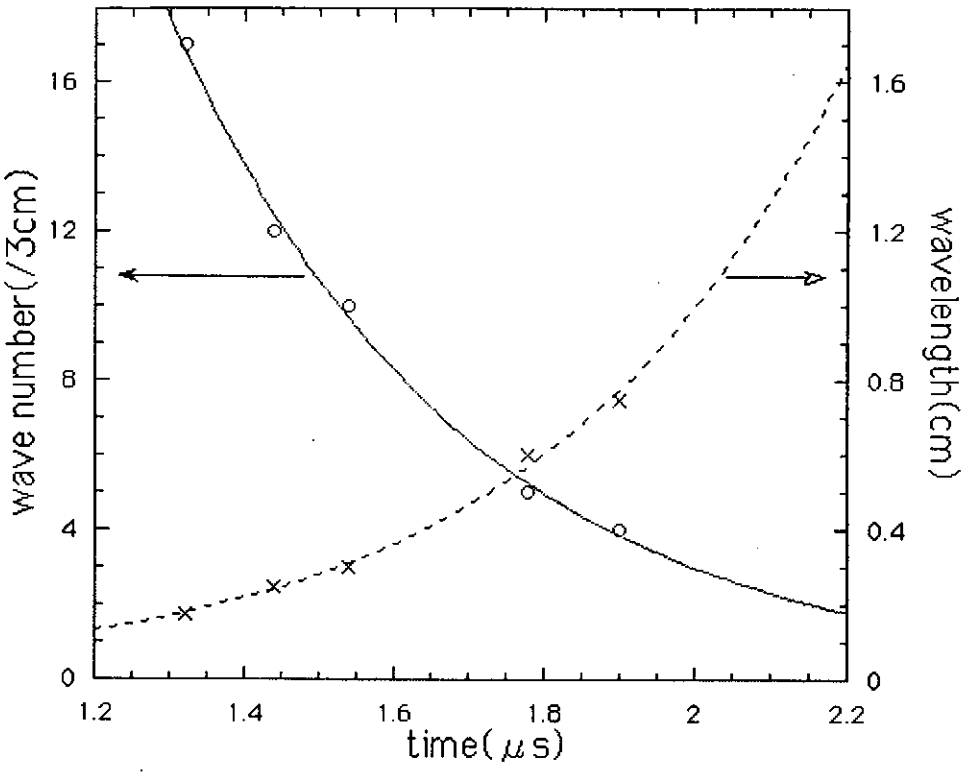

Figure 4: Wave number and corresponding wavelength of the instability.

IV. Discussion of Results

Well, how is the wavelength or the wave number determined ? And why does the wave number decrease with time ? A possible explanation is as follows.

The growth rate of Rayleigh-Taylor instability γ of ideal MHD plasma is $\sqrt{gk}$, where g is acceleration and k is wave number of the instability. Here the growth rate simply increases with k, and k cannot be determined for this case. Finite Larmor radius effect (FLR) is a possibility to limit the growth of the instability. The growth rate with FLR is expressed as

$$\gamma = \sqrt{gk - \frac{1}{4}\omega_{ci}^2 (k\rho_i)^4}, \tag{1}$$

where ω_{ci} is ion cyclotron frequency and ρ_i is ion Larmor radius. In Fig. 5 the growth rates of both cases are plotted for k. The rate γ becomes a maximum value at the wave number

$$k_0 = \left(g\omega_{ci}^{-2}\rho_i^{-4}\right)^{1/3}. \tag{2}$$

The instability will grow at this wave number k_0. As the Larmor radius $\rho_i = v_i/\omega_{ci} \propto \sqrt{T_i}/B$, and $g \propto B^2$. Then the wave number k_0 has the dependence of

$$k_0 \propto \left(B^4 T_i^{-2}\right)^{1/3}. \tag{3}$$

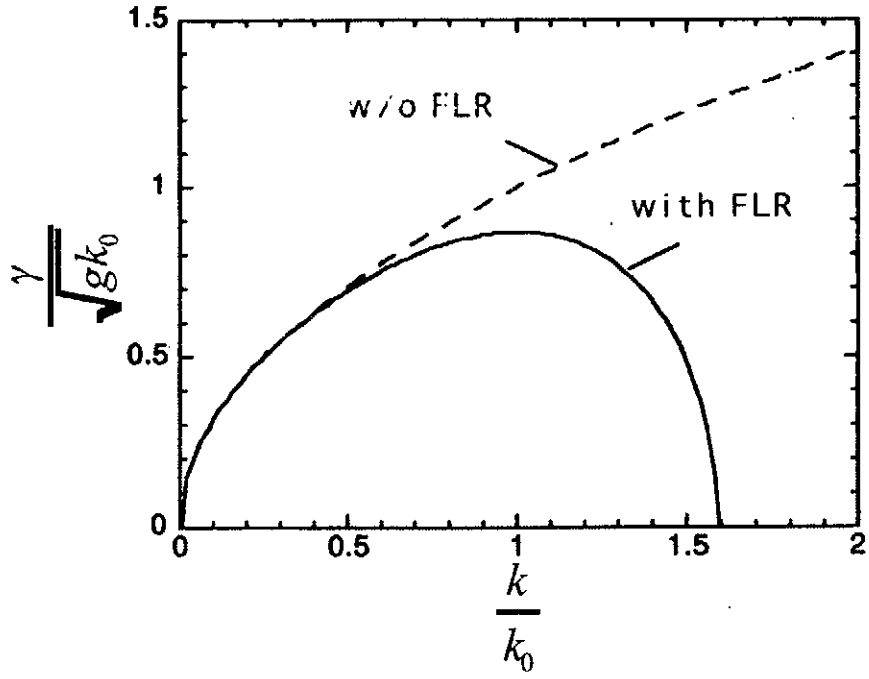

Figure 5: Growth rate of Rayleigh-Taylor instability with and without finite Larmor radius effect.

According to this model, the decrease of wave number k with the time is understood as decrease of B or increase of T_i. As the plasma current increases and the plasma radius increases with time, the magnetic field B must increase with time. So the temperature T_i must increase more than B^2. If magnetic moment conserves $T_i \propto B$. The result implies that there is some mechanism of extra acceleration or heating of ion that accounts more than the conservation of magnetic moment.

The goal of this research is to minimize the wavelength of the instability, so that the plasma column looks uniform macroscopically. As Eq. (4) shows that the wave number k_0 increases with B and decreases with T_i, we can maximize k_0 by increasing magnetic field or current without heating the plasma.

V. Summary

The imploding process of Ar z-pinch plasma was observed and investigated using a pulsed laser shadowgraphy. The Rayleigh-Taylor instability was observed on the surface of the contracting z-pinch plasma. The wavelength of the instability increased with implosion, and this lead $m = 0$ mode instability. The spatial pattern of the instability has strong relation to the formation of hot spots.

An analysis with finite Larmor radius effect indicates that the wave number of the instability is determined by plasma parameters as B and T_i. The decrease of wave number indicates that there is some accerelation of ions during the contraction process. It is important to increase plasma current without heating the plasma in order to keep the wavelength

of the instability small.

References

1) K. Takasugi, T. Miyamoto, K. Moriyama and H. Suzuki: AIP Conf. Proc. **299**, 251 (1993).
2) K. Moriyama, K. Takasugi, H. Suzuki and T. Miyamoto: NIFS-PROC-14, 43 (1993).
3) K. Moriyama, K. Takasugi, T. Miyamoto and K. Sato: NIFS-PROC-18, 90 (1994).
4) K. Moriyama: Master's thesis, "Study of macroscopic behavior and x-ray radiation of a gas-puff z-pinch plasma" (in Japanese), Nihon University (1994).

Diagnostics of capillary discharge plasma and soft X-ray laser using capillary discharge

Gohta Niimi, Mitsuo Nakajima, Akitoshi Okino, Masato Watanabe,
Kazuhiko Horioka and Eiki Hotta

Department of Energy Sciences,
Tokyo Institute of Technology,
Nagatsuta, Midori-ku, Yokohama Kanagawa 226-8502, Japan.

Abstract

Capillary discharge experiments were carried out to get a lasing of Ne-like Ar line (J = 0 - 1, λ = 46.9 nm). The capillary channel was 120 mm in length and 3 - 4 mm in inner diameter and it was filled with pre-ionized argon gas in an initial pressure range of 100 - 1000 mTorr. A current up to 37 - 57 kA with a rise time of 20 ns was generated by a fast pulsed power generator 'LIMAY-I'(3 Ω - 70 ns). Dynamics of capillary discharge plasma was observed with a streak camera. At the time of maximum pinch, laser amplification was detected by an X-ray diode.

1 Introduction

Since laser has properties that ordinary light does not posses - namely monochromaticity, directivity, high intensity, and coherency - it is fully applicable in various fields. Moreover soft X-ray laser has soft X-ray properties in addition to these laser properties, it may be applicable at molecular levels to the instrumentation, and material manipulation essential to leading-edge research and development in medicine, science and technology. Actual implementation is eagerly awaited [1].

However, the scaling of excitation power for soft X-ray lasing follows a 4.5 power rule of the lasing frequency. Producing an intense laser of shorter wavelength will therefore require a device of extremely large scale and high cost. For this reason, the development of high efficiency soft X-ray laser devices that could be implemented anywhere would be desirable, and great efforts have been made to achieve this.

In 1994, it was reported that a capillary discharge could produce a laser amplification at 3p - 3s level of Ne-like Ar (46.9 nm) [2]. In comparison with laser-driven X-ray laser devices, this device is inexpensive, compact in size and high conversion efficiency from electric energy to laser energy.

It is possible to enlarge laser energy by increase of a gain-length product or a laser pulse width. However, soft X-ray laser using capillary discharge can extract only a several ns pulse. Widths of the laser pulse may be restricted by the plasma dynamics and the

confining time of the optimal plasma condition. The object of our study is to reveal the cause, which restricts the duration of lasing, to enlarge a laser pulse width and to get a higher laser energy. In the present stage, our purpose is to understand the correlation between plasma dynamics and X-ray radiation process, and to reveal discharge conditions suitable for a laser amplification by LIMAY-I [3].

2 Experimental apparatus

A pulsed power generator "LIMAY-I (3Ω - 70 ns, 13 kJ; Max) [3]" was used as the driving power source for the capillary discharge. The drive current above 200 kA with a rise time of 20 ns was attainable with this generator. The typical experimental setup is shown in Figure.1. A capillary made of polyacetal with an inner diameter of $d = 3$ mm and a length of $l = 120$ mm was used. The capillary was installed on the axis inside the Z-stack insulator of the PFL. The space between the Z-stack insulator and the capillary was filled with deionized water to prevent breakdown along the capillary outer surface. Tungsten, a material with a highest melting point, was used for the capillary discharge electrodes at the both end of capillary. The cathode has an aperture of 2 mm for inlet of argon gas and observation of a capillary discharge.

After predischarge with a current of 10 - 20 A and a decay time of 30 μs, the main discharge current of 30 - 60 kA was sent into the capillary. A Rogowski coil was used for measurement of the discharge current.

The inside of the capillary was filled with 100 - 1000 mTorr of argon gas, and the background pressure of X-ray diode(XRD) chamber was kept lower than $\sim 10^{-4}$ Torr using a differential pumping. The pinhole was located at a distance of 2 cm from the end of capillary, and the XRD was positioned 60 cm from the pinhole. The pinhole and the XRD were positioned along the axis of capillary. The absorption coefficient for a wavelength $\lambda = 46.9$ nm (26.4 eV) was $\tau_0 = 900$ cm^{-1} [4]. The light of this wavelength, for example, argon gas filled with 500 mTorr attenuates by 30 % in a distance of 2 cm.

Photographs of the plasma were taken from the direction of the axis, using a high-speed camera (Hadland, IMACON 468), in order to confirm its pinch. An X-ray radiation process was measured with the XRD. The XRD consisted of a photocathode with a negative bias of -900 V, and a wire mesh anode with a transparency of 44 %, positioned at a distance of 2 mm from the cathode surface. In this experiment, improvement has been made to use gold, instead of aluminum, as the photocathode of XRD, which provides better sensitivity to the X-ray of energy lower than 100 eV. Photo electric yields of aluminum and gold at a wavelength of 46.9 nm were 0.14 and 0.11, respectively [5] [6].

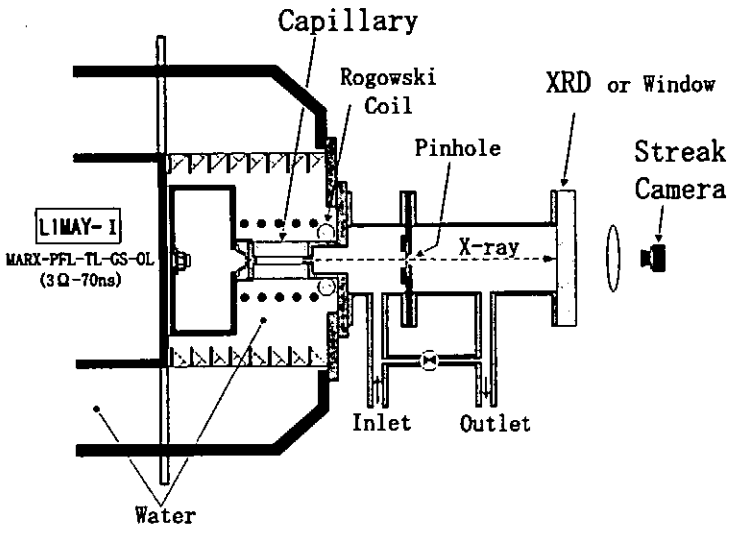

Figure 1. Schematic of experimental setup.

3 Experiments

3.1 Correlation between plasma dynamics and X-ray radiation process

Argon gas was filled at a pressure of $P = 500$ mTorr in a capillary with an inner diameter of $d = 3$ mm and length of $l = 120$ mm, and predischarged with a current of 10 A. Then, a current pulse with an amplitude of $I_0 = 40$ kA, a pulse rise time of 20 ns, and a pulse width of 105 ns was sent into the capillary. Figure 2 shows the waveforms of discharge current and the X-ray measured with an XRD with an aluminum photocathode. Figure 3 shows the streak photograph of a capillary discharge plasma taken from the direction of the axis taken under the same discharge condition. Figure 4 (A) - (D) show the framing photographs of capillary discharge plasma taken from the direction of the axis in vicinty of maximum pinch.

The contraction time of shock front τ_s was taken to be the time interval between a beginning of discharge and an arrival of the shock front at the axis. The maximum contraction time of current sheet τ_i was taken to be a time interval between a beginning of discharge and a maximum pinch of discharge plasma. From Figure 3, the beginning of strong radiation of light on the axis indicates the contraction of the shock front. Hence, the contraction time of shock front τ_s was 35 ns. The maximum contraction time of current sheet τ_i was 37 - 40 ns.

After τ_i, a stagnation of high energy density plasma produced in the vicinity of the axis. Simultaneously, the XRD signal shows the point of inflection. In addition, the slope of signal becomes steeper. The discharge plasma at this time was approximately 200 μm.

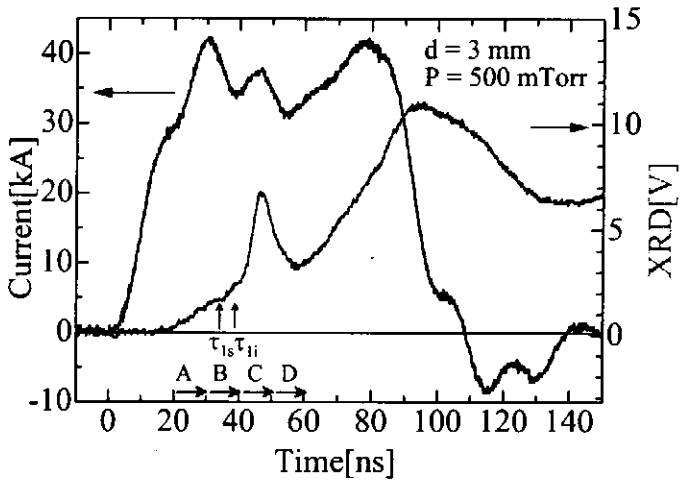

Figure 2. Waveforms of capillary discharge current and X-ray diode output: $P = 500$ mTorr, $d = 3$ mm

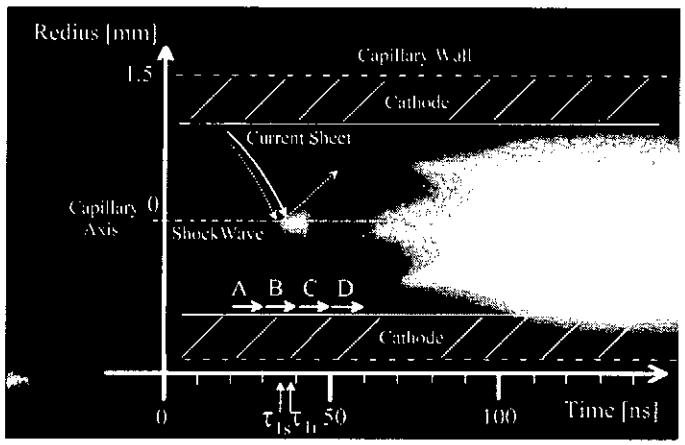

Figure 3. Streak photograph of capillary discharge plasma: $P = 500$ mTorr, $d = 3$ mm

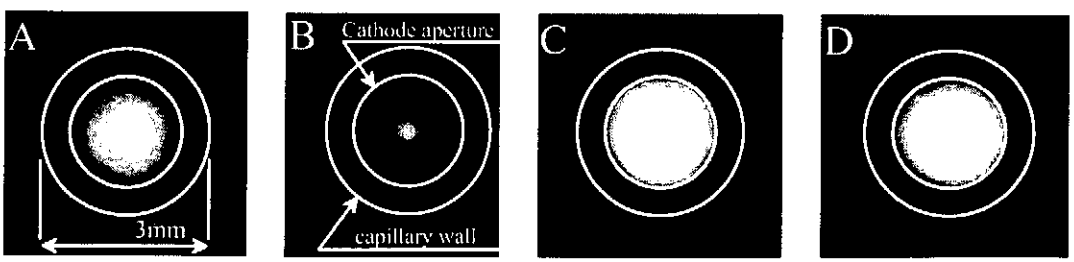

Figure 4(A). Framing photograph of capillary discharge plasma taken from 20 ns to 30 ns
Figure 4(B). Framing photograph of capillary discharge plasma taken from 30 ns to 40 ns
Figure 4(C). Framing photograph of capillary discharge plasma taken from 40 ns to 50 ns
Figure 4(D). Framing photograph of capillary discharge plasma taken from 50 ns to 60 ns

After stagnation, the plasma exploded and the XRD signal, which is to say the energy density of a plasma, decreased.

3.2 Dependence of discharge conditions

It is thought that the plasma condition for the amplification of neon-like argon soft X-ray laser is needed for the electron density of Ne $\sim 0.2-2\times10^{19}\mathrm{cm}^{-3}$, and the electron temperature of Te $\sim$ 60 – 80 eV [7]. The pinch plasma parameters can be controlled by charging an initial pressure, a current amplitude(dI/dt), and a capillary diameter. Experiments were conducted in which the initial pressure and the current amplitude were varied in the range of 100 - 1000 mTorr and 37 - 57 kA, respectively. A capillary with an inner diameter of 3.4 mm and a length of 120 mm was used, and gold was used as the photocathode of XRD.

Figure 5 shows the waveforms of current and the signals of XRD output at the initial pressures of 275, 412, and 950 mTorr. In the three shots, the measured waveforms were almost the same. However, as the pressure is increased, the initial peak of X-ray signal was shifted backward. The inertia of plasma increases at high pressures, although the magnetic force of the current remains the same, therefore there is a tendency for the pinch time to be delayed. In addition, the width of intense the X-ray pulse conforms that of the pinch plasma, and tends to be wider as the pressure increases.

When the pressure was low, 275 or 412 mTorr, the plasma could be rapidly heated by means of the shock waves. When the pressure was raised to, for example, 912 mTorr, however, the shock wave formation and the rapid heating were weaken, therefore the X-ray emission was moderated. Under these conditions, an XRD output was highest at pressures in the range of 400 - 500 mTorr. The current was changed in the range of 37 - 57 kA using a capillary with diameter of 3.4 mm and a pressure of 412 mTorr. Increasing the current amplitude, the X-ray signal becomes larger and the occurrence of the peak becomes forward shifted, because the energy density of the plasma also becomes higher.

As the current amplitude increased, the peak of X-ray signal grew larger, which higher energy density plasma was generated, and the occurrence of peak shifted forward. This indicated that strong pinches occurred in a short time, due to a strengthening of the magnetic force that is in proportion to the squares of current amplitude.

3.3 XRD signals of laser amplification

Figure 7 shows the current waveform and the signal of XRD output obtained under discharge condition of the capillary diameter of 3.4 mm, the initial pressure of 400 mTorr. We were able to detect a sharp signal of soft X-ray laser with FWHM of 0.6 ns in the vicinity of the maximum pinch (58.5 ns).

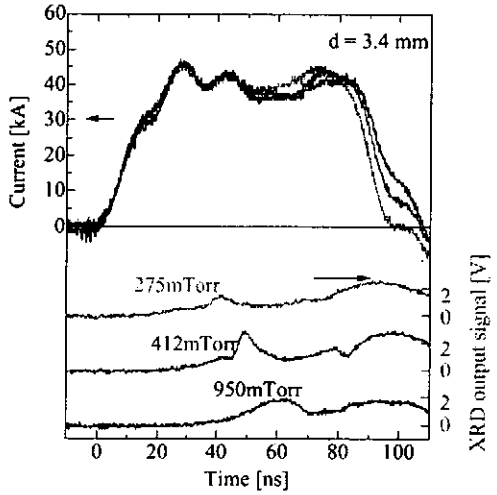

Figure 5. Waveforms of discharge currents and XRD output signals: P = 275 mTorr, 412 mTorr, 950 mTorr, d = 3.4 mm

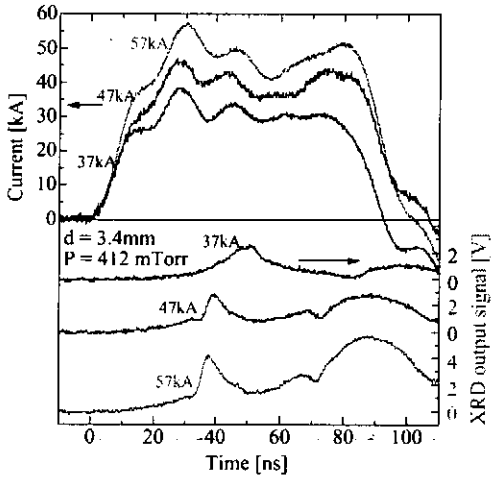

Figure 6. Waveforms of discharge currents and XRD output signals: I_0 = 37 kA, 47 kA, 57 kA, P = 412 mTorr, d = 3.4 mm

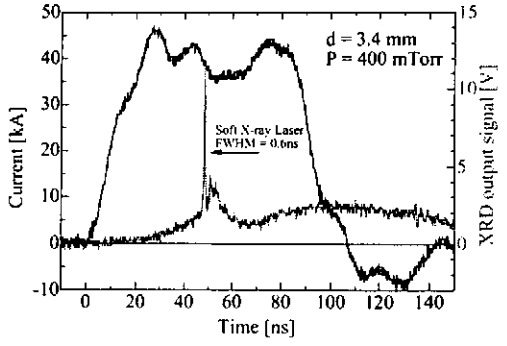

Figure 7. Waveforms of current and XRD output signal with a sharp peak

4 Summary

Argon was filled at 100 - 1000 mTorr in capillaries with diameter of 3 - 4 mm and length of 120 mm. After a predischarge current of 10 A was conducted, a current pulse with an amplitude of 37 - 57 kA, a pulse rise time of 20 ns, and a pulse width of 100 ns was driven. Formation of Z-pinch was confirmed using a streak camera. In addition, measurements of X-ray radiation process from discharge plasma were made using an X-ray diode, and the relationship between plasma dynamics and X-ray radiation process was clarified. When a capillary diameter of 3.4 mm, an initial pressure of 400 mTorr and a current amplitude of 47 kA were adopted, the laser amplification was measured in the vicinity of the maximum pinch. We are planning to study the correlation of soft X-ray laser and capillary discharge plasma using an XRD, a spectroscope and a high speed camera.

References

[1] Raymond C. Elton,*X-ray Laser* (Academic Press Inc.,USA,1990)p.252.

[2] J.J.Rocca, V.Shlyaptsev, F.G.Tomasel, O.D.Cortazar, D.Hartshorn, and J.L.A.Chilla, *Phys. Rev. Lett.* **73**, 2192 (1994).

[3] Tomonao HOSOKAI, Mitsuo NAKAJIMA, Takayuki AOKI, Masao OGAWA and Kazuhiko HORIOKA, *Jpn.J.Appl.Phys.* **36**, 2327 (1997).

[4] James A.R.Samson,
"Advances in Atomic and Molecular Physics" , **2**, p.177, Academic Press Inc. (1966)

[5] R.H.Day and P.Lee,
J.Appl.Phys., **52**, p.6965 (1981)

[6] H.N.Kornblum and V.W.Slivinsky,
Rev.Sci.Instrum. **49**, p.1204 (1978)

[7] V.N.Shlyaptsev, A.V.Gerusov, A.V.Vinogradov, J.J.Rocca, O.D.Cortazar, F.Tomasel, and B.Szapiro, *SPIE* **2012**, 99 (1993).

EFFECT OF PINCH DYNAMICS ON RADIATION TRAPPING IN DISCHARGE PUMPED NEON-LIKE KRYPTON-LASER

M. Masnavi , M. Nakajima and K. Horioka

Department of Energy Sciences,Tokyo Institute of Technology,
4259 Nagatsuta, Midori-ku ,Yokohama 226,Japan

ABSTRACT

The characteristics of the populations and gain coefficients in Neon-like (Ne-like) Krypton (KrXXVII) have been investigated considering the 18-levels of the $2s^2 2p^6, 2s^2 2p^5 3s, 2s^2 2p^5 3p$, and $2s^2 2p^5 3d$ configurations for cylindrical plasma. Introducing the effective rates for some spontaneous emissions approximated the influence radiation trapping phenomena. Then we calculated the gains using these modified rates. And, we have calculated relative sublevel populations and gains for different electron and ion temperatures for both stationary and dynamic plasmas. The effect of the energy trapping of the $2p^6\,{}^1S_0 - 2p^5 3s\,{}^1P_1$, $2p^6\,{}^1S_0 - 2p^5 3s\,{}^3P_1$, $2p^6\,{}^1S_0 - 2p^5 3d\,{}^3D_1$ and $2p^6\,{}^1S_0 - 2p^5 3d\,{}^1P_1$ transitions are investigated in the electron density regime $10^{20} - 10^{22}\,cm^{-3}$.

I. Introduction

Since Zherikhin et al[1] recognized that the populations of some levels in the configuration can be larger than those in the configuration for proper electron densities and temperatures, the x-ray laser schemes using transition between configurations in ionic systems have been studied both theoretically and experimentally. Feldman et al[2] and Kim et al[3] extended the calculation to Ne-like KrXXVII, and showed that a large number of KrXXVII ions can produce a significant gain in transition between some configurations. In recent years, Rocca and co-workers[4] has reported the observation of soft x-ray amplification and saturation of the $J = 0 - 1$ transition in Ne-like Ar using a fast capillary discharge.

In this paper we have performed a calculation for relative level populations and gain coefficients of the Ne-like Krypton. Also, we have taken into account the escape probability for both stationary and dynamic pinch plasmas to consider the effect of the energy trapping phenomena for lasing transitions. It is noted that the effect of the energy

trapping becomes important for the high electron densities and even increases[3] the gain for some lasing transitions.

II. Model for Calculation

The rate equation for the population N_l^i of an excited level l in the *ith* ionization stage is given by[5]

$$\frac{dN_l^i}{dt} = \sum_u R_{lu}^i N_u^i - n_e I_l^i N_l^i + n_e Q_l^{i+1} N_l^{i+1} \tag{1}$$

with

$$\begin{aligned} R_{lu}^i &= n_e C_{ul}^e , l > u \\ &= n_e C_{ul}^d + A_{ul} , l < u \\ R_{ll}^i &= -\sum_{m<l} (n_e C_{lm}^d + A_{lm}) - \sum_{m>l} n_e C_{lm}^e \end{aligned} \tag{2}$$

Where n_e is the electron density, $C_{ul}^{e(d)}$ the electron excitation (de-excitation) rate coefficient, and A_{ul} the radiative transition rate from an upper state u to a lower state l. The terms I_l^i and Q_l^{i+1} represent the electron collisional ionization rate coefficient from a level l and the total recombination rate coefficient to the level, respectively. The collisional excitation rate includes monopole excitation rate for the transition from the ground state to the $3p(J=0)$ level. The other dipole collisional excitation rates are calculated using the well-known formulas which include oscillator strengths as follows

$$C_{lu}^e (cm^3 \sec^{-1}) = 1.6 \times 10^{-5} \frac{f_{lu} < g(u,l) >}{\Delta E_{ul} T_e^{1/2}} \exp(\frac{-\Delta E_{ul}}{T_e}) \tag{3}$$

where $< g(u,l) >$ denotes the thermal averaged Gaunt factor, f_{lu} oscillator strength, T_e the electron temperature and ΔE_{ul} the transition energy of the $l \rightarrow u$ transition. The de-excitation rate coefficients are obtained using the detailed-balance relation[6]

$$C_{ul}^d = \frac{g_l}{g_u} \exp(\frac{\Delta E_{lu}}{T_e}) C_{lu}^e \tag{4}$$

Since an equilibrium between the excited levels is readily established due to their short lifetimes, the quasi-steady-state approximation has been adopted in our calculation $\frac{dN_l^i}{dt} = 0$. In the present calculation the level populations are normalized in such a way

that; $m_l = \frac{N_l^i}{N_l}, \sum_l m_l = 1$. Furthermore, the recombination and ionization processes between neighboring ionization stages can be ignored because these processes are negligibly slow compared to the excitation and de-excitation processes within the Ne-like ionization stage[3] under the densities and temperatures of our interest.

The absorption coefficient or gain of a medium is related to the intensity (I) of radiation by

$$I = I_0 \exp(\alpha Z) \tag{5}$$

Where I_0 is the incident intensity, Z is the length of plasma, and α is the gain coefficient. For a Doppler-broadened spectral line, the gain coefficient on a radiative transition between an upper level u and a lower level l is given by

$$\alpha = \frac{\lambda^3}{8\pi} A_{ul} (M / 2\pi k T_i)^{1/2} g_u (N_u / g_u - N_l / g_l) \tag{6}$$

Where λ is the wavelength of the transition between the upper and lower levels, M the atomic mass of the ions, k the Boltzmann constant, T_i ion temperature, N_u and N_l are the relative level population, and g_u and g_l are statistical weights of the level.

Using the relative populations, gain coefficient can be rewritten as follows

$$\frac{\alpha}{N_l} = 1.6 \times 10^{-7} T_i^{-1/2} \lambda^3 A_{ul} g_u (m_u / g_u - m_l / g_l) \tag{7}$$

The right-hand side of above equation consists of terms only related to Ne-like Kr. We have assumed a cylindrical plasma with length Z and radius r consisting of Krypton ions. N_l is the total number density of ions in all levels for ionization stage of the Ne-like Krypton.We have also assumed that $N_l / N_{Kr} = 1/4$, i.e., 1/4 of the Krypton is in the Ne-like degree of ionization, and rest of the ions is in nearby degrees of ionization. Under such conditions may be we have $N_{Kr} / n_e \approx 1/26$.

The optical depth at line center λ of plasma is given by[7]

$$\tau = \int_0^z k(\lambda).dz = k(\lambda).Z \tag{8}$$

where $k(\lambda)$ is the absorption coefficient and Z the length of plasma medium. The absorption coefficient for the line radiation may be written

$$k(\lambda) = \frac{e^2 f}{m_e c^2} \left(\frac{\pi Mc^2}{2kT_i}\right)^{1/2} N_l \lambda \tag{9}$$

where m_e and c are the electron mass, and speed of light, respectively.

To energy trapping calculations, we are taken into account four resonance lines that two of the lines are between the lower level to the ground state $2s^2\,2p^6\,{}^1S_0$, and the other are between the configuration $2s^2\,2p^5\,3d$ and the ground state. Radiation trapping increases the populations of the resonance levels that can be estimated using the effective radiation rate $E(\tau)A$, where $E(\tau)$ is the escape probability for a given optical depth and A the original radiative transition rate. For the escape probability we have used the following polynomial fit to the tabulated values calculated by Zemansky[8)]

For $0 < \tau \leq 4.5$

$$E(\tau) = 0.99900 - 0.69775\ \tau + 0.26653\ \tau^2 - 0.06191\ \tau^3 + 0.00811\ \tau^4 - 0.00045\ \tau^5 \quad (10)$$

and for $\tau > 4.5$

$$E(\tau) = \frac{1}{\tau\sqrt{\pi\ \ln\ \tau}} \quad (11)$$

We have recalculated the level populations with the modified escape factors for calculating gain coefficients for plasma that has radial motion with velocity gradients by[7)]

$$\gamma = \Delta(v / v_{th}) / \Delta\tau \quad (12)$$

We have also assumed that the opacity versus the flow velocity of a Doppler broadened line is varied same as laser-produced plasmas, (this assumption may be too optimistic) as follows[9)]

$$\tau_D = \tau \times 0.6\ \frac{v_{th}}{v} \quad (13)$$

With thermal velocity (v_{th}) and flow velocity (v).

III. Results and Discussion

Figure (1) shows the schematic energy level diagram for the 18-levels KrXXVII, which are taken into account in our study. In the calculation of the relative level population, we have used the atomic data presented by Feldman et al[2)].The relative level populations for two different temperatures at the electron densities 1×10^{20},1×10^{21} and $1\times10^{22}\,cm^{-3}$ are shown in Table(1). As can be seen, the relative sublevel populations increase with electron density and temperature due to the increase of collisional excitation rates under electron temperature regime of our interest. At the electron density $10^{22}\,cm^{-3}$, the populations are distributed close to the Boltzmann

distribution law, because the collisional de-excitation rates exceed the radiative decay rates. Due to the monopole interaction of the $2p^5 3p\,^1S_0$ level from the ground states, this level is largely populated. The optical depths in the lines emitted by a cylindrical plasma along its radius are also given in Table(2). The optical depths of two transitions from 3d levels to the ground state are greater than 3s levels due to higher oscillator strengths of these levels. As suggested by Palumbo and Elton[2], we have used a radius, which is 1/20 of the cylinder length.

We have recalculated the level populations using the modified rates of spontaneous emission by escape factor and the results are given in Table 3(4) for stationary (dynamic; $v = 10^7 cm/s$) plasma, respectively. Table (5) shows the gain coefficients of the two transitions at two electron densities and given temperature. The first number(g_0) is gain coefficient without reabsorption. The gain coefficient g_1 includes the reabsorption effect for stationary plasma. Furthermore, g_2 is calculated with reabsorption when the plasma has radial velocity. For an electron density below $10^{21} cm^{-3}$ these gain coefficients increase with the electron density due to the increase of the collisional excitation rates. From inspection of Table (5), it can be seen that for a density at $10^{20} - 10^{21} cm^{-3}$, the reabsorption of resonance lines can be increases the gain coefficients up to 2 or 3 times in both stationary and dynamic plasmas.

So far, we have assumed that the ion temperature (T_i) is equal to the electron temperature (T_e). However, it is expected that in capillary discharge plasmas, T_i will be much smaller than T_e during the implosion phase. We have recalculated the optical depths (gain coefficients) for different electron and ion temperatures, as shown in Table 6(7), respectively. Since $\alpha \approx T^{-1/2}$, the calculated gain coefficients using equation (4) should be multiplied by $(T_e/T_i)^{1/2}$ only in case of without reabsorption. From inspection of Table (7), it can be seen that, the reabsorption affect in the both stationary and dynamic plasmas up to 3 times increases the gain coefficients.

Conclusions

The analysis shows that a volume of Krypton in which significant number of the ions are in the Ne-like degree of ionization (KrXXVII) can produce a significant gain in transition between the $2s^2 2p^5 3p$ and $2s^2 2p^5 3s$ configurations. The effect of reabsorption of the resonance lines not only increases the population of the lower level, but also enhances the population of the 3d levels that decay to the upper level. This latter effect tends to enhance the population inversions. For electron densities $10^{20} - 10^{21} cm^{-3}$, the reabsorption of resonance lines increases the gain coefficients up to 3 times. In the regime of electron density of our study, the gain coefficients increase

for plasma that has radial velocity due to reduction of the optical depth. Also reduction of ion temperature than electron temperature will increase the gain coefficients. Those parameters (v, T_e, T_i) are closely connected to the pinch dynamics of capillary discharges. To make lasing condition at shorter wavelength estimation, we have to use more dynamic pinching process. A self-consistent estimation of the potentiality of soft x-ray lasing in capillary plasma, is the subject of future works, including the precise evaluation of the opacity in cylindrically moving plasma.

References

1)A.Zherikhin, K.N.Koshelev, V.S.Letokhov, ``Gain in the Far Vacuum Ultraviolet Region Due to Transitions in Multiply Charged Ions``, Sov. J. Quantum Electron, **6**, 82-86 (1976).

2)U. Feldman, A.K. Bhatia, S. Suckewer, ``Short Wavelength Laser Calculations for Electron Pumping in Neon-Like Krypton``, J. Appl. Phys., **54**, 2188-2197 (1983).

3)D.S.Kim, D.E.Kim,``The Effect of Radiation Trapping in Gain for Ne-Like Kr``, Japanese Journal Applied Physics,Part**1**,No.5A, 2693-2698 (1998).

4)J.J.Rocca, D.P.Clark, J.L.A.Chilla, V.N.Shlyaptsev,``Energy Extraction and Achievement of the Saturation Limit in a Discharge-Pumped Table - Top Soft X-Ray Amplifier``, Phys.Rev.Lett.,**77**, 1476-1479 (1996).

5)Y.T.Lee,``A Model for Ionization Balance and L-Shell Spectroscopy of Non-LTE Plasmas``,J.Quant.Spectrosc.Radiat.Transfer,**38**, 131-145 (1987).

6)H.Daido, S.Ninomiya, T.Imani, Y.Okachi, M.Takagi, R.Kodama, H.Takabe, Y.Kato, ``Atomic Number Scaling of the Nicle-Like Soft X-Ray Lasers``, Int. Journal Modern Physics,**11**, 945-990 (1997).

7)R.C.Elton, ``X-Ray Lasers``, Academic Press, New York (1990).

8)M.W.Zemansky, ``Absorption and Collision Broadenning of The Mercury Resonance Line``, Phys.Rev.,**36**, 219-238 (1930).

9)T.Ozaki, H.Kuroda ,``Controlling Opacity and Gain Coefficients of Soft X-Ray Transition by Ion Dilution``, Appl.Phys.Lett.,**67**, 3105-3107 (1995).

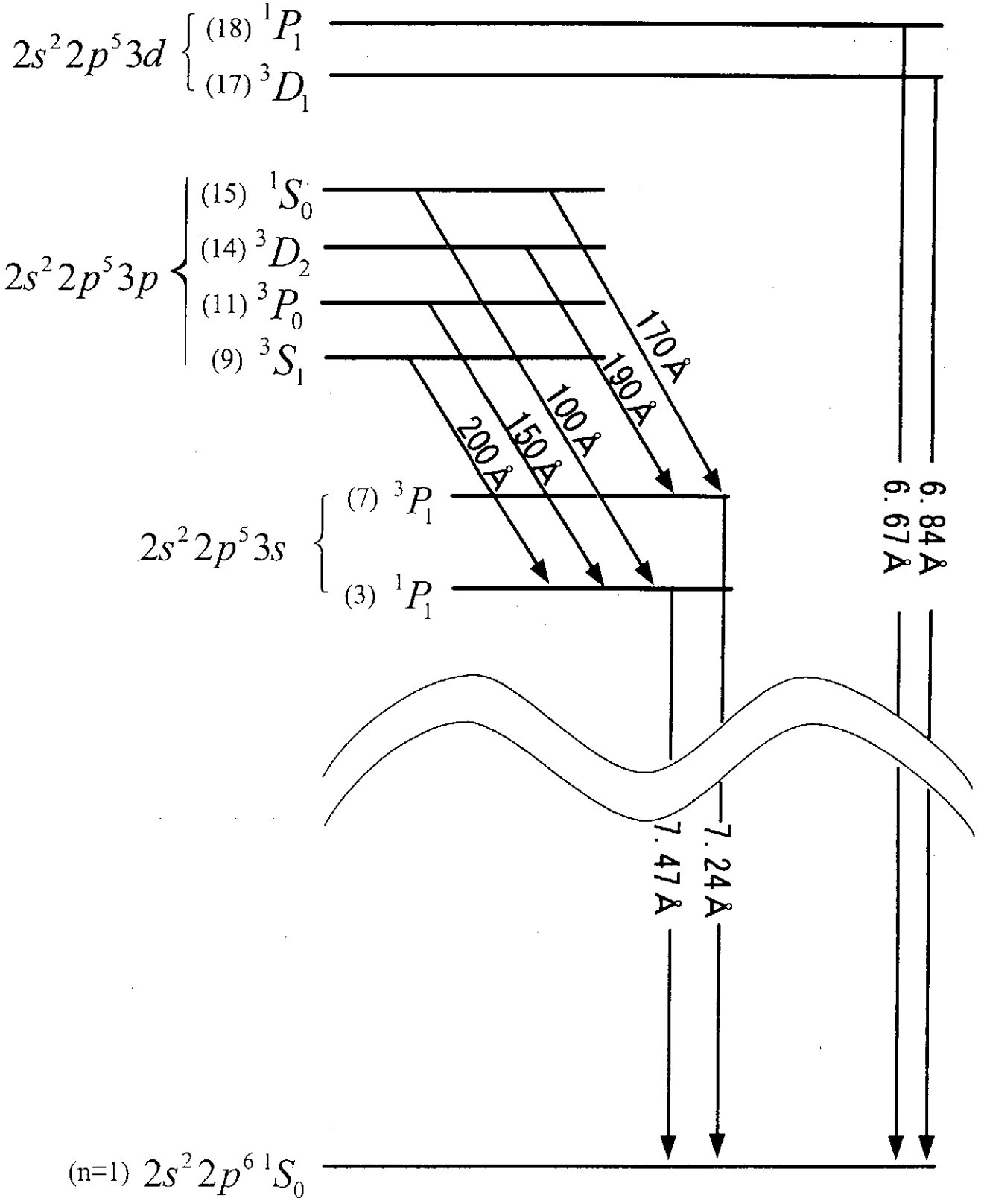

Figure (1). A schematic diagram for some of the energy levels in Ne-like Krypton ion. The principal quantum number is shown by (n).

Table (1). Energy levels and relative level populations for Ne-like KrXXVII given for two electron temperatures 1keV and 3keV (3keV in parentheses), for stationary plasma ($Te = Ti$).

i	Configuration	level	Energy (cm^{-1})	level Populations $n_e = 10^{20}\ cm^{-3}$	level Populations $n_e = 10^{21}\ cm^{-3}$	level Populations $n_e = 10^{22}\ cm^{-3}$
1	$2p^6$	$^1S_0$	0.0	9.91-1(9.883-1)	9.587-1(9.297-1)	7.566-1(6.057-1)
2	$2p^5 3s$	$^3P_2$	13367620	0.27-3(0.57-3)	0.283-2(0.56-2)	0.211-1(0.356-1)
3	$2p^5 3s$	$^1P_1$	13392937	0.21-3(0.41-3)	0.182-2(0.36-2)	0.125-1(0.212-1)
4	$2p^5 3p$	$^3P_1$	13783244	0.15-3(0.34-3)	0.155-2(0.32-2)	0.118-1(0.208-1)
5	$2p^5 3s$	$^3P_0$	13798566	0.12-3(0.17-3)	0.77-3(0.127-2)	0.473-2(0.71-2)
6	$2p^5 3p$	$^1D_2$	13803571	0.25-3(0.51-3)	0.272-2(0.559-2)	0.198-1(0.347-1)
7	$2p^5 3s$	$^3P_1$	13812078	0.3-3(0.46-3)	0.295-2(0.42-2)	0.182-1(0.232-1)
8	$2p^5 3p$	$^3D_3$	13895333	0.34-3(0.74-3)	0.37-2(0.766-2)	0.276-1(0.488-1)
9	$2p^5 3p$	$^3S_1$	13899903	0.17-3(0.36-3)	0.155-2(0.329-2)	1.106-2(0.198-1)
10	$2p^5 3p$	$^3P_2$	13931512	0.15-3(0.29-3)	0.25-2(0.51-2)	0.195-1(0.344-1)
11	$2p^5 3p$	$^3P_0$	14059763	0.4-4(1.07-4)	0.46-3(0.10-2)	0.34-2(0.62-2)
12	$2p^5 3p$	$^1P_1$	14223809	0.24-3(0.4-3)	0.25-2(0.38-2)	0.158-1(0.216-1)
13	$2p^5 3p$	$^3D_1$	14335770	0.14-3(0.32-3)	0.17-2(0.347-2)	0.118-1(0.203-1)
14	$2p^5 3p$	$^3D_2$	14343874	0.36-3(0.53-3)	0.44-2(0.657-2)	0.284-1(0.376-1)
15	$2p^5 3p$	$^1S_0$	14411330	0.58-2(0.56-2)	0.83-2(0.79-2)	1.108-2(0.112-1)
16	$2p^5 3d$	$^3P_1$	14434401	1.08-4(0.26-3)	0.13-2(0.29-2)	0.108-1(0.200-1)
17	$2p^5 3d$	$^3D_1$	14611481	1.07-4(0.27-3)	0.10-2(0.255-2)	0.82-2(0.166-1)
18	$2p^5 3d$	$^1P_1$	14997775	0.9-4(0.24-3)	0.9-3(0.235-2)	0.73-2(0.153-1)

Table (2). Optical depths at line center for transitions of the type 2p-3l ($Te=Ti$)

Transition	Temperature	Optical Depth $n_e = 10^{20}\ cm^{-3}$	Optical Depth $n_e = 10^{21}\ cm^{-3}$	Optical Depth $n_e = 10^{22}\ cm^{-3}$
$3 \rightarrow 1$	1keV	6.2(Z=6.0 cm)	6(Z=0.60cm)	11(Z=0.14cm)
	3keV	1.8(Z=3.0cm)	1.7(Z=0.30cm)	2.8(Z=0.075cm)
$7 \rightarrow 1$	1keV	5.1(Z=6.0cm)	4.9(Z=0.6cm)	9(Z=0.14cm)
	3keV	1.5(Z=3.0cm)	1.4(Z=0.30cm)	2.3(Z=0.075cm)
$17 \rightarrow 1$	1keV	79.7(Z=6.0cm)	77.1(Z=0.60cm)	142(Z=0.14cm)
	3keV	23(Z=3.0cm)	21.6(Z=0.30cm)	35.1(Z=0.075cm)
$18 \rightarrow 1$	1keV	116.5(Z=6.0cm)	112.5(Z=0.60cm)	207(Z=0.14cm)
	3keV	33.5(Z=3.0cm)	31.5(Z=0.30cm)	52(Z=0.075cm)

Table. (3). A modified set of relative levels populations for Ne-like KrXXVII is given for two electron temperatures 1keV and 3keV(3keV in parentheses), for stationary plasma ($Te = Ti$)

i	level Populations $n_e = 10^{20}$ cm^{-3}	level Populations $n_e = 10^{21}$ cm^{-3}	level Populations $n_e = 10^{22}$ cm^{-3}
1	8.018-1(8.799-1)	3.294-1(4.499-1)	0.975-1(0.644-1)
2	0.101-1(0.41-2)	0.521-1(0.301-1)	0.854-1(0.813-1)
3	0.86-2(0.21-2)	0.351-1(0.181-1)	0.509-1(0.483-1)
4	0.48-2(0.24-2)	0.275-1(0.173-1)	0.48-1(0.474-1)
5	0.129-1(0.52-2)	0.182-1(0.145-1)	0.167-1(0.175-1)
6	0.101-1(0.34-2)	0.513-1(0.295-1)	0.805-1(0.793-1)
7	0.7-2(0.17-2)	0.353-1(0.178-1)	0.496-1(0.473-1)
8	0.127-1(0.53-2)	0.681-1(0.410-1)	1.12-1(1.113-1)
9	0.141-1(0.94-2)	0.374-1(0.328-1)	0.478-1(0.498-1)
10	0.59-2(0.19-2)	0.467-1(0.266-1)	0.789-1(0.783-1)
11	0.6-2(0.46-2)	0.140-1(0.162-1)	0.157-1(0.175-1)
12	0.13-1(0.85-2)	0.391-1(0.326-1)	0.472-1(0.495-1)
13	0.2-1(0.118-1)	0.502-1(0.452-1)	0.465-1(0.519-1)
14	0.85-2(0.24-2)	0.536-1(0.288-1)	0.772-1(0.771-1)
15	0.96-2(0.98-2)	0.154-1(0.206-1)	0.161-1(0.182-1)
16	0.13-2(0.7-3)	0.202-1(0.131-1)	0.433-1(0.446-1)
17	0.224-1(0.193-1)	0.456-1(0.681-1)	0.438-1(0.548-1)
18	0.314-1(0.275-1)	0.608-1(0.977-1)	0.431-1(0.617-1)

Table (4). A set of relative level populations for Ne-like KrXXVII is given for two electron temperatures 1keV and 3keV(3keV in parentheses), for dynamic plasma ($Te = Ti$)

i	level Populations $n_e = 10^{20}$ cm^{-3}	level Populations $n_e = 10^{21}$ cm^{-3}	level Populations $n_e = 10^{22}$ cm^{-3}
1	6.98-1(5.637-1)	2.43-1(1.944-1)	0.906-1(0.456-1)
2	0.209-1(0.84-2)	0.606-1(0.488-1)	0.863-1(0.887-1)
3	0.213-1(0.53-2)	0.418-1(0.318-1)	0.515-1(0.532-1)
4	0.9-2(0.42-2)	0.316-1(0.272-1)	0.484-1(0.515-1)
5	0.152-1(0.295- 1)	0.193-1(0.208-1)	0.167-1(0.158-1)
6	0.226-1(0.72-2)	0.602-1(0.492-1)	0.814-1(0.868-1)
7	0.186-1(0.75-2)	0.495-1(0.298-1)	0.507-1(0.429-1)
8	0.263-1(0.109-1)	0.792-1(0.665-1)	1.131-1(1.214-1)
9	0.211-1(0.166-1)	0.406-1(0.468-1)	0.481-1(0.534-1)
10	0.131-1(0.42-2)	0.547-1(0.44-1)	0.797-1(0.856-1)
11	0.71-2(0.69-2)	0.141-1(0.211-1)	0.157-1(0.181-1)
12	0.206-1(0.47-1)	0.484-1(0.483-1)	0.478-1(0.447-1)
13	0.216-1(0.667-1)	0.497-1(0.641-1)	0.462-1(0.469-1)
14	0.222-1(0.106-1)	0.749-1(0.477-1)	0.788-1(0.699-1)
15	0.107-1(0.308-1)	0.172-1(0.256-1)	0.162-1(0.165-1)
16	0.23-2(0.11-2)	0.231-1(0.202-1)	0.434-1(0.485-1)
17	0.211-1(0.2-1)	0.411-1(0.831-1)	0.434-1(0.556-1)
18	0.28-1(1.594-1)	0.508-1(1.305-1)	0.419-1(0.549-1)

Table (5). Gain coefficients for two transition 3p-3s (Te = Ti = 3keV). The calculation was done for two electron densities and also length of cylinder (Z). Gain coefficient (g_0) is calculated for plasma without reabsorption effect. Gain coefficient g_1 (g_2) is calculated using escape probability for resonance lines in stationary(dynamic) plasma, respectively.

Transition	Gain (cm^{-1}), Z= 3.0 cm	Gain (cm^{-1}), Z= 0.30 cm
	$n_e = 10^{20}$ cm^{-3}	$n_e = 10^{21}$ cm^{-3}
$15 \rightarrow 3$	g_0=0.33(g_1=0.55; g_2=1.7)	g_0=4.1(g_1=8.8; g_2=10)
$15 \rightarrow 7$	g_0=1.89(g_1=3.2; g_2=9.8)	g_0=22.9(g_1=51; g_2=54.5)

Table (6). Optical depths at line center for transitions of the type 2p-3l for two electron temperatures and an ion temperature Ti =0.5 keV for stationary plasma (Te ≠ Ti).

Transition	Electron Temperature	Optical Depth $n_e = 10^{20}$ cm^{-3}	Optical Depth $n_e = 10^{21}$ cm^{-3}	Optical Depth $n_e = 10^{22}$ cm^{-3}
$3 \rightarrow 1$	1keV	8.7(Z=6.0 cm)	8.4(Z=0.60cm)	15.5(Z=0.14cm)
	3keV	4.4(Z=3.0cm)	4.1(Z=0.30cm)	6.8(Z=0.075cm)
$7 \rightarrow 1$	1keV	7.2(Z=6.0cm)	6.9(Z=0.6cm)	12.7(Z=0.14cm)
	3keV	3.6(Z=3.0cm)	3.4(Z=0.30cm)	5.6(Z=0.075cm)
$17 \rightarrow 1$	1keV	112.7(Z=6.0cm)	109(Z=0.60cm)	200(Z=0.14cm)
	3keV	56.3(Z=3.0cm)	52.9(Z=0.30cm)	85.9(Z=0.075cm)
$18 \rightarrow 1$	1keV	164.7(Z=6.0cm)	159(Z=0.60cm)	292(Z=0.14cm)
	3keV	82(Z=3.0cm)	77.1(Z=0.30cm)	127(Z=0.075cm)

Table (7). Gain coefficients for two transition 3p-3s (Te ≠ Ti). The calculation was done at Te=3keV and, Ti =0.5 keV two electron densities and also length of cylinder (Z). Gain coefficient (g_0) is calculated for plasma without reabsorption effect. Gain coefficients g_0 (g_2) is calculated by rates of spontaneous emission for resonance lines in stationary (dynamic) plasma, respectively.

Transition	Gain (cm^{-1}), Z= 3.0 cm	Gain (cm^{-1}), Z= 0.30 cm
	$n_e = 10^{20}$ cm^{-3}	$n_e = 10^{21}$ cm^{-3}
$15 \rightarrow 3$	g_0=0.8(g_1=1.8; g_2=3.3)	g_0=10(g_1=14.4; g_2=22.3)
$15 \rightarrow 7$	g_0=4.6(g_1=10; g_2=21)	g_0=56(g_1=83.4; g_2=136)

Measurement of spatial distribution of the nonlinear collapsing wave packets by an electron beam shadowgraph

Ritoku ANDO, Hisashi FUJII, Masaru MASUZAKI, Tomohiro KONDO,
Norio TOYOSUGI, Fumiko OSAWA, Satoshi WADA, Hiromasa MORISHITA,
and Keiichi KAMADA

Department of Physics, Faculty of Science, Kanazawa University,
Kanazawa 920-1192, Japan

ABSTRACT

An electron beam probing technique is examined to measure the electric field, which remains in the plasma after the interaction between an intense relativistic electron beam (IREB). The electric field of the nonlinear wave packet of Langmuir wave is called a caviton. An electron beam with large cross-section is used as a probe beam to take a shadowgraph of spatial distribution of the electric field. Many holes were observed on the shadowgraph in the period of 450-700ns from the IREB injection. The average size of the holes is evaluated to have dimensions of 20 Debye lengths. The deflection of probe beam is analyzed by assuming the electric field based on the caviton theory. The experimental results show good agreement with the theory.

1 Introduction

We have been carrying out experiments on the beam-driven strong Langmuir turbulence by injecting an intense relativistic electron beam (IREB). Study of the nonlinear collapsing wave packet called a caviton is important for understanding of Langmuir turbulent plasma. In contrast with propagating wave, the electric field of a caviton is spatially localized. Inside the caviton, a density well is caused by the ponderomotive force due to the localized high frequency electric field. The phenomenon of self-focusing, leading to an increasing tendency for the waves to refract and be trapped in regions of highest intensity, was investigated by Zakharov, et al. There has been major progress in two- and three-dimensional numerical simulations of such systems, leading to many significant new insights [1]. Many cavitons appeared simultaneously in the simulation. The experiments have been carried out specifically to examine the predictions of strong-turbulence theory

[1]. For example, the ionospheric-modification experiments have provided a rich proving ground for the theory. Overall responses of a many-cavitons system can be examined there. Experiments in which a low-energy electron beam is injected into a cylindrical plasma showed some of the evidence for self-focusing and wave collapse in plasma [2]. On the other hand, relativistic beam-plasma experiment produces strong electric field where the field-strength distributions and interactions with electrons are interpreted in terms of strong turbulence. That is, the plasma is strongly heated by an IREB instantaneously. Spectroscopic observation of forbidden lines indicated that the strong electric field was produced through the IREB injection [3][4]. Microwave with broadband frequency emitted from the plasma [5][6]. In the measurement of IREB passing through the plasma, large scattering was observed, which was considered to be due to the turbulence electric field in the plasma [7].

An electron beam probing technique applicable to IREB-plasma system has been developed [8]-[10]. It will be reported here that the signal-to-noise ratio, S/N, is improved as a result of improvement of the detector. A probe beam which has a large cross section and lower current density is employed. The detail of the deflection becomes clear. It seems to provide the new prospects about the turbulence field.

2 Experimental setup

An IREB with energy of 1.5MV, current of 30kA, and duration of 30ns is employed to inject a plasma. A drift chamber, 60cm long and 16cm in diameter, is used [Fig.1]. No external magnetic field is applied. A plasma is produced with rail-type guns. The average of plasma density n_p is a function of the time, τ, from a start of the discharge. The plasma density was measured with a microwave interferometer and Langmuir probes. The n_p has about $\pm$ 50% of reproducibility due to the plasma gun. The gun was set at the position of z = 100mm, where z is the distance from the anode. The density of the plasma at z= 100mm reaches $3\times10^{13}\mathrm{cm}^{-3}$ at $\tau = 12\mu$s. At z= 305mm, the highest density $2\times10^{12}\mathrm{cm}^{-3}$ is obtained at $\tau = 15\mu$s. After the plasma reaches at the chamber wall at $\tau = 20\mu$s, the density starts to decrease. Since the external magnetic field is not applied, propagation of IREB depends on the injection time which related to the density of the plasma. It was also measured by using spectroscopy that the plasma electron temperature is heated from 1eV to about 50eV [4].

The outline of the electron probe used for this experiment is shown in Fig.1. An electron gun for the probing was set at the position z=305mm. The probe beam passes

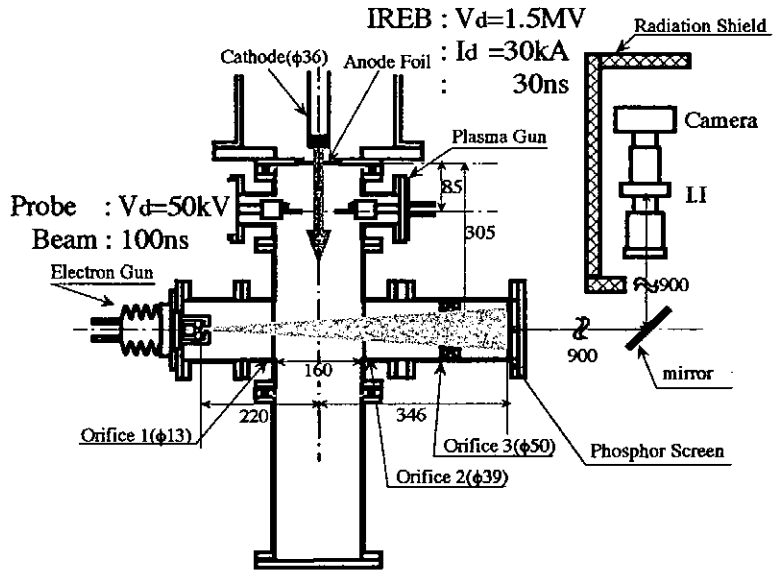

Figure 1: Experimental setup

through the chamber perpendicularly to the IREB. A probe beam with current of $\sim$ 50mA is obtained by applying a pulse voltage of 50kV to the electron gun. The probe beam diverges slightly. The cross-section increases with the distance from the gun. The distance from the electron gun to the center of the main chamber is 22.0cm, and that from the center to the phosphor screen is 34.6cm. The orifices are set along the path of the probe beam as shown in Fig.1.

A phosphor screen is used to detect the probe beam. The camera system has a high-speed response up to 5ns. The system is composed of an image intensifier unit and a digital camera. The gate function of this system can prevent mixing of the noise of the IREB. The phosphor, P47, is used, whose decay time of emission is $\sim$ 25ns to 50%. The pulse length of probe beam is 100ns, and it gives the resolution time of the diagnostic system.

Deflection of the probe beam was tested with the known static electric field, before the probe beam injected into the plasma.

3 Experimental results

The time schedule is shown in Fig.2. The time from IREB injection to the probing is taken as a parameter, δ.

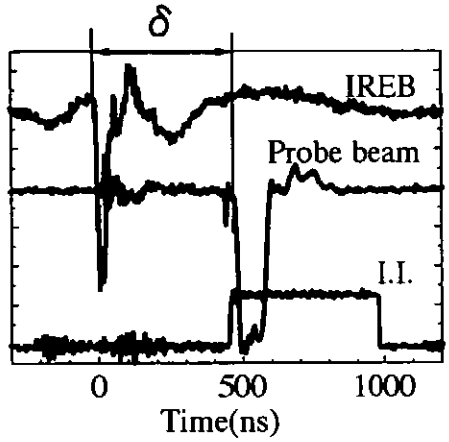

Figure 2: An operation for the probing. From a top, (1) the waveform of V_d of IREB, (2) the waveform of the accelerating voltage for the probe beam, and (3) the gating pulse for the image intensifier are shown. A plasma gun was fired the τ second before the injection of IREB. Moreover, the time from IREB injection to the probing is taken as the parameter, δ.

3.1 The pattern with many holes

The photographs of a phosphor screen are shown in Fig.3. The dark part on the photograph is the part where the electrons hit the screen. The length of one side of the photograph is 75mm. Figure 3(a) is the case of a vacuum. It corresponds to the beam pattern without deflection. The diameter of the probe beam is limited by the first orifice placed at the entrance of the main chamber. The cross-section of the probe beam passing through the plasma is observed as a circle in the figure. Inhomogeneity in the cross-section of the probe beam is observed.

Both of figures 3(b) and 3(c) are taken at $\tau = 80\mu$s, when the chamber is filled with the plasma. Figure 3(c) is the case that the IREB is injected into the plasma. As no difference between Fig.3(a) and 3(b) is observed, the probe beam is not affected by the plasma. However, many holes with various sizes are observed in Fig.3(c). The probe beam was affected by the IREB injected plasma. Though the similar pattern with many holes is observed in every shot, the position of the holes changes.

Many holes are observed in the case of the IREB injection at $\tau = 60 - 100\mu$s. The plasma density decreases as τ increases. As shown in Fig.4, when the plasma density is increased, the size of the hole decreases, and the number of holes increases. For example, a number of holes are seen at the whole surface in Fig.4(a).

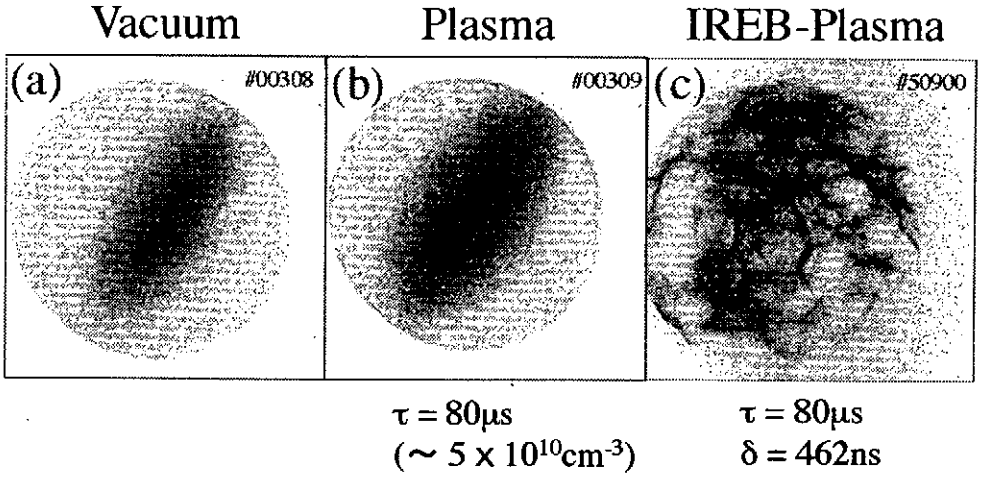

Figure 3: Examples of the beam pattern before and after the deflection. (a) a vacuum, (b) a plasma, and (c) the plasma after an interaction of IREB. (b)-(c); τ = 80μs, (c) δ=462ns.

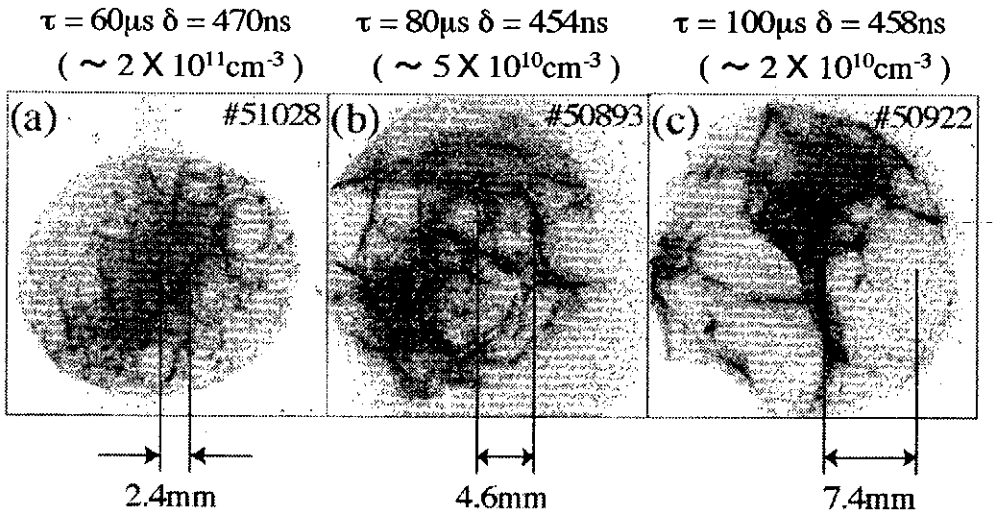

Figure 4: Examples of beam pattern with many holes. The density dependence is shown here. (a) $\tau = 60\mu s$, (b) $\tau = 80\mu s$, (c) $\tau = 100\mu s$. For each cases, the plasma density is (a) $n_p = 2 \times 10^{11}\text{cm}^{-3}$, (b) $n_p = 5 \times 10^{10}\text{cm}^{-3}$ and (c) $n_p = 2 \times 10^{10}\text{cm}^{-3}$ respectively. The dimension of 20 Debye lengths is shown in the figure for comparison.

A characteristic size of the holes changes with n_p clearly. As the density decreases, the diameter of the hole increases. The scale of $20\lambda_D$ is shown in the figure for comparison. The dimension of $20\lambda_D$ is estimated to be (a) 2.4mm, (b) 4.6mm, and (c) 7.4mm, where, the electron temperature was assumed to be constant, 50eV. The divergence angle of the beam was taken into account. The average size of the holes is evaluated to be the order of $20\lambda_D$.

The hole in the shadowgraph indicates lower current density. The area where holes overlap has high current density instead of the density reduction. It is thought that the probe beam was piled in drifts.

3.2 Time transition

The measurement becomes possible after δ=300ns because of the S/N. The measurement was carried out after this time. The clear image of the hole is not observed for any shot at the time δ=300-450ns. The number density of holes is not large and the picture is not so sharp. Holes are clearly recognized at the time of δ=450-700ns. Since the picture is sharp, it suggested that the pattern and the size do not change in the time duration of 100ns, which is the pulse length of the probing pulse. The size of the holes depends only on the τ, but does not have dependency to the δ. At the time δ=700-1600ns, the picutre of the holes becomes thinner and fewer. It becomes impossible to observe any deflection after $\delta > 1600$ns. The pattern returns to that observed before the IREB injection.

4 Discussion

Generally, in the case of electron beam probing, the deflection angle is measured. The deflection angle is given as proportional to both the intensity and the size of the electric field. Here, we know neither of them now. Then we presume the caviton electric field and its self-similarity, which is predicted by strong-turbulence theory. The calculated deflection angle and the beam pattern after the deflection by a caviton will be given. Comparisons between the theory and experiment will be carried out.

4.1 Theory of deflection

4.1.1 Angle

First of all, we pay attention to the deflection by one caviton. Inside the caviton, high frequency electrostatic wave oscillates with plasma frequency. The period of the electric

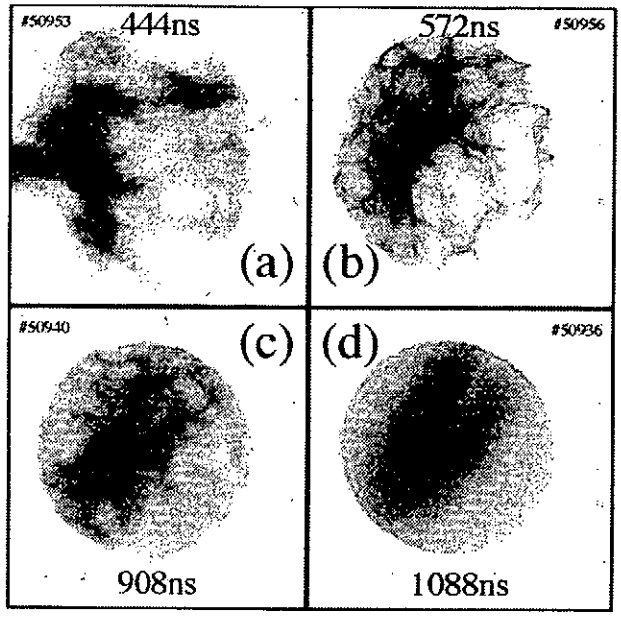

Figure 5: The typical patterns showing the time transition after the IREB pulse. (a) δ =444ns, (b) 572ns, (c) 908ns, and (d) 1088ns in the case of $\tau = 60\mu s$

field oscillation is assumed much shorter than the pulse width, 100ns, of the probe beam. The probe beam will be deflected in the plus and the minus direction within the angle θ_{max}, just as a scattering. The amplitude of θ_{max} is calculated by assuming the dipole potential with Gaussian envelope. For simplicity, the linearly polarized field is considered. And the polarization is perpendicular to the probe beam. The probe beam propagates along the y-axis. The electric field in the x-y plane is expressed as [1],

$$E_x(y) = E(0)\exp(-y^2/a^2)\cos(\omega_p\, t). \tag{1}$$

Here a is the characteristic width of caviton and E_0 is the central-field strength. The E_0 corresponds the maximum field in a caviton. The maximum angle of deflection ,θ_{max}, for the electron with a velocity v_b, and energy of eV_0 is calculated from

$$\tan\,\theta_{max} \approx \int E_x dy/2V_0 \approx E(0)\int_{-\infty}^{+\infty}\cos(y\,\omega_p/v_b)\,\exp\,(-y^2/a^2)\,dy \approx \theta_0\, e^{-\xi^2}, \tag{2}$$

where

$$\xi = \frac{a\,\omega_p}{2v_b} = a'\sqrt{\frac{T_e}{8V_0}}\ \text{rad.} \tag{3}$$

The T_e is the electron temperature in eV, and $a' = a/\lambda_D$. Here,

$$\theta_0 = \sqrt{\pi}\,aE(0) = \sqrt{\pi\Theta}\,T_e/V_0 \tag{4}$$

Θ is the threshold value for collapse, $\Theta \approx 61.8$. The deflection angle is proportional to T_e, but dose not depend on n_p. The experimental conditions, V_0=50 kV, T_e=50 eV, lead,

$$\theta_0 \approx 0.014 \text{ rad.} \approx 0.80 \text{ deg.} \tag{5}$$

While the collapse of a caviton, a becomes small and $E(0)$ increases with keeping the $aE(0)$ constant[1]. Although $theta_0$ does not change with the size of caviton, $theta_{max}$ is deduced by the factor e^{-xi^2}, when the caviton is large. For example, θ_{max} decreases by a factor more than 0.5 from the θ_0, at $a' > 50$. The caviton with large size, i.e. $a' \gg 50$, the deflection of the probe beam becomes too small to detect. When a' becomes small, θ_{max} is nearly equal to θ_0. As a result, the deflection by the small caviton can be detected.

4.1.2 Pattern

The probe beam projects the caviton field on a phosphor screen, see Fig.6. A hole with elliptic shape, whose minor axis is in the direction of polarization, is typically obtained at $10 < a' < 50$. The beam density becomes lower in side the hole, though the higher density regions are appeared at the periphery, especially at the locations of the poles of electrostatic potential. Theoretically the distance between the two poles is $\sqrt{2}\,a$ here. If the caviton size becomes small, $a' < 10$, the electrons on different paths inside a caviton cross each other before reaching the screen. Then the shape of the pattern becomes more intricate. When $a' > 50$, the hole cannot be observed.

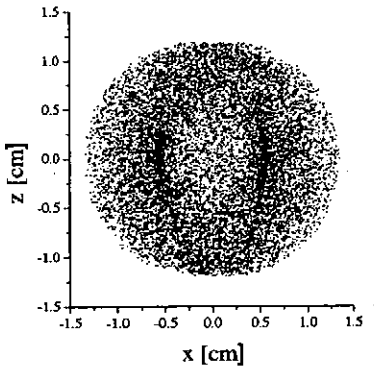

Figure 6: Calculated deflection pattern. $n_p = 2 \times 10^{10}\text{cm}^{-3}$, T_e=100eV, V_0=50kV, $a = 15\lambda_D$, Θ=61.8, y=34.6cm.

4.2 Experimental results

(i)

The size of the hole obtained by the calculation agree with the experiment. The dimension of the hole is observed to be $\sim 20\lambda_D$.

(ii) The IREB density is considered to be high enough to excite the Langmuir wave whose energy density is comparable to the thermal energy. The number of the caviton, N_C can be estimated from the theory in Ref. [1]. $N_C = 1\text{cm}^{-3}$ at $n_p = 1 \times 10^{10}\text{cm}^{-3}$, $N_C = 22\text{cm}^{-3}$ at $n_p = 1 \times 10^{11}\text{cm}^{-3}$, and $N_C = 698\text{cm}^{-3}$ at $n_p = 1 \times 10^{12}\text{cm}^{-3}$ are estimated. The N_C changes due to the small change of n_p. The number density of holes obtained in the experiment is nearly equal to those numbers.

(iii) The large deflection was observed after IREB injection and for a while, $\sim 1\mu s$. The property of the time transition of the deflection can be explained as following. Many cavitons with various sizes will be created by an IREB with duration of 30ns. After the IREB passed through the plasma, the first caviton becomes small enough to give the observable deflection. The deflection occurs similarly until the last caviton burning out. The time duration that the observable deflection continues is evaluated by the time that ion sound wave propagates the dimension of $10\lambda_D$. It is estimated to be $\sim$ 260ns for a carbon plasma. This agrees with the time scale of our experiment, *i.e.* $\sim$ 250ns.

(iv) In previous experiment[9], the probe beam, which was well focused to a spot, was employed. A scattering of the beam was occurred at the similar condition for τ and δ. The observed deflection angle agreed also with the calculation mentioned in this paper.

5 Summary

Although the deflection by two or more cavitons has not been investigated yet, the hole in the deflected pattern can be explained by the caviton model using proper parameters.

Acknowledgement

This work was supported in part by a grant-in-aid from the Ministry of Education, Science, Sport and Culture of Japan.

References

[1] P. A. Robinson, "Nonlinear wave collapse and strong turbulence," Rev. Modern Phys., **69**, 507–573 (1997).

[2] M. D. McFarland, A. Y. Wong, "Spatial, spectral, and statistical properties of the high-frequency electrostatic fluctuations in a beam-driven turbulent plasma," Phys. Plasmas, **8**, 110–121 (2001).

[3] M. Yoshikawa, *et al.*, "Spectroscopic measurements of intense relativistic electron beam driven turbulence," J. Phys. Soc. Jpn., **63**, 3303–3310 (1994).

[4] M. Yoshikawa, *et al.*, "Correlation between high-power broadband microwave radiation and strong Langmuir turbulence in an intense relativistic electron beam-plasma system." J. Phys. Soc. Jpn., **65**, 2081–2086 (1996).

[5] R. Ando, *et al.*, "Microwave power emission from a beam-plasma system," J. Phys. Soc. Jpn., **65**, 2518–2521 (1996).

[6] H. Yoshida, *et al.*, "Measurements of broad-band millimeter-wave radiation from an IREB-plasma interaction system," IEEE Trans. Plasma Sci., **27**, 682–687 (1999).

[7] H. Koguchi, *et al.*, "Time evolution of beam energy distribution and perpendicular velocity scattering due to strong Langmuir turbulence," J. Phys. Soc. Jpn., **26**, 1273–1280 (1998).

[8] R. Ando, *et al.*, "Measurement of strong Langmuir turbulence fields using an electron beam probe," in Proc. 12th Int. Conf. High-Power Particles Beams, Haifa, Israel, 1998; vol. I, pp. 361-364, ISBN:0-7803-4287-9.

[9] R. Ando, *et al.*, "Electron beam probing of strong Langmuir fields in an intense beam-plasma system," IEEE Trans. Plasma Sci., **27**, 1545-1547 (1999).

[10] R. Ando, *et al.*, "Measurement of IREB-driven strong Langmuir field using electron beam probing technique," in Proc. 13th Int. Conf. High-Power Particles Beams, Nagaoka, Japan, 2000; pp. 893-896.

DISCHARGE EVOLUTION IN A PULSED METAL POWDER PLASMA CREATION

T. Kuraoka*, H. Nozawa, H. Naito, S. Ibuka, K. Yasuoka and S. Ishii

Department of Electrical and Electronic Engineering
Tokyo Institute of Technology
2-12-1 O-okayama, Meguro-ku, Tokyo, Japan

ABSTRACT

A plasma created from metal powder was obtained under pulsed high current discharges. Powder flow was injected transiently between the electrodes in vacuum. The powder particles are spherical and are accelerated by pulsed electrostatic fields. Other control methods for powder flow were discussed. Discharge evolution in a pulsed metal powder plasma was examined using a high-speed cameras and a spectrometer.

1. Introduction

We proposed to use powders instead of gases as an initial matter for creating plasmas by high-current pulsed discharge. The powder plasmas have various advantages compared with gaseous plasmas. To control spatial distribution of powders is easier than gases because of its larger mass when they are transiently injected between discharge electrodes. Since powders are solid state, there are more kinds of material to be used as plasma medium in comparison with gaseous plasmas. Generally, dust particles in the plasma were unfavorable in processing plasmas[1] or in magnetically confined plasma apparatus[2]. In our study, powders are positively used to create plasmas, that takes a different direction to the research on dusty plasmas. Powder produced plasmas have a possibility of various applications such as z-pinch, analysis of arc physics in vacuum circuit breakers, thin film deposition in material science, intense soft X-ray source, and so on.

Gas-puff z-pinches and wire array z-pinches are the typical examples of the z-pinch created from locally isolated initial medium in vacuum. The feature of the gas-puff z-pinch is that dense plasmas can be created in a reproducible manner at a high repetition rate. The gas-puff z-pinch requires fast-acting electromagnetic valves and well-designed gas nozzles to establish the initial gas distribution. Since the puffed gas spread with a sonic speed in vacuum, it is difficult to control the initial density distribution. The wire array z-pinch can also produce a high-density plasma from solid matter. However, mounting the wire array in the proper position between the electrodes is so difficult, that the repetition rate becomes low. The powder z-pinch has both advantages of high repetition rate operation and high initial mass density. In addition, it may be possible to obtain more complex discharge characteristics using multi-coated powders.

In order to create plasmas from powder, it is necessary to inject powders between discharge electrodes. We employed an electrostatic control of the powder injection system, in which electrostatic fields accelerate particles between parallel plate electrodes.

In this study, we produced pulsed powder plasmas and observed early stage of the discharge using a high-speed image converter camera and a spectroscopic analyzer.

2. Experiment

2.1 Control of powder injection

Powders are transiently injected between the discharge electrodes in vacuum prior to the discharge. There may be many kinds of powder injection methods. The powder injection system is required to have easiness of operation, compact in size, and reproducible operating properties. By taking this requirement, we designed an electrostatic controlled powder acceleration system.

Two plane electrodes are placed in parallel separated by an insulator spacer. The upper electrode has a hole at the center for powder ejection and the bottom one has a shallow conical structure with nine-degree slope down toward the center and with the circumference of 16mm in diameter. The conical structure prevents powders from spreading around and makes them gathering into the center again. When a pulsed voltage is applied between the electrodes, powders on the bottom electrode are charged to Q with the same polarity of the electrode. The charge Q is written as[3],

$$Q = \frac{2}{3}\pi^3 \varepsilon_0 r^2 E_0$$

where ε_0 is permittivity in vacuum; r particle radius; and E_0 electric field between the electrodes; respectively. Powders are attracted to the upper electrode by the electrostatic force F_e ($=QE_0$). When F_e becomes greater than the gravitational force F_g, the powders are accelerated toward the upper electrode and some part of those will be ejected from the hole[3].

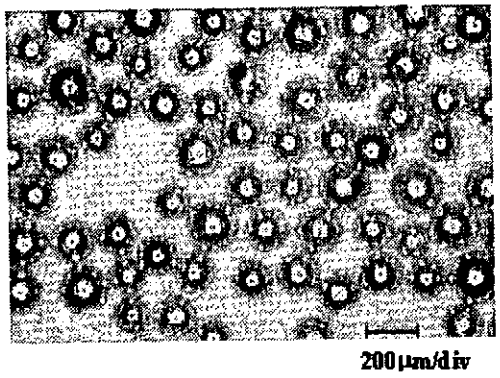

Figure 1. Photomicrograph of the spherical copper powder

2.2 Experimental procedure

We employed spherical copper powder with a particle diameter of 75μm in the experiments. Figure 1 shows a photomicrograph of the copper powder particles with a diameter of 150mm. Figure 2 shows the experimental setup for powder discharges. The discharges were powered by a capacitor of 4.5μF charged to -20kV. The discharge electrodes with the powder injection system were placed in a vacuum chamber evacuated to a pressure of 10^{-5} Torr.

Main discharge electrodes made of titanium were placed above the powder injection system. The lower electrode of the main discharge connected to the ground potential acted as a upper electrode of the powder injection system. The upper electrode had a hole at the center with a diameter of 2mm for particle injection. The electrode separation was 10mm for the main discharge.

The acceleration electrodes of the powder injection system were separated by an acrylic insulating spacer with the thickness of 10mm in height and the inner diameter of 16mm. A driving voltage applied to bottom electrode was 8kV and its pulse width was 100ms. The rectangular pulsed voltage applied to the powder injection electrodes was generated by switching on and off using a high voltage relay.

Since the injected particles were located apart from each other between the electrodes in vacuum, breakdown processes were complicated. The particles are supposed to be ionized preceded by heating and evaporation processes. However, the breakdown voltage between the electrodes with powder was almost similar to that in vacuum. Consequently the discharge time delay was long and reproducibility of the discharges was poor. To establish reproducible powder discharges, a pre-ionization system was necessary to supply initial electrons. We placed an additional electrode at the center of the high voltage electrode. When the main capacitor was fired, a surface discharge current flew between the additional electrode and the high voltage electrode. The surface discharge provided sufficient amount of initial electrons for pre-ionization. The pre-ionization discharge ceased when a 500pF capacitor was charged up.

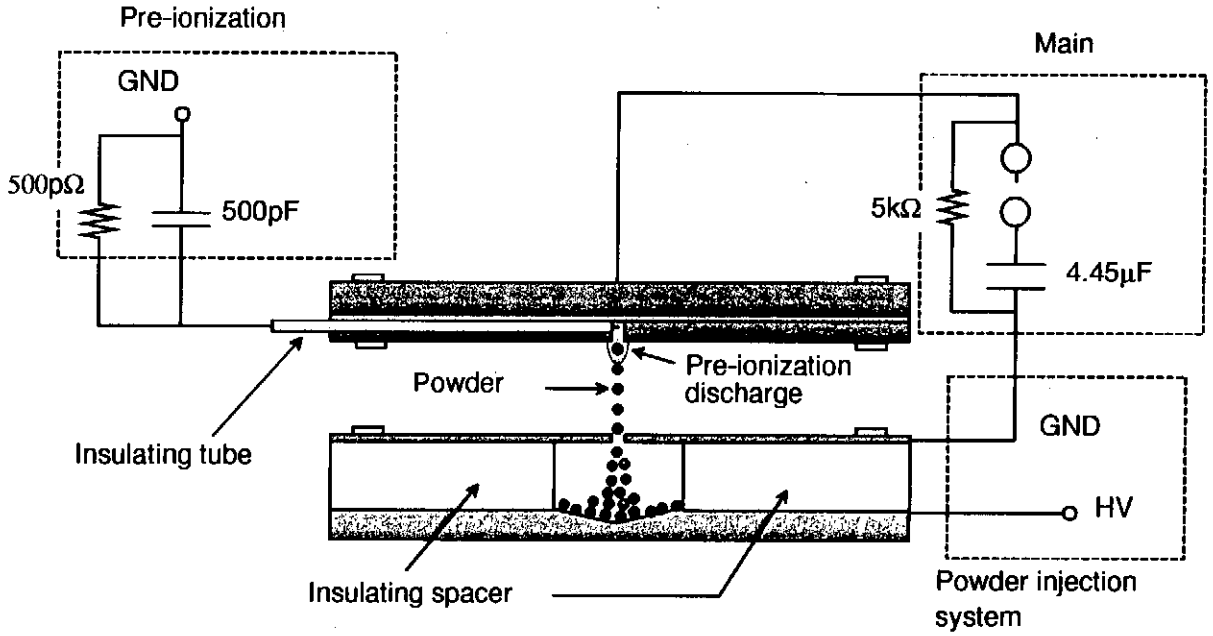

Figure 2. Experimental setup of the pulsed powder discharge with an electrostatic powder injection system

3. Results and Discussion

3.1 Injected powder distribution

The spatial distribution of injected powder was observed by taking a photograph of particles illuminated by a flashlamp in the air. Figure 3 shows a photograph of the injected copper powder taken at the timing of 120ms after applying the acceleration voltage pulse when the number of particles reached the maximum. About seventy-particles were observed above the injection hole. The behavior of the particles in vacuum will not be so different from that in the air because the viscous drag force by the air is negligibly small. The number of particles is plotted in figure 4 when the injection operation is repeated. Almost the same number of particles was obtained until two hundred shots. The number of shots being able to inject constant amount of powder depends on the initial mass placed on the electrode. Since the measurements were performed without the main high voltage electrode, particle flow pattern would change slightly if the discharge electrode was placed above the injection hole.

Figure 3. Photograph of the injected powders

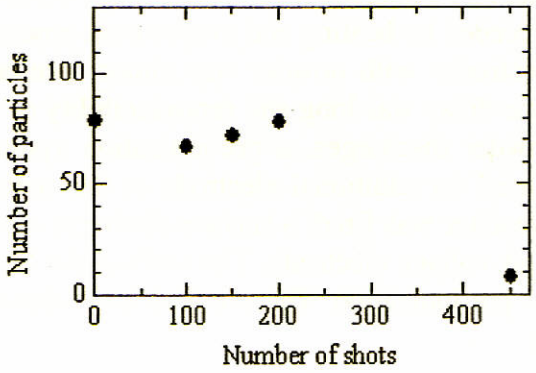

Figure 4. Number of the injected powders

3.2 Discharge experiments

The early stage of powder discharge was observed using the image converter camera (Hadland Photonics, Imacon468) by framing mode with the exposure time of 100ns. Each frame has the time interval of 150ns.

When the powder was not injected between the electrodes, the discharge developed as a vacuum discharge. A set of framing photographs is shown in Figure 5. Although they are not taken in a single discharge, they are selected as showing the typical profile at each time among many data. The temporal behavior of the discharge is explained as follows. When the capacitor was fired, initial electrons created by the pre-ionization discharge were accelerated and bombarded the anode. Anode plasma was generated from the anode vapor that was boiled off by the electron bombardment. The anode plasma expanded toward the cathode. At this stage, filamentary plasma channel was sometimes formed between the cathode and the anode plasma. Finally, the anode plasma reached the cathode. A bright plasma column was formed between the electrodes.

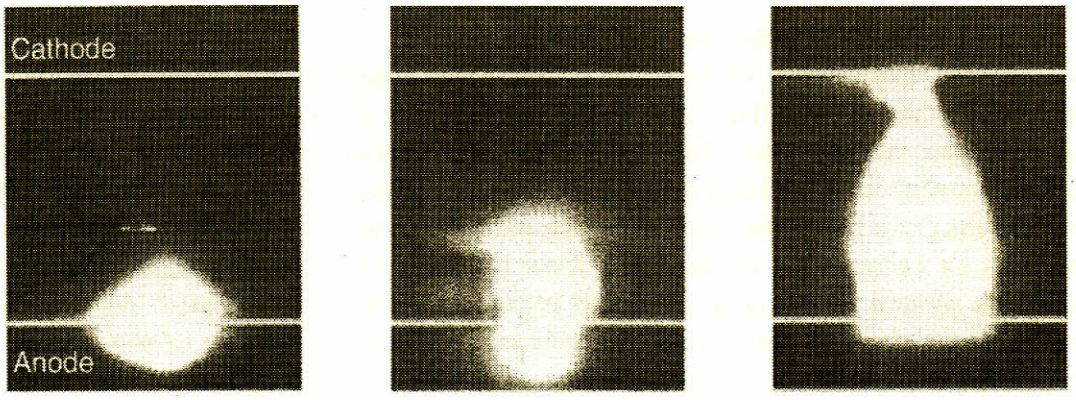

Figure 5. Framing photographs of the early phase of the discharge without powder injection.

The typical framing photographs of temporal development of the powder discharge are summarized in figure 6. The temporal behaviors are classified into two types as shown in Figure 6(a) and (b).

At the beginning of the discharge, spot-like light emission from the particles is observed. The emission seems to be originated from evaporation and ionization of the particles by electron collisions. In Figure 6(a), although the anode plasma grew from the anode to the cathode, the particles were clearly seen between the electrodes. However, the macroscopic behavior of the discharges was almost similar to that without powder as shown in figure 5. In the other case, shown in Figure 6(b), narrow plasma channel bridged between the cathode and growing anode plasma region. The diameter of the channel was irregular.

From the viewpoint of applications, powder must be uniformly ionized to form a plasma channel. In our experiment this is not the case. The discharge was a combination of powder discharge and the vacuum discharge. However the effective cross section of electron to the anode surface was much larger than that to particles. Since the mass of evaporated material from the anode was also larger than that from the particles, the discharge current was supported by the anode plasma.

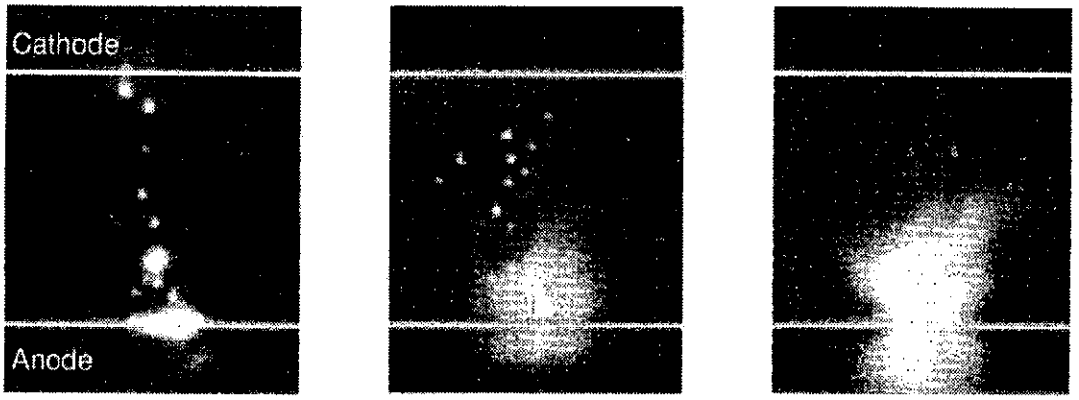

Sequential photographs (a)

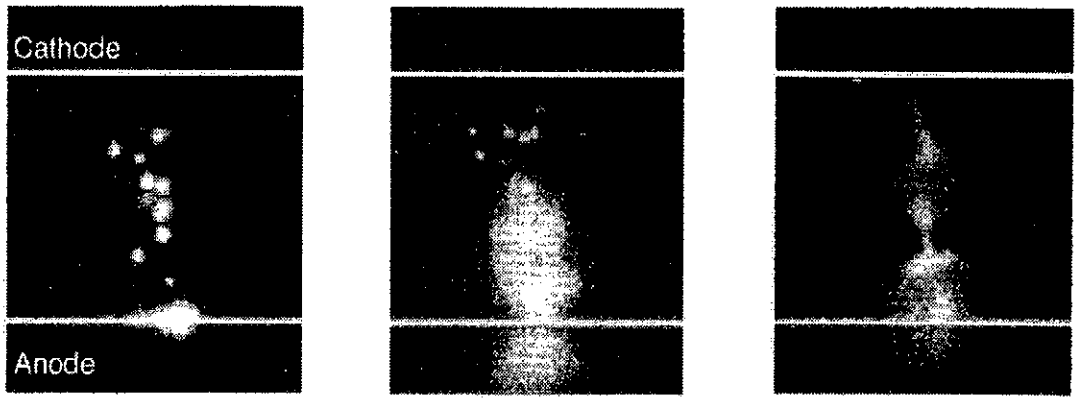

Sequential photographs (b)

Figure 6. Framing photographs of the early phase of the powder discharge

In order to examine vaporization and ionization process of the particles, spectroscopic measurements were done using the spectrometer of visible wavelength range. However, meaningful difference was not observed between the vacuum discharges and the powder discharges.

4. Conclusions

In this work, we generated the pulsed powder discharge that is a new scheme for creating plasmas from solid materials. We constructed the electrostatic powder injection system and achieved the stable injection until two hundred shots. Observation of the early stage of the discharge was performed using the image converter camera. Spot-like light emission from the powders was observed at the beginning of the discharge. Two kinds of discharge development were observed. The one was macroscopically similar to vacuum discharge and the other had narrow plasma channels between the cathode and the anode plasma. The obtained discharge was a combination of powder discharge and the vacuum discharge because the evaporation from the particle was poor.

References

1) Andre Bouchoule: *Dusty Plasmas* (John Willey & Sons, Ltd., 1999)
2) J.Winter: Phys. of Plasmas, 7, no.10 (2000) p.3682
3) A.Y.H. Cho: J.Appl.Phys. 35, no.9 (1964) p.2561
4) L.Dascalescu, M.Mihailescu and R.tobazeon: IEEE Trans. Ind. Appl. 34, no.1 (1998) p.66-74

OPTICAL OBSERVATION OF THE INSTABILITY IN MICROSECOND GAS-PUFF Z-PINCH

Koichi Murayama , Sunao Katsuki[1] and Hidenori Akiyama[1]

Department of Mechanical and Electrical Engineering, Yatsushiro National College of Technology, Hirayama-shinmachi, Yatsushiro 866-8501, Japan
[1]Department of Electrical and Computer Engineering, Kumamoto University, Kurokami 2-39-1, Kumamoto 860-8555, Japan

ABSTRACT

The growth mechanism of instability in gas-puff z-pinch plasma was investigated using laser diagnostic systems. An interferometer system was employed to investigate the temporal evolution of the structure in the plasma column during the pinch. The z-pinch plasma was driven by a fast bank, which provided a current of 160 kA for 1.5 μs quarter period of oscillation. The plasma layer moved toward the z-axis and its shape gradually changed into columnar. The plasma layer splits into two layers on the way to implosion. The inner layer, which was indicated to be shock front, propagated toward the z-axis faster than the outer layer. The outer layer seemed quite smooth while the implosion by the inner layer took place at the z-axis. After the blast from the implosion expanded and came across the outer layer, the disturbance occurred at the outer layer and then the instability was caused in plasma column.

1. Introduction

Intense soft X-rays radiated from z-pinch devices have a potential to be used for several industrial applications, for example lithography in semiconductor device processing,[1)] soft X-ray microscopy etc. Although these devices are quite simple, small and inexpensive, they are expected to be of high efficiency in comparison with the synchrotron obituary radiation (SOR). The gas-puff z-pinch scheme [2-6)] enables the production of soft X-ray radiation with a high repetition rate. However, the gas density gradients not only in the axial direction but also in the radial direction are considered to lead the z-pinch plasma to instabilities, which degrade the reproducibility of X-ray radiation. On the other hand, a current of up to 200 kA is easy to handle and to generate using a simple fast capacitor bank. A typical rise time of the current provided by such a small bank is in the microsecond range. The instability grows significantly in this range. There are plenty of computational and experimental works on plasma instabilities to explain the process of its growth for a wide variety of devices. However, they do not describe the triggering mechanism of the instability in detail.

The purpose of this paper is to experimentally observe the temporal behavior of gas-puff z-pinch plasma and to figure out what triggers the plasma instability in the slow implosion system. A compact gas-puff z-pinch device driven by a 1.9 kJ fast capacitor bank was used in this experiment. The temporal behavior of the z-pinch plasma is discussed using the interference images of z-pinch plasma at different times and of different shots obtained using a holographic pulsed laser interferometer and a shadowgraph.[10-13)]

2. Experimental Setups and Procedures

Figure 1 shows the schematic diagram of the z-pinch electrodes. The z-pinch device consists of a brass anode that is equipped with an annular nozzle. A stainless steel mesh

cathode is used to avoid the gas stagnating on the cathode surface.[10] The nozzle is slightly inclined to the z-axis to in order to suppress the diffusion in the radial direction. The transparency of the mesh cathode is 81%. Ar gas is puffed from the anode nozzle. The plasma current is provided from a 6 μF capacitor bank, which is charged up to 25 kV (1.9 kJ). The main gap switch for the current is fired at 1.4 ms after the gas-puff actuator is triggered.

The X-ray is obtained by using a PIN photo diode. Since it is equipped with a 3 μm thick Al film, the photon energy to be detected is limited to more than 1 keV, which is from photons in the K-shell of Ar.[14].

Figure 2 shows the schematic arrangement of the Mach-Zehnder pulsed laser interferometer. Second harmonic wave (532 nm) of the Nd-YAG laser (Continuum, Surelite-II, 600 mJ, 5 ns) was used. The interference image was recorded on instant films after passing through a neutral density (ND) and laser line filters. A window with appropriate thickness is inserted in the reference arm of the interferometer to compensate the difference in the optical length of each arm. The system can be easily changed into a shadowgraph configuration by inserting a screen in the reference arm. The temporal behavior of the z-pinch plasma is discussed from the images at different times, which were acquired in different shots.

3. Experimental Results and Discussions

Figure 3 shows typical waveforms of the driving current and a signal from PIN diode. The current reached 160 kA and slightly dropped when X-ray was radiated.

Figure 4 shows the sequential interference images of z-pinch plasmas during the process to the implosion. Figure 5 shows the shadowgraph images of z-pinch plasmas. Each image in Figs. 4 and 5 was obtained from an independent shot. The first image shows the view of sight just before the plasma was initiated. The fringes around the nozzle were shifted due to the annular plasma at 300 ns. However, the shape in the cathode side is still not clear. The whole feature of the plasma column came out around 500 ns and the discharge was formed in conical shape. The diameter of the plasma near the anode did not change so much while that near the cathode was dynamically reduced, despite the larger J x B force should take place at the current layer with the reduced radius. This is explained to be caused by the gas density gradient along z-axis. High gas density near the anode sustained the J x B force. Figure 6 shows the time evolution of the plasma column diameter near the both of electrodes. The initial drift velocity of the plasma layer near the cathode is estimated to be 2 cm/μs that was more than 4 times faster than that near the anode. The plasma drift velocity near the anode was gradually reduced. The gas density gradient in the radial direction might influence the drift velocity. Finally the plasma diameter near the cathode was stagnated as well as that near the anode and the plasma radius along the z-axis became almost the same. All the data acquired at Δt of more than 1200 ns showed perturbations on the plasma surface as shown in Fig 5 (c).

Returning back to Figs. 4 and 5, in order to see what happens in detail until the perturbation appears on the plasma surface. A double layer structure came out around 600 ns. This structure was observed also in the shadowgraph in Fig. 5 (a). The outer and inner structures were supposed to be the current sheet and the shock front, respectively. The inner layer moved faster than the outer layer and imploded at the z-axis. The outer layer was stagnated but its surface seems quite smooth during the implosion by the shock front. After the implosion, something complex like a blast from the implosion started expanding. The temporal behaviors of the structures at the cathode and at the anode surfaces are summarized in Figs. 7 (a) and (b), respectively. The instability on the outer layer started growing after collision with the inner structure. This indicates that the plasma instability was initiated by the

shock wave. In the last image in Fig. 4, high density plasmas, which might be produced by X-rays from z-pinch plasma, appeared on the anode. As shown in Figs. 6 and 7, the behavior of the plasma structure until 1100 ns was reproducible in this experiment.

This paper describes the z-pinch plasma driven by a microsecond current. Plasmas driven by a current with short rise time in the range of several tens of ns is an interesting objective for the next experiment. An inductive voltage adder machine, which is equipped with a POS[15], are being prepared for the experiment.

4. Conclusions

Measurement of the gas density distribution and the temporal observation of the z-pinch plasma, which had been driven by a small and slow-rise current, were conducted using laser diagnostic systems. The plasma layer moved toward the z-axis and its shape gradually changed into columnar. The plasma layer splits into two layers on the way to implosion. The inner layer propagated toward the z-axis faster than the outer layer. After the blast from the implosion expanded and came across the outer layer, the disturbance occurred at the outer layer and then the instability was caused in plasma column.

References

[1] E. W. Becker, W. Ehrfeld, P. Hagmann, A. Maner and D. Munchmeyer: Microelectron. Eng. **4** (1986) 35.

[2] M. Badaye, R. Stempork and R. P. Gupta: Rev. Sci. Instrum. **61** (1990) 1457.

[3] J. Du, T. Ohata, K. Shimoda and K. Hirano: Jpn. J. Appl. Phys. **64** (1995) 4185.

[4] K. Takasugi, H. Suzuki, K. Moriyama and T. Miyamoto: Jpn. J. Appl. Phys. **35** (1996) 4051.

[5] I. Okada, Y. Saitoh, S. Itabashi and H Yoshihara: J. Vac. Sci. & Technol. **B4** (1986) 243.

[6] K. Murayama, T. Shinkai, S. Katsuki and H. Akiyama: Jpn. J. Appl. Phys. **37** (1998) 2676.

[7] B.V. Weber and S.F. Fulghum: Rev. Sci. Instrum. **68** (1997) 1227.

[8] B.V. Weber and D.D. Hinshelwood: Rev. Sci. Instrum. **63** (1992) 5199.

[9] I.V. Lisitsyn, S. Kohno, S. Katsuki and H. Akiyama: Rev. Sci. Instrum. **69** (1998) 1584.

[10] S. Katsuki, K. Murayama, T. Nishi, I.V. Lisitsyn and H. Akiyama: Proc. of 12th IEEE Pulsed Power Conf., Monterey, USA, 1999, p. 1067.

[11] E. Wyndham, H. Chuaqui, M. Favre, L. Soto and P. Choi: J. Appl. Phys. **71** (1992) 4164.

[12] R.A. Riley, R.H. Lovberg, J.S. Shlachter and D.W. Scudder: Rev. Sci. Instrum. **63** (1992) 5202.

[13] L. Soto, H. Chuaqui, M. Favre, R. Saavedra, E. Wyndham, R. Aliaga-Rossel and I. Mitchell: Proc. 11th Intern. Conf. High Power Particle Beams (BEAMS '96), Prague, Czech, 1996, p.762.

[14] H.J. Hagemann, W. Gudat and C. Kunz: J. Opt. Soc. Am. **65** (1975) 742.

[15] S. Kohno, Y. Teramoto, S. Katsuki, I.V. Lisitsyn and H. Akiyama: Jpn. J. Appl. Phys. **39** (2000) 2829.

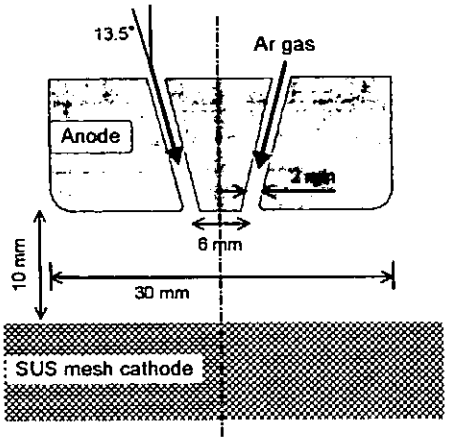

Fig. 1. Schematic diagram of the z-pinch electrodes.

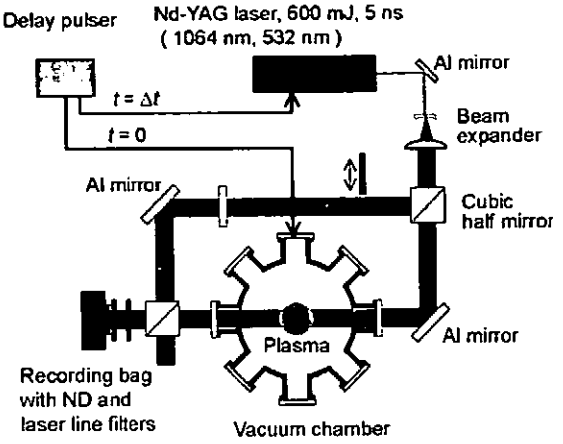

Fig. 2. Schematic diagram of the Mach-Zehnder pulsed laser interferometer.

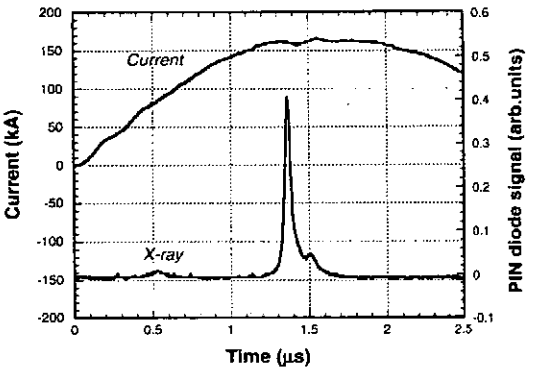

Fig. 3. Typical waveforms of the driving current and X-ray radiaion.

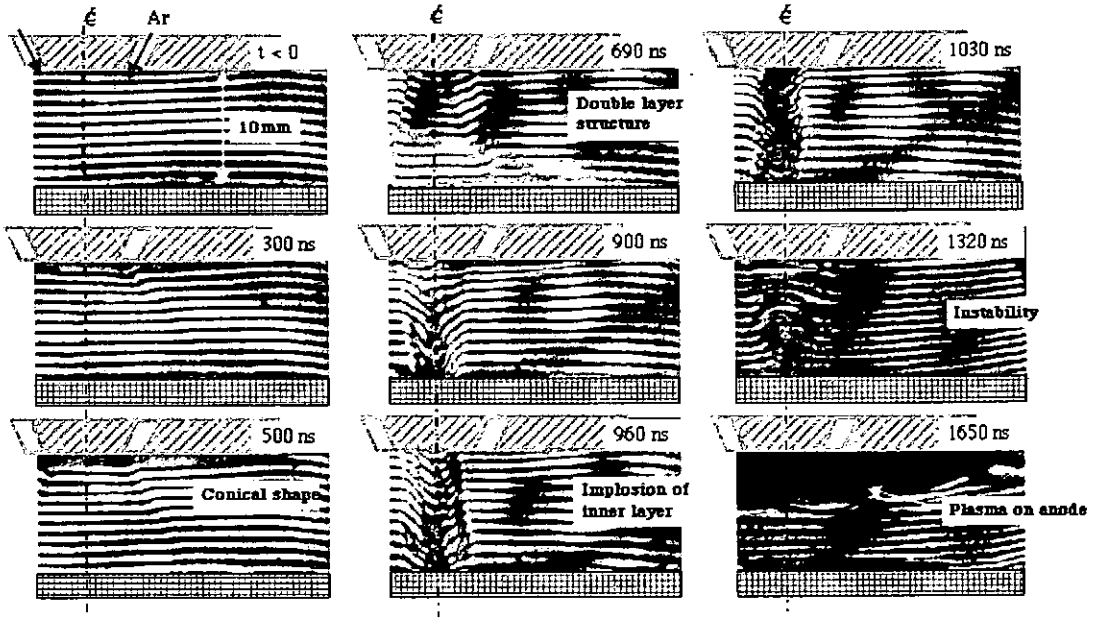

Fig. 4. Temporal behavior of z-pinch plasma column obtained by the laser interferometer.

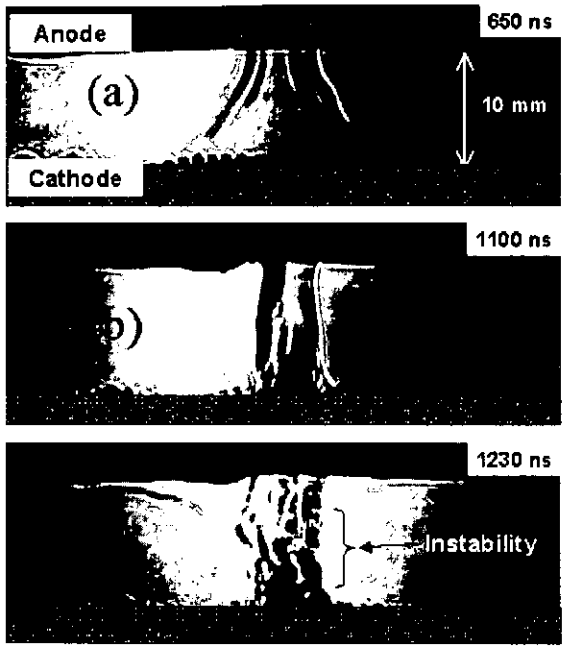

Fig. 5. Shadowgraph images of z-pinch plasma at different time during implosion.

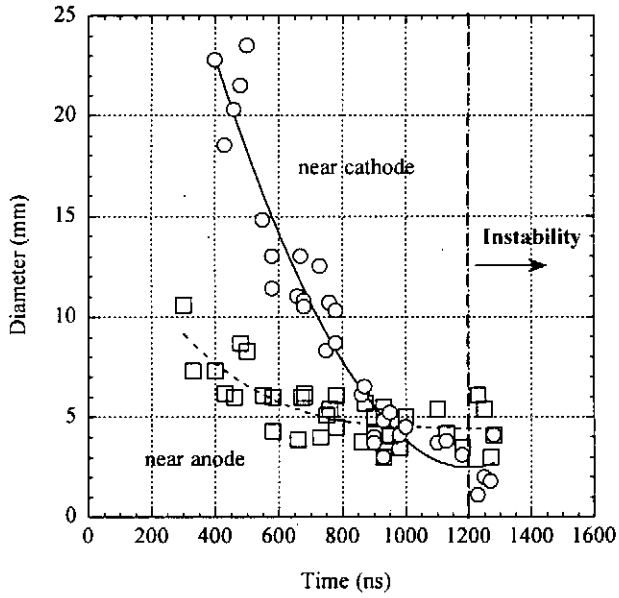

Fig. 6. Time evolutions of plasma diameters near the electrodes.

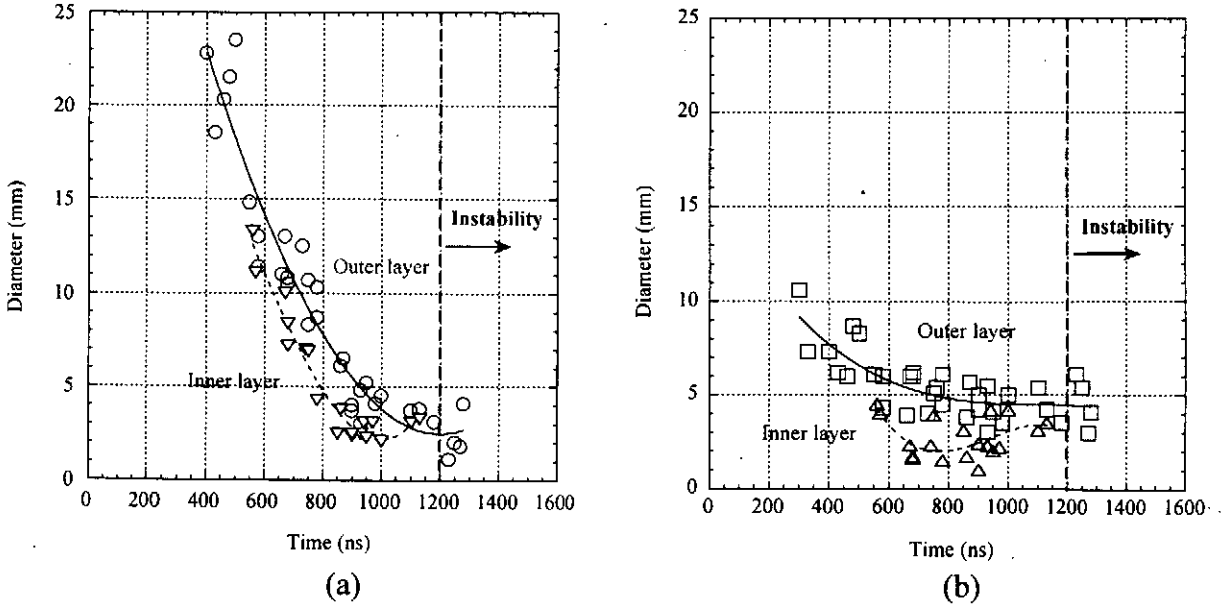

Fig. 7. Time evolutions of the diameter of outer and inner structures near the electrodes. : (a) near the cathode. (b) near the anode.

MEASUREMENT OF CURRENT DISTRIBUTION IN A WIRE-ARRAY Z-PINCH PLASMA SOURCE DURING EXPLODING PHASE

Y. Teramoto, S. Kohno*, N. Shimomura**, S. Katsuki***, and H. Akiyama

Graduate School of Science and Technology, Kumamoto University,
2-39-1 Kurokami, Kumamoto 860-8555, Japan
** Department of Electrical Engineering, Ariake National College of Technology,*
150 Higashihagio-machi, Omuta, Fukuoka 836-8585, Japan
*** Department of Electrical and Electronic Engineering, The University of Tokushima,*
2-1 Minamijosanjima, Tokushima 770-8506, Japan
**** Department of Electrical and Computer Engineering, Kumamoto University,*
2-39-1 Kurokami, Kumamoto 860-8555, Japan

ABSTRACT

The current in a wire array during its exploding phase has been studied. The wire array consisting of many thin wires is used as a plasma source in a z-pinch x-ray radiation system. The current distribution in the exploding wire array plays an important role in producing an initial symmetrical plasma. In the present experiment, four tungsten wires of 0.1 mm in diameter were exploded in vacuum. The experiment was carried out with an inductive voltage adder pulsed power generator providing a current of 160 kA at quarter period of 1.8 μs. The currents through and the voltage across the wires were measured simultaneously. It was found that the currents in the wires were inhomogeneous especially after the wires became plasma. Once the currents became inhomogeneous, the inhomogeneity remained throughout the discharge. It was also studied how the dimensions of the wires affected the homogeneity of the currents. Wires of different lengths or different cross sectional areas resulted in strong inhomogeneities of the currents. The wires with shorter length or smaller cross sectional area became plasmas earlier than other wires. Thus the resistances of the wires were not equal. These differences in the resistance caused the inhomogeneity of the currents.

I. Introduction

X-ray radiated from z-pinches has recently been of much interests in applications as an inertial nuclear fusion driver in a similar way to lasers and heavy ions [1]. The development of fast and high-energy pulsed power technology has allowed the use of a thin metal wire

array as a z-pinch plasma source. A highly-symmetrical thin metal wire array can provide a symmetrical initial plasma, which then leads to a very uniform plasma implosion. The uniform implosion allows the production of an efficient x-ray radiation thus providing extremely high power and energy. The Z accelerator located at Sandia National Laboratories, in which currents up to 20 MA were delivered into a tungsten wire array in approximately 100 ns, has successfully produced x-ray radiation of up to 200 TW and nearly 2 MJ [1].

The behavior of the current through the wire array in water has been investigated numerically in terms of the resistivity change of the wire [2], [3]. It has been predicted that the behavior of currents through the wire array is unstable [4]. If the wires in an array could not be exploded simultaneously by the unstable current behavior, an inhomogeneous mass distribution of the initial plasma would be produced and cause a Rayleigh-Taylor plasma instability [5], [6]. It is very important in obtaining uniform implosions of z-pinch plasmas to investigate whether the currents flowing through parallel wires in vacuum are homogeneous or not during transitions from solid wires to plasmas.

In this paper, the currents measured through parallel wires during their exploding phase are reported. Four parallel tungsten wires were exploded in vacuum to simulate and predict the current distribution in the wire array z-pinch during its exploding phase. The resistances of the parallel wires were calculated from the measured voltage and currents. Flows of inhomogeneous currents through the wires were observed. Also, time resolved pictures of exploding wire array were taken to observe how the wire array consisting of four wires explodes.

II. Experimental setup

Fig. 1 shows the schematic diagram of the experimental setup. The wire array was driven by ASO-X generator [7], [8]. ASO-X was operated at a charging voltage of 30 kV. The rise time of the current, current peak and the output voltage were 1.8 μs, 160 kA and 90 kV, respectively. The POS was not used here. The wire array consisted of four tungsten wires having a diameter of 0.1 mm. The diameter and the length of the array were 140 mm and 40

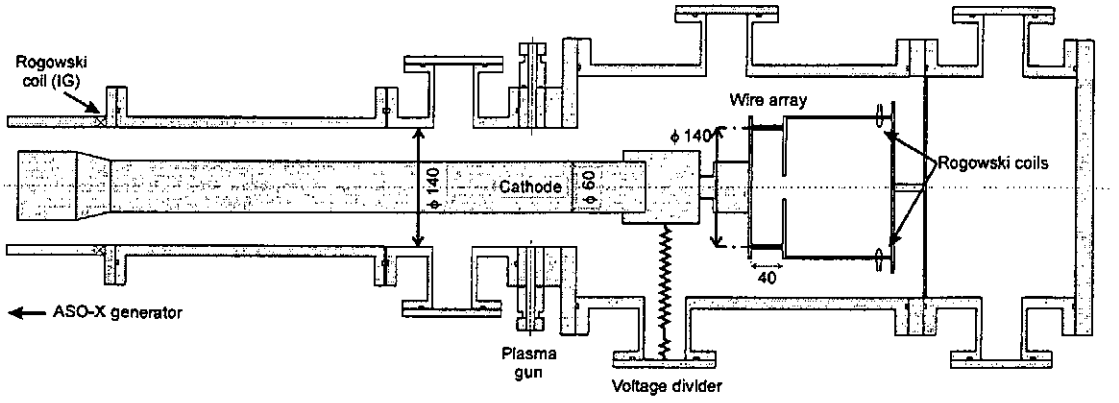

Fig. 1. Configuration of wire array load chamber.

mm, respectively. Though this wire array is different from that used in the Sandia National Laboratories both in the number and the diameter of wires, the current phenomena of parallel wires might simulate the current distribution in the wire array during the transition from solid wires to plasmas.

The wire array was set in the vacuum chamber load section of ASO-X. The tips of parallel wires were connected to a cathode plate directly and to an anode plate through a thick rod. The wires were tensioned by the same weights. The surfaces of the wires were contacted to the surfaces of holes of the electrodes. The pressure of the vacuum chamber was about 3×10^{-4} Torr achieved in this machine. The generator current was measured with a Rogowski coil placed upstream the wire array. The currents flowing through each wire were measured individually by Rogowski coils placed at the thick rods. Also, the voltage was measured by a resistive voltage divider placed near the cathode plate. The voltage was corrected with an inductive voltage drop at the load section. These signals were recorded with a 1.5-GHz, 4-GSa/s digital oscilloscope (Hewlett Packard, 54845A).

From the viewpoint of how the dimensions of wires affect the inhomogeneity of the currents, three different sets of wires were studied; wires of equal dimensions in length and cross sections (A), wires of different lengths (B) and wires of different cross sectional areas (C).

For the experiment of the wires of equal dimension, the time resolved picture of the exploding wire array were also taken by a high-speed framing camera (Hadland Photonics, IMACON 790).

III. Results and discussions

A. Wires of equal dimension

Typical waveforms of the wire currents and the resistive voltage across the wire are shown in Fig. 2. Although the voltage has an opposite sign before 50 ns due to the correction error, it is not significant for diagnostics because it is at much earlier time than that of interest here. When ASO-X was fired, the currents started to flow almost equally through all the wires. There are no large differences in the current values. Although the resistances of the wires increased with increasing current, the rates of increase in the resistance of the wires were almost equal before about 230 ns. This led to the currents through the wires to increase

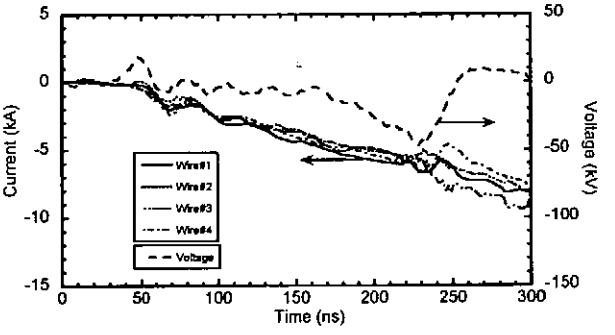

Fig. 2. Typical waveforms of currents through the wires and voltage across the wire.

simultaneously. However, at about 230 ns, the currents rapidly deviated from each other and became non-uniform. Note that the sum of the currents through the wires corresponded to the generator current measured upstream the wire array. Therefore the deviations of the currents were caused by differences in the resistances of the wires. The voltage across the wire increased before 230 ns due to increases in the resistances of the wires. The voltage decreased after reaching the peak voltage at 230 ns though the total current was still increasing. The currents became inhomogeneous around the time when the voltage reached its peak. Once the currents had become inhomogeneous, they did not become homogeneous again and the deviations among the currents lasted to the end of the discharge.

From Fig. 2, it is seen that the current through wire #4 decreased and the current through wire #3 increased to compensate for the change in their resistances and in order to maintain the same total current. The other two currents did not change so much. Since the currents through the wires compensate the other currents, there was no change in the total current which was measured downstream or upstream the wire array load. Once the currents became inhomogeneous, these deviations were maintained during the discharge and the currents did not become equal. Although the currents in the wires either increased or decreased in different shots, the same phenomena were observed in all the shots. This suggests an external factor, that is, the conditions of the contacts between wires and electrodes could not be the same for wire-to-wire and shot-to-shot.

Fig. 3 shows the resistances of the wires during the discharge calculated from the current and the voltage waveforms. R is determined from eqn.(1) since L_{array} was found to be 105 nH. It is seen that the resistances increased with time and had their peaks at about 230 ns. At ≥230ns, the resistances decreased, when a plasma was produced. The resistances were not equal (±15 %) at their peaks (Fig. 3).

Calculating the power dissipation in the wires, it was confirmed that the time when the resistances rose sharply corresponded to the melting point. It was also confirmed that the

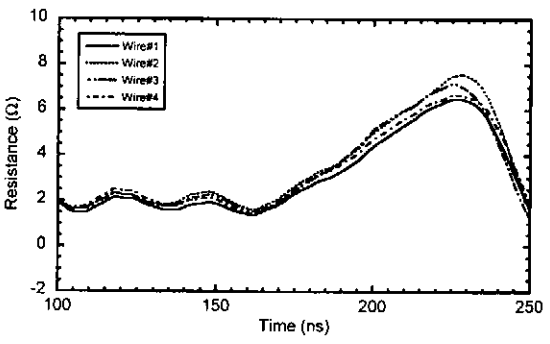

Fig. 3. Variations of resistances of the wires during the discharge calculated from the current and the voltage waveforms.

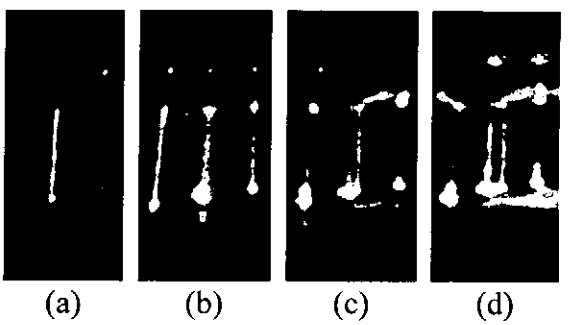

Fig. 4. Time resolved pictures of exploding wire array at 325 ns (a), 525 ns (b), 725 ns (c) and 925 ns (d). The exposure time was 20 ns.

resistances fell down before reaching the evaporating point. From these results, it was understood that the evaporations of the wires were not volumetric and breakdown might have occurred at the surface of the wires [9].

Fig. 4 shows the time resolved picture of the exploding wire array taken at 325 ns (a), 525 ns (b), 725 ns (c) and 925 ns (d), respectively, having an exposure time of 20 ns. All the pictures were taken after the current became strongly inhomogeneous. However, in Fig. 4(a), only one of four wires was luminous. In addition, although the currents through the wires were increasing with time, the intensities of luminosities of the wires were alternating. Moreover, the luminosities were not uniform along the wires. Considering these results and the power dissipations in the wires, the following conclusion was derived; the evaporations of the wires were not volumetric and, hence, the discharges did not occur uniformly in the wires.

B. Wires of different lengths

In order to investigate what is dominant for such an inhomogeneous current distribution, the experiment was done using four wires of different lengths. The lengths of wire #1, #2 and #3 were 40 mm and that of wire #4 was 20 mm. Fig. 5 shows the waveforms of the currents through the wires and the voltage across the wire. The behavior of the currents through the wires before 210 ns was similar to that in the experiment described before. At ≥210 ns, the current through the wires became much more inhomogeneous (Fig. 5) compared to the wires of the same length (Fig. 2). Especially, the current through the shorter wire #4 increased. From subsequent shots, it was confirmed that the current through the wire of the shorter length increased and became larger than in the other wires.

Fig. 6 shows the resistance during the discharge. Although the length of wire #4 was half of that of the other wires, the resistances of all the wires up to 180 ns were equal within ±16 %. However, the resistance of wire #4 firstly reached its maximum and then decreased. The mass of wire #4 was half of that of the other wires. The shortest wire that had the lightest mass

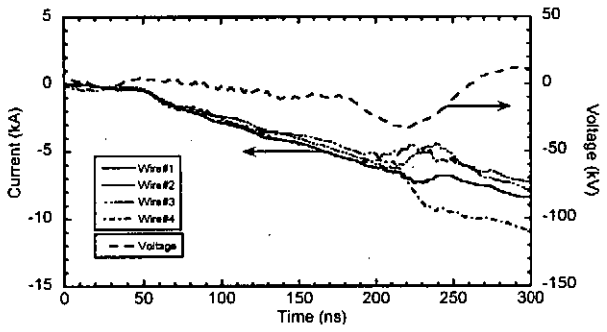

Fig. 5. Typical waveforms of currents through the wires and voltage across the wire. Length of wire #1, #2 and #3 were 40 mm and length of wire #4 was 20 mm.

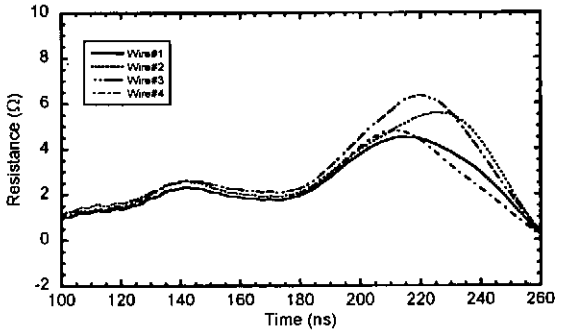

Fig. 6. Variations of resistances of the wires during the discharge calculated from the current and the voltage waveforms. Length of wire #1, #2 and #3 was 40 mm and length of wire #4 was 20 mm.

became plasma first. When the resistance of wire #4 was decreasing, the other wires, except wire #1, were still increasing. The resistance of wire #1 (Fig. 6) was observed to be different from the wires of the same length (wire #2 and #3). The current through wire #1 (Fig. 5) was also different from the current in the wires of the same length (wire #2 and #3) and it did not deviate from the average current so much when the current distribution became inhomogeneous. These phenomena were observed in all shots.

C. Wires of different cross sectional areas

Fig. 7 shows the current and the voltage waveforms, where two wires (wire #2) were used in parallel to increase the cross sectional area. During the early phase of the discharge, the currents through all the wires were about the same though the dimensions of the wires were different. This is explained by the dominance of resistances and inductances of the rods connecting the wires to the anode plate as well as the inductance of each wire. The resistances and inductances of the rods were estimated to be several hundreds of mΩ and several tens of nH, respectively. The resistances of the wires increased with time, and became dominant in deciding the current flows. The current through wire #2 deviated from the others because the resistance of wire #2 was smaller than the others. Then, they approached each other after 240 ns because wire #1, #3 and #4 became plasma. Fig. 8 shows the resistances of the wires. During the early phase of the discharge, the resistances of the wires were similar because the inductances of the wires were dominant. The resistance of wire #2 increased slowly compared with those of the other wires except wire #3 because of its heavier mass. When the resistances reached their peaks, the resistance of wire #2 was half of either wire #1 or #4 due to the difference of their cross sectional areas. The wires having smaller mass (wire #1, #3 and #4) became plasma faster than wire #2. Therefore the resistances approached each other. The behavior of wire #3 was different from the wires of the same dimension.

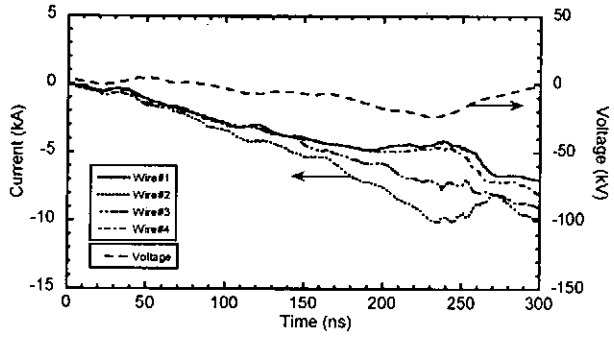

Fig. 7. Typical waveforms of currents through the wires and voltage across the wire. Two wires were set as wire #2.

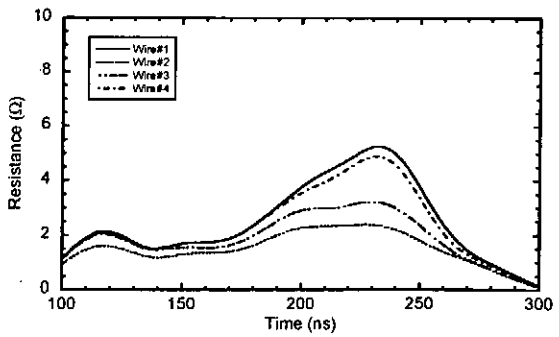

Fig. 8. Variations of resistances of the wires during the discharge calculated from the current and the voltage waveforms. Two wires were set as wire #2.

From these experiments, it was found that even if the length, cross sectional area and material were the same, the currents through the wires became inhomogeneous during their exploding phases. One of the reasons was thought to be the small differences in the dimensions of the wires. If the inhomogeneity of the dimensions exists or connections between the wires and the electrodes were not exactly identical, the transitions from solid wires to plasmas must be different. It was noteworthy that the currents through the wires of the array became inhomogeneous when the wires became plasmas. From the numerical analysis in reference [4], even if the differences in the dimensions or connections are small, the currents tend to be inhomogeneous. The inhomogeneous current could cause an inhomogeneous mass distribution, leading to unequal implosion speeds and a spoiling of the pinch. However, in the present experiment, the rise time of the current was much longer than that in the resent z-pinch experiments. If the rise time of the current is short enough for the inductances of the wires to be dominant and the inductances of the wires are equal to each other, the inhomogeneity of the currents might be diminished. The inhomogeneity of the currents occurred during the exploding phase. Therefore, the inhomogeneity of the currents is independent of the array radius. On the other hand, if the cross sectional area is small enough to evaporate both uniformly and volumetrically, the inhomogeneity of the currents reported in this paper might also be diminished.

IV. Conclusions

The current distribution of the wire array in vacuum was studied. Individual measurements of the currents flowing through the wires allowed us to know how currents behave during the discharge. Voltage and current measurements were also carried out to calculate the resistance variations of the wires. The resistance of the wire increased with time due to heating by the current. Melting wire became vapor and then plasma causing a decrease in its resistance. A strong current deviation occurred when the resistance started to decrease. The deviations were held during the discharge. Such an inhomogeneous current distribution might be caused by small differences in the wire dimensions.

Inhomogeneous current distribution might occur in an actual wire array z-pinch system. This might affect the initial plasma production and implosion.

References

[1] R. B. Spielman, C. Deeney, G. A. Chandler, M. R. Douglas, D. L. Fehl, M. K. Matzen, D. H. McDaniel, T. J. Nash, J. L. Porter, T. W. Sanford, J. F. Seamen, W. A. Stygar, K. W. Struve, S. P. Breeze, J. S. McGurn, J. A. Torres, D. M. Zagar, T. L. Gilliland, D. O. Jobe, J. L. McKenney, R. C. Mock, M. Vargas, T. Wagoner, and D. L. Peterson, " Tungsten wire-array

Z-pinch experiments at 200 TW and 2 MJ," Phys. Plasmas, vol. 5, no. 5, pp. 2105-2111, May 1998.

[2] N. Shimomura, M. Nagata, C. Grabowski, and H. Akiyama, " Mechanism of unstable behavior of parallel fuses as an opening switch," IEEE Trans. Plasma Sci., vol. 23, no. 5, pp. 860-864, Oct. 1995.

[3] N. Shimomura, M. Nagata, C. Grabowski, K. Murayama, and H. Akiyama, " Effects of wire shape on unstable behavior of parallel fuses," IEEE Trans. Plasma Sci., vol. 24, no. 3, pp. 1192-1193, Jun. 1996.

[4] N. Shimomura, M. Nagata, Y. Teramoto, H. Akiyama, " Unstable behavior in exploding wire array," Jpn. J. Appl. Phys., vol. 39, part 1, no. 10, pp. 6051-6054, Oct. 2000

[5] T. W. L. Sanford, R. C. Mock, R. B. Spielman, M. G. Haines, J. P. Chittenden, K. G. Whitney, J. P. Apruzese, D. L. Peterson, J. B. Greenly, D. B. Sinars, D. B. Reisman, and D. Mosher, " Wire array Z-pinch insights for enhanced X-ray production," Phys. Plasmas, vol. 6, no. 5, pp. 2030-2040, May 1999.

[6] I. V. Lisitsyn, S. Katsuki, and H. Akiyama, " Two-dimensional implosion of liners," Phys. Plasmas, vol. 6, no. 5, pp. 1389-1392, May 1999.

[7] S. Kohno, Y. Teramoto, I. V. Lisitsyn, S. Katsuki, and H. Akiyama, " High-current pulsed power generator ASO-X using inductive voltage adder and inductive energy storage system," Jpn. J. Appl. Phys., vol. 39, part 1, no. 5A, pp. 2829-2833, May 2000.

[8] S. Kohno, Y. Teramoto, I. V. Lisitsyn, S. Katsuki, and H. Akiyama, " Cable guns as a plasma source in a plasma opening switch," IEEE Trans. Plasma Sci., vol. 27, no. 3, pp. 778-785, Jun. 1999

[9] S. A. Pikuz, T. A. Shelkovenko, D. B. Sinars, J. B. Greenly, Y. S. Dimant, and D. A. Hammer, "Multiphase foamlike structure of exploding wire cores," Phys. Rev. Lett., vol. 83, no. 21, pp. 4313-4316, Nov. 1999

EFFECT OF WIRE SHAPE ON WIRE ARRAY DISCHARGE

N. Shimomura, Y. Tanaka, Y. Yushita, M. Nagata,
Y. Teramoto*, S. Katsuki* and H. Akiyama*

Department of Electrical and Electronic Engineering, The University of Tokushima,
2-1 Minamijosanjima, Tokushima, 770-8506, Japan
*Department of Electrical and Computer Engineering, Kumamoto University,
2-39-1 Kurokami, Kumamoto, 860-8555, Japan

ABSTRACT

Although considerable investigations have been reported on z-pinches to achieve nuclear fusion, little attention has been given from the point of view of how a wire array consisting of many parallel wires explodes. Instability existing in the wire array discharge has been shown. In this paper, the effect of wire shape in the wire array on unstable behavior of the wire array discharge is represented by numerical analysis. The claws on the wire formed in installation of wire may cause ununiform current distribution on wire array. The effect of error of wire diameter in production is computed by Monte Carlo Method.

I. Introduction

Recently, z-pinches have been expected to achieve power generation by nuclear fusion [1)-4)]. Wire arrays are exclusively used as a z-pinch plasma source. The behavior of the plasma produced from a wire array and the wire explosion have been investigated by numerical analyses and experiments. It has been reported that the initial mass distribution of the plasma has a significant influence on the development of the Rayleigh-Taylor instability [4),5)]. On the other hand, the unstable behavior of parallel two exploding wires has been investigated from the viewpoint of an opening switch [6),7)]. However, little attention has been given to the point of view of how a wire array consisting of numerous parallel wires explodes. When the wires of the array do not explode simultaneously, owing to an unstable behavior, an inhomogeneous mass distribution of the plasma, as well as a deviation of the current flow, may be yielded.

The unstable behavior of wire array discharge has been predicted from numerical analysis and resistivity variation of wire.[8)] Here, the effect of wire shape in the wire array on

unstable behavior of the wire array discharge is represented by numerical analysis. The claws on the wire formed in installation of wire may cause ununiform current distribution on wire array. The effect of error of wire diameter in production is computed by Monte Carlo Method.

II. Prediction of unstable behavior

Figs. (1a) and (1b) show whether the wire array system is stable or unstable. ρ_1 and ρ_0 represents the resistivity of a wire in n wire array and the resistivity of other wires, respectively. Either stable or unstable state is discriminated for one wire to the other, thereby, current concentration and division are found. Figure 1 is calculated on a copper resistivity variation measured in single wire explosion in water. The gray areas and white areas represent unstable and stable state, respectively, and the gray depth means strength of unstable drive. The equilibrium of wire array operation is represented as the straight diagonal line from a left-down corner to a right-up corner, since the resistivities of each wire are same on the line. Figs. 1 (a) and (b) are for the case of $n = 2$ and $n = 10$, respectively.

In the case of $n = 2$, the distribution of unstable regions is symmetrical about the diagonal, since a bundle of n-1 wires is just one wire. In the case of $n = 10$, the strength of the tendency to the unstable behavior on the left hand side of the diagonal is larger than that on the right hand side of it, although it is not clear on Fig. 1(b) because of the rough separation of the depth of the gray scale. Also, the same tendency occurs for the stable, although the strength of stable drive is not indicated in the Fig. 1. The distribution is no longer symmetrical about the diagonal. Furthermore, the strength of the tendency to the unstable

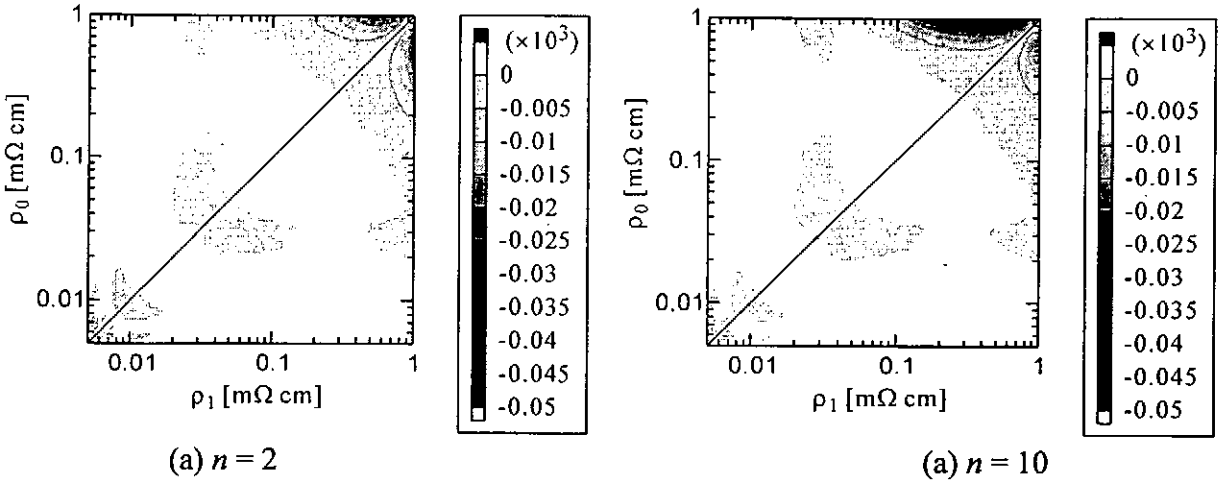

Fig. 2. The contour maps of the instability in exploding; the unstable strength is represented as minus magnitude and stability is represented by zero (white-painted).

and the stable behavior increases with increasing the wire number. The enhancement of the strength of the tendency to the unstable behavior at the left hand side of the diagonal implies that one wire explodes later than the others and the current concentrates into the wire.

III. Effect of wire shape difference: claw on unstable behavior

The probability of unstable behavior in wire array discharge is represented. However, it is not clear that all wire array system will behave unstably or not, the degree of unstable behavior, and what to effect on it. In this chapter, the unstable behaviors are simulated when a wire in the wire array has different shape. Here, a section of different diameter is given to a wire, and the diameter and length of the section are changed.

Figure 2 shows the schematic for the numerical simulation. The wire array consists of n 2 cm wire of 0.05 mm in diameter. A wire (the most right wire in Fig. 2) has a section of different diameter, which is assumed as a claw in installation. The total current through the wire array is 100 kA and constant. The computed current waveforms are shown in Fig. 3. The total wire number is 10 and the claw consists of a section of 0.046 mm in diameter and 0.2 mm in length. The solid line and broken line represents the currents of normal wire and a wire having the claw, respectively. Appreciable ununiform current distributions are shown at 1.8 ns, 2.3 ns and after 2.8 ns. Although current ununiformity is no wonder because of different wire shape, they are eventful and the distribution is not constant. We call the current ununiformity at 2.3 ns concentration and the others dispersal, respectively. The lower waveforms of Fig. 3 represent the resistivity variation. The unstable behavior are

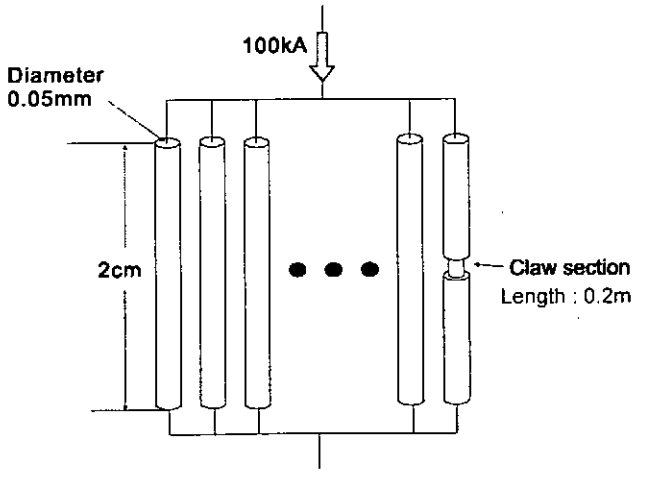

Fig. 2. Schematic of wire array for the numerical simulation.

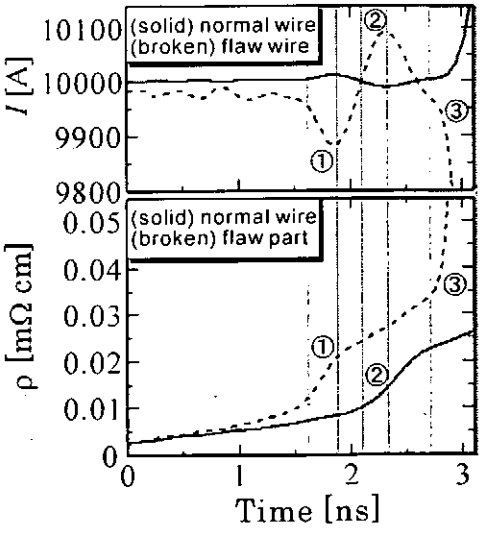

Fig. 3. Waveforms of wire array current and resistivities.

produced by the rapid resistivity variation of wire.[8)]

The peak values of Fig. 3 are calculated for several different diameter of the claw section. Figure 4(a) and (b) shows peak value corresponding to the dispersal at 1.8 ns and to the concentration at 2.3 ns, respectively. As the diameter of claw section becomes further from normal diameter, the current distribution become more ununiform. In Fig. 4(a), the ununiformity relaxes below 0.044 mm. It is because the period #3 approaches to the period #2, that is to say, the current concentration is cancelled by the dispersal.

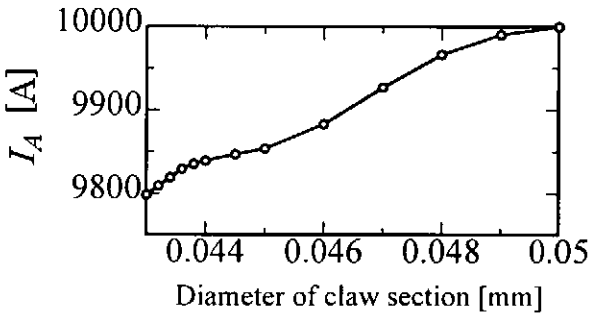

(a) Current dispersal: I_A

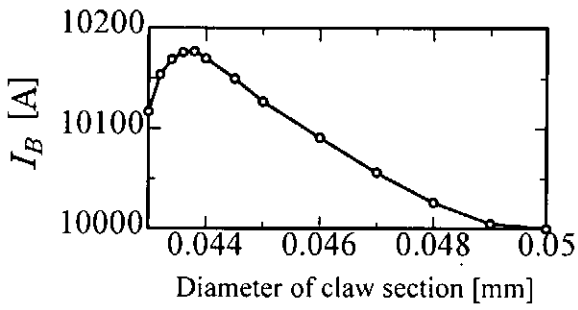

(b) Current concentration: I_B

Fig. 4. Peak values of current dispersal and current concentration.

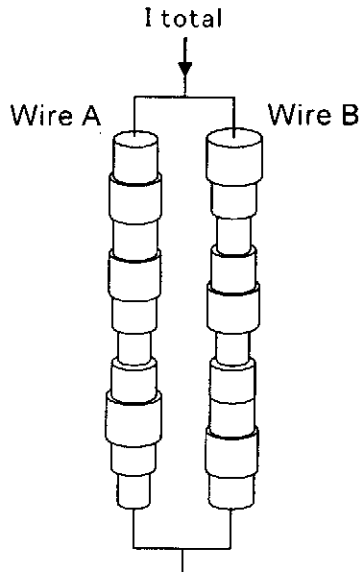

Fig. 5. Schematic of wire for the numerical simulation by Monte Carlo Method.

IV. Effect of wire shape difference: manufacturing error on unstable behavior

The fluctuation of wire diameter is obtained by the distribution function of wire diameter and Monte Carlo Method. Figure 5 represents the schematic of wire array in the case of two wires and the distribution function of wire diameter, respectively. The fluctuation by this procedure simulates wire shape considering the manufacturing error. In this analysis, the current per wire is constant; the total current changes by wire number. Figures 6 represent the typical current waveform of wire array with wire shape obtained by Monte Carlo Method, in the cases of wire number: n = 4, 6, 8 and 10. Appreciable ununiform current distributions

are observed around 4 ns although the distribution function of wire diameter would be too wide. The uniformity will be enough to make the z-pinch ununiform and bring a seed of R-T Instability. Since the resistivity data used finish on vaporization phase, the simulations do not support the transition from vapor and plasma and plasma phase. In these phases, the uniformity may be recover or the ununiformity may grow. Moreover, the inductance of wire array is not considered. These influences are important for z-pinch experiment, will be discussed another paper.

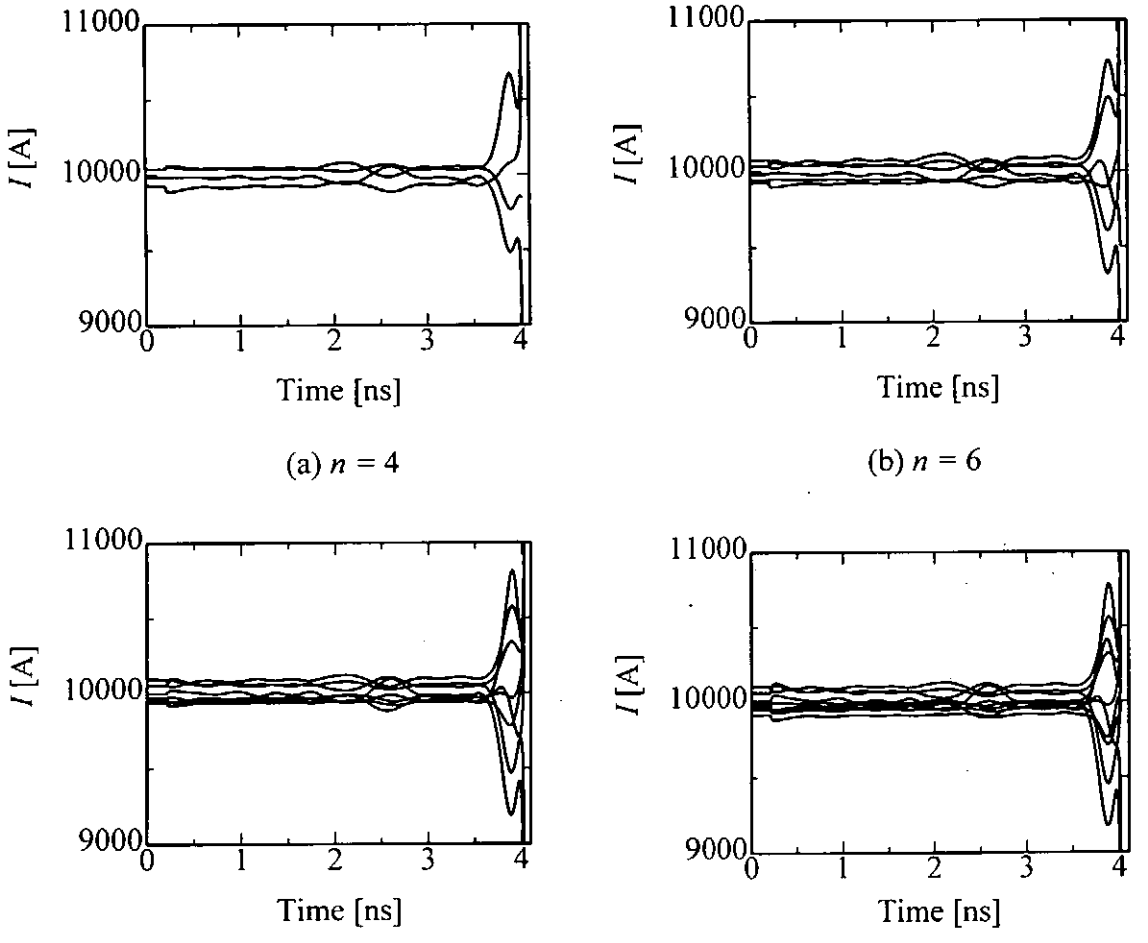

Fig. 4. Typical current waveform of wire array with wire shape obtained by Monte Carlo Method

V. Summary

The unstable behaviors of the wire array discharge with wire shape difference are discussed by numerical analysis. The claws on the wire formed in installation of wire cause

ununiform current distribution on wire array. The error of wire diameter in manufacturing is estimated by Monte Carlo Method and the unstable behavior are also computed. These simulations show the appreciable ununiform current distributions in wire arrays and the effect on pinches should be considered. Further simulation including transition from vapor to plasma and inductive effect for fast drive is expected immediately.

References

1) M. K. Matzen, "Z pinches as intense x-ray sources for high-energy density physics applications", *Phys. Plasmas*, **4**, 1519-1527 (1997).
2) J. H. Brownell, R. L. Bowers, K. D. McLenithan, and D. L. Peterson, "Radiation environments produced by plasma z-pinch stagnation on central targets", *Phys. Plasmas*, **5**, 2071-2080 (1998).
3) R. B. Spielman, C. Deeney, et al., "Tungsten wire-array Z-pinch experiments at 200 TW and 2 MJ", *Phys. Plasmas*, **5**, 2105-2111 (1998).
4) T. W. L. Sanford, R. C. Mock, R. B. Spielman, M. G. Haines, J. P. Chittenden, K. G. Whitney, J. P. Apruzese, D. L. Peterson, J. B. Greenly, D. B. Sinars, D. B. Reisman, and D. Mosher, *Phys. Plasmas*, **6**, 2030-2038 (1999).
5) I. V. Lisitsyn, S. Katsuki, and H. Akiyama, "Two-dimensional implosion of liners", *Phys. Plasmas*, **6**, 1389-1292 (1999).
6) N. Shimomura, M. Nagata, C. Grabowski, and H. Akiyama, "Mechanism of Unstable Behavior of Parallel Fuses as an Opening Switch", *IEEE Transactions on Plasma Science*, **23**, 860-864 (1995).
7) N. Shimomura, M. Nagata, C. Grabowski, K. Murayama, and H. Akiyama, "Effects of Wire-Shape on Unstable Behavior of Parallel Fuses", *IEEE Transactions on Plasma Science*, **24**, 1192-1193 (1996).
8) N. Shimomura, M. Nagata, Y. Teramoto, and H. Akiyama, "Unstable Behavior in Exploding Wire Array", *Jpn. J. Appl. Phys.*, Vol.39, Part 1, No.10, pp.6051-6054 (2000).

BEHAVIOR OF ABLATION PLASMA PRODUCED BY PULSED ION-BEAM EVAPORATION

Shinji Kitayama, Koji Ide, Weihua Jiang, and Kiyoshi Yatsui

Extreme Energy-Density Research Institute, Nagaoka University of Technology
Nagaoka, Niigata 940-2188, Japan

ABSTRACT

The ablation plasma produced by pulsed ion-beam evaporation (IBE) has been successfully utilized in the preparation of thin films of many kinds of materials. To understand the basic process of thin-film deposition by the IBE, high-density ablation plasma produced by intense pulsed ion beam has been studied experimentally by using high-speed photography. The results have given us visual understanding of the plasma behavior. In addition, the ablation process is also studied by investigating the mass variation of the target.

I. Introduction

When an intense pulsed light ion-beam (LIB) is irradiated onto a target, high-temperature, high-density ablation plasma is produced by the ion-beam energy deposition. Intense pulsed ion-beam evaporation (IBE)[1-3] has been proposed for the first time at the Nagaoka University of Technology (NUT) as a technique for preparing thin films. After that, various kinds of crystallized thin films have been prepared successfully.[4] Recently, IBE has been applied to the thin-film preparation of $SrAl_2O_4$:Eu, B_4C, amorphous Si and others.[5-9] It is understood that the characteristics of thin films produced by IBE depend on the behavior of the ablation plasma This paper presents an investigation on the behavior of ablation plasma by the use of high-speed photography.

II. Principles of IBE

II - I. Generation of ablation plasma

When charged particle beam is irradiated onto a solid target, each particle of the target gains its kinetic energy in a volume between the surface and the range of ions which depends on the initial ion energy and the target material. When a very short pulsed ion beam is utilized, the part of the surface within the ion range is heated rapidly. Since the range of LIB is very short (for example the range of 1MeV proton (H^+) ion ~ 10 μm), the energy of the ion

beam is deposited in a very thin layer near the surface. When its energy is deposited, the layer can be heated, melted, vaporized, ionized etc. As a consequence, high-density ablation plasma is produced. Solid materials such as ceramic, metal or alloys, can be used as the targets for IBE.

II - II. Expansion of ablation plasma and deposition of thin film

The ablated plasma that is produced near the surface of the target expands in vacuum, resulting in a plasma flow in a direction perpendicular to the target. When the ablation plasma reaches the substrate which is located near the target, a thin film is deposited by the solidification part of the ablation plasma.

The features of IBE method are summarized as follows. 1) Since the temperature of the target surface is heated up to more than several thousand degrees, materials with high melting point can be easily ablated.[5] 2) Due to the high-density plasma, the instantaneous deposition rate exceeds more than a few cm/s. For the same reason, mask-side deposition (MS/IBE)[5,8] and backside deposition (BS/IBE)[9-12] are available, where the substrate is placed by the target holder and the reverse side of the holder, respectively. 3) Since the pulse width is short compared with the conduction time of heat, we do not heat the substrate to prepare the films.[4,13]

III. Experiment

III- I. Preparation chamber

The experiment was carried out using an intense pulsed charged-particle beam generator, "ETIGO- II ".[14] Figure 1 shows the schematic of the experimental arrangement for the preparation of thin films by the IBE method. The left-hand side the ion beam diode chamber that produces the LIB, while the right-hand side represents the thin film preparation chamber. The LIB is produced by a magnetically insulated diode (MID)[15] with a geometrically focused configuration. In this experiment, the target that was tilted at 30° or 90° to the beam axis. The vacuum chamber was evacuated to $\sim 10^{-4}$ Torr.

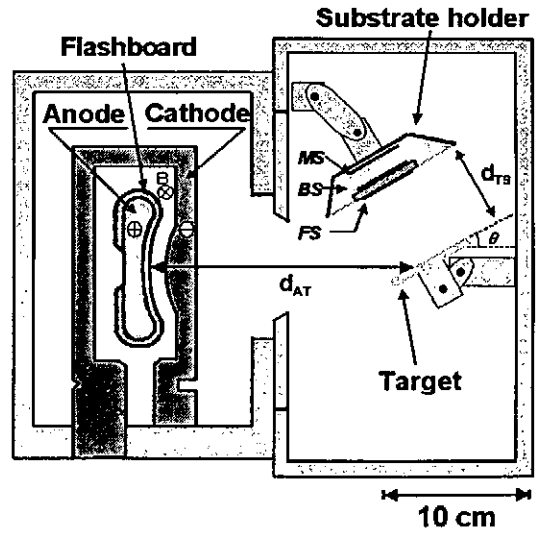

Fig. 1 Schematic of experimental setup for IBE.

Table I Technical specification of high-speed camera

Frame speed	5.000～20.000.000 frames/sec
Exposure time	10ns～200 μs
Interframe	40 μs～200 μs
Inner delay	30ns～40ns
Photographic sensitivity	400nm～900nm

Ⅲ-Ⅱ. High-speed camera

Table I shows the specification of high-speed camera (Ultra NAC FS501) used in this experiment. As the observation window, acryl resin was used, which has uniform transparency in the range of photographic sensitivity of high-speed camera. The camera was separated with a distance (3 m) from the window to avoid the noise generated by "ETIGO-Ⅱ" (Fig. 2).

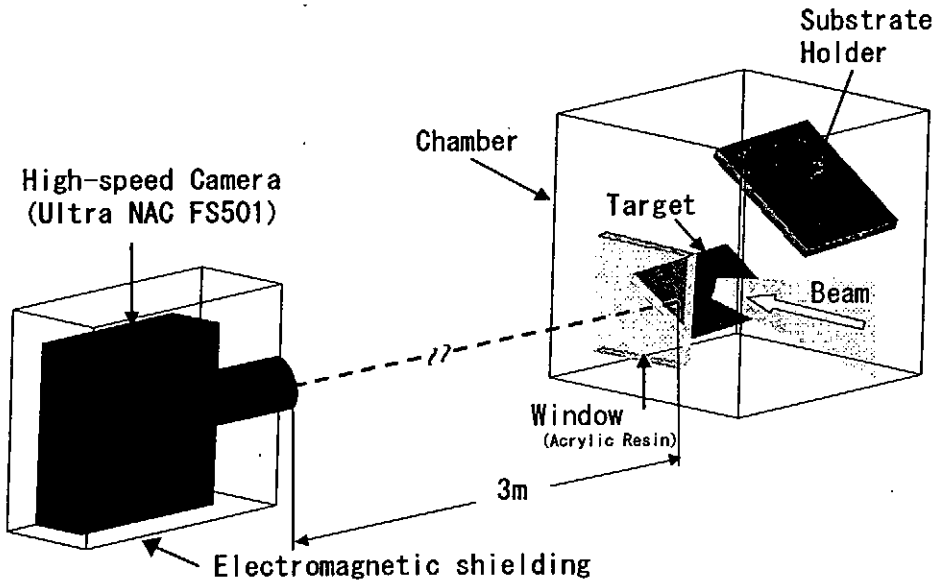

Fig. 2 Schematic of experimental arrangement for the measured of the ablation plasma.

Table Ⅱ Experimental conditions.

Ion species	mostly H^+ (>85%)
Maxmum ion energy	1 MeV
Pulse width (FWHM)	70 ns
Ambient pressure	2×10^{-4} Torr
Target	Pb, Ag, W, Cu, Al
Energy density	50 J/cm^2
d_{AT}	180 mm
d_{TS}	50, 90 mm
θ_T	30, 90 °

Table Ⅲ Physical constants of Pb, Ag and W.

Target	Pb	Ag	W
Melting point (°C)	327.5	961.9	3387
Boiling point (°C)	1750	2184	5927
Vapor pressure* (°C)	559	824	2756
Range** (μm)	9.02	6.83	5.3

* 10^{-4} Torr

** 1 MeV proton (H^+)

Ⅲ-Ⅲ. Target

Table Ⅱ summarizes the experimental conditions. In this investigation, various kinds of targets, such as Cu, Al, Pb, Ag and W were used. Here, Pb, Ag, and W were utilized to measure the behavior of ablation plasma and ablated mass (cf. TableⅢ). The copper mask shown in Fig. 3 was placed on the target to detect the ablated mass. The target tilted at 30° or 90° to the beam axis was used to diagnose the target mass loss by difference of ion range. If the tilt angle is 30°, as shown in Fig. 4, the ablated depth (d) is halved as compared with that of 90°.

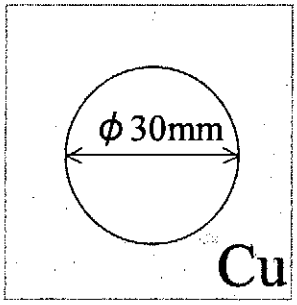

Fig. 3 Copper mask (50×50×1 mm^t, hole diameter = 30 mm) attached on the target.

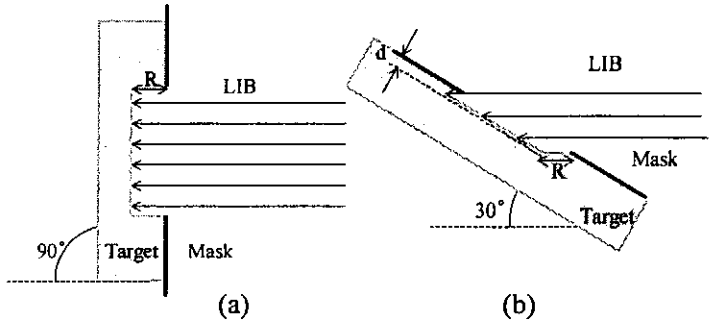

Fig. 4 Cross-sectional view of the target setup with the tilt angles of (a) 90° and (b) 30° .

Ⅳ. Experimental results and discussion

Ⅳ- Ⅰ. Behavior of ablation plasma

High-speed photographs obtained in this experiment are shown in Figs. 5 to 9. Figure 5 shows photographs obtained for the hybrid target, where Pb and Cu are arranged as shown the insert of Fig. 5. Light emission from the ablation plasma can be observed first from Pb (left side), and later from Cu (right side). Figure 6 shows the photographs of the hybrid target of Al and Cu. Where both materials are placed 5 mm intervals. Three lines of light emission were observed for the first 0～12 μs, which was followed by four lines of due to light emission for 18～42 μs. The behavior of ablation plasma, such as the expansing velocity and lifetime, changes by the target material.

Figures 7 ~ 9 show high-speed photographs of three kinds of materials of Pb, Ag and W target, respectively. For the Pb and Ag target shown in Fig. 7 and Fig. 8, the ablation plasma instantly expands toward the direction of the substrate holder. As a result, the plasma exists near the holder while emitting light. At the same time, it turned out that the ablation plasma expands even at the backside region. On the other hand, from Fig. 9, the emissions of near the ablation plasma from the W target continues for a long time, and expands almost linearly.

The differences of the behavior seems to be due to the difference of vaporizing temperature. In other words, materials with lower vaporizing temperature (such as Pb) are relatively easily evaporated, while higher vaporizing materials (such as W) are hard to be evaporated instantly.

IV-II. Ablated mass

Table IV and Figure 10 show the average mass ablated per shot. The ablated mass was determined by measuring the target mass before and after the beam irradiation. It is evident that the target mass loss is larger for the low vaporizing temperature materials than the high vaporizing temperature materials. Comparing the target with the tilt angle, the ablated masses of 90° are larger than that of 30° masses. Particularly, for the W and Ag target, the ablated depth (*d*) for the tilt angle of 30° is roughly halved compared with that of 90°. Thus, ablated masses are dependent on the ion ranges of the materials.

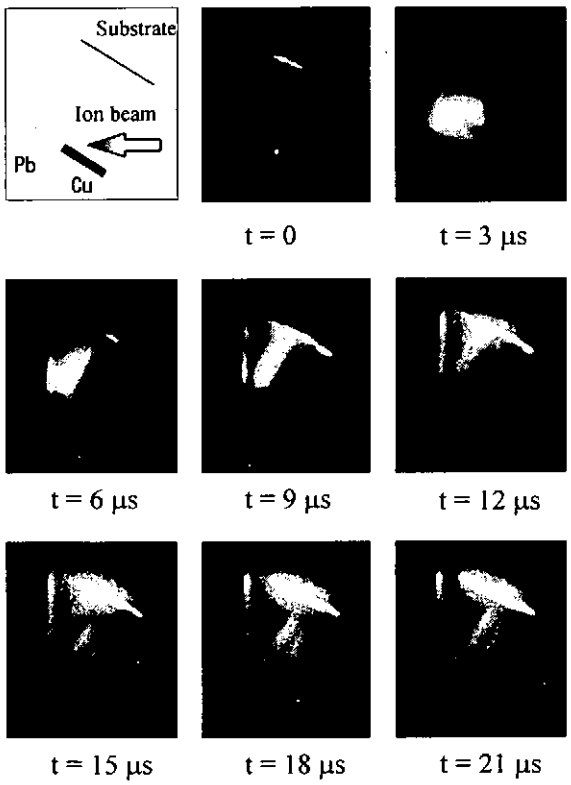

Fig. 5 High-speed photographs for a hybrid target of Pb and Cu. d_{TS} = 90 mm

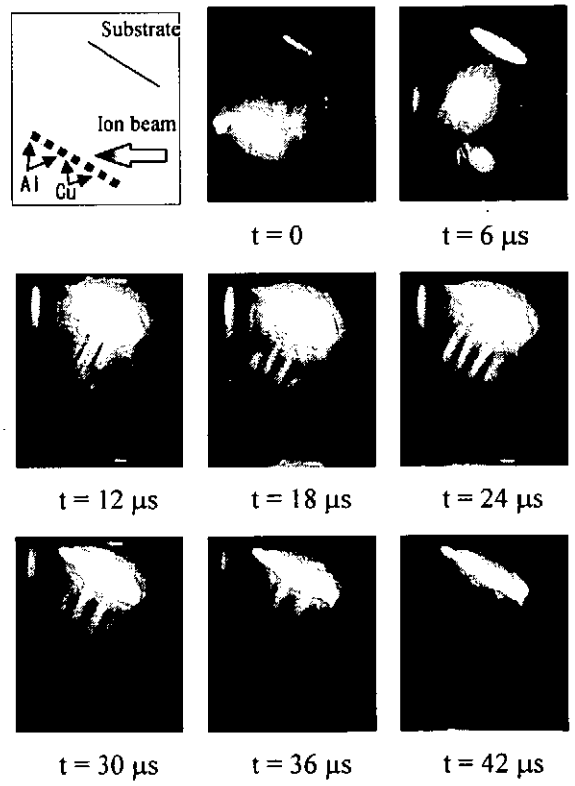

Fig. 6 High-speed photographs for a hybrid target of Al and Cu arranged 5 mm intervals alternatively. d_{TS} = 90 mm

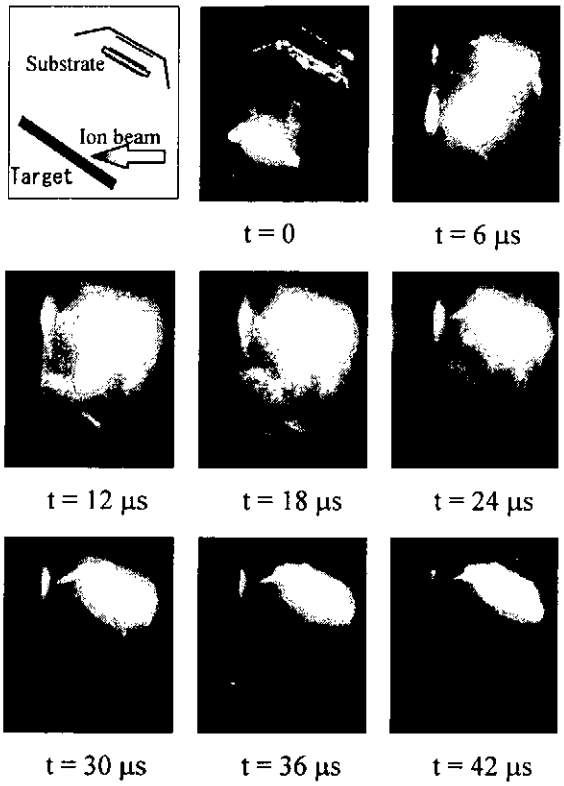

Fig. 7 High-speed photographs for Pb target.
d_{TS} = 50 mm

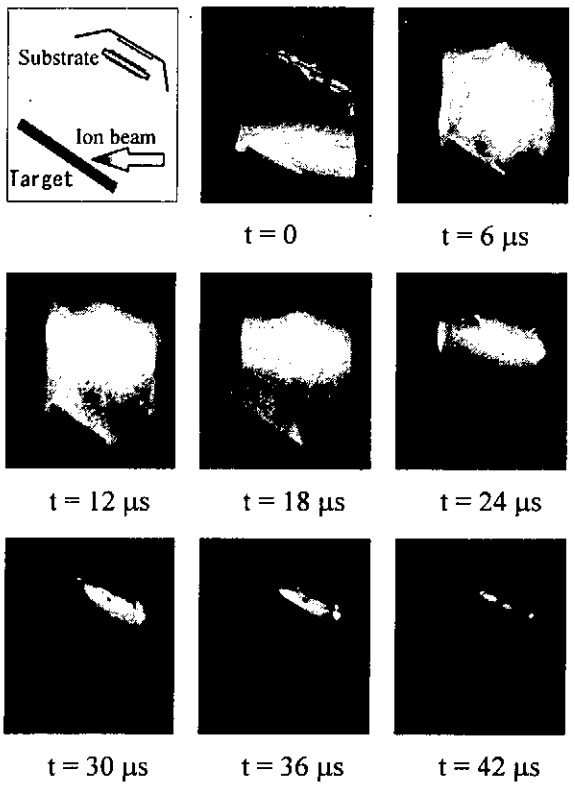

Fig. 8 High-speed photographs for Ag target.
d_{TS} = 50 mm

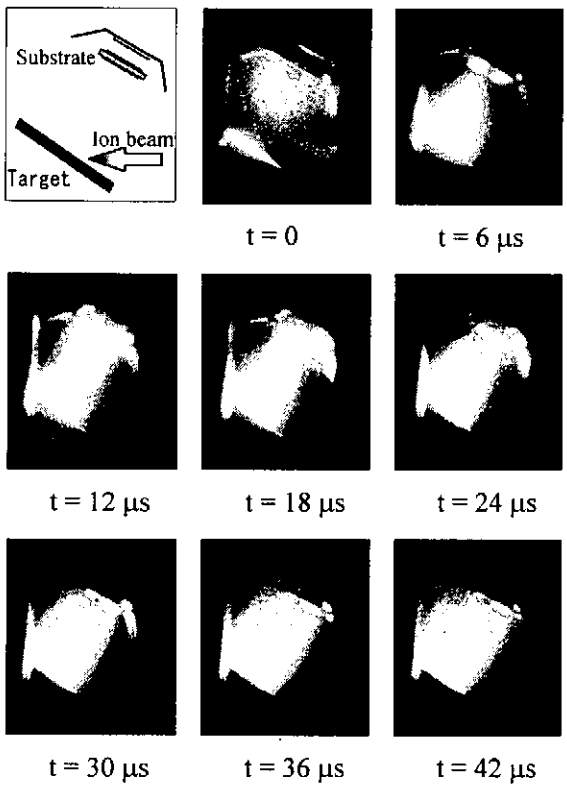

Fig. 9 High-speed photographs for W target.
d_{TS} = 50 mm

Table IV Target mass loss per one shot.

Target	θ =30° mg/shot	θ =90° mg/shot	Ratio
W	3	6.8	0.44
Ag	6	14	0.43
Pb	37	45	0.82

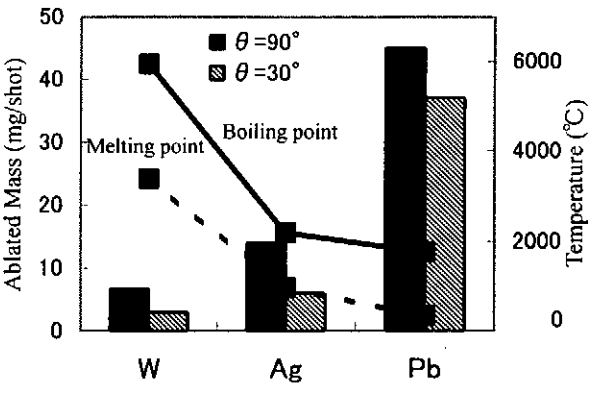

Fig. 10 Ablated mass, melting and boiling temperatures for different kinds of targets.

V. Conclusions

The following conclusions were derived from the results and discussion.

1) The ablation plasma observed by high-speed photographs behaves strongly by dependent on the target materials. The ablation for Pb and Ag target takes place instantaneously with the beam irradiation, the emissions of the ablation plasmas with the tungsten target continue for a longer time.
2) The ablation mass strongly depends on the vaporization temperature of the target material.
3) The ion range is a major factor to determine the ablation depth.

References

1) Y. Shimotori, M. Yokoyama, H. Isobe, S. Harada, K. Masugata and K. Yatsui: J. Appl. Phys. 63 (1988) 968.
2) K. Yatsui: Laser & Particle Beams 7 (1989) 733.
3) Y. Shimotori, M. Yokoyama, H. Isobe, S. Harada, K. Masugata and K. Yatsui: Jpn. J. Appl. Phys. 28 (1989) 468.
4) K. Yatsui, X. D. Kang, T. Satoh, S. Furuuchi, Y. Ohuchi, T. Takeshita, and H. Yamamoto: Phys. Plasmas 1 (1994) 1730.
5) K. Kitajima, T. Suzuki, W. Jiang and K. Yatsui: Jpn. J. Appl. Phys. 40 (2001) 1030.
6) M. Sengiku, Y. Oda, W. Jiang, K. Yatsui, Y. Ogura, K. Kato, K. Shinbo and F. Kaneko: Jpn. J. Appl. Phys. 40 (2001) 1035.
7) T. Suzuki, M. Kishima, W. Jiang and K. Yatsui: Jpn. J. Appl. Phys. 40 (2001) 1042.
8) T. Suzuki, K. Shioiri, W. Jiang and K. Yatsui: Jpn. J. Appl. Phys. 40 (2001) 1045.
9) T. Sonegawa, T. Arakaki, T. Maehama, W. Jiang and K. Yatsui: Jpn. J. Appl. Phys. 40 (2001) 1049.
10) T. Sonegawa, C. Grigoriu, K. Masugata, K. Yatsui, Y. Shimotori, S. Furuuchi and H. Yamamoto: Appl. Phys. Lett. 69 (1996) 2193.
11) T. Sonegawa, C. Grigoriu, K. Masugata, K. Yatsui, Y. Shimotori, S. Furuuchi and H. Yamamoto: Laser & Particle Beams 14 (1996) No. 4.
12) T. Sonegawa, C. Grigoriu, K. Masugata, K. Yatsui, Y. Shimotori and H. Yamamoto: Trans. IEE Jpn. 177A (1997) 398 [in Japanese]
13) X. D. Kang, K. Masugata and K. Yatsui: Jpn. J. Appl. Phys. 33 (1994) 1730.
14) A. Tokuchi, N. Nakamura, T. Kunimatsu, N. Ninomiya, M. Den, Y. Araki, K. Masugata and K. Yatsui: Proc. 2nd Int'l Top. Symp. on ICF Res. by High-Power Particle Beams, ed. K. Yatsui (1986) 430.
15) K. Yatsui, A. Tokuchi, H. Tanaka, H. Ishizuka, A. Kawai, E. Sai, K. Masugata, M. Ito and M. Matsui: Laser & Part. Beams 3 (1985) 119.

DEVELOPMENT OF LASER ION SOURCE WITH RECTANGULAR WAVE FORM

M.Nakajima, T.Miyayama and K.Horioka

Department of Energy Sciences, Tokyo Institute of Technology, 4253 Nagatuta, Midori-ku, Yokohama, 226-8502, Japan

J.Hasegawa, M.Ogawa

Research Laboratory for Nuclear Reactors, Tokyo Institute of Technology, 2-12-1 Ookayama, Meguro-ku, Tokyo, 152-8550, Japan

ABSTRACT

We have developed a laser ion source. It makes high current and good quality beam that has rectangular wave form with fast rising. It has the short drift length of 1cm. The effect of temporal changing of plasma flux to the meniscus of the emitting surface was investigated. It was found the meniscus was rather stable even at mismatched condition. It supplied a copper ion beam of 200mA(255mA/cm^2) with duration of 400ns and 30ns rise time. The beam emittance was about 0.8π mm•mrad.

I. Introduction

Heavy ion fusion(HIF) requires high brightness and high current ion sources with a low charge state and needs a current level exceeds the maximum capabilities for static plasma ion sources which supply ions with Bohm's current density.[1] Moreover HIF scheme demands rectangular beam wave forms. For a gaseous discharge type, it may be difficult to produce such low temperature and high dense plasmas. A pulsed solid vapor type like vacuum arc source[2] or laser ion sources may be a unique solution.

A laser ion source is an attractive candidate. Because, the laser ablation plasma expands spherically from one fixed point and long life is expected owing to high energy efficiency.

The expansion length of ablated plasmas must be short to extract rectangular wave form beams because prefill of plasma in an extraction gap must be avoided. So, laser intensity must be suppressed, but it is known laser ablation plasmas still have high translational kinetic energy up to 100eV.[3] So ions are supplied enough with the product of density and drift velocity. Moreover, it is thought the plasma temperature is so low that a pure singly ionized state is expected selecting a proper target.

However plasma flux changes temporary in short drift length, which may disturb the ion emitting surface. Then we investigated the meniscus of the emitting surface and the beam wave forms under such temporally changing condition. It was found that beams behaved as if matching condition during 400ns at least.

II.Experimental Setup

A schematic diagram of experimental apparatus is shown in Fig.1. Four induction cavities made of ferrite cores, connected to a pulse forming line, can generate voltages up to 50kV

during 400ns. Four cavities were stacked in a voltage adder configuration. In our experiments, extraction voltage was about 140kV with 400ns duration.

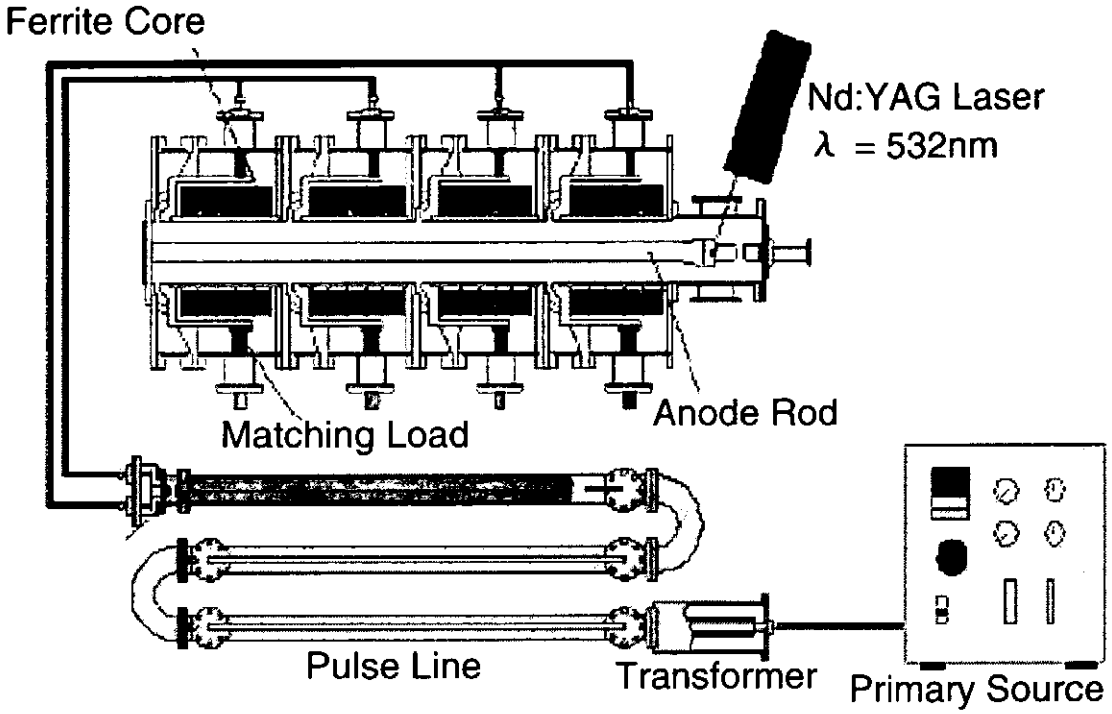

Fig.1 A schematic view of experimental apparatus

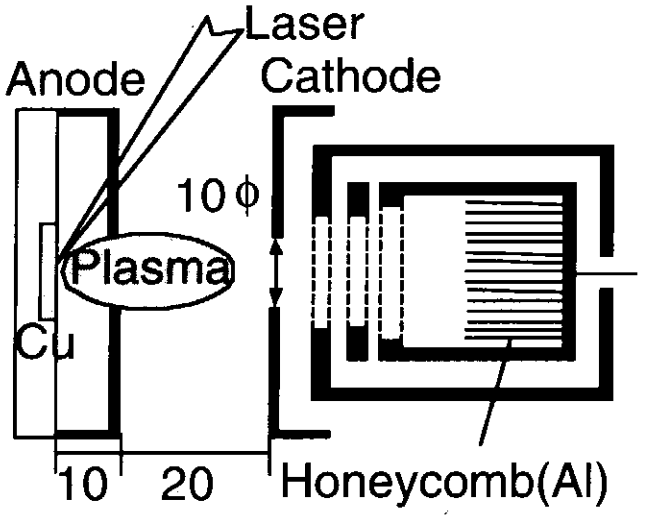

Fig.2 Laser ion source and extractor and Faraday cup

Fig.2 shows a schematic view of our ion source. A copper rod was used as the target. The Laser pulse focused on it with 300mm focal length lens and incident angle was 70°. The spot size was 1.6 × 0.7mm. We used a frequency doubled Nd:YAG laser with pulse duration of 7nsec. The drift length was 1cm. Both electrodes are made of plane SUS plates and each extraction hole was 1cm in diameter. The gap length was 2cm which was double of extraction hole diameter.

We used a Faraday cup with a honeycomb lattice which suppressed the secondary electrons. Emittance measurements were done using the pepper-pot method.[4] The beam

images were amplified by a MCP gated with a 300ns cable pulsar. A tantalum pepper-pot plate with 50μm thickness has holes of 200μm in diameter and their interval are 2mm. We performed the experiments under a background pressure of the order of 10^{-5} torr.

III.Results and Discussion

We measured wave forms and pepper-pot images of the beam as a function of time duration between laser irradiation and the voltage application. Fig.3 shows typical beam wave forms and pepper-pot images at three timings. When the timing of applying gap voltage was delayed, plasma prefilled the gap. The beam wave form was similar to that of the plasma opening switch. As shown with the pepper-pot image, the beam was largely divergent because of strong space charge repulsion. When applying voltage preceded it could be seen a strange pepper-pot image in which small divergent pattern was overlaid on the medium divergent beam. In case of the preceded timing, the meniscus of the emitting surface might be curved with its center of curvature outside the plasma. But it was not clear that two beams were coexistence at a time.

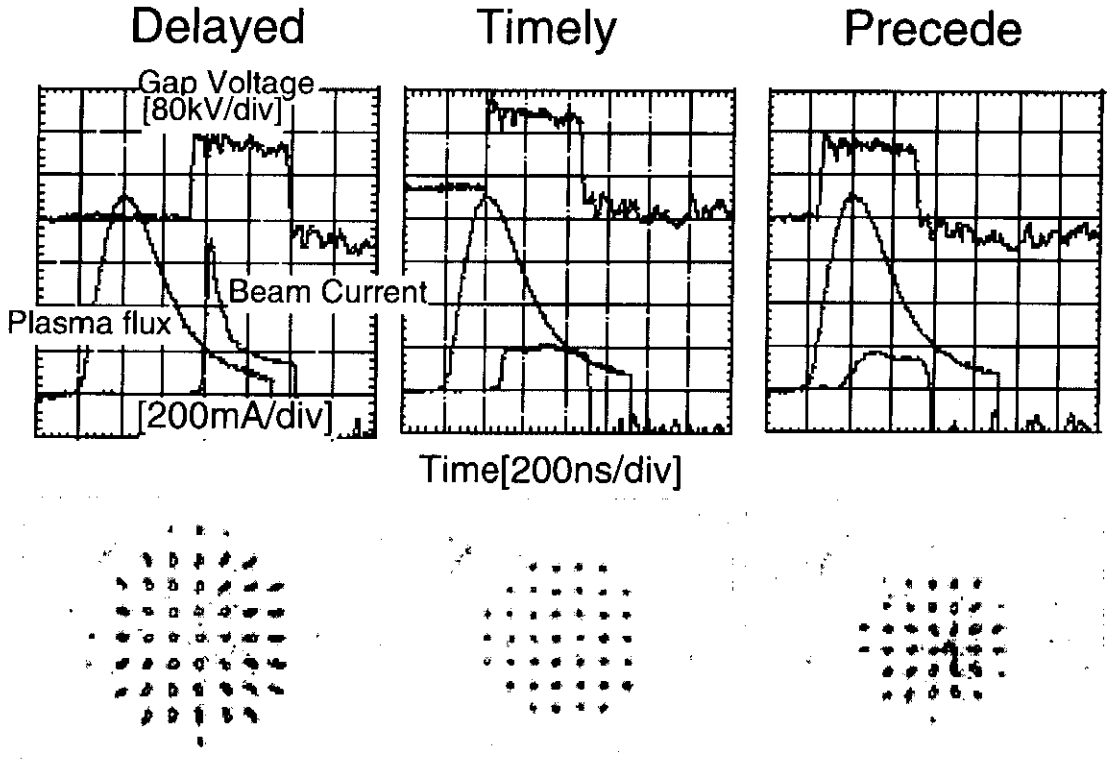

Fig.3 Typical beam wave forms and pepper-pot Images at different timings.

Surprisingly, when the timing was on time, the beam behaved as if under the absolute matching condition though the plasma flux changed temporally. The meniscus was very stable and the emittance was rather small. As shown in fig.4, the emittance had the minimum value when the supplied current matched the extracted current. When we further increased the current supply, the divergent angle of one fixed point began to increase slowly. It was thought the emitting surface became to convex shape as the plasma flux increased over the extraction current.

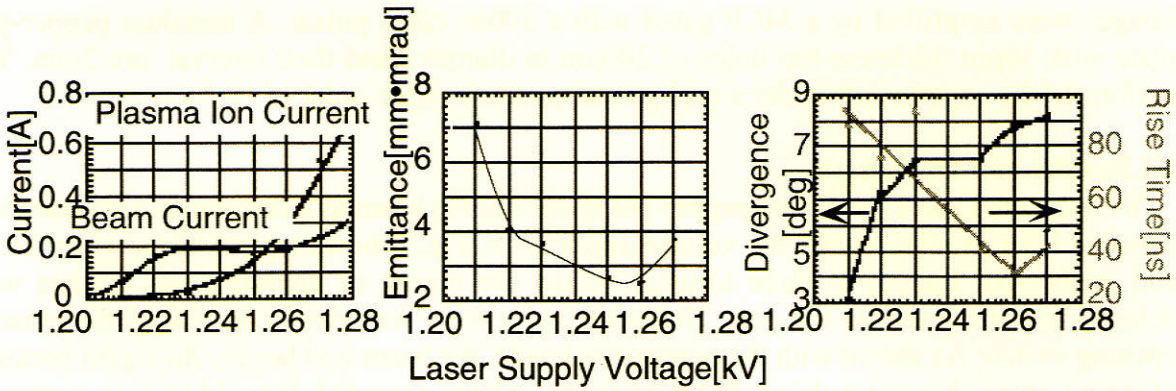

Fig.4 Beam characteristics versus laser intensity.

It was unexpected that beam current was larger than supplied current(more than 10 times). As shown in fig.5, the slightly divergent beam could be seen and it was observed at any timing whenever plasma was under dense. As shown in fig.6, beam current limited by Child-Langmuir's law could be extracted above the laser intensity corresponding to supplying voltage 1.22kV. A secondary ionization process, such as field-ionization of excited neutral atoms may be taking place around the anode region.[5] It is noted that the laser intensity was just above the threshold of laser ablation plasma.

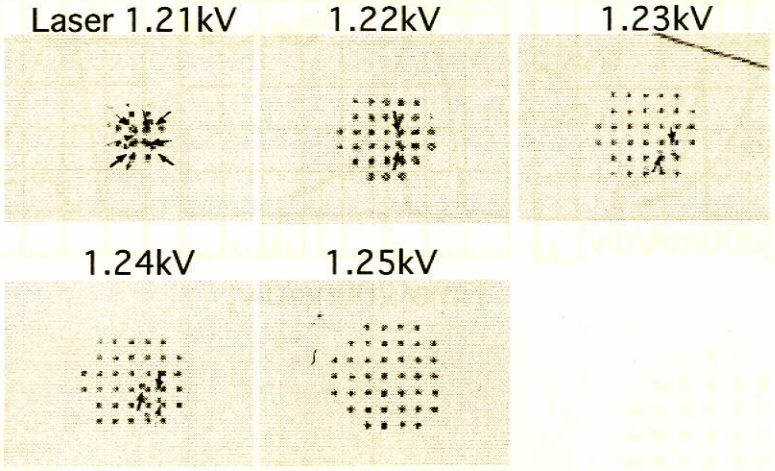

Fig.5 Beam images at matching timings

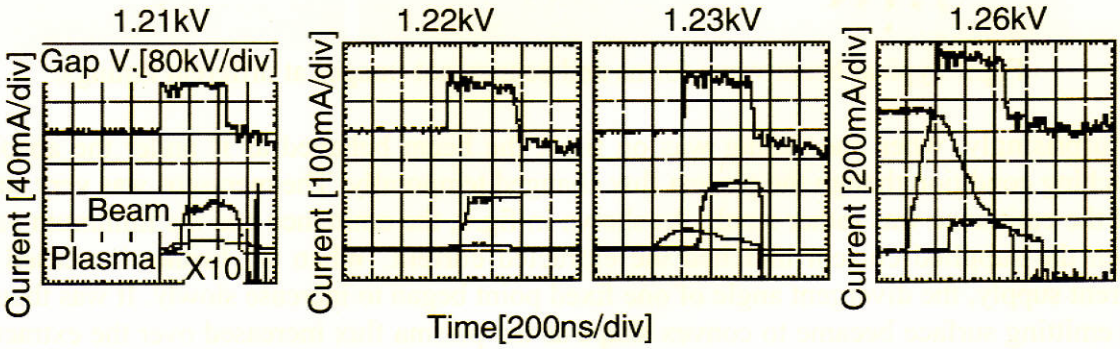

Fig.6 Beam wave forms at matching timings.

IV.Conclusion

By adjusting the timing between laser plasma and the voltage application, the effect of temporal change of plasma flux to the meniscus of the emitting surface was not seen during 400ns. We extracted a copper ion beam of 200mA (255mA/cm^2) with flat-top wave form duration of 400ns and 30ns rise time. At this operating condition, the beam emittance was about 0.8π mm•mrad.

References

1) E.P.Lee, et.al., "High current heavy ion beams for inertial confinement fusion", AIP Conf. Proc., **249**(2), 1713-24(1992)
2) I.G.Brown, "Vaccum arc ion sources", Rev. Sci. Instrum., **65**(10), 3061-81(1994)
3) G.C.Tyrrell, et.al., "Energy-dispersive mass spectrometry of high energy ions generated during KrF excimer and frequency-doubled Nd:YAG laser ablation of metals", Appl. Surface Sci. **96-98**, 227-32(1996)
4) J.G.Wang, et.al., "Beam emittance measurement by the pepper-pot method", Nucl. Instr. Meth. **A307**, 190-4(1991)
5) J.C.S. Kools, et.al., "Concentrations and Velocity Distribuitons of Positive Ions in Laser Ablation of Copper", Appl. Phys. **B53**, 125-30(1991)

TRANSIENT POTENTIAL HUMP IN LOW FLUENCE LASER ABLATION PLASMA

T. Kikuchi, T. Miyayama, M. Nakajima and K. Horioka

Department of Energy Sciences, Tokyo Institute of Technology, Nagatsuta 4259, Midori-ku, Yokohama, 226-8502, Japan

ABSTRACT

It is considered that ions in a laser ablation plasma are accelerated by the hydrodynamic pressure and/or electric field in the plasma. The acceleration mechanism of ions in the ablation plasma must be clarified for several applications, especially in an energy region of low fluence laser irradiation. We investigate the ion acceleration mechanism in the low fluence laser ablation plasma using computer simulation. As a result, it is found that a transient potential exceeds the floating potential level, is created in an early stage of the ablation process. The ions are accelerated by the electrostatic potential hump, and anisotropy of ion acceleration is induced by the interaction between conductor walls and the laser ablation plasma.

I. Introduction

Plasmas generated by laser irradiation are applied to pulsed laser deposition method for a material processing and inertial confinement fusion (ICF) using intense laser, etc. In fields of high-energy physics and ICF using heavy ion beam (HIF), an intense-heavy-ion beam is essentially needed. The charged particle beam is generated using high flux ion source and particle accelerator. Ion sources using laser ablation plasma were proposed for these purposes.[1,2] It is desirable that the ions extracted from those sources have low charge state to decrease the space charge effect during the high-current beam transport. Consequently, low fluence laser should be used for these ion sources.[3]

In the case of intense laser irradiation, ions in the ablation plasma are mainly accelerated due to two mechanisms: hydrodynamic force derived from pressure gradient caused by the dense ablation plasma and electrostatic force induced by the escape of high energy electrons; so-called Coulomb explosion. The high-energy electrons accelerated by the intense laser field, immediately escape from the plasma region. Consequently, the remained ions create a potential hump, so that the self-electrostatic field accelerates the ions.

On the contrary, the experimental results[4] show that the ions in the ablation plasma are accelerated up to several hundred electron volts (eV) even using low fluence lasers. Furthermore, the ions are mainly accelerated to perpendicular direction of ablation target, i.e. anisotropic acceleration.[4] In the early stage of ablation process, as already mentioned, dense plasma is generated near the target surface, and the plasma has a large-pressure gradient. As a result, the generated plasma is pushed out to outer free space by the pressure gradient. However, the hydrodynamic acceleration occurs only in the early stage of ablation, and the Coulomb explosion does not play a significant role because of the low (~ eV) electron temperature in the ablation plasma. The ions accelerated up to a few hundred eV from the low temperature plasma are of great interest from above two reasons.[5]

In this study, we discuss the anisotropic ion acceleration mechanism from laser ablation plasma in the case of low fluence laser. We have carried out a numerical computer simulation using a simplified model and the particle-in-cell (PIC) method [6,7] to clarify the cause of anisotropic ion acceleration in copper plasma produced in a vacuum gap.

II. High Energy Ion Generation Mechanism from Laser Ablation Plasma

The calculation model in this section is schematically shown in Fig.1. In this section, the ablation plasma generation process is treated as one-dimensional. The gap distance between the conductor target (ablation surface) and the opposite electrode, i.e. total calculation region, is 1cm, and both boundaries are grounded conductor walls. The exact self-consistent calculation for ablation process is difficult due to the treatment of the phase change from solid to neutral gas and plasma. To simplify the problem, we neglect the laser-plasma interaction process and assume that the ablation plasma is placed near the left side electrode, and the plasma consists of Cu^+ and electrons. These particles are uniformly distributed in the above region at constant supplying rate. The width of plasma region is assumed to be 0.5mm. The Cu^+ temperature is 0eV, and the electron has Maxwell distribution of 10eV.

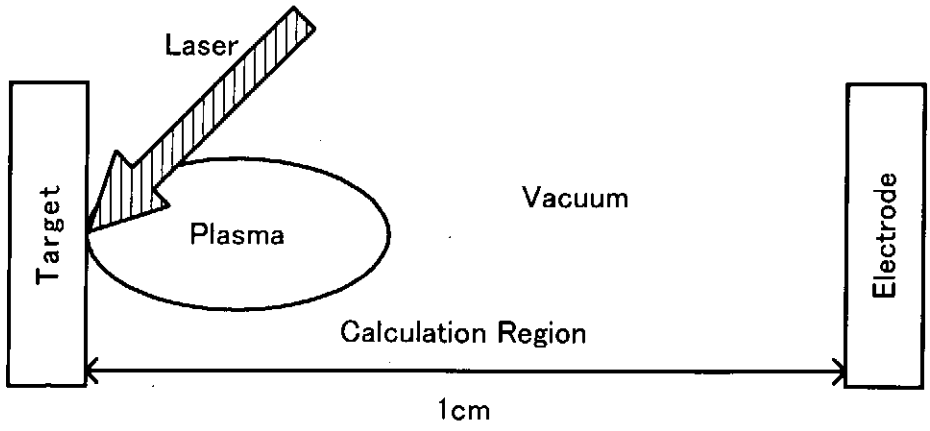

Figure 1: One-dimensional calculation model for Laser ablation plasma.

For the above plasma simulation, we use one-dimensional electrostatic PIC code [6,7] in this section. Our PIC code uses forth-order Runge-Kutta method for time integration of relativistic particle motion. For efficient integration of the Poisson equation, we use dynamic mesh refinement depending on time. The Poisson equation is solved by Successive Over Relaxation (SOR) method, and the SOR Poisson equation solver is effectively calculated using the Multi-Grid method.[8]

The typical calculation results in these conditions are as follows: Fig.2 and Fig.3 show the results for case of initial Cu^+ drift velocity of 0eV. Fig.2 (a) and (b) are particle maps for Cu^+ ions on phase space, and then (c) and (d) are shown for electrons. Fig.3 presents the number

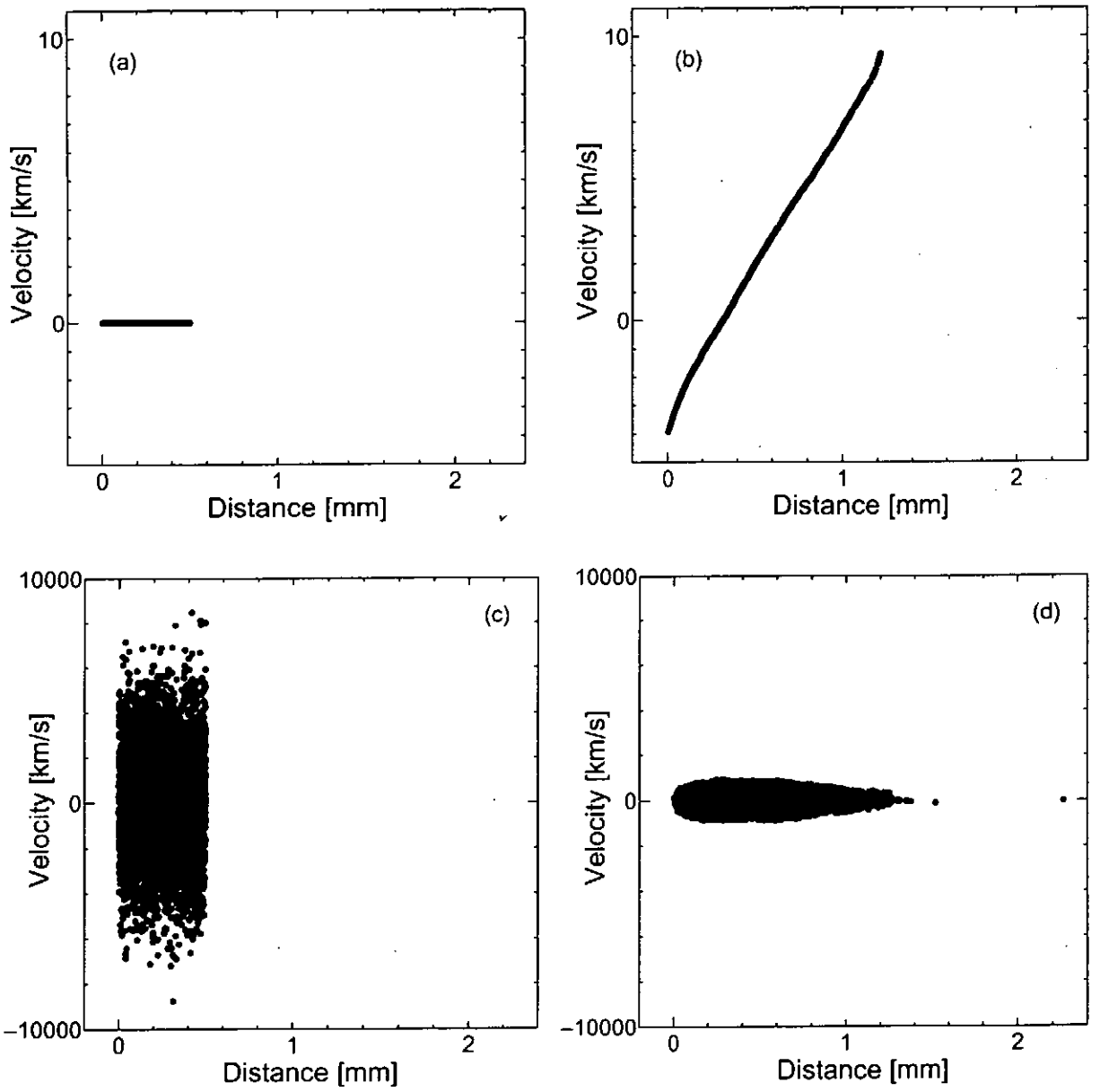

Figure 2: Cu^+ and electron particle maps on phase space, (a) Cu^+ ions at initial state, (b) Cu^+ ions at 100ns, (c) electron at initial state, (d) electron at 100ns, respectively.

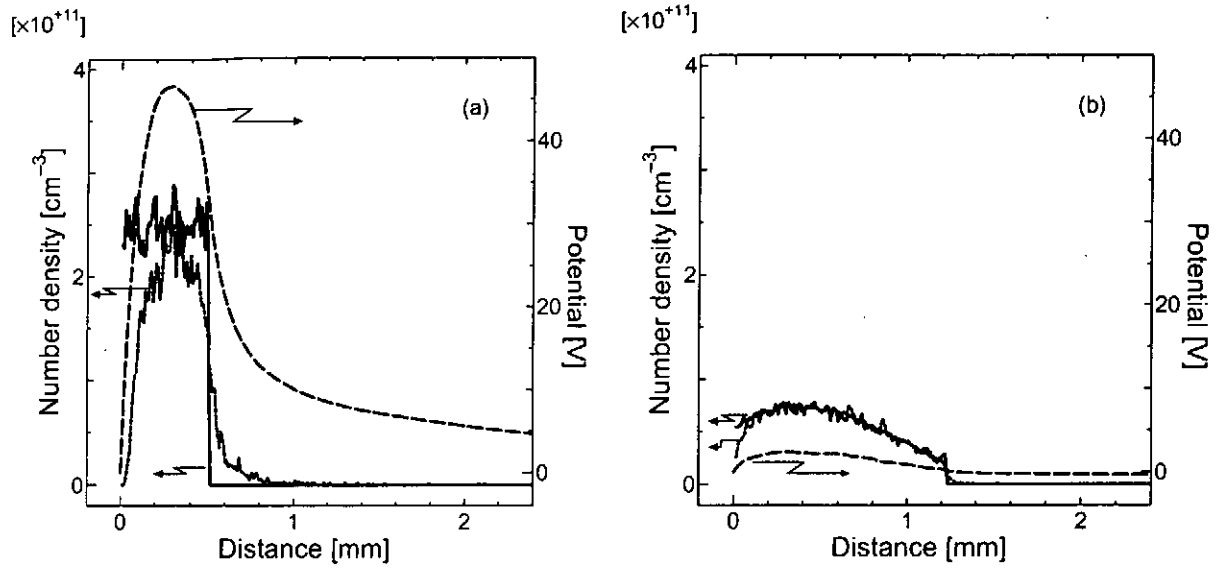

Figure 3: Cu^+ and electron number density and potential distribution, (a) at 5ns and (b) at 100ns, respectively. Solid lines are Cu^+ number density, doted lines are electron number density and dashed lines are potential.

density of the plasma and created potential distribution. Fig.3 (a) and (b) are the values at 5nsec and at 100nsec, respectively. As can be seen from Fig.2 (b), the ions were accelerated into free space. The increase of the potential could be observed from Fig.3. The potential transiently increased more than 40V during several 10 nsec. As assumed previously, electrons in the plasma escape to the target side, and it is found that the potential increased by the space charge build-up. This transient potential is held until the ions in the plasma also escape to the left side electrode.

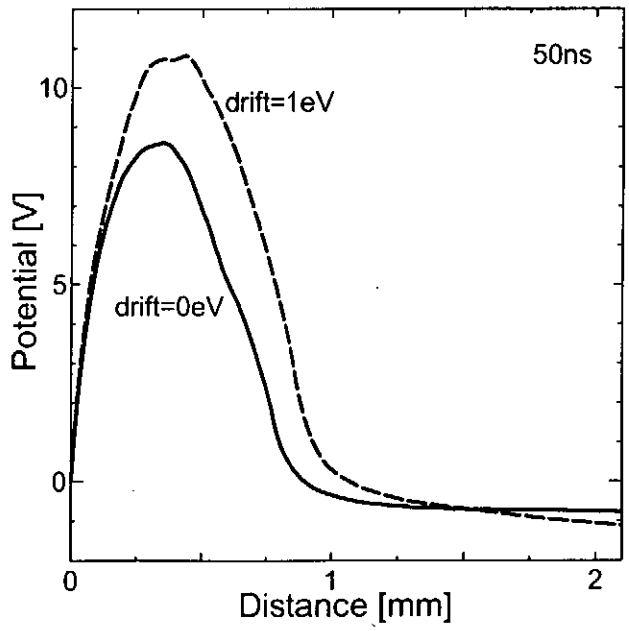

Figure 4: Comparison of created potential between case of ion drift=0eV and drift=1eV at 50ns.

As mentioned earlier, laser ablation plasma is accelerated by hydrodynamic effect so that the ions have drift velocity toward from the target side to the free space. Keeping this in mind, we will consider the effect of this drift velocity. Fig.4 shows the results with and without drift velocity of ions. The assumed ion drift velocity is 1eV in this calculation. As can be seen from Fig.4, the drift velocity additionally increased the potential value.

From those results, we can deduce the behavior of the ion acceleration from laser ablation plasma as follows: conductor (copper: Cu) target evaporates due to the laser irradiation. The electrons in the dense neutral gas absorb the irradiated laser energy, and ionize it. A part of electrons in the generated plasma escapes to the target side, i.e. the electrons are absorbed into the conductor target. On the other hand, velocity of the ions in the ablation plasma is very slow as compared with the electrons if the ion temperature is the order of the electron's one. Therefore, the electrons in the ablation plasma can easily move, but the ions can hardly escape to the conductor target. Consequently, potential hump exceeds the floating potential of Te=10eV plasma, is transiently formed in the ablation plasma only during the charge separation phase, i.e. ion transit time. The electrostatic field caused by the transient potential accelerates the ions.

III. Anisotropic Ion Acceleration in Laser Ablation Plasma

In this section, we discuss the anisotropic ion acceleration mechanism. From the experimental results[4], it is found that the accelerated ions have directivity. As discussed in previous section, the acceleration results from electrostatic field caused by transient potential. However, potential is scalar value, so that it is difficult to explain the anisotropy in the ion acceleration. Therefore, we have to investigate the acceleration mechanism using multi-dimensional particle simulation.

Fig.5 shows the simple two-dimensional calculation model used here. The centerline of r=0 in the model is the cylindrical axis, at which the cylindrically symmetric boundary condition is imposed. The other three outer boundaries are grounded conductor walls. The calculation area is supposed to be in vacuum. For the numerical simulation, two-dimensional PIC code is used, the field component (E_r, E_z), and the particle position and velocity (r, z, v_r, v_z) are solved using the Maxwell equations and the relativistic equation of motion.[6,7] The calculation area is $0 \leqq r \leqq 1$cm and $0 \leqq z \leqq 1$cm. The plasma consists of Cu^+ and electron, and is placed in $0 \leqq r \leqq 0.5$mm and $0 \leqq z \leqq 0.5$mm at the initial condition (see Fig.5).

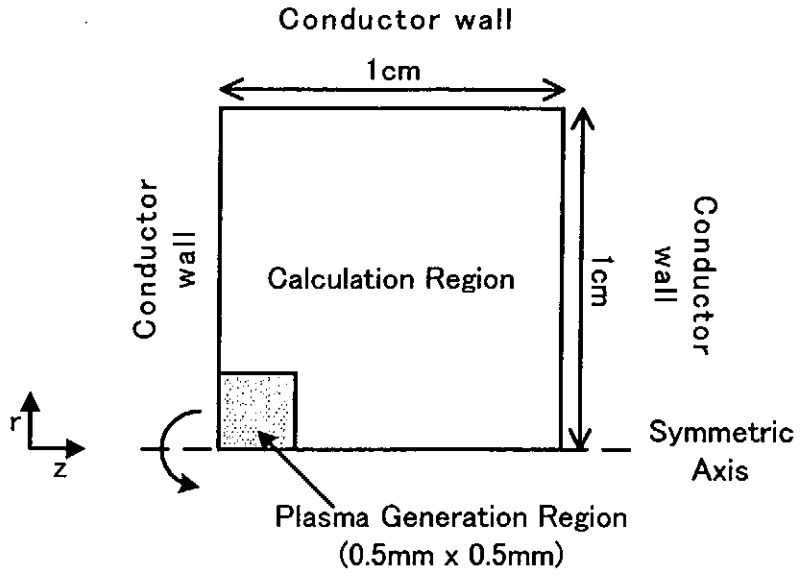

Figure 5: Two-dimensional calculation model for investigation of anisotropic ion acceleration from ablation plasma.

The calculation results are shown in Fig.6~8. Fig.6 shows the ion particle maps on r-z coordinate space. As can be seen from Fig.6, the ions were anisotropicaly accelerated. Fig.7 presents particle maps in electron and ion on velocity space. The anisotropic acceleration of ions was also shown from Fig.7. Fig.8 presents potential distribution at the early stage. The contour lines on r-z plane show the potential distribution. From Fig.8, the potential has anisotropic distribution because the plasma was placed near the left side electrode at initial condition. These results suggest that the electrostatic field induced by the anisotropic potential

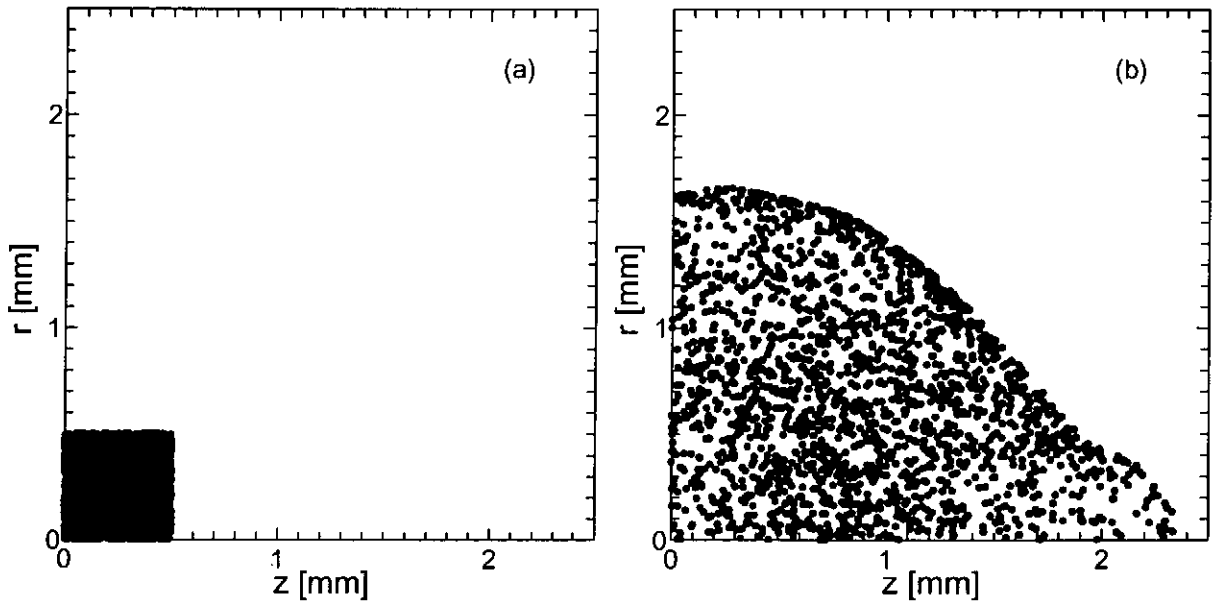

Figure 6: Cu^+ particle maps on r-z space, (a) at initial state and (b) at 200ns.

creation is the cause of the experimentally observed anisotropic ion acceleration in the ablation plasma.

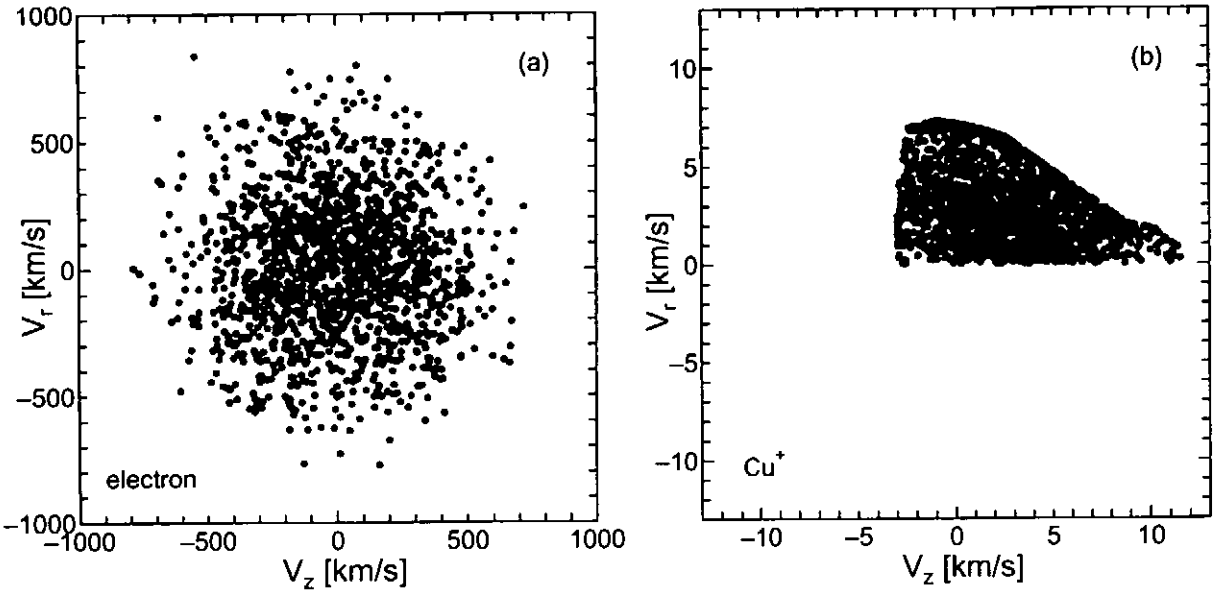

Figure 7: Particle maps on velocity space at 200ns, for electron (a) and for Cu^+ (b), respectively.

IV. Summary

The ion acceleration mechanism in ablation plasma produced by low fluence laser irradiation was investigated by numerical particle simulation. The results showed that high-energy electrons in the plasma escaped to the target electrode in the early stage of the process. For this reason, electrostatic field induced by the space charge build-up, accelerated the remained ions in the plasma. In addition, two-dimensional PIC simulation results

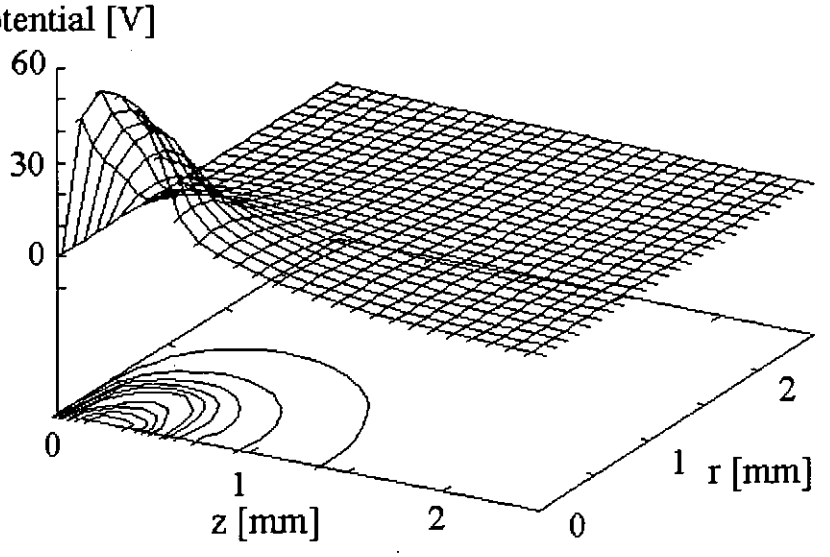

Figure 8: Created potential distribution on two-dimensional space at 1ns.

indicated that the electrostatic field induced by the interaction between the plasma and the electrode caused anisotropic ion acceleration. This means the electrode effect plays an essential role for ion acceleration in low fluence laser ablation plasma. Although the phenomena treated in this paper is based on the simplified model, the plasma behavior and the ion energy are similar to the experimental observation.

References

1) M. Yoshida, J. Hasegawa, S. Fukata, Y. Oguri, M. Ogawa, M. Nakajima, K. Horioka and M. Shiho, "Development of a high-current laser ion source for induction accelerators", Rev. Sci. Instrum., Vol.71, No.2, pp.1216-1218. (2000).
2) J. Hasegawa, M. Yoshida, Y. Oguri, M. Ogawa, M. Nakajima and K. Horioka, "High-current laser ion source for induction accelerators", Nucl. Instrum. and Meth. in Phys. Res. B, Vol.161-163, pp.1104-1107. (2000).
3) M. Nakajima, T. Miyayama, K. Horioka, J. Hasegawa and M. Ogawa, "Development of high brightness laser ion source with rectangular wave form", this proceedings (2001).
4) P. E. Dyer, "Electrical characterization of plasma generation in KrF laser Cu ablation", Appl. Phys. Lett. Vol.55, No.16, pp.1630-1632. (1989).
5) J. Hasegawa, Ph.D dissertation Tokyo Inst. of Tech. (1998).
6) C. K. Birdsall and A. B. Langdon, "Plasma Physics via Computer Simulation", New York: McGraw-Hill Press, (1985).
7) R. W. Hockney and J. W. Eastwood, "Computer Simulation using Particles", Philadelphia: Institute of Physics Publishing, (1988).
8) K. Sakurai and T. Aoki, private communications.

Conservative Constrained Interpolation Profile Scheme for the Simulation of the High-Energy Plasma

T.Nakamura, Y.Uchida, K.Shimizu, M.Shitamura, S.Kawata

Department of Electrical and Electronic Engineering, Utsunomiya University
7-1-2 Yoto, Utsunomiya 321-8585, Japan
ntakashi@cc.utsunomiya-u.ac.jp

Abstract

A new numerical scheme for simulation of the distribution function according to the Vlasov-Poisson equation is described. At each time step, the distribution function and its first derivatives are advected in phase space by the Cubic Interpolated Propagation (CIP) scheme. Although a cell within grid points is interpolated by a cubic-polynomial, any matrix solutions are not required. The scheme still gives the stable, accurate and reasonable results with memory storage comparable to particle simulations. Furthermore, by using the CIP-Conservative Semi-Lagrange (CIP-CSL) scheme developed by one of the authors, the scheme guarantees the exact conservation of the mass.

Keywords: Vlasov equation, Distribution function, CIP, CIP-CSL, Mass conservation

1 Introduction

In recent years, various numerical methods have been used for solving the nonlinear Vlasov equation and these methods are roughly divided into two classes. One numerical approach is the particle method that directly follows the trajectories of particles, such as the PIC method (see for review [1]). This method has been considered to be quite stable even if only few computational particles are used. On the other hand, it is known that this scheme essentially involves some serious disadvantages stemming from statistical numerical noise particularly when detailed structure of distribution is needed for the purpose of transport phenomena like viscosity and heat conduction and for atomic processes.

Another approach is the Eulerian method that uses a hyper-dimensional computational mesh in phase space and the time integration of the distribution function is carried out on each computational mesh point. Because these methods don't involve any source of

the statistical noise intrinsic to the particle methods and the profile of the distribution function is stored equally, this numerical approach is more suitable for the simulations in which the particle distribution in a certain velocity region plays an important role. However, since this method covers all the phase space with grid points, the memory storage and computation time rapidly increases. However, in the recent works, one of the authors have applied the Constrained Interpolation Profile (CIP) scheme to Vlasov equation and successfully show a possibility to realize high accurate numerical plasma simulation with extreme lower computational costs.[12]

The Cubic Interpolated Propagation (CIP) scheme is a novel unified numerical scheme developed by Yabe et al.[2–5] for the solving hyperbolic equations. The CIP scheme is a low diffusion and stable scheme. In the CIP scheme first spatial derivatives are introduced as free parameters on each grid point and the time evolution of the derivatives is calculated from the spatial derivatives of a model equation that is consistent with the master equation. Thus, the coefficients of the cubic-polynomial are analytically determined from the physical values and these first derivatives on the neighboring two grid points without any matrix solutions. These facts allow us to easily extend the scheme to hyper-dimensional scheme and solve hyperbolic equations with lower computational effort.

In contrast in these excellent numerical features, it is also well known that the CIP scheme not guarantees an exact mass conservation. In the previous work, we improved the CIP scheme to guarantee the exact mass conservation in the special case, when a non-uniformly mesh condition is used, mass conservation is not guaranteed. This fault concerning the conservation proceeds from CIP's non-conservative formulation. In order to overcome this disadvantage, we have developed new CIP scheme called as CIP-Conservative Semi-Lagrange (CIP-CSL) scheme that is based on a conservative formulation. This paper presents a brief review on the CIP scheme and CIP-CSL2 scheme from a viewpoint of application to Vlasov equation.

2 Numerical Procedure

2.1 Basic Principle of the CIP-CSL Scheme

In this section, the CIP-CSL scheme is briefly reviewed by the use of a simple one-dimensional hyperbolic equation:

$$\partial f/\partial t + v\partial f/\partial x = 0. \tag{1}$$

If the velocity v is constant, the theoretical solution of Eq.(1) is obtained by shifting a profile like $f(x, t + \Delta t) = f(x - v\Delta t, t)$. Similarly even if the velocity is not constant, an approximate solution can be given by

$$f(x_i, t + \Delta t) \cong f(x_i - v\Delta t, t), \tag{2}$$

where x_i is the grid point. Equation (2) represents a simple translation of profiles with a velocity v.

For simplicity, in this paper, we take an assumption that the velocity v is independent of x. In this case, the advection equation (1) is rewritten into a conservative equation,

$$\frac{\partial f}{\partial t} + \frac{\partial (vf)}{\partial x} = 0. \tag{3}$$

The CIP-CSL scheme require an additional constraint of the value integrated within neighboring two grid points

$$\rho_i = \int_{x_i}^{x_{i+1}} f(x)dx. \tag{4}$$

Thus, the time development of ρ is calculated according to the following equation which is derived by rewriting down Eq.(3) in a conservative finite difference form:

$$\rho_i^{n+1} = \rho_i^n + \Delta\rho_{i+1} - \Delta\rho_i \tag{5}$$

where the superscript "n" indicates the time, and $\Delta\rho_i$ represents the mass flux passing through x_i during $[t, t + \Delta t]$;

$$\Delta\rho_i = \int_{x_i}^{x_i+\xi} f(x)dx \tag{6}$$

where $\xi = -u_i\Delta t$. Since Eq.(5) is written as the difference of $\Delta\rho_i$ for the time evolution of ρ, the sum of $\Delta\rho_i$ over the entire computational domain will vanish exactly, thus guaranteeing the conservation defined in terms of sum of integral between grid points $\sum_i \rho_i$ defined by Eq.(4) instead of a sum over values at grid points $\sum_i f_i$.

By the analogy of the CIP scheme, we shall introduce a function:

$$D_i(x) = \int_{x_i}^{x} f(x')dx'. \tag{7}$$

In view of Eq.(6), $D_i(x)$ is merely $\Delta\rho_i^n$ if x is set to $x_i + \xi = x_i - v_i^n \Delta t$, therefore $D_i(x)$ represents the accumulated mass from x_i to the upstream point. We shall use a cubic polynomial to approximate this profile:

$$D_i(x) = \phi_i X^3 + \eta_i X^2 + f_i^n X \tag{8}$$

where $X = x - x_i$. The role of spatial gradient in the CIP method is now played by f which is the spatial gradient of $D(x)$ in the present scheme. By using the above relation, a profile of $f(x)$ between x_i and x_{iup} is then obtained by taking the derivative of Eq.(8):

$$f(x) = \frac{\partial D_i(x)}{\partial x} = 3\phi_i X^2 + 2\eta_i X + f_i^n \tag{9}$$

From the definition of D in Eq.(7), it is clear that

$$D_i(x_i) = 0, \qquad D_i(x_{iup}) = \mathrm{sgn}(\xi)\rho_{icell}^n \tag{10}$$

where ρ_{icell}^n is the total mass of upwind cell defined at the cell center $i \pm 1/2$ and $icell = i + sgn(\xi)/2$. Since $\partial D/\partial x$ gives a functional value f, it is also clear that

$$\frac{\partial D_i(x_i)}{\partial x} = f_i^n, \qquad \frac{\partial D_i(x_{iup})}{\partial x} = f_{iup}^n \tag{11}$$

Therefore, the coefficients ϕ_i and η_i are determined so as to satisfy the constraints Eqs.(10) and (11). As a result of above simultaneous equations, the coefficients are determined explicitly without any matrix solution as follows,

$$\phi_i = \frac{f_i^n + f_{iup}^n}{\Delta x_i^2} - \frac{2\mathrm{sgn}(\xi)\rho_{icell}^n}{\Delta x_i^3} \tag{12}$$

$$\eta_i = -\frac{2f_i^n + f_{iup}^n}{\Delta x_i} + \frac{3\mathrm{sgn}(\xi)\rho_{icell}^n}{\Delta x_i^2} \tag{13}$$

where $\Delta x_i \equiv x_{iup} - x_i$. Then, $\Delta\rho_i$ is calculated as,

$$\Delta\rho_i = \int_{x_i}^{x_i+\xi} f(x)dx = D_i(x_i + \xi) = \phi_i\xi^3 + \eta_i\xi^2 + f_i^n\xi. \tag{14}$$

The time development of ρ can be calculated from Eq.(5) with the aid of Eq.(14).

Then, let us turn to the time evolution of the value f. We calculate the value f in the same way as the original CIP scheme. The conservation equation (3) is rewritten as

$$\frac{\partial f}{\partial t} + u\frac{\partial f}{\partial x} = 0, \tag{15}$$

For the solution of f, we make use of the local analytic solution in the same way in the CIP scheme, that is well known as the Lagrangian invariant solution:

$$f_i = \frac{\partial D_i(x_i + \xi)}{\partial x} = 3A1_i\xi^2 + 2A2_i\xi + f_i^n \tag{16}$$

2.2 Application to Vlasov-Poisson Equation

In order to show the numerical features, we shall treat the simplest case in two-dimensional phase space composed of space x and velocity v_x [12]. The Vlasov-Poisson equation is rewritten as

$$\partial f(x, v_x, t)/\partial t + v_x \partial f(x, v_x, t)/\partial x - E_x(x, t)\partial f(x, v_x, t)/\partial v_x = 0, \tag{17}$$

and

$$\partial E_x/\partial x = 1 - \int f(x, v_x, t)dv_x. \tag{18}$$

We use the Cartesian mesh to represent the x-v_x phase space with the computational domain $R = \{(x, v_x)|0 \leq x < L, |v_x| \leq v_{off}\}$, where L is the spatial periodic length and v_{off} is the cutoff velocity. The number of mesh points used in x- and v_x- directions is designated by N and $2M$ respectively. After the calculating of the advection in the x-direction, the scalar potential of the electrical field ϕ is introduced and the following discrete Poisson equation is solved with results of the advection in x-direction.

$$\frac{\phi_{i+1} - \phi_{i-1}}{\Delta x} = 1 - \Delta v_x \sum_{j=1}^{2M} f_{ij}^{step1}. \tag{19}$$

Then, the electrical field $E_x^{n+1/2}$ is given by taking derivative of ϕ.

3 Summary

In the present work, we show a possibility of an application of new numerical schemes, namely CIP and CIP-CSL scheme to the solution of the Vlasov equation. The time integration of the distribution function was carried out by a shift of the distribution function in phase space and the advection was calculated by these schemes. The CIP scheme solves the advection explicitly and does not require any matrix solution. Furthermore, in addition to the lower computational cost, the CIP-CSL scheme came to exactly guarantee the total mass conservation in the solution of the Vlasov equation.

References

[1] R. W. Hockney and J. W. Eastwood, Computer simulation using particles (*MacGraw-Hill international com*, 1981)

[2] H. Takewaki, A. Nishiguchi, T. Yabe, *J. Comput. Phys.* **61**, 261 (1985).

[3] H. Takewaki, T. Yabe, The cubic-interpolated pseudo particle (CIP) method: application to nonlinear and multi-dimensional hyperbolic equations, *J. Comput. Phys.* **70**, 355 (1987).

[4] T. Yabe, T. Aoki, A universal solver for hyperbolic equations by cubic-polynomial interpolation I. One-dimensional solver, *Comput. Phys. Commun.* **66**, 219 (1991).

[5] T. Yabe, T. Ishikawa, P. Y. Wang, T. Aoki, Y. Kadota, F. Ikeda, A universal solver for hyperbolic equations by cubic-polynomial interpolation II. Two- and three-dimensional solver, *Comput. Phys. Commun.* **66**, 233 (1991).

[6] T. Utsumi, T. Kunugi, T. Aoki, Stability and accuracy of the Cubic Interpolated Propagation scheme, *Comput. Phys. Commun.* **101**, 9 (1997).

[7] T. Yabe and F. Xiao, *Nucl. Eng. Des.* **155**, 45 (1995).

[8] T. Yabe, Unified solver CIP for solid, liquid and gas, *Computational Fluid Dynamics Review 1997 Ed.by M.M.Hafez and K.Oshima (Wiley,1997).*

[9] T. Aoki, *Comput. Fluid Dyn.* **4**, 279 (1995).

[10] S. T. Zalesak, *J. Comput. Phys.* **31**, 335 (1979).

[11] E. Kreyszip, Advanced Engineering Mathematics (*John Wiley and Sons, Inc., New York.* 1983)

[12] T. Nakamura and T. Yabe, Cubic Interpolated Propagation scheme for solving the hyper-dimensional Vlasov-Poisson equation in phase space,*Comput. Phys. Commun.* **120**, 122 (1999).

[13] R. Tanaka, T. Nakamura, T. Yabe,Constructing exactly conservative scheme in non-conservative form, *month. Weath. Rev.*, in press.

As an example, we show a numerical result of the symmetric two-stream instability. Initial condition is

$$f(x, v_x, 0) = 1/\sqrt{2\pi} v_x^2 \exp(-v_x^2/2)(1 - A\cos k_x) \tag{20}$$

where $A = 0.05$, $k_x = 0.5$, $L = 4\pi$ and $v_{off} = 5.0$. we used $N = 32$, $M = 24$ and $\Delta t = 1/8$. The results are shown in Figs.1, 2, 3 and 4.

Figure 1 shows the time development of distribution function in phase space by using the CIP-CSL scheme. At $t \cong 8.5$, trapping and formation of a vortex starts. From $t \cong 8.5$ to $t \cong 17.8$, the instability grows rapidly and a hole structure appears. After $t \cong 18.0$ until the end, trapped particles oscillate in the electric field and the vortex rotates with a period $T \cong 18$. In Fig.2 (b), Over-view profile of the distribution function in phase space at t=16.6 is also shown. For comparison, numerical results of the original CIP (Fig.2 (a)) and PIC (Fig.2 (c)) method for the same initial condition are shown. Although the CIP scheme provides the quite similar profile with the CIP-CSL scheme, the PIC scheme gives a poor resolution and unclear profile because of the statistical noise of the particles.

Furthermore, the development of the electric field energy $W_{el} = 1/2 \sum_i |E_x(x_i, t)|^2 \Delta x$ is plotted in Fig.3. The CIP-CSL (Fig.3 (b)) and CIP (Fig.3 (a)) scheme described well the rapidly growth of the instability and the oscillations due to the particle trapping after the end of the growth. Although the number of particles corresponds to twice larger storage than $M = 24$ of the CIP-CSL and CIP scheme, as shown in Fig.3 (c), the electric field energy is also poorly described and unclear with the PIC method. Therefore, at least as far as the two-dimensional Vlasov equation concerned, we think that the CIP can solve an entire profile of the distribution function more accurately with a lower computational cost.

Figure 4 (a) shows the mass conservation error as a function of time. Mass conservation rate is checked with 10^{-4} due to the escape of the particle from the computational domain in v_x - direction. In order to verify this fact, we change a cutoff velocity and mesh condition into $v_{off} = 10.0$ and $M = 48$ with another conditions same, and the result is shown in Fig.4 (b). The vastly reduction of the conservative error is caused by the reduction of the number of particles which escape from domain, and it can be actually verified that the mass conservation is exactly guaranteed by using the CIP-CSL scheme.

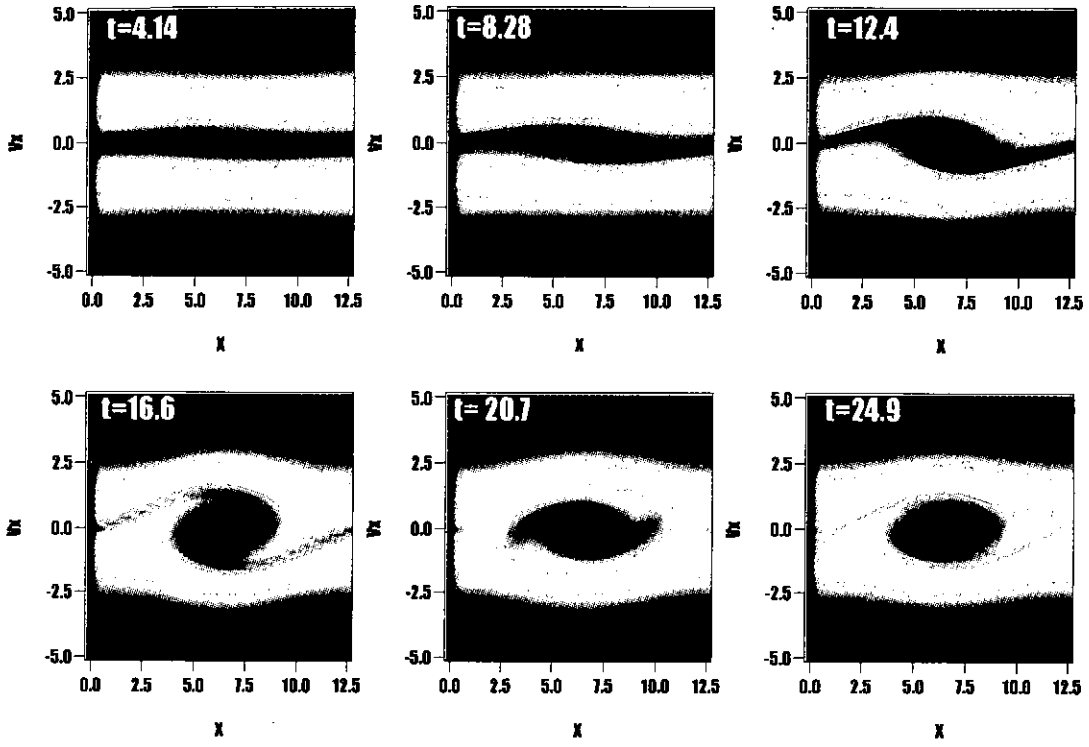

Fig.1 Time evolution of the distribution function in solution of the two-stream instability by using the CIP-CSL scheme.

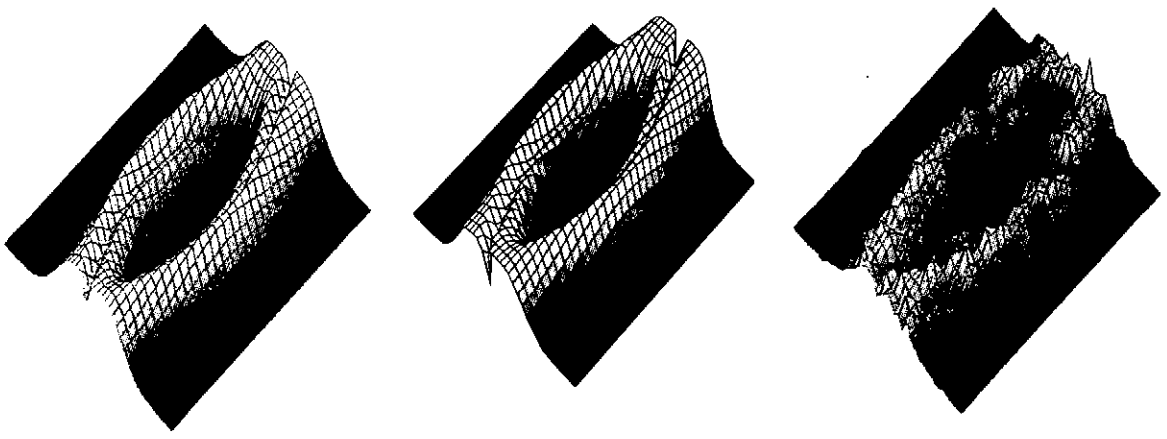

(a) CIP (b) CIP-CSL (c) PIC

Fig.2 Over-view profile of the distribution function in phase space at t=16.6 using (a) CIP, (b) CIP-CSL (c) PIC (4608 "particles", correspond to twice larger storage than M=24 of CIP and CIP-CSL).

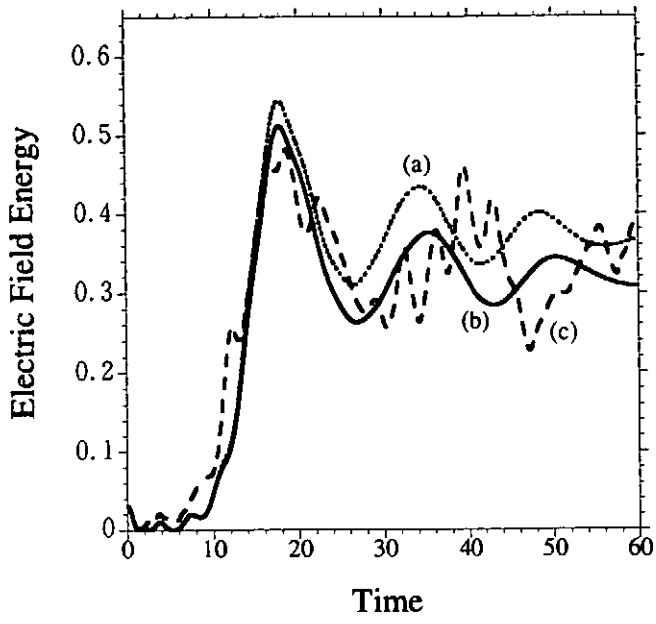

Fig. 3 The time evolution of the total electric field energy for the two-stream instability. Dotted curve(a) and solid curve(b) represent the numerical results of the CIP and CIP-CSL scheme, respectively. Dashed curve(c) represents the result of the PIC scheme with 4608 "particles" which corresponds to M=24 (curve (a) and (b)) as far as storage is concerned.

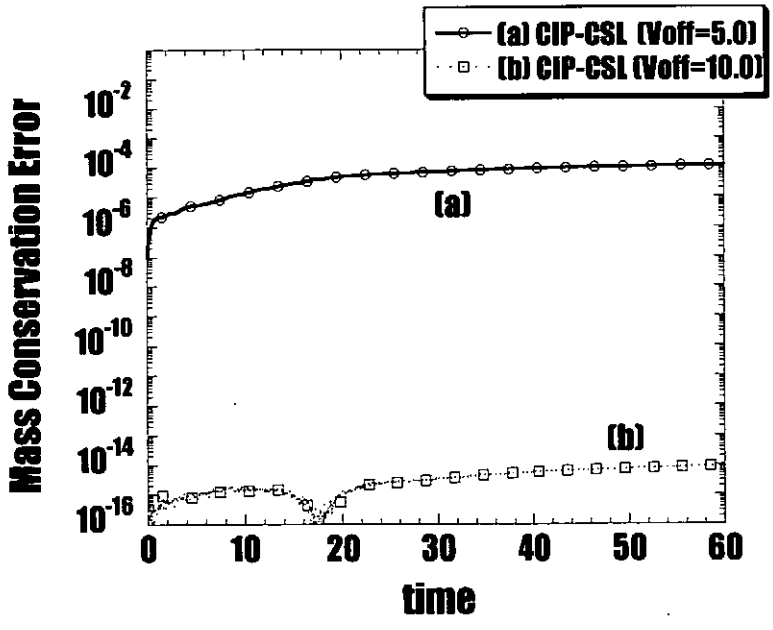

Fig. 4 The mass conservation error for the two-stream instability by using the CIP-CSL scheme. Dotted curve (b) represents the result with a cutoff velocity v_{off} =10.0 that is twice as large as solid curve (a).

NANOSIZED γ-ALUMINA WITH DISPERSED ZIRCONIA SYNTHESIZED BY PULSED WIRE DISCHARGE

Y. Kinemuchi, H. Mouri, K. Ishizaka, T. Suzuki, H. Suematsu, W. Jiang and K. Yatsui

Extreme Energy-Density Research Institute, Nagaoka University of Technology, Nagaoka, Niigata 940-2188

ABSTRACT

Nanosized γ-alumina particles with dispersed zirconia have been synthesized by pulsed wire discharge. An influence of the zirconia dispersion to the transition of alumina from γ to α phase was studied. It is found that the phase transition is restrained by the dispersion of zirconia. In the X-ray diffraction data, no peak shift of alumina has been detected, which indicates no Zr-ion dissolved in an alumina structure. It is considered that the dispersed zirconia behaves as a barrier for the diffusion of alumina, and that it retards the transition of alumina.

I. Introduction

Activated alumina, η, γ and δ-Al_2O_3, has been widely used in chemical industry as catalyst and absorbent. They have the same spinel structure, which are generally called as γ-Al_2O_3 type. It is also known that γ-Al_2O_3 irreversibly transforms to α-Al_2O_3 above 1,100°C. The phase transition to α-Al_2O_3 is accompanied by considerably coarsening and a marked decrease in the surface area, which affects the sinterability and the catalytic activity of γ-Al_2O_3.

The effect of additives on the phase transition temperature has been reported elsewhere[1-6]. For instance, Fe and V_2O_5 reduce the transition temperature[1,2]. In order to increase the transition temperature, ZrO_2 is mostly effective among B_2O_3, SiO_2, Li_2O, LiF, V_2O_5, CuO/Cu_2O, TiO_2+MnO/MnO_3, TiO_2+CuO/Cu_2O and ZnF_2[4]. The increase in the transition temperature was also reported on the ZrO_2 addition [5,6].

In the papers mentioned above, particles were synthesized by wet process that requires complicated process such as washing, drying and heat treatment. In most cases, synthesized particles are strongly agglomerated after drying.

In the present paper, we have synthesized the nanosized γ-Al_2O_3 particles by pulsed wire discharge (PWD)[7-9]. The advantages of PWD are simple, high energy-conversion-efficiency, cheap cost, high production rate and so on[7]. The characteristics of the particles will be mentioned in this paper.

II. Experimental procedures

The experiment was carried out by pulsed wire discharge. The experimental setup is shown in Fig. 1. Stored energy in the capacitor is discharged to thin Al wire, resulting in the formation of aluminum plasma. The ambient gas of oxygen cools the plasma due to the gas molecules interaction with plasma particles. Finally, nanosize particles of γ-Al_2O_3 are formed as a result of condensation. In order to disperse ZrO_2 into γ-Al_2O_3, Zr and Al wires (ϕ 0.25 x 20 mm) were discharged simultaneously in an oxygen gas (400 Torr).

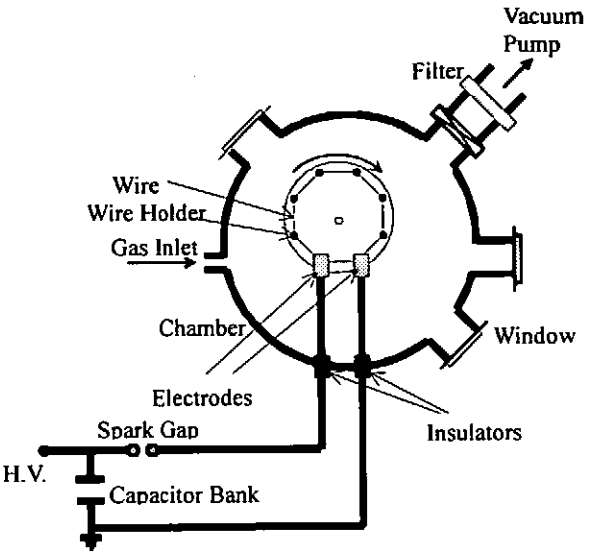

Fig. 1 Schematic of pulsed wire discharge

The distance between wires is less than 1 mm, which were contacted at several points. The capacitor of 10 or 20 μF was discharged by the charging voltage of 5.6 or 6 kV. The molar ratio was adjusted by the number of wires. The composition and the number of wires are summarized in Table I. After the discharges of 8 times, the nanosized particles were collected by being evacuated through membrane filters.

In order to observe the behavior of the discharge of wires, a Zr and an Al wires were first set at a distance of 20 mm. The discharge was observed by high-speed photography (exposure time of 100 ns). The pressure of oxygen was 600 Torr at that time.

Synthesized particles were treated by heating in air between the temperature of 1,000-1,200°C. Heating rate and holding time were 20 K/min and 1 h, respectively.

Powders were characterized by X-ray diffraction (XRD) and transmission electron microscopy (TEM) with energy dispersive X-ray spectroscopy (EDX).

Table I Details of Al and Zr wires and additives

Notation	Zr: Al ratio	ZrO_2 amount (mol%)	Al wire		Zr wire	
			Diameter (mm)	Number of wire	Diameter (mm)	Number of wire
AL	0 : 100	0	0.25	1	0.254	0
AZ11	11 : 89	20		6		1
AZ20	20 : 80	33		3		1
AZ42	42 : 58	60		1		1
ZR	100 : 0	100		0		1

III. Results

Figure 2 shows typical waveforms of current and voltage. Half cycle of the current is 14 μs, and the peak current is 6.5 kA. The oscillation of the current continued for 100 μs. From the current form, inductance was estimated to be 2 μH.

Figure 3 shows high speed photographs of PWD. Explosion of Al wire occurred prior to that of Zr wire. Initially, the shape of the plasmas was cylindrical, and later changed to irregular. Even though the boiling temperature is different, 2,486°C and 3,578°C for Al and Zr, respectively, the discharge happens simultaneously. It seems that the plasmas coexists for 60 μs. Until 1 ms from the switching, emission and/or radiation was observed.

Figure 4 shows a TEM photograph of synthesized particles. Clearly, we see nano particles and submicron particles. The shape of most particles was spherical. From EDX analysis, it was found that submicron particles were ZrO_2 or Al_2O_3 particles.

Figure 5 shows typical XRD patterns of particles as synthesized and after being heat treated. The synthesized particles consisted of γ-Al_2O_3 and ZrO_2 with tetragonal structure. After the heat treatment, γ-Al_2O_3 transformed to α-Al_2O_3. It is found that ZrO_2 partially transformed from tetragonal to monoclinic by heat treatment. According to the phase diagram of ZrO_2, however, it was reported that tetragonal phase is stable above 1,200°C, and monoclinic is stable below the temperature.

Figure 6 shows XRD patterns after heat treatment at 1,150°C. It is clear that the dispersion of ZrO_2 is effective to retard the phase transition of Al_2O_3 from γ to α.

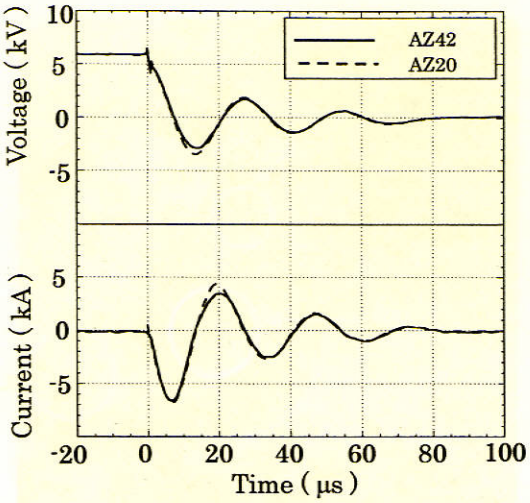

Fig. 2 Typical wave forms of voltage and current. charging voltage 6 kV, capacitance 10 μF

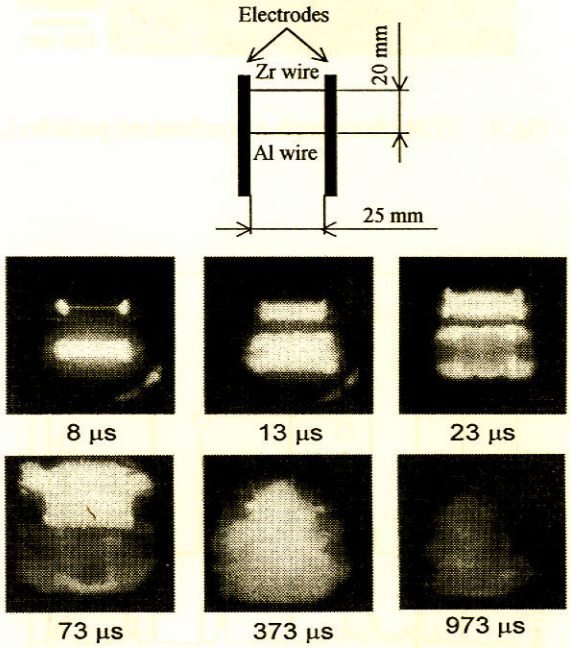

Fig. 3 High speed photographs of Al and Zr dischages

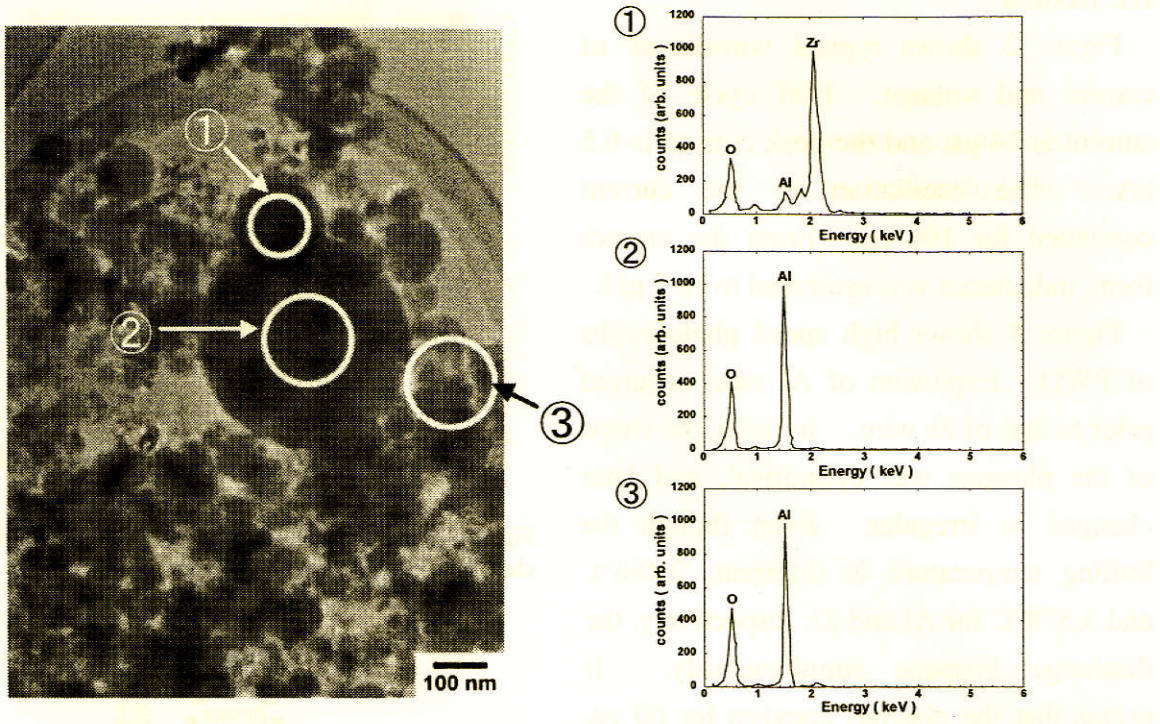

Fig. 4 TEM photograph of synthesized particles (AZ11), and composition by selected area analysis

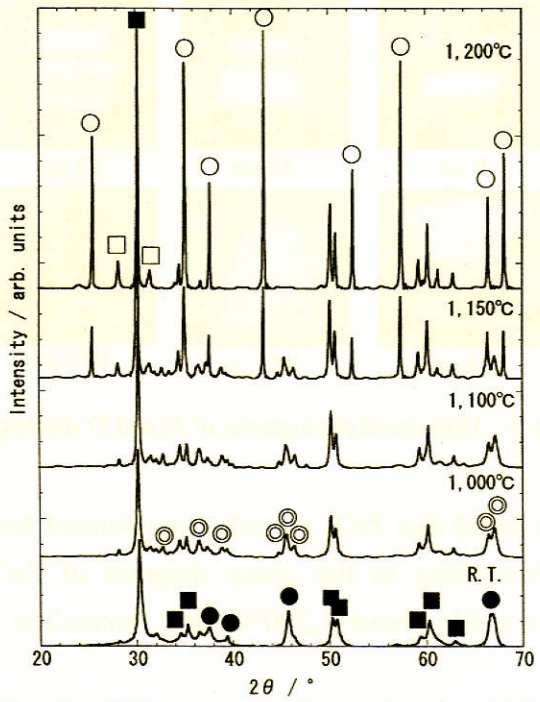

Fig. 5 XRD patterns of particles by AZ11 as synthesized and after heat treatment. Marks ●, ◎, ○, ■ and □ indicate γ-, δ-, α-Al_2O_3, tetragonal ZrO_2 and monoclinic ZrO_2, respectively.

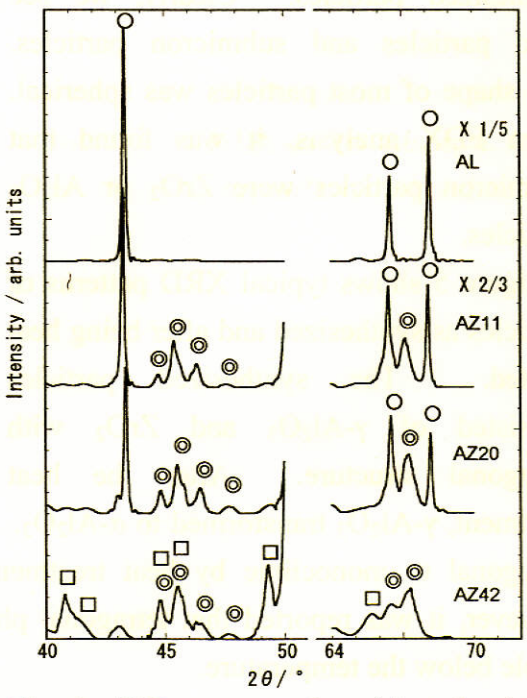

Fig. 6 XRD patterns of particles after heat treatment at 1,150°C. Marks ◎, ○ and □ refer to δ-, α-Al_2O_3 and monoclinic ZrO_2, respectively.

IV. Discussions

By the discharge of Zr and Al wires, it is possible to synthesize Al_2O_3 with dispersed ZrO_2 particles. Mixing different materials in gas phase is expected to be much better, however, it was too difficult to observe by TEM. Most of the particles are several 10 nm in diameter, and some are submicron in size. The dispersion of particle size is larger than that of the particles synthesized from single wire[8]. This may be related to homogeneity of plasma. Multi wire setting may lead inhomogeneity of plasma density compared with that of single wire configuration.

Regarding the influence of ZrO_2 dispersion on the phase transition of Al_2O_3, increase in ZrO_2 is effective to restrain the transformation. Proposed effects of ZrO_2 for the transition may be summarized as follows.

1. Zirconia is a diffusion barrier for the alumina, which restrains the phase transition[4,6].
2. At low temperature, alumina dissolves in ZrO_2. At high temperate, α-Al_2O_3 particles precipitated from ZrO_2 may behave as a seed for the phase transition, which promote the phase transition[6].
3. Zirconia may dissolve in γ-Al_2O_3, which stabilizes the γ-Al_2O_3 structure because of larger ionic radius of Zr^{4+} than that of Al^{3+}. As a result, the γ-phase is sustained at higher temperature than the phase transition temperature of non-doped γ-Al_2O_3[5].

In this experiments, no change in the lattice constant has been observed for Al_2O_3 and ZrO_2 as observed from XRD analysis, which indicates no solid solution in the particles synthesized by PWD. Hence, the effect 2 and 3 above seem to be disregarded. In order to study the effect 1, AZ11 was heat treated at 1,100°C for 10 h and XRD analysis was examined. As a result, clear peaks of α-Al_2O_3 were observed. Therefore, it is believed that ZrO_2 behaves as a diffusion barrier in the present experiment.

V. Concluding remarks

Pulsed wire discharge was applied to synthesize nanosized γ-Al_2O_3 with dispersed ZrO_2. It was observed from XRD measurement that synthesized particles consist of γ-Al_2O_3 and ZrO_2 with tetragonal structure. It was found from TEM photograph that nanosize particles and submicron particles coexist. The phase transition of Al_2O_3 from γ to α was observed by XRD after heat treatment at 1,000 - 1,200°C for 1 h in air. It was found that the increase in ZrO_2 amount is effective to restrain the transition. It is believed that ZrO_2 behaves as a diffusion barrier.

References

1) G. C. Bye and G. T. Simpkin, "Influence of Cr and Fe on Formation of α-Al_2O_3 from γ-Al_2O_3", J. Am. Ceram. Soc., **57**, 367-371 (1974).

2) R. A. Shelleman and G. L. Messing, "Liquid-Phase-Assisted Transformation of Seeded γ-Alumina", J. Am. Ceram. Soc., **71**, 317-322 (1988).
3) I. M. Low and R. Mcpherson, "Crystallization of Gel-Derived Alumina and Alumina-Zirconia Ceramics", J. Mater. Sci., **24**, 892-898 (1989).
4) L. A. Xue and I. W. Chen, "Influence of Additives on the γ- to α- Transformation of Alumina", J. Mater. Sci. Lett., **11**, 443-445(1992).
5) M. Balasubramanian, S. K. Malhotra and C. V. Gokularathnam, "Transformation in Composite Powders of Aluminium and Zirconium Hydroxides", Br. Ceram. Trans., **95**, 263- 266 (1996).
6) K. Daimon, Y. Hikichi, H. Murakami, H. Matsunaka and S. Yamada, "Solid Solution of Zr into Anhydrous $Al_2(SO_4)_3$ Crystanl Lattice and η→α Phase Transformation of Al_2O_3 Formed by Thermal Decomposition of the Sulfate Solid Solution", J. Ceram. Soc. Jpn., **107**, 41-46 (1999). (in Japanese)
7) W. Jiang and K. Yatsui, "Pulsed Wire Discharge for Nanosize Powder Synthesis", IEEE Plasma Sci., **26**, 1498-1501 (1998).
8) T. Suzuki, K. Komson, W. Jiang and K. Yatsui, "Nanosize Al_2O_3 Powder Production by Pulsed Wire Discharge", Jpn. J. Appl. Phys., **40**, 1073-1075 (2001).
9) C. Sangurai, Y. Kinemuchi, T. Suzuki, W. Jiang and K. Yatsui, "Synthesis of Nanosize Powders of Aluminum Nitride by Pulsed Wire Discharge", Jpn. J. Appl. Phys., **40** 1070-1072 (2001).

Recent Issues of NIFS-PROC Series

NIFS-PROC-31 岡本 正雄
講義「核融合プラズマ物理の基礎 - II」
平成 8 年度 総合研究大学院大学 数物科学研究科 核融合科学専攻 1997年 4月
M. Okamoto
"Lecture Note on the Fundamentals of Fusion Plasma Physics - II" Graduate University for Advanced Studies: Apr. 1997 (in Japanese)

NIFS-PROC-32 代表者 河合 良信
平成8年度 核融合科学研究所共同研究 研究会報告「プラズマ中のカオスとその周辺非線形現象」
Y. Kawai (Ed)
Report of the Meeting on Chaotic Phenomena in Plasmas and Beyond, 1996: Apr. 1997 (mainly in Japanese)

NIFS-PROC-33 H. Sanuki,
Studies on Wave Analysis and Electric Field in Plasmas: July 1997

NIFS-PROC-34 プラズマ対向機器・PSI・熱・粒子制御合同研究会報告
平成 9 年 6 月 27 日（金）9:00 ～16:20 核融合科学研究所・管理棟 4 F 第 1 会議室
1997年 10月
T. Yamashina (Hokkaido University)
Plasma Facing Components, PSI and Heat/Particle Control June 27, 1997, National Institute for Fusion Science T. Yamashina (Hokkaido University) : Oct. 1997 (in Japanese)

NIFS-PROC-35 T. Watari,
Plasma Heating and Current Drive: Oct. 1997

NIFS-PROC-36 T. Miyamoto and K. Takasugi (Eds.)
Production and Physics of High Energy Density Plasma: Production and Physics of High Energy Density Plasma: Oct. 1997

NIFS-PROC-37 (Eds.)T. Fujimoto, P. Beiersdorfer,
Proceedings of the Japan-US Workshop on Plasma Polarization Spectroscopy and The International Seminar on Plasma Polarization Spectroscopy January 26-28, 1998, Kyoto: June 1998

NIFS-PROC-38 (Eds.) Y. Tomita, Y. Nakamura and T. Hayashi,
Proceedings of the Second Asian Pacific Plasma Theory Conference APPTC '97, January 26-28, 1998, Kyoto: Aug. 1998

NIFS-PROC-39 (Ed.) K. Hirano,
Production, Diagnostics and Application of High Energy Density Plasmas: Dec. 1998

NIFS-PROC-40 研究代表者 加古 孝（電気通信大学）
所内世話人 渡辺 二太
平成 10 年度核融合科学研究所共同研究 研究会「プラズマ閉じ込めに関連する数値計算手法の研究」
Ed. by T. Kako and T. Watanabe
Proceeding of 1998-Workshop on MHD Computations "Study on Numerical Methods Related to Plasma Confinement Apr. 1999

NIFS-PROC-41 (Eds.) S. Goto and S. Yoshimura,
Proceedings of The US-Japan Workshop and The Satellite Meeting of ITC-9 on Physics of High Beta Plasma Confinement in Innovative Fusion System, Dec. 14-15, 1998, NIFS, Toki: Apr. 1999

NIFS-PROC-42 (Eds.) H. Akiyama and S. Katsuki,
Physics and Applications of High Temperature and Dense Plasmas Produced by Pulsed Power: Aug. 1999

NIFS-PROC-43 (Ed.) M. Tanaka,
Structure Formation and Function of Gaseous, Biological and Strongly Coupled Plasmas: Sep. 1999

NIFS-PROC-44 (Ed.) T. Kato and I. Murakami,
Proceedings of the International Seminar on Atomic Processes in Plasmas, July 29-30, 1999, Toki, Japan: Jan. 2000

NIFS-PROC-45 (Eds.) K. Yatsui and W. Jiang,
Physics and Applications of Extreme Energy-Density State, Nov. 25-26, 1999, NIFS: Mar. 2000

NIFS-PROC-46 研究代表者 加古 孝（電気通信大学）
所内世話人 渡辺 二太
平成 11年度核融合科学研究所共同研究 研究会「プラズマ閉じ込めに関連する数値計算手法の研究」
Ed. by T. Kako and T. Watanabe
Proceeding of 1999-Workshop on MHD Computations "Study on Numerical Methods Related to Plasma Confinement June. 2000

NIFS-PROC-47 岡本正雄、村上定義、中島徳嘉、汪衛生
プラズマ物理におけるモンテカルロシミュレーション
WatanabeM. Okamoto, S. Murakami, N. Nakajima, W.X. Wang,
Monte Carlo Simulations for Plasma Physics: July 2000

NIFS-PROC-48 K. Miyamoto,
Fundamentals of Plasma Physics and Controlled Fusion: Oct. 2000

NIFS-PROC-49 (Ed.) K. Kawahata,
Proceeding of the 5th International Workshop on Reflectometry, 5-7 march, 2001: May 2001

NIFS-PROC-50 (Ed.) S. Ishii
Workshop on Extremely High Energy Density Plasmas and Their Diagnostics, Mar. 8-9, 2001, National Institute for Fusion Science, Toki, Japan: Sep. 2001